The University Of Sheffield.

The production of Ti-Fe alloys using solid-state, powder-based extraction and processing technologies

SIMON JOHN GRAHAM

A thesis submitted in partial fulfilment of the requirements for the degree of
Doctor of Engineering

Department of Materials Science and Engineering
Faculty of Engineering
The University of Sheffield

Supervisor: Prof. Martin Jackson

February 2022

Sheffield Titanium Alloy Research

advanced metallic systems

Abstract

This thesis demonstrates the ability to create Ti-Fe alloys using two solid-state, powder-based technologies: the FFC-Cambridge process and field assisted sintering technology (FAST). Together, these technologies have many proposed benefits for Ti alloy production compared to the conventional route, with potential to significantly reduce the cost of Ti, provided they are effectively scaled up. This work assesses these technologies for the production and processing of Ti alloys, whilst focussing on inexpensive Fe as the major alloying element.

Ti-Fe diffusion couples produced using FAST highlighted that the Fe diffusion rate into Ti increases dramatically from 800–1000°C. Chemical and microscopic analysis revealed that an intermetallic layer formed at the interface, and a gradual decrease in Fe content resulted in microstructural layers of α, $\alpha+\beta$ and β Ti, due to varying β stabilisation.

FAST was then used to consolidate pseudo-binary Ti-Fe alloy powders produced via the FFC-Cambridge process and derived from mixtures of synthetic rutile and Fe_2O_3. Although the powders were chemically heterogeneous, FAST provided the conditions to consolidate to >99% theoretical density and facilitate the Fe diffusion required to generate homogeneous microstructures. Alloys containing up to 9 wt.% Fe were produced, but final compositions were inconsistent compared to the amounts of Fe_2O_3 used, indicating Fe loss to the electrolyte. Despite poor ductility of the alloys due to high O contents, this production route combining the FFC-Cambridge process with FAST shows promise, with this work representing a proof of concept which can be improved upon by future optimisation.

Solid-state alloying of blended Ti and Fe powders was also investigated, establishing that homogeneous, fully dense alloys with compositions up to Ti-10Fe can be produced using

FAST with no intermetallic phase formation. These alloys also exhibited low ductility, although using an alternative, lower O content, Ti powder could improve the results.

Acknowledgements

Firstly, I wish to thank my supervisor, Prof. Martin Jackson, for his support and guidance throughout the project. His enthusiasm about the pursuit of low-cost titanium has been motivational, making me realise and appreciate the value of my work. Thanks to him, I have developed confidence and belief in myself as a researcher, which will benefit me for the rest of my career.

I feel fortunate to have been a part of the Sheffield Titanium Alloy Research (STAR) group, and although members must continually join and leave, everyone has been so kind and helpful. I am grateful to Dr. Ben Thomas and Dr. Nick Weston for training and assistance on the FAST equipment, along with Dr. Oliver Levano Blanch, who has always made himself available for valuable discussions and advice.

The project was funded by Engineering and Physical Sciences Research Council grant code EP/L016273/1 through the Centre for Doctoral Training (CDT) in Advanced Metallic Systems. Thanks to Dr. Claire Hinchcliffe, Sharon Brown and all other staff who were involved in running the CDT.

Experiments on the FFC-Cambridge process were performed using equipment at Metalysis' Materials Discovery Centre. It was a great experience working there and I wish it could have been for longer. I am grateful to all staff for their contributions to this work, including Claire Seddon, Joe Hardman, Dr. Nader Khan, Sarah Boot, Basharat Ali, Dan Kitson, Dr. Stephen Repper, Tim Johnson, Dr. Luke Marshall, and Dr. Ian Mellor. Special thanks to my industrial supervisor, Dr. Lyndsey Benson, for all her support and advice, especially when it came to publishing the journal article presented in Chapter 5.

The EPMA data in Chapter 4 was collected by Dr. Dikai Guan, whose efforts were much appreciated. Some of the following results contributed to a journal article in collaboration with researchers at The University of Sheffield, KTH Royal Institute of Technology, and

Contents

Chapter 1

Introduction

1.1 Background

Titanium (Ti) and its alloys are materials in high demand due to their unique and impressive set of properties. These include an exceptional strength to weight ratio, excellent chemical and corrosion resistance, biocompatibility, and their ability to be used over wide temperature ranges. Ti alloys make ideal material candidates for a wide variety of components, spanning many different industries. Despite this, their use has generally been limited and inferior materials used instead for many applications. This is due to the significant costs associated with commercial scale production and processing of Ti, despite the ore being relatively abundant. For some industries, these high costs are considered acceptable as there are instances where alternative materials are simply inadequate in comparison. For example, Ti alloys are commonly used for the manufacture of components in the aerospace industry, where the balance between weight and performance is critical. Significantly reducing the cost of Ti would have a major impact for many industries, especially automotive where it could be used to replace steel, reducing component weights and subsequently improving the fuel efficiency of vehicles [1]. This would, however, either require major changes to the current production route or the realisation of a new low-cost alternative.

Therefore, it is important to understand the current commercial production route, from ore to finished component, and the costs associated with each stage. The main steps involved are as follows, with Figure 1.1 illustrating an example of how costly each of the steps can be relative to each other:
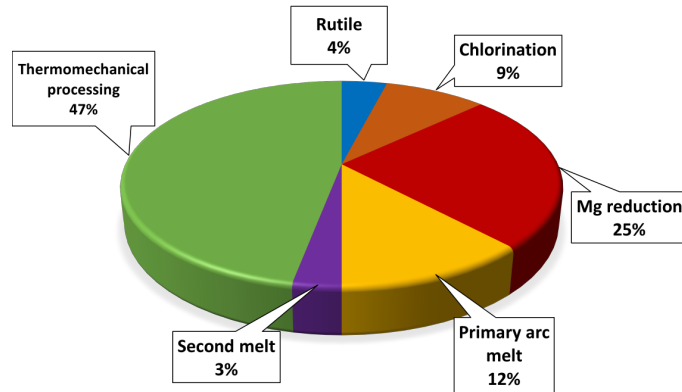
FIGURE 1.1: The relative costs associated with conventional production of a 1" Ti plate (from data reported in [2]).

1. Mining and processing of mineral sands containing Ti ores

2. Extraction of Ti metal from ore via the Kroll process

3. Addition of alloying elements and vacuum arc melting

4. Thermomechanical processing, such as open-die forging

5. Shaping via casting, closed-die forging and/or machining

Although Ti ores are relatively abundant, rutile (TiO_2) is more commonly used for white pigment production rather than for Ti metal production and so price and availability is dependant on other markets. Chlorination and Mg reduction in the Kroll process are expensive, as are the multiple melting stages required to ensure alloy homogeneity. Ti has a relatively high melting point of 1668°C compared to other commonly used metals (aluminium =660°C, stainless steels ~1400–1500°C), and therefore more energy is required in the melting stages. Downstream processing, which includes both steps 4 & 5, is clearly the most expensive part of the route, however. This is due to the many challenges in hot working and machining Ti, most notably its high reactivity with atmospheric O_2 and N_2 gases, therefore requiring many processing stages to be performed under vacuum or inert gas atmospheres. Final components often have complex geometries and so extensive machining is required, consequently resulting in considerable material wastage and poor buy-to-fly ratios. It is common to have final parts weigh < 10% of the initial forging mass, with most of the billet converted to machining swarf [3]. Ti is also notoriously difficult to machine compared to aluminium alloys and steels, due to its high strength at high temperatures and low thermal conductivity which cause considerable tooling wear [4].

Overall, the costs associated with each of these stages combine to make Ti component production relatively expensive compared to commodity metals. This work therefore considers the use of alternative technologies which can potentially offer a wide range of benefits over those used in conventional processing.

A number of alternative extraction methods to the Kroll process have been proposed, many of which do not require the conversion to the intermediate volatile compound $TiCl_4$, and instead directly convert the oxide to the metal. These could replace both 'Mg reduction' and 'chlorination' from Figure 1.1 and, provided the alternative costs are lower, would reduce overall Ti component cost.

The FFC-Cambridge process is one such alternative extraction process and uses electro-chemical deoxidation to directly reduce TiO_2 into pure Ti metal [5]. On paper, it is much simpler than Kroll-based extraction, whilst producing similar results with far fewer steps involved and potentially lower costs [6], [7]. The process is also capable of reducing many different metal oxides as well as mixtures of metal oxides to directly produce alloys. Various Ti alloys have subsequently been produced, including the most commonly used alloy, Ti-6Al-4V [8]. Since its discovery, the FFC-Cambridge process has continued to be developed by Metalysis, a UK startup company created to commercialise this technology. There has been much interest in the process and the company, especially due to the potentially positive impact it could have on the Ti industry [9].

Another advantage of the FFC-Cambridge process is that metals/alloys are directly produced in powder form, and so combining this promising extraction process with powder metallurgy offers an attractive prospect of a simpler processing route from ore to component. Near-net shape manufacturing using powder metallurgy has been a growing area of interest, due to the benefits of reduced material waste and ability to create complex geometries [10]. Much focus has been on additive manufacturing powder metallurgy techniques akin to 3D printing, which melt metal powders in layers to form intricate shapes from computer-aided design models. Unfortunately, these techniques are quite particular in regard to the morphology and size of the metal powders used, and therefore powders produced via the FFC-Cambridge process would require an extra atomisation step to make them suitable for use [11]. Although this is a valid area of research, other powder metallurgy techniques exist which are capable of consolidating metal powders in

the solid state and being flexible in terms of powder characteristics.

Field assisted sintering technology (FAST), also known as spark plasma sintering, is an effective solid-state consolidation technique for metal powders [12]. One of the main advantages of this technique is the rapid heating rates achievable due an applied electric current flowing directly through the material. This, combined with uniaxial pressure, allows for efficient consolidation within minutes, rather than hours for other sintering techniques [13]. The consolidated material can be forged to create near-net shape components whilst minimising machining wastage, developed as the FAST-*forge* process at The University of Sheffield. Using this technology can replace the melting stages and reduce fabrication costs shown in Figure 1.1. A continually increasing number of FAST machines are being produced and installed worldwide, with their scale also increasing, with apparatus allowing the production of parts up to 400 mm in diameter [14], [15]. This shows that the technology has potential to be used for the processing of Ti powders on industrial scales.

A further consideration is the feedstock used for extraction. Although pure TiO_2 has been used in many alternative extraction processes, which is acceptable for proof of concept, it would not be economical to use it on larger production scales. Therefore, the use of lower purity TiO_2 must be considered to further reduce costs. Ilmenite ore ($FeTiO_3$) is far more abundant and therefore cheaper than natural rutile, with 95% of minable Ti in the form of ilmenite [16]. This ore can be processed to remove the iron (Fe) to leave a material containing 90–95% TiO_2, known as synthetic rutile (SR). SR has been directly reduced using the FFC-Cambridge process to create a Ti alloy powder containing impurities as alloying elements [17].

Reducing SR alongside other metal oxides can be done to produce a range of SR derived alloys which build upon this research. Ti is often used as an alloy, for example as Ti-6Al-4V, rather than in its elemental form. Addition of alloying elements can be another significant expense, with costly elements like Mo often used. Therefore, use of cheaper alloying elements such as Fe is appealing, with some manufacturers developing alloys which replace some costly elements with Fe. An example of this is TIMET's LCB (low cost beta) alloy with composition Ti-6.8Mo-4.5Fe-1.5Al, designed for automotive springs, which reduces the cost compared to heavily alloyed alloys like Beta-C (Ti-3Al-8V-6Cr-4Mo-4Zr)

[18]. Fe has limited use in Ti alloys though, due to segregation issues which occur during solidification [19]. Solid-state extraction and processing via the FFC-Cambridge process and FAST can avoid these issues and allow for the production of Ti alloys with greater Fe contents.

Exploiting Fe as an alloying element via solid-state alloying from blended elemental powders is another avenue of research which has gained some attention recently [20]. Ti and Fe powders are blended together, pressed, sintered and heat treated to fully dissolve the Fe into Ti and achieve homogeneous microstructures. Work thus far, however, has used very fine powders, high temperatures and long sintering times [21]. Therefore, the cost-reduction achieved by use of Fe may be negated by these processing issues. This could be improved by using coarser powders and FAST, which combines press and sinter into one step. Coarser powders would require longer processing times to achieve homogeneity and so a balance must be found between powder and processing costs. Understanding the solid-state diffusion behaviour of the Ti-Fe system during FAST processing is also key in understanding required processing conditions.

Overall, compiling these ideas together leads to three main areas of novel research, explained in the following research objectives. The results of this research presented in this thesis further develop some future possibilities in the cost reduction of the production of Ti alloys, potentially leading to their greater usage in currently non economically viable applications, such as in the automotive industry.

1.2 Research objectives

The main objectives and how they are achieved is listed here for the novel research presented in Chapters 4, 5 and 6. In addition, important aspects of materials science and Ti production and processing methods are covered in Chapter 2, along with an up-to-date review of relevant published research. Chapter 7 then summarises the results, reflects on the original objectives, and suggests areas of future research.

The diffusion behaviour of the Ti-Fe system during FAST processing

As this research focusses heavily on solid-state processing of the Ti-Fe system, it is important to first investigate and understand the diffusion expected to occur during FAST.

Main objectives:

- To accurately measure the diffusion distance of Fe into Ti at different temperatures and dwell times

- To understand and quantify the effect of Fe content on the resulting Ti phases present and microstructure after processing

- To understand the formation of intermetallic phases at the interfaces between Ti and Fe

Experimental work required:

- Production of Ti-Fe diffusion couples and processing using FAST. The diffusion couples can be produced from elemental powders using FAST, then held at set temperatures and times to create a range of samples for analysis

- Use of various techniques for elemental and microstructural analysis across the Ti-Fe interfaces, including scanning electron microscopy and electron microprobe analysis

Direct electrochemical production of pseudo-binary Ti-Fe alloys from synthetic rutile and iron oxide

Combining material produced via the FFC-Cambridge process with FAST processing is an attractive area of research to propose an alternative Ti production route. Use of SR as the feedstock has also been successful, with further Ti alloy development possible by combining SR with other metal oxides.

Main objectives:

- To utilise low-cost starting materials (SR and Fe_2O_3) for the production of Ti-Fe alloys

- To use unconventional, solid-state processes to convert the mixed oxide powders to solid alloy material

- To understand the effect of Fe content on the microstructure and properties of the Ti alloy derived from SR

- To assess the potential of this processing route for Ti alloy production

Experimental work required:

- Use electrolysis cells at Metalysis' Materials Discovery Centre to reduce blends of SR and Fe_2O_3 to Ti-Fe alloy powders via the FFC-Cambridge process

- Consolidate the Ti-Fe alloy powders into bulk material using FAST

- Analyse the chemistry and microstructure of the material at each stage of this processing route

- Assessment of mechanical properties by tensile and hardness testing

Production of binary Ti-Fe alloys from blended elemental powders using FAST

FAST provides the necessary conditions to achieve both powder consolidation and solid-state diffusion, therefore it should be an effective technique for the production of Ti-Fe alloys from blended elemental powders.

Main objectives:

- To assess the ability to produce homogeneous Ti-Fe alloys from blended elemental powders using FAST

- To produce a range of Ti-Fe alloys in which the only variable is Fe content, preventing chemistry variation seen in alloys produced via the FFC-Cambridge process

- To investigate the maximum Fe content which can be achieved without formation of intermetallic phases

- To assess the mechanical properties of Ti-Fe alloys produced by this method

- To compare binary Ti-Fe alloys with the pseudo-binary ones produced via the FFC-Cambridge process and understand the effect of other alloying elements remaining from SR

- To compare FAST with other technologies which have been used to process blended elemental powders

Experimental work required:

- Mixing and FAST processing of Ti and Fe powders

- Optimisation of FAST processing parameters required to homogenise chemistry and microstructure

- Microstructural analysis of the resulting consolidated material

- Assessment of mechanical properties by tensile and hardness testing

Chapter 2

Literature review

2.1 Titanium and titanium alloys

2.1.1 Basic properties

Titanium (Ti) is a transition metal element which is highly desirable as a material due to its unique combination of properties:

- Strength to weight ratio: Ti is considered a light metal as it has a density of 4.5 g/cm^3, but has similar a yield stress to iron which is much denser at 7.9 g/cm^3

- Corrosion resistance: Ti readily reacts with O_2 gas and will immediately form a stable surface oxide layer, protecting the underlying metal against many corrosive environments

- Biocompatibility: Ti is non-toxic, remains inert within the body and has good mechanical properties for its weight. This makes it ideal for use in biomedical implants, prosthetics and orthodontics

- Operating temperature: different alloys can be utilised over wide temperature ranges, from cryogenic (-252°C) in rocket engines to ∼600°C in gas turbine engines [22]

Pure Ti exists as two different allotropes, with the transformation between them occurring at 882°C at standard pressure. Below this temperature, the atoms are arranged in a hexagonal close packed (HCP) crystal structure, referred to as α phase. Above 882°C, up to the melting point of 1668°C, a body centred cubic (BCC) crystal structure is more

thermodynamically stable, referred to as β phase. Figure 2.1 shows the unit cells of the two phases. The transition temperature, above which Ti is entirely in the β form, is known as the β-transus.
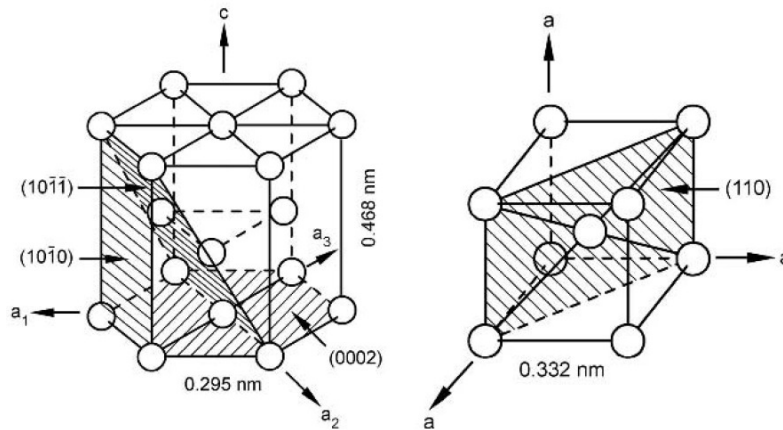
FIGURE 2.1: Diagrams of Ti units cells, with labelled dimensions and crystallographic planes. Left: α phase HCP unit cell, right: β phase BCC unit cell [3].

2.1.2   Effects of alloying elements

Alloying elements and impurities can affect the β-transus and, consequently, the ratio of the phases present in the material. They can also introduce new phases to the system, such as intermetallics which further influence the microstructure. They are categorised by their ability to stabilise the α and β phases. α stabilisers, including Al and the interstitial elements O, N and C, raise the β-transus with increasing content. β stabilisers lower the β-transus, and are either of the isomorphous or eutectoid type. Isomorphous stabilisers, including Mo, V, Ta and Nb, have unlimited solid solubility in β Ti and therefore will reduce the β-transus with increasing content. These elements can reduce the β-transus to around room temperature if sufficient amounts are used. Eutectoid stabilisers, including Fe, Mn, Cr, Co, Ni, Cu, Si and H, have lower solubility in β Ti and can form intermetallic compounds at relatively low concentrations. Lowering of the β-transus will only occur down to the eutectoid temperature and so these elements are limited in their ability to retain β at room temperature. Other elements, e.g. Sn, Zr and Hf are generally considered as neutral elements as they have little effect on the β-transus. Figure 2.2 highlights these effects of different alloying elements on Ti and the resulting phase diagrams.
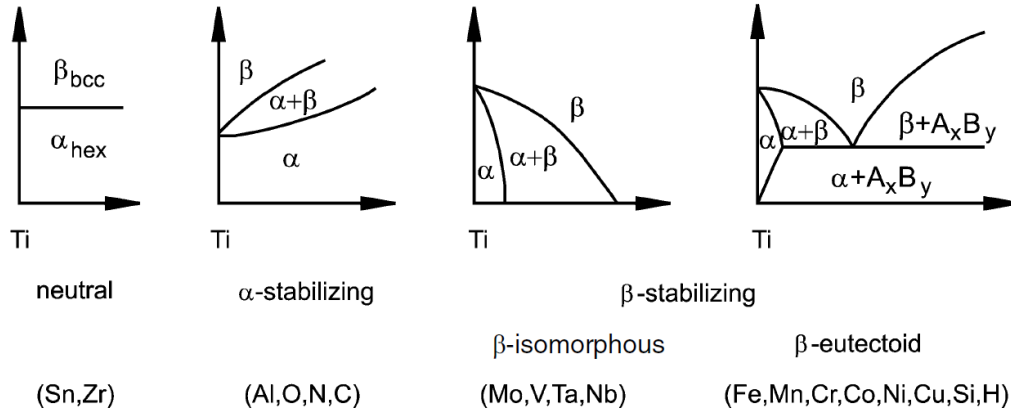
FIGURE 2.2: The types of Ti alloy phase diagrams and the elements associated [23].

The phase stability of an alloy can be estimated by calculating the Al equivalency, $[Al]_{eq}$, (for α phase stability) and Mo equivalency, $[Mo]_{eq}$ (for β phase stability). These equations use both the concentration of each element in the alloy and their relative stabilising strength for α or β [24]. All coefficients are based on weight % (wt.%).

$$[Al]_{eq} = [Al] + 0.17[Zr] + 0.33[Sn] + 10[O + N] \tag{2.1}$$

$$[Mo]_{eq} = [Mo] + 0.22[Ta] + 0.28[Nb] + 0.44[W] + 0.67[V] + 1.25[Ni] + 1.60[Cr]$$
$$+ 1.70[Mn] + 1.70[Co] + 2.9[Fe] - 1.0[Al] \tag{2.2}$$

Although Sn and Zr are classed as neutral elements as they do not affect the β-transus, they do have some α stabilising ability when Al is present and are therefore included in Equation 2.1 [3]. It is important also to note the strong α stabilising ability of the interstitial elements. $[Al]_{eq}$ is usually limited to ~9% due to formation of intermetallic phases and reductions in ductility [25]. The β stabilising elements are all transition metals and have a range of potencies, with the β eutectoid elements being more effective at low concentrations than the β isomorphous.

By exploiting the stabilising effects of different alloying elements, and combining multiple elements, a wide range of alloys can be created. The ratio of the phases in the alloy is determined by the alloying elements used, their quantities and the thermal processing history. This ratio plays a crucial role in determining the mechanical properties of the

material and therefore Ti alloys are classified by the phases present in the microstructure at room temperature. Figure 2.3 shows the main different alloy types.
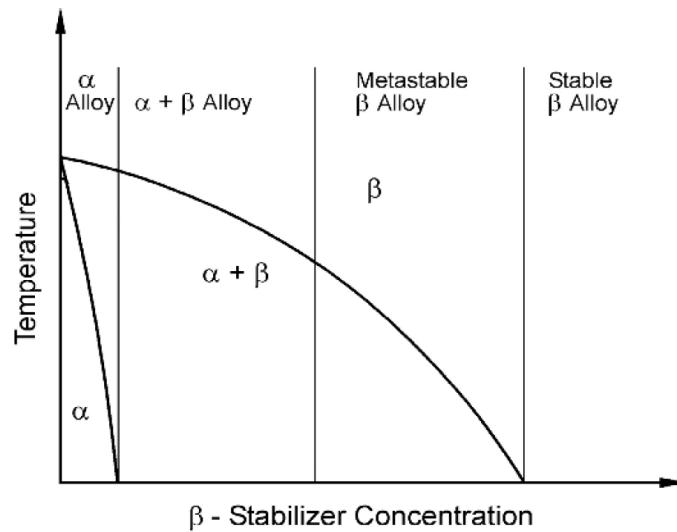
FIGURE 2.3: The different types of alloy classification, using a β isomorphous phase diagram, modified from [3].

Effect of interstitial elements

O, N, C and H have atomic diameters <0.6 times the atomic diameter of Ti and therefore can occupy interstitial sites in the lattice structure [26]. These elements all have profound effects on Ti, even at low concentrations. Therefore, there are limits on their contents in commercial alloys due to some undesirable effects and so their presence must be carefully monitored and controlled during production and processing.

Equation 2.1 shows that O and N are very potent α stabilisers, with high solubility in this phase. Unfortunately, Ti has a high affinity for O, making processing the metal difficult as it is easily re-oxidised, especially at elevated temperatures. Surface oxide formation is especially important when considering Ti powders due to their large exposed surface area, so powders with smaller particle sizes will inherently contribute to higher O contents in material resulting from powder metallurgy techniques. N has an even greater effect than O, although is generally not such an issue as it does not react as readily with Ti [27]. The O content has a significant effect on the mechanical properties of Ti alloys, for example, going from commercially pure (CP) Ti grade 1 (containing 0.18 wt.% O) to CP Ti grade 3 (containing 0.4 wt.% O) increases the yield strength substantially, from 170 MPa to 480

MPa under identical processing conditions [28]. This is explained by a change in slip character above 0.25 wt.% O and a reduced likelihood for twinning to occur [29].

C has very limited solubility of 0.48 wt.% in α and 0.15 wt.% in β at 920°C, and therefore forms a carbide (TiC) ceramic phase, even at low concentrations. TiC is a brittle phase and therefore is detrimental to the ductility. Small amounts in solid solution increase the strength considerably, in a similar way to O and N [30].

H is unlike the other interstitial elements and is a β stabiliser. It has relatively high solubility in the β phase, but none in α at low temperatures. Above around 3 wt.% (depending on temperature), a face centred cubic phase known as δ forms. Ti is susceptible to absorption of H, which leads to H embrittlement, where the formation of brittle hydrides causes enhanced crack propagation [31].

2.1.3 Titanium alloy classifications

There are three main classifications of Ti alloys: α, $\alpha+\beta$ and β alloys. Alloys are named based on their mass compositions, e.g. Ti-6Al-4V, which contains 6 wt.% Al and 4 wt.% V. Commerical alloys are also often referred to by their 'grade' (e.g. Ti-6Al-4V is grade 5), of which there are 39 according to ASTM International [32].

α alloys include CP Ti and alloys which essentially contain only the α phase when processed below the β-transus. These alloys are known for their excellent corrosion resistances and formability. Figure 2.3 shows that α alloys cannot benefit from heat treatments as they are single phase and this differentiates them from the other alloy classes. There are four CP grades (grades 1-4) which differ in increasing O content from 0.18 to 0.40 wt.% (Table 2.1). The small increase in O content has a profound effect on the mechanical properties however, as discussed in Section 2.1.2. Higher O causes reduced ductility alongside increased strength, however, so each grade is suited to different applications. Other α alloys include those containing Al, Sn, and Pd, which improves corrosion resistance [3]. A small group of alloys can be categorised as near-α alloys, as they contain small amounts of β stabilisers and retain some β phase on cooling. These alloys have improved strength and are well suited to high temperature applications, up to around 550°C [23], [25].

$\alpha + \beta$ alloys are a diverse range of alloys including Ti-6Al-4V, which, because of its good balance of properties, is by far the most used Ti alloy. As these are dual-phase alloys, they can be heat treated and when quenched from above the β-transus will undergo a martensitic (diffusionless) transformation (as shown in Figure 2.3). This class is diverse because the microstructures of these alloys can be tailored by thermo-mechanical processing to give materials with a wide range of properties for many applications.

The last class are β alloys, which contain sufficient β stabilising elements that they will not undergo a martensitic phase transformation when quenched from above the β-transus, resulting in retained metastable β phase [27]. These alloys are attractive due to their high strengths from fine α precipitation, whilst maintaining good ductility by controlling β grain sizes [33]. Most β alloys are metastable β alloys as α precipitation can occur on cooling. Stable β alloys are single phase at room temperature, as α formation is thermodynamically prevented. These alloys are less common however, and contain relatively high amounts of other elements, leading to very high $[\text{Mo}]_{\text{eq}}$ values, e.g. Ti-35V-15Cr (Alloy C) has a $[\text{Mo}]_{\text{eq}}$ of 47.5 [24].

2.1.4   Commercial titanium alloy examples

Table 2.1 compares a small range of common commercial Ti alloys. Despite the many different alloys available, Ti-6Al-4V is by far the most popular with greater than 50% of all Ti alloys in use being this composition [23]. The comparisons also highlight the relationship between $[\text{Al}]_{\text{eq}}$, $[\text{Mo}]_{\text{eq}}$ and the β-transus temperature.

TABLE 2.1: Examples of some commercially available Ti alloys, with corresponding Al and Mo equivalences, β transus temperatures and some applications.

Alloy type	Alloy	Composition	$[Al]_{eq}$	$[Mo]_{eq}$	β-transus (°C)	Applications
α	CP Grade 1	max 0.2% Fe, 0.18% O	-	-	890	Jet engine shrouds, cases and airframe skins, corrosion-resistant equipment for marine and chemical processing industries
	CP Grade 4	max 0.5% Fe, 0.40% O	-	-	950	
α	Ti-5-2.5 (Grade 6)	5% Al, 2.5% Sn	5.8	-5.0	1040	Gas turbine engine castings, chemical processing equipment for use up to 480°C
Near-α	Ti-811 (Grade 8)	8% Al, 1% Mo, 1% V	8.0	-6.3	1040	Forgings for jet engine components
$\alpha+\beta$	Ti-64 (Grade 5)	6% Al, 4% V	6.0	-3.3	995	High strength prosthetic implants, chemical-processing equipment, airframe structural components
$\alpha+\beta$	Ti-662	6% Al, 6% V, 2% Sn	6.7	-2.0	945	Rocket engine case airframe applications and high-strength airframe structures
β	Ti-5553	5% Al, 5% V, 5% Mo, 3% Cr, 0.5% Fe	5.0	9.6	850–880	High strength alloy used in aerospace structural components e.g.airframe and landing gear
β	Ti-Beta C (Grade 19)	3% Al,8% V, 6% Cr, 4% Mo, 4% Zr	3.7	19.0	793	Parts of aircraft landing gear and in fasteners used in the automotive industry

Adapted from [34]. β-transus values from [25], [35], [36], applications from [34]

2.1.5   Strengthening mechanisms in titanium

There are two main strengthening mechanisms which are important for the following Ti alloy development: grain boundary strengthening and solid solution strengthening.

Grain boundary strengthening

Grain size has a major impact on strength of many materials, including Ti alloys. There is an inverse relationship between yield strength and grain size, known as the Hall-Petch relationship. This is explained by the effect of grain boundaries have on impeding dislocation motion through a metal. Dislocation motion, and therefore deformation, occurs along a slip plane within a grain. When it encounters a grain boundary, the direction of the slip plane must change based on the orientation of the next grain, requiring more energy. Therefore, a fine grained structure has more grain boundaries and more energy is required for deformation, increasing the strength [34]. This is important in α and $\alpha+\beta$ Ti alloys, rapid cooling from the β region causes the formation of fine α grains, giving the material high strength [3]. Grain growth occurs when metals are held at high temperatures, for example during heat treatments, and therefore hold times and temperatures should not be excessive to prevent this.

Solid solution strengthening

Alloying elements or impurities in solution cause strains in the crystallographic lattice due to their differing atomic size to the host. For example, relatively small O atoms occupy interstitial sites within the HCP or BCC lattice, causing neighbouring Ti atoms to experience tensile strain. The opposite effect occurs with a substitutional atom, such as Mo, where the Ti atoms instead experience compressive strain. Solute atoms segregate around dislocations causing a reduction in the overall strain energy. This means that more energy is required to begin and continue dislocation movement, leading to an increase in strength [34].

2.1.6   Solid-state diffusion in titanium

Diffusion occurs many orders of magnitude slower in the solid state compared to in liquid and gaseous. In densely packed metals, diffusion rates are approximately on the μm/s

scale when close to the melting point, dropping to nm/s at half the melting point. At room temperature, diffusion rates are essentially zero, except for some small interstitial atoms [37]. Therefore, alloying of metals is typically achieved during melting to ensure homogenisation over short time periods. Solid-state diffusion is still important in conventional alloying however, with homogenisation heat treatments below the liquidus commonly used to eliminate segregation of alloying elements resulting from solidification. It is also an important consideration when using alloys for prolonged use in high temperature environments, and to understand phenomena such as H embrittlement.
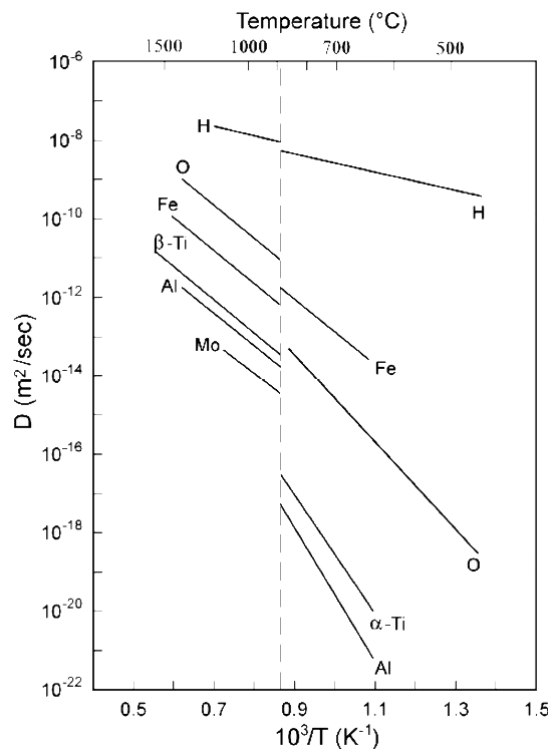
FIGURE 2.4: Temperature dependence of diffusion rates of various elements, as well as self diffusion, in α and β Ti [3]. The dashed line represents the β-transus temperature.

The diffusion rates of alloying elements vary considerably, as shown in Figure 2.4. This means that different processing temperatures and durations are required to achieve homogeneity during heat treatments for different alloys. The variation in diffusion rates can be explained by the following variables:

1. Diffusion mechanism - There are two main mechanisms by which atomic diffusion occurs in crystalline materials, interstitial diffusion and vacancy diffusion. Interstitial diffusion occurs when atoms move via unoccupied interstitial sites within the lattice.

Vacancy diffusion occurs when an atom within the matrix moves to a vacant site in the matrix. Vacant sites are common point defects within crystal structures and facilitate diffusion in this way. Vacancy diffusion is slow compared to interstitial, as there must be a vacancy present for an atom to move position and vacancies are less available than interstitial sites [37].

2. Ti crystal structure - Diffusion generally occurs more slowly in the α phase due to the higher packing efficiency of atoms in HCP versus BCC, making movement of atoms within the lattice more difficult [23].

3. Temperature - Higher temperatures cause higher diffusion rates due to increased thermal vibration of the atoms, making it easier for atoms to overcome any energy barriers to movement. The temperature dependence of diffusion coefficients is given by Equation 2.3. Taking the log_{10} of each side gives an equation in the form $y = mx + c$, where linear relationships between D and T can be obtained, as shown in Figure 2.4 [34].

$$D = D_0\, exp\left(-\frac{Q_d}{RT}\right)$$
(2.3)

D_0 = a temperature-independent pre exponential (m^2/s)

Q_d = activation energy for diffusion (J/mol)

R = gas constant ($8.31 J/molK$)

T = temperature (K)

4. Concentration gradient - presence of a concentration gradient increases the diffusional flux.

The diffusion of specific elements in Ti is therefore determined by whether they can move by a vacancy or interstitial mechanism, which is ultimately governed by their atomic size. O, C, N and H are referred to as interstitial alloying elements, due to the fact that they have small atomic radii and so can diffuse via interstitial sites. As discussed in Section 2.1.2, these elements can all be detrimental to the mechanical properties of Ti alloys. Their high diffusion rates makes it particularly important to avoid prolonged exposure during Ti production and processing. β eutectoid elements have smaller atomic diameters than β

isomorphous ones, as explained by the Hume Rothery rules which state that if the atomic size differs too much from that of Ti then solubility is limited. Due to their smaller atomic size, β eutectoid elements also diffuse via interstitial sites, unlike β isomorphous elements which move via the vacancy mechanism, hence their faster diffusion rates.

The Kirkendall effect

When two metals, A and B, are brought into contact with each other, diffusion will begin to occur across the interface. If the diffusion rate of A into B is different to B into A, then there will be an imbalance in the diffusion taking place. This leads to a net flow of matter across the interface, in the direction of the faster diffusing species. This phenomenon, known as the Kirkendall effect, confirms that diffusion occurs via vacancies and not by an atomic exchange mechanism, as this would not cause a net transfer of matter. The Kirkendall effect often leads to the formation of porosity, known as Kirkendall porosity or voiding. This occurs because the net transfer of matter via vacancy diffusion leaves excess vacancies at the interface, on the side of the slower diffusing species. Over time, these vacancies can agglomerate to form significant porosity, which can be detrimental to mechanical properties of the join [37].

2.2   Conventional titanium production route
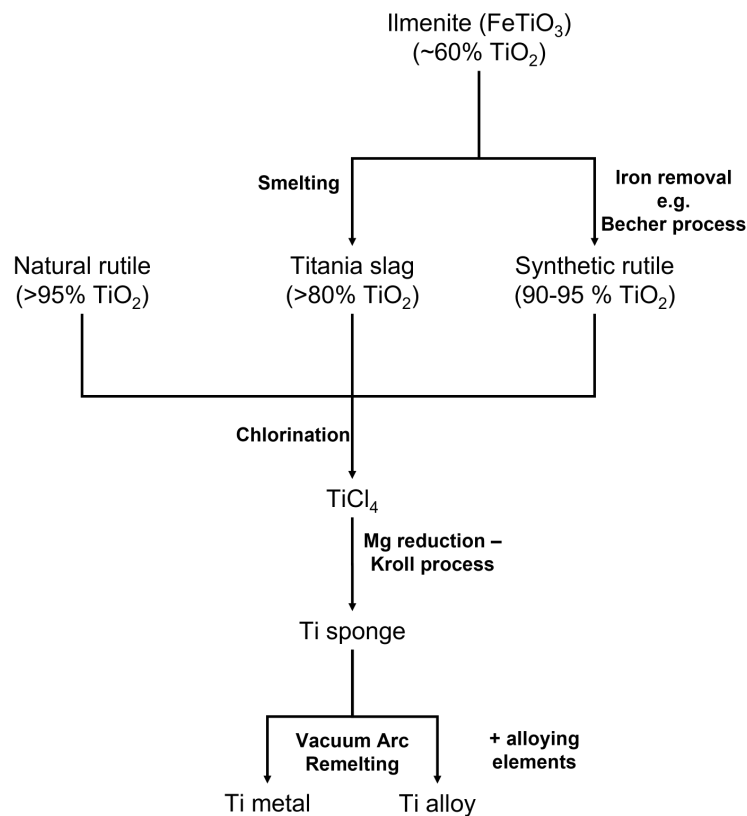
FIGURE 2.5: Flowchart summarising the process steps involved in conventional Ti ore refining and Ti metal production.

2.2.1   Titanium ores and refining

Despite being expensive in its metallic form, Ti is the ninth most abundant element in the Earth's crust and the ores are easily accessible as heavy mineral sands [38]. Therefore, it is clear that the cost involved in producing Ti are at the extraction and processing stages and not with the sourcing of raw materials. Only about 5% of the world's annual production of Ti minerals goes to make Ti metal, however, with the rest used to make pure TiO_2 as a pigment for use in many products such as paints, paper, plastics, rubbers and even foods [39]. TiO_2 is the most widely used white pigment due to its high brightness and refractive index, and so has a high global demand and price which has significant impacts on the Ti industry.

Ti is naturally found in several mineral forms, as either oxides or silicates, the most abundant, and therefore important, of which are rutile and ilmenite (Table 2.2). Rutile is a

TABLE 2.2: Most common naturally occurring Ti containing compounds.
*Stoichiometric values . Adapted from [40].

Mineral	Theoretical formula	TiO_2 content (%)
Rutile	TiO_2	>95
Anatase	TiO_2	>95
Brookite	TiO_2	>95
Ilmenite	$FeTiO_3$	52*
Perovskite	$CaTiO_3$	59*
Titanate (sphene)	$CaTiSiO_5$	41*

high purity, natural form of TiO_2, and can be used directly in most extraction processes. Ilmenite is a more abundant mineral with an idealised chemical formula of $FeTiO_3$, although the exact composition varies depending on geographical location and processing conditions. The significant Fe content present must be removed prior to Ti extraction. As it is more abundant than rutile, it is also cheaper to use despite the additional processing stage. According to the U.S. Geological Survey, in 2020, average year end price of rutile was $1200 per metric ton, compared to $210 for ilmenite. Approximately 7,600 tons of ilmenite were mined in 2020, compared to only 630 tons of rutile, indicating just how much more abundant ilmenite is [41].

Ilmenite is upgraded to a Ti enriched synthetic rutile by Fe removal via the Becher process. The TiO_2 content of the material is increased from $\sim$60 wt.% to up to 95 wt.%, making it chemically similar to rutile [42]. The Becher process was first developed in 1961 in Australia, where large ilmenite reserves exist, to make the mining of ilmenite more lucrative [43]. It involves multiple steps to remove the Fe. Firstly, the ilmenite is heated using coal in rotary kilns at $\sim$1100 °C. This allows carbon monoxide to reduce most of the Fe oxides to metallic Fe. Additions of sulphur can be used here to assist later removal of Fe and Mn (another significant impurity present in ilmenite), by preventing formation of irreducible compounds to yield a higher grade synthetic rutile. The reduced ilmenite then undergoes dry magnetic and screening separations. This removes non-magnetic impurities and partially burnt coal. The metallic Fe is removed by mixing with water and air in an accelerated rusting process known as aeration. NH_4Cl is added to catalyse this

process. The Fe dissolves, migrates through the particles and precipitates as a variety of Fe oxides and hydroxides. A wet separation using hydrocyclones then removes these oxides, leaving synthetic rutile [44]–[46]. This material can be directly used in the chlorination step of Ti extraction as an alternative to rutile, as the impurities are removed during the process.

2.2.2   Titanium extraction

Despite ore abundance, Ti production had been severely hindered as it is inherently more difficult to extract compared to other metals such as Fe, Sn and Cu. This is due to the high affinity Ti has for the interstitial elements, meaning that smelting (reduction of the oxide with carbon) is not possible as nitrides and carbides will form. It was discovered however that the metal could be extracted by reducing $TiCl_4$ with Mg and this led to the development of the Kroll process in the 1940s [47]. This process allowed production of Ti on an industrial scale and, despite first being developed almost eighty years ago, is still used for almost all commercial Ti production today. Figure 2.6 outlines the steps involved in the Kroll based extraction of Ti from its oxide by using $TiCl_4$ as an intermediate.
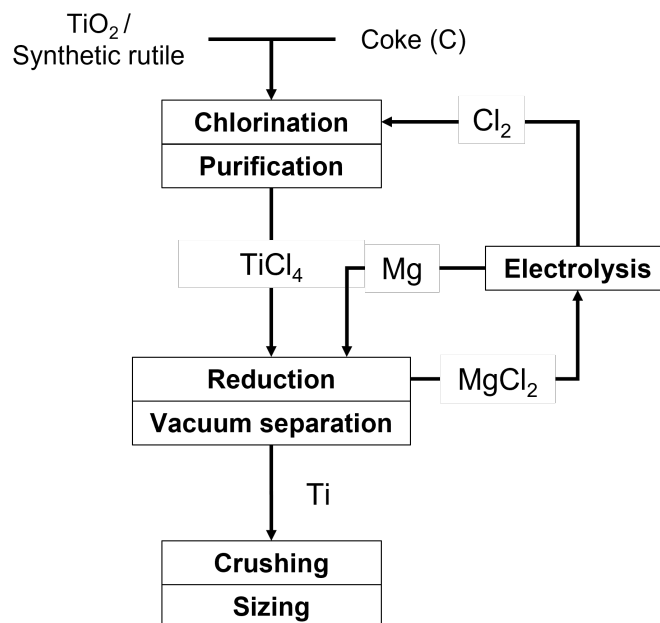
FIGURE 2.6: Flowchart summarising the commercial Ti extraction steps, recreated from [48].

Prior to use in the Kroll process, the oxide is converted into $TiCl_4$. TiO_2 is reacted with Cl_2 and C in a fluid-bed reactor at 1000°C to produce $TiCl_4$ and CO/CO_2 (Equation 2.4) [49].

$$TiO_2 + 2Cl_2 + C \rightarrow TiCl_4 + CO_2 \tag{2.4}$$

The reaction is exothermic and generates enough heat to be self-sustaining. The reaction has high conversion rates (>95%), but the product does require purification due to presence of other chlorides. This is achieved using multiple fractional distillation steps, which separates the various chlorides by their boiling points and is crucial for the production of high purity Ti later in the Kroll process [49].

In the Kroll process, $TiCl_4$ is reduced using Mg to produce Ti and $MgCl_2$ (Equation 2.5). $TiCl_4$ is poured into a retort containing excess molten Mg at 800–900°C over several days with the $MgCl_2$ periodically tapped off [49]. The reaction is exothermic so the rate of $TiCl_4$ addition can be used to control the temperature. When the reaction is finished, a porous Ti sponge is recovered. The sponge is then purified to remove remaining unreacted Mg and $MgCl_2$. This is done either by an inert gas sweep method or vacuum distillation process. The inert gas sweep method selectively removes the $MgCl_2$ by evaporation, using Ar as a carrier gas for removal. The vacuum distillation process involves the reaction vessel being heated under a vacuum which allows the $MgCl_2$ and Mg vapours to be continuously transferred to another vessel. They then re-condense and this secondary vessel becomes the reaction vessel for the next batch. $MgCl_2$ can be converted back into Mg and Cl by electrolysis and therefore reused in the chlorination and reduction stages [48]. The purified Ti is then crushed to an appropriate size for later processing.

$$TiCl_4 + 2Mg \rightarrow 2MgCl_2 + Ti \tag{2.5}$$
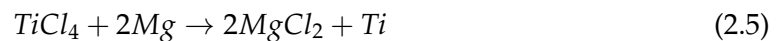
The Hunter process is very similar method, however it uses Na reduction instead of Mg [50]. This process is not used on a commercial scale however due to the use of Mg being more economically viable than Na [3].

2.2.3 Melting of titanium

The porous Kroll sponge requires melting to produce fully dense ingots. Alloying additions are also added at this stage to give homogeneous alloys after solidification. There are

many difficulties in the melting of Ti as it is very reactive in its molten form and thus easily contaminated. There are also many potential defects which can occur during solidification such as voids and segregation of alloying elements.

Vacuum arc remelting

Vacuum arc remelting (VAR) is the commonly used method for melting Ti. The Kroll sponge is blended with the desired amount of the alloying elements and mechanically compacted into blocks. Multiple blocks are then welded together to form a rod which is used as the electrode in the process. A small amount of the material is placed at the bottom of the crucible and the electrode is lowered to a set length above it, called the arc length. The furnace is evacuated and a current run across the two metal electrodes. This causes an arc to form which continuously melts the electrode and the molten metal falls to the bottom of the crucible to later solidify. Multiple melts are often required to ensure chemical homogeneity of the ingot [28], [51]. Figure 2.7 depicts the equipment setup for VAR.
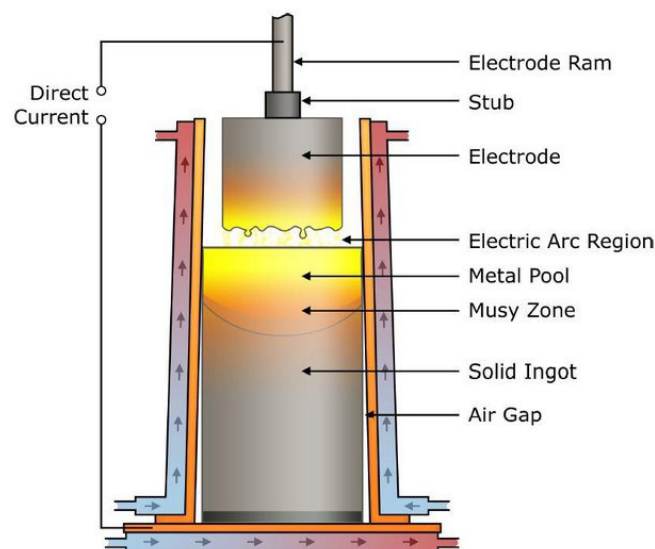
FIGURE 2.7: Diagram of a vacuum arc remelting vessel [52].

Cold hearth melting

Another more recent method used is cold hearth melting (CHM). The metal is melted in a water cooled Cu vessel by a electron beam. This means that there is a solid Ti layer on the Cu surface which prevents contamination. It has many benefits over VAR as it prevents

many defects by controlling the volume of the molten metal and can be directly cast into different shapes other than cyclinders [3].

The molten Ti from either of these processes can be directly cast into moulds, or the ingots can undergo thermomechanical processing into more general mill products.

2.2.4 Thermomechanical processing

The thermomechanical processing of Ti, like many other metals, is extremely important for both shaping and tailoring the mechanical properties by careful control of the microstructures formed. Although alloy materials may be chemically identical, their mechanical properties can vary significantly depending on their thermomechanical processing history.

After melting, alloy ingots often undergo a homogenisation heat treatment to ensure chemical homogeneity and cure any melt related defects. This processing is dependant on the specific alloy, but is typically done for 20–30 hours at temperatures 200–450°C above the β-transus [3]. The ingots are then shaped via various fabrication methods.

Primary fabrication

Primary fabrication converts ingots into general mill products: billets, bars, plates, sheets, strips, extrusions, tubes or wires. The processes by which these are made involve deforming the material at elevated temperatures (hot working). Primary fabrication has a far more significant effect on the final material properties compared to secondary fabrication, therefore it is crucial that this step is carefully controlled [28]. The exact processing methods and conditions are dependent on both the alloy chemistry and final desired properties.

Ingots firstly have their cross-sectional area reduced via open die forging. This is normally done above the β-transus as the β phase is more ductile [27]. Intermediate forging stages are then done either above or below the β-transus to improve compositional homogeneity and the material's response to further thermomechanical processing . Final forging is done in the $\alpha+\beta$ temperature range for macrostructural and microstructural refinement [3].

Various mill products can be made from the resulting billets. Bars, plates or sheets using a rolling mill by forcing the material through rollers at high temperatures which reduces

the thickness. Ti can also be hot extruded to produce tubes with various cross-sectional geometries. CP Ti can be wire drawn at room temperature, however most alloys are drawn at elevated temperatures (540–650°C) [27].

Secondary fabrication

Secondary fabrication involves techniques which convert mill products into finished or near-net shape products. These include: machining, closed die forging, extrusion, and superplastic forming.

Machining allows for the most accurate shaping possible and is often used for making components with complex geometries. Ti is well known for its poor machinability, for example in comparison to high strength steels, due to the following [53]:

- Ti has a low thermal conductivity which prevents effective heat dissipation during machining and increasing wear of cutting tools

- Ti has a relatively low elastic modulus, leading to spring back and chatter during machining and causing a poor surface finish

- Ti has a tendency to react with many cutting tool materials, causing tool wear

Final machining of Ti components from ingots can involve material removal rates up to 95%, which is extremely inefficient and further adds to the final cost [54].

2.3 The FFC-Cambridge process

The FFC-Cambridge process is a molten salt electrolysis method capable of extracting most metals from their respective oxides. It is named after the researchers George Chen, Derek Fray and Tom Farthing who discovered it at the University of Cambridge, with their findings published in *Nature* in 2000 [5]. They discovered that pellets of TiO_2 could be reduced to pure Ti metal in a matter of hours using an electrolytic cell, despite it being an electrically insulating material. It was later shown to be effective for reducing a wide variety of metal oxides, however Ti production has been of most interest due to the potential benefits over conventional Kroll production. There remains hope that the FFC-Cambridge process could have a big impact on the Ti industry, in a similar way that the Hall-Héroult process revolutionised aluminium production. This requires successful scale-up of the technology, a challenge which spin-off company Metalysis has since been attempting to solve.

2.3.1 The electrolytic reduction process

The electrolytic cell usually consists of a metal oxide cathode and a consumable graphite anode suspended in a molten salt electrolyte (Figure 2.8). $CaCl_2$ is usually the electrolyte of choice as it is more stable than most metal oxides, so will not decompose, and has a high solubility for O ions [55]. Therefore, the process is performed at $\sim$950°C, well above the melting point of the salt. A voltage of $\sim$3 V is applied, causing ionisation of the O at the cathode which diffuses into the electrolyte (Eq. 2.6). The O^{2-} ions are then transported through the electrolyte to combine with the C at the anode to produce CO and CO_2 gases (Eq. 2.7 & 2.8). Therefore, overall the O is transferred from the oxide to the graphite anode, leaving behind the reduced base metal [8]. The metal oxide cathode is usually prepared by pressing powder into pellets, which yields a porous metal pellet after reduction. This can then be directly used in conventional metallurgy by melting, or ground into powder for use with powder metallurgy techniques.

$$M_xO_y + 2ye^- \longrightarrow xM + yO^{2-} \tag{2.6}$$

$$C + 2O^{2-} \longrightarrow CO_2 + 4e^- \tag{2.7}$$
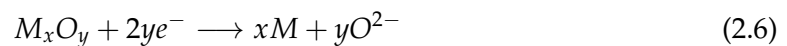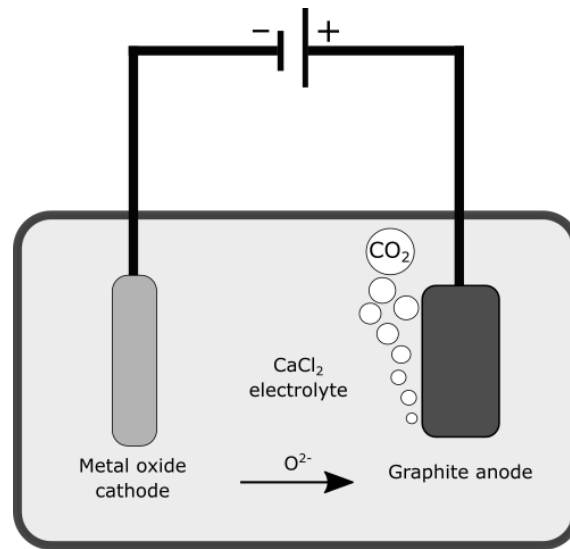
FIGURE 2.8: Simplified diagram of the electrolytic cell used in the FFC-Cambridge process.

$$C + O^{2-} \longrightarrow CO + 2e^- \tag{2.8}$$

2.3.2   Developments of the FFC-Cambridge process

Since its discovery, there has been considerable research interest in the process, leading to several important developments.

Although the process was discovered to reduce TiO_2, it has since been proven to work with many other metal oxides and sulfides. Examples of non-Ti metals produced include Cr, Zr, Fe, V, Mo, Ce, Ta and Sc [56]–[63]. Other interesting materials have been produced, such as high entropy alloys and those derived from lunar regolith simulant material, showing how flexible the process is in regards to the oxides which can be reduced and the potential materials which can be created. [64]–[66].

The possibility of using inert (non-reactive) anodes has also been researched, with a SnO_2 based material giving promising results [67]. Using an inert anode in place of a graphite one is beneficial as they are not consumed so do not need replacing and no CO and CO_2 are produced. O_2 gas is directly produced instead and this can be captured and used for other purposes. This has generated interest in using the FFC-Cambridge process as a possible method of creating metal, for materials, and O_2, for fuel, on the Moon from lunar regolith [65].

Direct reduction of free-flowing oxide powders, without the need for compaction into pre-forms, has been developed by Metalysis, a spin-off company created from the University of Cambridge to capitalise on the process. The conventional preform cathode is replaced by a stainless steel basket in which the powder is placed and electrically connected [68]. This development provides various improvements for scale up of the process. Using powder directly streamlines the process and removes the costs involved in producing the oxide preforms. The metal product removed from the cell post-reduction is loosely sintered which can be easily broken down mechanically into a powder product [8]. This ability to directly produce powdered metals is of great benefit to the powder metallurgy industry, as conventionally produced powders require additional processing steps and are expensive (discussed further in Section 2.5.1).

Direct production of near-net shape parts from the process by using shaped oxide precursors has also been proposed. The reduced metal retains the shape of the oxide precursor used, albeit with some shrinkage due to volume reduction. This has been investigated with Ti, with precursors made via moulding an oxide slurry prior to heating or, more recently, by 3D printing as shown in Figure 2.9. The porosity of the resulting part is up to 30% however, meaning that further processing would be required, such as hot isostatic pressing, to achieve material with high density and acceptable mechanical properties [69], [70].
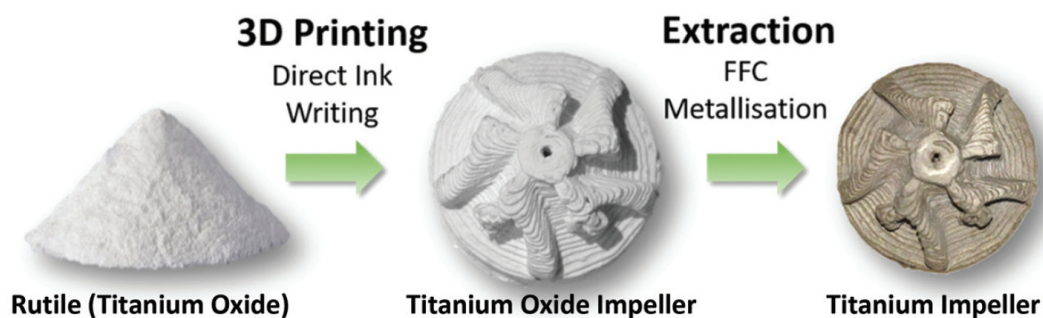
FIGURE 2.9: Near-net shape electrochemical metallisation (NEM) processing route [70].

2.3.3 Titanium extraction mechanism

Ti production via the FFC-Cambridge process has been extensively researched to understand the reduction mechanism and allow for improvement and optimisation. Focus on Ti is due to the many potential benefits of this process over the traditional Kroll process [71]:

- It is a single step process, directly converting TiO_2 into Ti metal

- Higher yield and less wastage

- Directly uses oxide feedstock in contrast to the corrosive $TiCl_4$ intermediate in the Kroll process

- Reduced energy consumption and lower projected plant operating costs

- Ability to directly create alloys by use of mixed metal oxides

- The powder product requires no further processing once cleaned and is ready for use in some powder metallurgy techniques

The reduction mechanism has been investigated by analysis of partially reduced samples. This is achieved by halting the process at set intervals prior to complete reduction, and shows that deoxidation occurs via formation of several intermediate Ti suboxides [72]. These phases are known as Magnéli phases, with chemical formulas Ti_nO_{2n-1}, where 3<n<10. X-ray diffraction studies reveal the presence of these phases, with analysis of current/time plots also suggesting when reaction stages start and finish compared to the electrode potentials of the individual reaction steps. The rate of each reduction is dependant on the conductivity of the oxide. Despite TiO_2 having poor electrical conductivity, the overall reduction is relatively fast as the Magnéli phases are highly conductive [73].

The determined reaction steps are as follows:

$$5TiO_2 + Ca^{2+} + 2e^- \longrightarrow Ti_4O_7 + CaTiO_3 \tag{2.9}$$

$$4Ti_4O_7 + Ca^{2+} + 2e^- \longrightarrow 5Ti_3O_5 + CaTiO_3 \tag{2.10}$$

$$3Ti_3O_5 + Ca^{2+} + 2e^- \longrightarrow 4Ti_2O_3 + CaTiO_3 \tag{2.11}$$

$$2Ti_2O_3 + Ca^{2+} + 2e^- \longrightarrow 3TiO + CaTiO_3 \tag{2.12}$$

$$TiO + CaTiO_3 \longrightarrow CaTi_2O_4 \tag{2.13}$$

$$CaTi_2O_4 + 2e^- \longrightarrow 2TiO + Ca^{2+} + 2O^{2-} \tag{2.14}$$

$$TiO + 2(1-\delta)e^- \longrightarrow Ti[O]_\delta + (1-\delta)O^{2-} \tag{2.15}$$
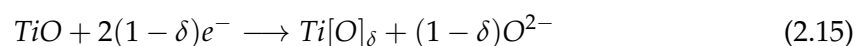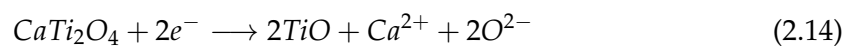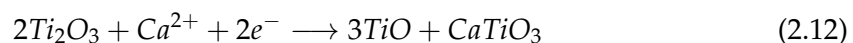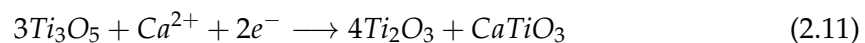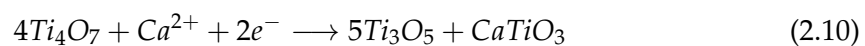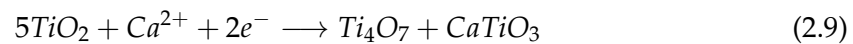
In Equations 2.9-2.12, Ca ions supplied by the electrolyte react with the TiO_2 and sub-oxides at the cathode to form $CaTiO_3$ and lower O content suboxides. $CaTi_2O_4$ is also formed via Equation 2.13, a chemically driven reaction as no free electrons are involved. Equations 2.14 & 2.15 describe formation of O^{2-} ions from the breakdown of $CaTi_2O_4$ and subsequently TiO. The O^{2-} ions then react with the graphite anode, as explained in Equations 2.7 & 2.8. The final reduction step leads to a solid solution of O in Ti ($Ti[O]_\delta$).

Further research led to even greater understanding of different aspects of the process. Additions of CaO were found to accelerate the reduction rate by providing an initial source of O^{2-} ions in the electrolyte which prevents any transport limitations for the oxide ions [74]. This sustains the ionic current, preventing Cl_2 formation and increasing current efficiency. There has been some debate on the nature of O^{2-} ion transport through the electrolyte, with one study suggesting that when low amounts of CaO are present, transport occurs by diffusion and not migration [75].

It was also discovered that the mechanism can vary depending on the porosity of the oxide precursor, due to differences in the incorporation of the electrolyte into the material. It was found that denser TiO_2 precursors with porosity of $\sim$11–12 % incorporated less Ca and therefore reduced via a more direct mechanism, avoiding significant formation of Ca containing species. Deoxidation of the metallic state was found to still be possible in these dense samples, due to a decrease in the solid volume during reduction of TiO_2 to Ti. This creates porosity, allowing the electrolyte to reach further into the material and continue to transport O^{2-} ions [76].

2.3.4 Titanium alloy production

Given that a wide range of metal oxides can be reduced using the FFC-Cambridge process, it is possible to co-reduce mixtures of metal oxides to directly produce alloys. Oxide powders can be milled together and mixed as slurries with a binding agent to achieve even distribution. Various binary Ti alloys have been produced in this way, including NiTi, Ti-Mo, Ti-W, Ti-Fe [77]–[80]. Some more complex Ti alloys have also been produced, including Ti-6Al-4V, Ti-8V-5Fe-1Al and Ti-5Ta-2Nb [8], [81]. It has also been found that co-reduction of TiO_2 with oxides of β stabilising elements can also increase the reduction

rate [78]. This is because O diffuses much faster through Ti β phase and so β stabilisation improves ion mobility and, subsequently, the reduction efficiency.

Use of alternative titanium feedstock

Most research on Ti and Ti alloy production via the FFC-Cambridge process has used pigment or reagent grade TiO_2. This material has undergone various processing stages and is mainly used as a white pigment, therefore comes at a significant price increase compared to the original ore. Lower purity alternatives, which have either experienced less processing or are waste products from conventional production, are available though. Using these cheaper feedstocks is especially impactful when considering any future scale-up of the FFC-Cambridge process, and can provide an opportunity to further reduce the cost of final Ti components.

Various industrial waste products have been investigated as feedstock, including TiO_2 dust from anatase production, H_2TiO_3 (metatitanic acid) from the conversion of ilmenite to TiO_2 via the sulfate process, and Ti rich slag from smelting of Ti concentrate [82], [83].

Natural rutile and ilmenite ores have be directly reduced via the FFC-Cambridge process to produce Ti and ferrotitanium respectively, with exact compositions depending on the purity of the ore [8], [84]. Synthetic rutile is a particularly interesting feedstock because it has a similar chemical composition to natural rutile, but is derived from more abundant ilmenite.

Synthetic rutile derived titanium alloy production

Synthetic rutile (SR) powder has been directly reduced using the FFC-Cambridge process to produce a Ti alloy containing naturally occurring impurities as alloying elements [17]. Various elements, including Fe, Al and Mn, are present in the SR as oxides and reduce alongside the Ti, dissolving into solid solution as alloying elements. Despite this, the SR powder was found to reduce in essentially the same way as pure TiO_2 precursors, although with intermediate formation of TiFe and $TiFe_2$ intermetallics due to the significant presence of Fe. Consolidation of the resulting alloy powder via field assisted sintering formed bulk Ti alloy material with a homogeneous $\alpha+\beta$ microstructure. Figure 2.10 shows the evolution of the material from SR powder to Ti alloy powder to bulk Ti alloy.

The mechanical properties of this SR derived Ti alloy were investigated via a small-scale testing approach, with similar compressive yield strengths and strain to failure values as Ti-6Al-4V under the same processing conditions reported (Figure 2.11) [85].

Co-reduction of SR with other metal oxides has also been investigated, with the aim being to create a range of low-cost Ti alloys derived from SR [86]. The Al content was enhanced by additions of Al_2O_3, producing a range of pseudo-binary Ti-Al alloys up to 5.3 wt.%. Similar $\alpha+\beta$ microstructures to the standard SR derived alloy were observed, however Fe and Cr contents were not consistent so the amount of β stabilisation varied slightly. Al additions increased the compressive yield strength at the expense of some reduction in ductility. MoO_3 additions were used to create alloys containing up to 17 wt.% Mo. Due to the slow diffusion rate of Mo in Ti however, homogenisation was not achieved, either in the alloy powders or consolidated material.
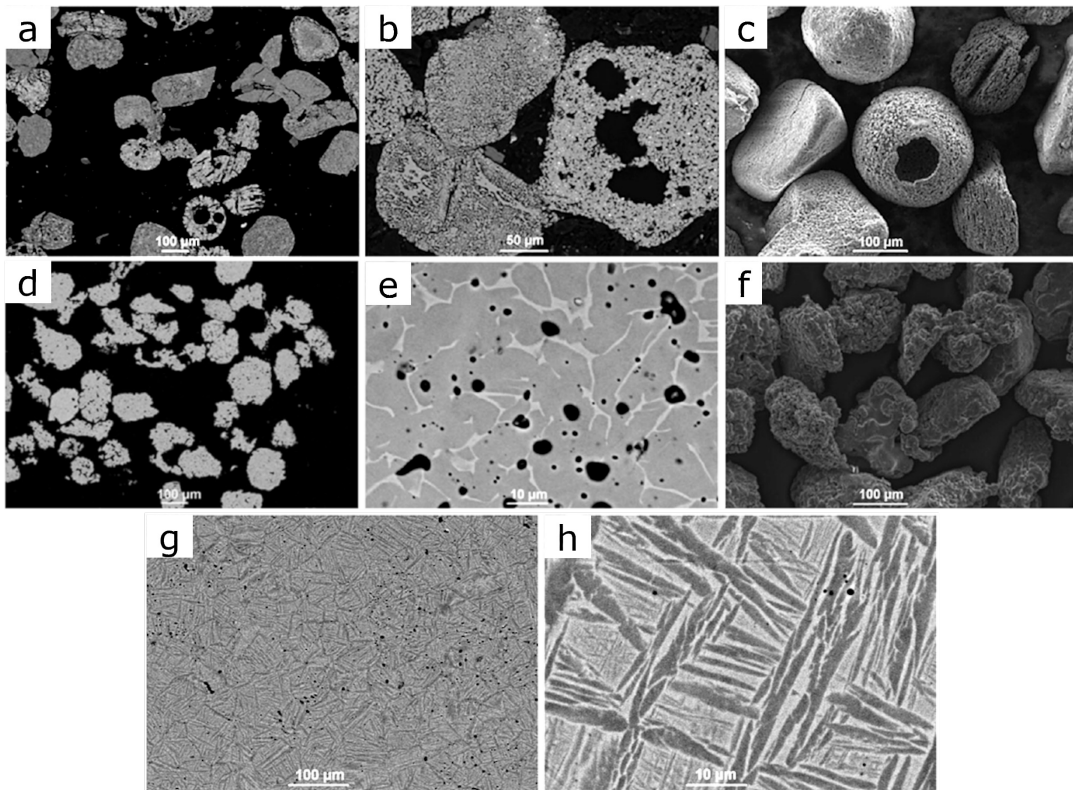
FIGURE 2.10: Electron micrographs of a–c) synthetic rutile particles, d–f) resulting Ti alloy particles after reduction via the FFC-Cambridge process, g+h) Ti alloy microstructure after consolidation via FAST [17].
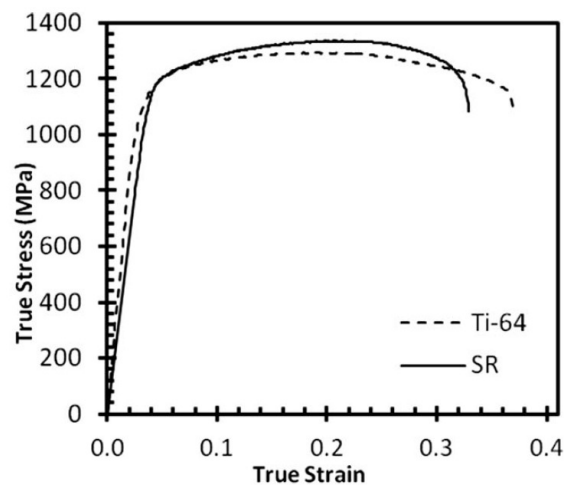
FIGURE 2.11: Stress/strain plot from thermomechanical compression data of FAST consolidated synthetic rutile derived Ti alloy [85].

2.4 Other unconventional titanium extraction methods

There are many other alternative extraction processes in addition to the FFC-Cambridge process. They can be split into three categories: those which are modifications of the Kroll process, those which use thermochemical reactions with other species, and those which use electrochemistry (similarly to the FFC-Cambridge process). These processes are at a range of technology readiness levels, with none to date producing significant amounts relative to the conventional process described in Section 2.2.

2.4.1 TiCl$_4$ based extraction methods

The TIRO process

The TIRO process has been in development by CSIRO (The Commonwealth Scientific and Industrial Research Organisation - an Australian Government agency) as a continuous process for Ti powder production. Although it is chemically the same as the Kroll process (Mg reduction of TiCl$_4$), it uses a fluidised bed reactor which allows for continuous addition of reactants and withdrawal of product. Mg powder is used which, on reaction with TiCl$_4$, directly forms Ti metal particles dispersed within larger MgCl$_2$ ones. The product the goes through a continuous vacuum distillation process which separates the Ti from the MgCl$_2$. A sintered Ti 'biscuit' is produced, which can then be ground by hand or milling to achieve a range of particle sizes [87], [88].

One of the main limitations of the conventional Kroll process is its batch nature, and therefore this process offers a more efficient alternative. The technology has been acquired by Australian chemical company Coogee, who are scaling up the technology and even boast the ability to directly create Ti alloy powders too, although the details on their methods are not disclosed [89].

The Armstrong process

US based company International Titanium Powder (now Cristal Metals Inc.) similarly developed a continuous Ti production method named the Armstrong process. Unlike the Kroll and TIRO processes, Na is used as the reductant instead of Mg, like in the Hunter process. TiCl$_4$ vapour is continuously injected into a flowing loop of liquid Na metal,

causing formation of Ti metal particles and NaCl. These are removed at a separation point in the loop using a filter, and the Ti particles washed to remove the NaCl salt. The NaCl can then be electrolytically broken down to recover the Na metal, which is re-used in the loop. Ti alloy powders can also be directly produced by mixing $TiCl_4$ with other metal chloride gases [90].

The company has operated this process on a full commercial scale reactor and claim that it is around twice as energy efficient as the conventional Kroll process [91]. The powders have been used with several downstream powder metallurgy techniques, including using cold spray [92].

The ADMA process

ADMA Products Inc., another US based company, developed a Ti extraction method which produces TiH_2 powder from $TiCl_4$. The powder is then dehydrogenated during sintering to give high purity Ti and alloys such as Ti-6Al-4V can be produced using the blended elemental powder metallurgy approach. Equation 2.16 shows the reaction which takes place and how the process partially replaces molten Mg with H_2 gas as a reducing agent, producing TiH_2 instead of Ti [93].

$$TiCl_4 + H_2 + Mg \rightarrow TiH_2 + MgCl_2 + HCl \tag{2.16}$$

One of the main benefits of this process is the ability to produce TiH_2 powders with very low O contents, which are then retained in the sintered material. A value of 0.063 wt.% O is quoted in one publication, where it is also claimed that a pilot-scale plant used 50% less energy and 20% lower cost than the commercial Kroll process [94].

2.4.2   Thermochemical extraction methods

There are several extraction methods which do not use $TiCl_4$ as an intermediate species, and instead directly reduce TiO_2 in an attempt to reduce costs. As explored earlier, the oxide can be reduced using either Ca or Mg metal via Equation 2.17:

$$TiO_2 + Ca/Mg \rightarrow Ti(O) + CaO/MgO \tag{2.17}$$

Complete deoxidation is not achievable due to thermodynamic limits, with a minimum of 0.5 wt.% O using Mg and 0.02 wt.% O using Ca remaining in solid solution [95]. Ca is, therefore, a more effect reductant than Mg, however the latter is cheaper. This is especially important when considering scaling up any technology and when comparing to the Kroll process, which uses Mg. Despite this, processes using Mg can undergo additional steps to remove some of the remaining O, enabling the production of good quality material.

The Bradford process

A Ca reduction process has been developed at the University of Bradford, UK, which claims to produce Ti metal powder without any O impurity [96]. TiO_2, in the form of anatase powder, is mixed with Ca metal powder and heated to 900–1000°C for 3–7 hours. The resulting material is washed with water and dilute acid, then dried to give Ti powder. Although still being developed at a laboratory scale, a spin-off company, Bradford Metallurgy, has been created in an attempt to gain further funding and commercialise the process. Exact details of the processing conditions and final Ti composition is not publicly available, but if this process is producing high quality Ti powder, it could have a big impact on Ti production, at least in the UK.

The preform reduction process (PRP)

This process, developed at The University of Tokyo, also uses Ca as the reductant. It is used as a vapour rather than by direct physical contact as this prevents the transfer of interstitial impurities from the Ca to the Ti metal during the reduction. TiO_2 preforms are used with a CaO or $CaCl_2$ flux, rather than loose powder to prevent contamination and ease scalability. The process is done at 800–1000°C for 6 hours, to allow the generation of Ca vapour which can react with the TiO_2 preforms. Figure 2.12 shows a diagram of the experimental apparatus for this process. The resulting material is then treated with acid to remove the CaO product, flux from the preform and excess Ca to give a Ti powder with O levels as low as 0.28 wt.% [97].
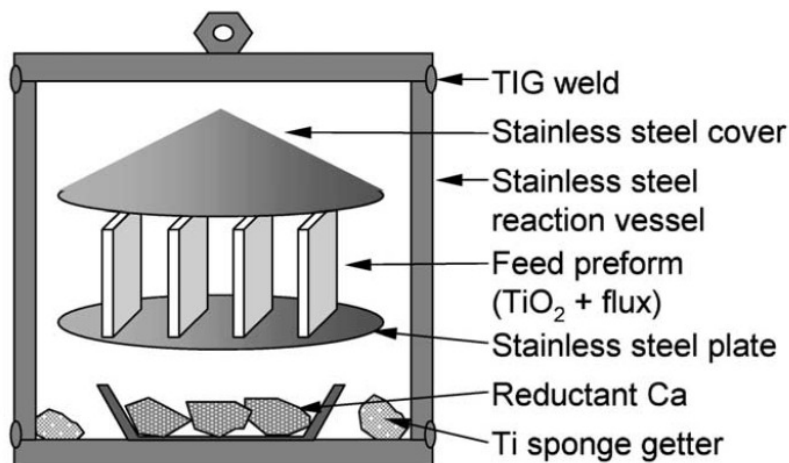
FIGURE 2.12: Diagram of experimental setup used in the preform reduction process [97].

The metal-hydride reduction (MHR) process

Similar to the later developed ADMA process, H can be used as a co-reductant alongside Ca or Mg. This can be achieved without prior chlorination of the TiO_2. Instead, the TiO_2 is reacted with CaH_2 at 1100–1200°C, with reduction occurring as shown in Equation 2.18. It has been used to produce CP Ti powder, with <0.1% O, and alloy powders by using mixtures of TiO_2 and other metal oxide powders in the reaction [98]. The process has not been successfully scaled up however due to the high costs associated with using Ca over Mg.

$$TiO_2 + 2CaH_2 \rightarrow Ti + 2CaO + 2H_2 \tag{2.18}$$
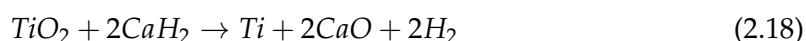
The hydrogen assisted magnesiothermic reduction (HAMR) process

Despite Mg only being able to deoxygenate TiO_2 to 0.5 wt.% O, this process is able to give powders with O contents as low as 0.05–0.06 wt.% by using H_2 gas to assist the reduction [99]. This works by forming a Ti-O-H solid solution which is less-stable than the Ti-O solid solution and can be deoxygenated further by the Mg. The remaining H can then be removed by heating to leave high purity Ti [100]. Figure 2.13 describes the steps involved in this process. The ability to use cheaper Mg as the reductant and still be able to achieve low O content Ti powders is impressive, making this an exciting development in the search for low-cost Ti.
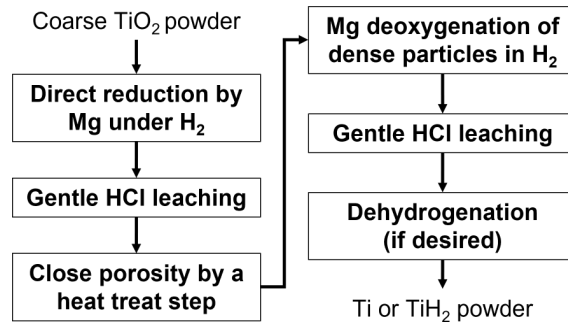
FIGURE 2.13: Flowchart summarising the hydrogen assisted magnesiothermic reduction processing route, recreated from [100].

2.4.3 Electrochemical extraction methods

The Ono and Suzuki (OS) process

This process, named after its founders, uses Ca dissolved in molten $CaCl_2$ as the reductant as in Equation 2.17, combined with electrolysis which causes the CaO by-product to decompose into ions as in Equation 2.19. The O^{2-} ions then react at a C anode to produce CO and CO_2 gas (Equations 2.20 and 2.21). The Ca^{2+} ions then pick up electrons at the cathode to reform Ca metal (Equation 2.22), which can then further reduce the Ti. The $CaCl_2$ salt is then dissolved away leaving behind Ti metal in powder form. Figure 2.14 shows the basic concept, with both the reduction and electrolysis processes occurring simultaneously in the same vessel. O levels below 0.1 wt.% have been reported using this method [101].

$$CaO \rightarrow Ca^{2+} + O^{2-} \tag{2.19}$$

$$C + 2O^{2-} \rightarrow CO_2 + 4e^- \tag{2.20}$$

$$C + O^{2-} \rightarrow CO + 2e^- \tag{2.21}$$

$$Ca^{2+} + 2e^- \rightarrow Ca \tag{2.22}$$
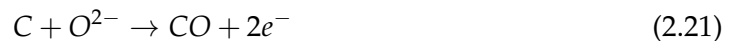
Processes using Ti containing material as the anode

There are several other electrochemical based processes which instead use a Ti containing material as the anode, rather than the cathode as is the case in the FFC-Cambridge process.
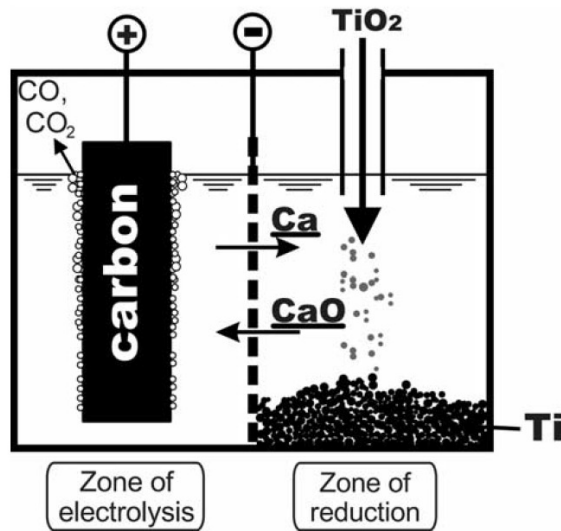
FIGURE 2.14: Diagram of the Ono and Suzuki process [102].

The USTB (University of Science and Technology Beijing) process uses a consumable anode composed of a solid solution of TiC and TiO, prepared via carbothermic reduction of TiO_2. This anode material has an electrical conductivity four orders of magnitude greater than TiO_2. It is then used in electrolysis, with a mixture of NaCl and KCl as the electrolyte and a non-consumable steel cathode. A diagram of the process is shown in Figure 2.15. At the anode, Equation 2.23 occurs, and at the cathode Equation 2.24 [103].

$$TiC.TiO \rightarrow 2Ti^{2+} + CO + 4e^- \tag{2.23}$$

$$Ti^{2+} + 2e^- \rightarrow Ti \tag{2.24}$$
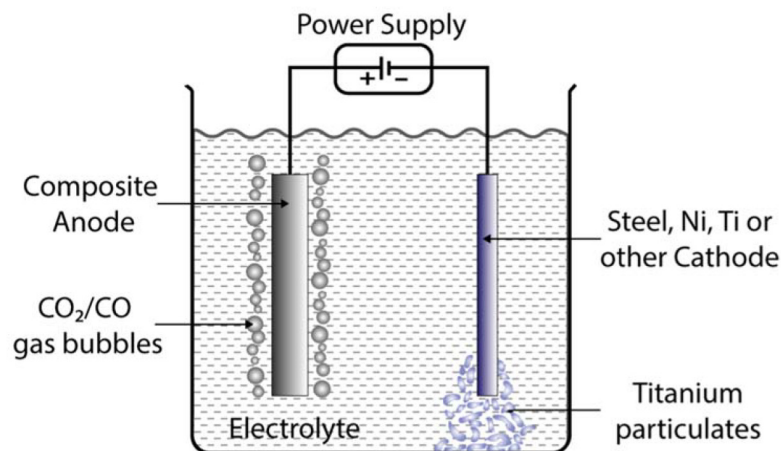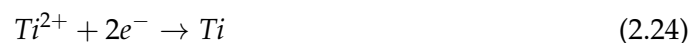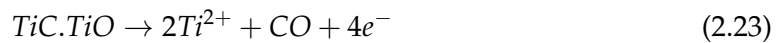
FIGURE 2.15: Diagram of USTB process [104].

Other processes such as the MER (Materials & Electrochemical Research Corporation) process and the Chinuka process work in a similar way, by using anodes composed of Ti suboxides mixed with TiC or C [105], [106].

2.5   Titanium powder metallurgy

Powder metallurgy (PM) covers a range of technologies which can convert metal powders into solid components, and is becoming an increasingly attractive alternative to traditional metallurgy. This is due to the many benefits PM can offer. These include the ability to generate components with complex geometries using greater precision, reduced material wastage and fast prototype production [107]. PM is also very flexible in terms of the alloy powders, and facilitates the use of alloys which may not be suitable in traditional metallurgy due to issues such as segregation. A range of different techniques use powder feedstock, and either involve the sintering of powders into consolidated material via pressing or melting layers of powder via additive manufacturing (AM).

The benefits of PM techniques make them obvious areas to explore in Ti component production. Machining Ti leads to the wastage of large amounts of high value material and PM can prevent this by directly creating net or near-net shape products, making production more cost-effective. It is important to consider the costs associated with the powder itself however, as powders are generally more expensive by mass than conventional mill products.

2.5.1   Powder production methods

A clear stumbling block with Ti PM is sourcing the powders themselves and the costs associated with their production. They have conventionally been produced using pre-alloyed ingots from vacuum arc remelting. This makes the powders rather costly as making them requires additional steps on top of an already expensive production route. There are several commercial Ti powder production methods, most of which use agitation of molten metal to give powders with spherical particles [108]. These include inert gas atomisation (GA), plasma atomisation (PA) and the plasma rotating electrode process (PREP).

There are two main GA techniques, vacuum inert gas atomisation (VIGA) and electrode induction gas atomisation (EIGA). In VIGA, the alloy is first melted in a vacuum induction melting furnace. The melt is then poured through a tundish into a gas nozzle, where high pressure inert gas breaks it up into spherical powder particles. The particles then
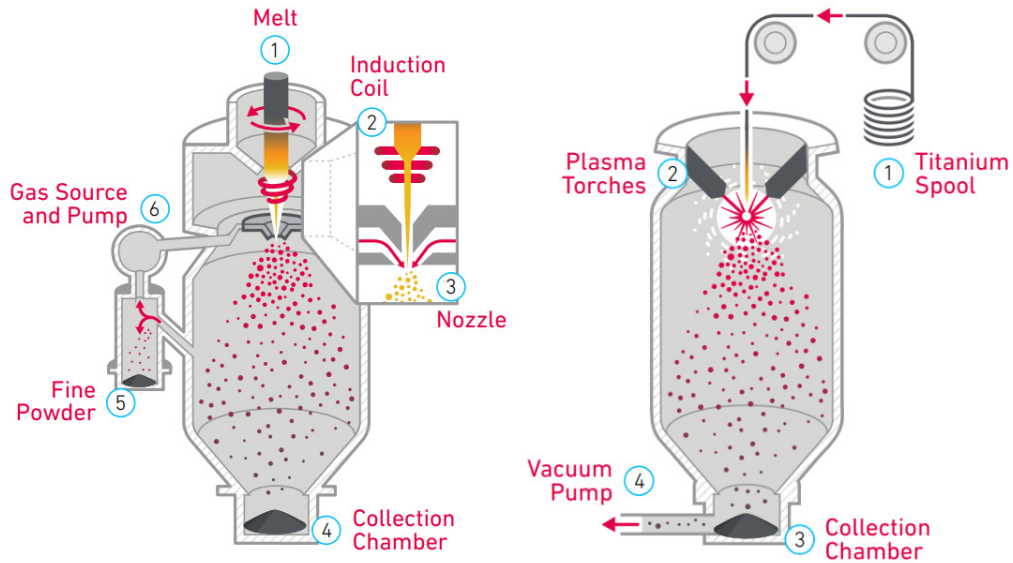
FIGURE 2.16: Diagrams of electrode induction gas atomisation (left) and plasma atomisation (right) processes [110].

solidify as they fall to the bottom of the chamber, where they are collected. EIGA is the same except that the melting is achieved by slowly rotating and lowering pre-alloyed rods through a conical induction coil. EIGA has benefits for Ti alloy powder production as the melt is not in contact with any other materials (e.g. crucible walls, tundish and nozzle) which it can react with [109]. This minimises pickup of high-density contaminants.

PA instead uses a pre-alloyed wire feedstock, which is fed into plasma torches. This creates molten droplets which rapidly solidify to give highly spherical powder particles. The wire feedstock required makes this process more expensive for Ti, therefore EIGA is generally preferred. There is also a possibility of W contamination resulting from erosion of the plasma torches. Figure 2.16 shows how EIGA and PA are very similar, with the main difference being the method used to melt the pre-alloyed feedstock.

PREP is a centrifugal atomisation process where a pre-alloyed bar is rapidly rotated at approximately 15,000 rpm whilst being melted by a plasma arc. The rotation causes the molten metal to be ejected, which then solidifies into spherical particles [111].

Another commercial method of Ti powder production exists which is quite different to the atomisation techniques and produces angular powder particles rather than spherical. The hydride-dehydride (HDH) process involves using H as a temporary alloying element to create brittle TiH_2, which can then be ground into a powder and the H removed to

leave the alloy powder. Firstly, Ti sources below 5 cm in thickness must be used to achieve complete hydriding. The Ti is then heated in a furnace with a H_2 gas flow, with the reaction being exothermic and self sustaining if the initial temperature is above 700°C. Once the hydriding is complete, the material is crushed, and the H can be removed by heating between 350°C and 700°C in a vacuum furnace. The material is once again broken apart due to some sintering which occurs during the dehydriding [112].

The powders produced via HDH and processes reviewed in Section 2.4 are angular, due to mechanical crushing stages or the way in which the Ti is reduced. Angular powders are unsuitable for some PM techniques which require spherical powders for better flow properties. Induction plasma spheroidisation is used to transform powder with angular morphologies into spherical ones, making them suitable for use in such techniques. The process works by melting the angular powder using an induction plasma, followed by rapid solidification and retention of spherical morphology [108].

There are many factors affecting the quality of a powder and its suitability for different PM techniques. Particle size is an important property, for instance <45 μm powders are required for some AM techniques, however O content can be an issue with smaller powders due to their increases surface area and oxide layer. Powder morphology is significant as it can affect packing characteristics in sintering and flow properties in AM, with spheroidised powders required for the latter. Porosity is important as it can remain in the finished material, as well as Cl content which can cause porosity as entrapped gas [113].

As explored earlier, alternative Ti extraction methods are capable of producing powder directly, negating the need for atomisation processes on pre-alloyed ingots. The FFC-Cambridge process can produce a variety of Ti alloys directly in powder form and therefore is ideal to be combined with PM downstream. The many laborious and costly steps involved in both Kroll Ti extraction and powder production can be replaced by the FFC-Cambridge process to potentially give the same results.

2.5.2   Additive manufacturing

Additive manufacturing (AM) techniques can create 3D shapes by stacking many individual layers of material, with each being a thin cross-section of the total structure. Models

are made using computer aided design and an AM machine is then able to build the part, layer by layer, based on the model. The technology allows for the high precision production of parts with complex geometries, by using fine powders, accurate heat sources and sophisticated software. AM is seen as an effective technology for the production of Ti components for both aerospace and medical applications. There is potential for significant cost reduction compared to conventionally produced components, mainly because only final surface machining is required and therefore there is reduced material wastage [114].

There are two main classes of AM technology which Ti powders are used in: powder bed fusion (PBF) and directed energy deposition (DED). PBF methods work by laying a track of the metal powder and then using a heat source, such as a laser or electron beam, to melt the layer. This process repeats until the part is complete. DED methods instead inject the powder into a meltpool formed by a laser. This allows it to generate parts quicker than by PBF but with less control and a poorer surface finish [115]. Figure 2.17 compares the equipment used in these methods. Both of these technologies cause some undesirable features in the microstructure of the resulting material. Porosity is often an issue, caused either due to the entrapment of gas within powder particles, or insufficient melting in certain regions leading to poor fusion between particles. During solidification, prior β grains are known to preferentially grow epitaxially in the build direction, leading to a microstructure with columnar grains. This causes undesirable anisotropic mechanical performance in parts [10]. Optimisation of processing parameters can somewhat prevent these issues, although there are many other variables aside from machine parameters, including the machine being used, the powder, the alloy and the part being produced. This makes AM a challenging process for right first time manufacturing, especially considering future scale up and mass production of components.

Another, less widely adopted AM technique, is the cold spray process. The process is relatively simple, pressurised gas is used to accelerate powder particles to 300–1200 m/s to impact with a substrate. The process occurs at temperatures well below the melting point of the powder and so powders remain in the solid state [116]. When the particles impact the substrate, they experience localised heating and high strain rate deformation, causing adhesion between particles. This can be used to build components continuously with a high deposition rate by directing the powder stream to desired locations on the
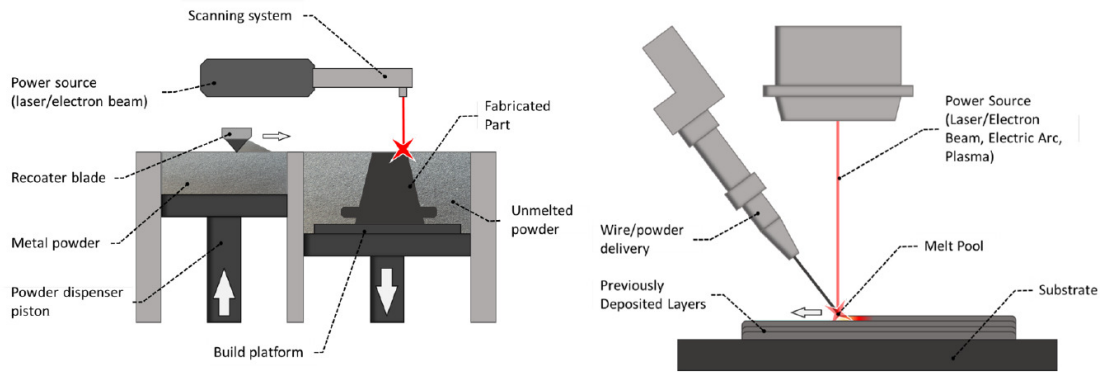
FIGURE 2.17: Diagrams of additive manufacturing processes. Left: powder
bed fusion, right: directed energy deposition [10].

substrate. As with other AM techniques, porosity is an issue, but can be overcome through optimisation of various parameters. The resulting material also does not have optimal mechanical properties and heat treatments are required to give properties in line with conventional material [117].

2.5.3   Press and sinter

Conventional press and sinter methods are able to consolidate metal powders into parts by first cold pressing to form a green compact, followed by sintering in a vacuum furnace. Pressing can be achieved through use of closed dies, direct powder rolling, or cold isostatic pressing. The green density of the pressed material is dependant on the compaction pressure, with pressures of 200–600 MPa generally used for Ti. High sintering temperatures are then required to further increase the density to a level for acceptable mechanical performance, with a range of 1100–1400°C used for around 1–4 hours [118]. Despite the relatively extreme processing conditions in each step, 100% density is challenging to achieve.

Metal injection moulding (MIM) is a development of the traditional press and sinter approach, with the benefit of being able to produce parts with more intricate geometries. Metal powders are blended with organic compound binders to create a slurry. The slurry is then injected into a shaped mould, allowed to cool, and ejected as a green part. The binder material is then removed using an appropriate solvent or by heating the part to evaporate it. The resulting porous parts are then sintered by heating in a furnace, in the same way as other press and sinter techniques. Components produced by MIM generally

have final densities >96% theoretical. This technique is only effective for the production of small components and requires the use of very fine (<40 μm) spherical powders produced by atomisation, which makes the process less cost effective [119].

2.5.4 Pressure assisted sintering

Application of pressure during sintering is far more effective for consolidation than separate press and sinter steps. Significantly lower pressures, temperatures and dwell times are required to achieve high density material. Metals, including Ti, soften at higher temperatures and therefore can plastically flow when pressure is applied [120].

Hot pressing is performed by placing powder between punches, within a graphite die. Uniaxial pressure is applied by the punches and external resistance or induction heating increases the temperature of the die and subsequently the powder within. External heating does present some challenges due to potential temperature gradients across the sample causing heterogeneity in the final microstructure [121].

Hot isostatic pressing (HIP) is another technique combining the application of heat and pressures. Powders are put inside a can, usually made from sheet steel, which is closed by welding. The can is then placed inside a furnace and heated to a temperature $\sim$0.8 times the solidus temperature of the metal being processed. During heating, Ar gas is fed into the furnace until the desired pressure is reached. The pressurised gas applies pressure to the can from all directions, causing the powder to consolidate and the can to collapse around it. The system is then held at the maximum temperature and pressure for the desired dwell time, followed by cooling. A typical HIP cycle lasts from 8–24 hours [122].

HIP is a very effective technique for achieving full density parts from metal powders. A vast array of Ti components have been produced via this method by using shaped cans and a good understanding of the can deformation behaviour. Compared to other PM processes, much larger components can be produced using HIP as it is relatively easy to scale as larger furnaces and cans can be used. HIP is not only used for consolidation of powders, but also for healing internal porosity resulting from casting defects or AM processing. One of the main issues is the removal of the can after processing. This is usually done by machining, which is time consuming and costly [123].

2.5.5   Field assisted sintering technology

Field assisted sintering technology (FAST), also commonly known as spark plasma sinter-ing (SPS), is an effective, solid-state technique for the consolidation of various powdered and particulate materials. It is similar to hot pressing, in that consolidation is achieved through a combination of heat and pressure, simultaneously applied in one processing step. Heating in FAST is provided by Joule heating resulting from a pulsed direct current, in contrast to hot pressing when external heating is applied. Powders are placed within graphite tooling, as shown in Figure 2.18, which is electrically conductive. The tooling is then positioned between two electrodes which provide the electric current and a hydraulic pressing system applies uniaxial force. A high current (on the order of 10^3 A) and low voltage (<10 V) is used, with the overall power required dependent on the heating rate, temperature and tooling size. Processing chambers can be either evacuated to process under a vacuum, or flooded with an inert gas such as Ar or N_2.
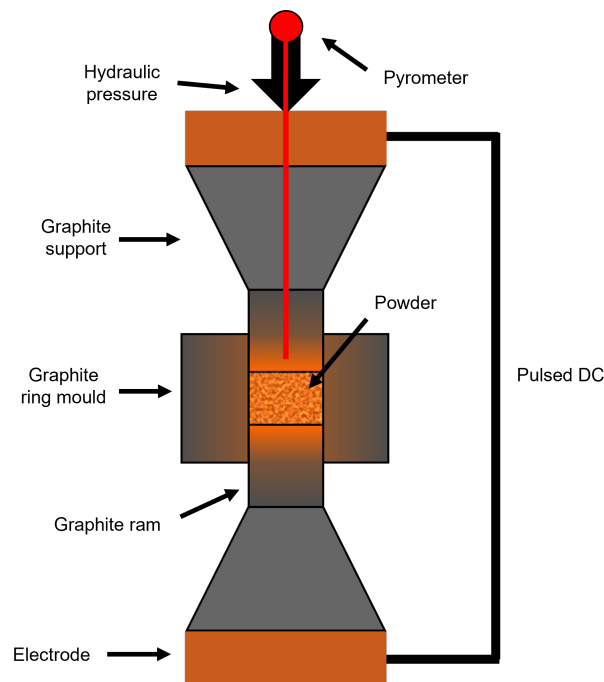
FIGURE 2.18: Diagram of field assisted sintering technology equipment
within a water cooled vacuum chamber.

There are a number of advantages of FAST over other sintering techniques [13]. In keeping with its acronym, FAST can achieve full consolidation of powders in relatively short processing times. This is due to the high heating rates possible through internal Joule heating (up to 1000°C/min), which directly heats the tooling and powders (if electrically

conductive)[15]. Combined with the simultaneous application of force, the required conditions for powder consolidation can be quickly met. The short processing brings several benefits. Grain growth is limited, as materials do not need to be held at high temperatures for long periods of time. This means that FAST consolidated material can have improved mechanical properties compared to other techniques and, consequently, the production of nanostructured materials has been a particular research focus [124].

A wide range of materials has been processed using FAST, including metals and alloys, ceramics, intermetallics, and composites, and it is a very flexible technique with regard to both input material chemistry and particle size [125]. Even materials which are electrically insulating can be processed, as heat from the graphite tooling transfers to the powder.

FAST processing of titanium

FAST is a suitable method for the consolidation of Ti powders, with many published works available in the literature. The temperature required to achieve full density depends on the alloy, with CP powders around 900°C and Ti-6Al-4V around 1000°C [126], [127]. Temperatures above the β-transus are preferred as the material becomes more ductile and diffusion rates are higher, both of which enhance sintering. Lower temperatures can be used if combined with higher pressures, however this requires the use of an alternative tooling material to graphite, which is limited due to its brittle nature, such as tungsten carbide [128].

Additionally, FAST has previously been used to successfully consolidate Ti alloy powders produced via the FFC-Cambridge process. The sintering behaviour of CP-Ti powders produced by Metalysis from pigment grade TiO_2 and natural rutile was studied alongside that of more conventional GA and HDH powders. Results showed slightly inferior final densities of around 98% compared to >99% when processed at 991°C with 35 MPa of pressure for 10 min. It was postulated that this was due to the pre-existing porosity within the powder particles, although it was also expected that processing at a higher pressure and dwell time could remove this [129]. Ti alloy powders derived from synthetic rutile using the FFC-Cambridge process have also been consolidated using FAST, as describe in Section 2.3.4, with a 98.6% density achieved, using parameters of 1200°C and 50 MPa for 30 min [17].

FAST is seen as a promising technology for the reprocessing of waste Ti materials, for example using oversize powders from atomisation and machining swarf. Although currently only simple geometry parts are produced due to limitations of the graphite tooling, billets can be forged into near-net shape components. This two-step consolidation and forging concept is being developed at the University of Sheffield under the term FAST-*forge* [130]. FAST processed Ti-6Al-4V and Ti-5553 alloys both exhibited similar flow behaviours and microstructures to conventionally produced billets, proving that FAST processing has no detrimental effects [131]. More recently, FAST-*forge* has been proposed to convert waste Ti-6Al-4V machining swarf into automotive components, with the swarf consolidated back to full density and subsequently possessing equivalent forging flow behaviour and microstructures compared to conventionally produced material [132]. This highlights just how flexible FAST is in regard to feedstock size and morphology.

The production of multi-alloy materials by bonding different Ti alloy powders in FAST, has also been investigated. The approach, named as FAST diffusion bonding (FAST-DB), has the aim of creating components with different alloys, and therefore different properties, in distinct regions where their properties are more suited. Powders are divided within the graphite mould prior to processing, where they remain during consolidation, leading to a multi-alloy billet. Unlike many conventional joining methods such as welding, there is no loss of mechanical integrity across the bond and tensile failure occurs in the weaker alloy [133], [134]. FAST-*forge* of two FAST-DB cylindrical preform samples (CP-Ti bonded with Ti-6Al-4V and Ti-6Al-4V bonded with Ti-5553) was done to create an eye bolt component using drop hammer forging (Figure 2.19, further pushing the possibilities for processing Ti powders using FAST [135].

2.5.6   The Conform process

The Conform process, also known as continuous rotary extrusion, schematically depicted in Figure 2.20, is a method for consolidating metal powder feedstock into a rod or wire. The powders experience high pressure and temperature resulting from the mechanical friction between them and the abutment tool. This causes consolidation via severe plastic deformation, followed by extrusion through the die exit. It is a continuous process as powder can be continually fed into the system and the extruded rod or wire can

theoretically be as long as required. Although previously mainly used to process Al and Cu powders, it has more recently been used with Ti powders and shown to achieve consolidation to full density [136]. The process has also been investigated for its potential for processing waste Ti swarf, as well as powders, which again achieved full density, although contamination issues and fast wearing of the abutment material are currently barriers to further adoption [137].
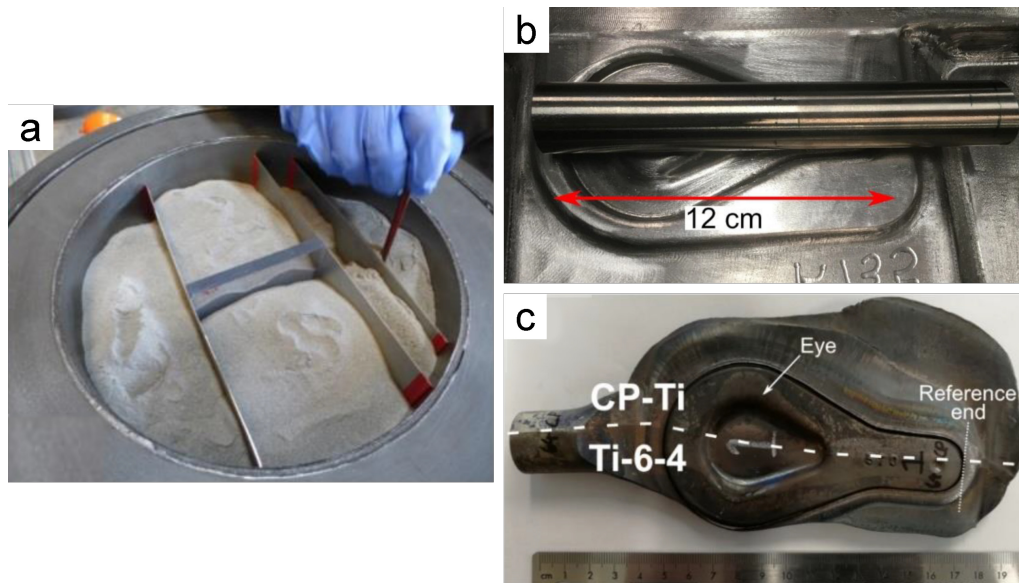
FIGURE 2.19: Photographs demonstrating a combination of the FAST-*forge* and FAST-DB techniques: a) separation of Ti alloy powders within graphite mould prior to FAST processing, b) Cylinder preform machined from resulting FAST billet, composed of two Ti alloys, c) Eye bolt near-net shape component from hot forging of preform [135].
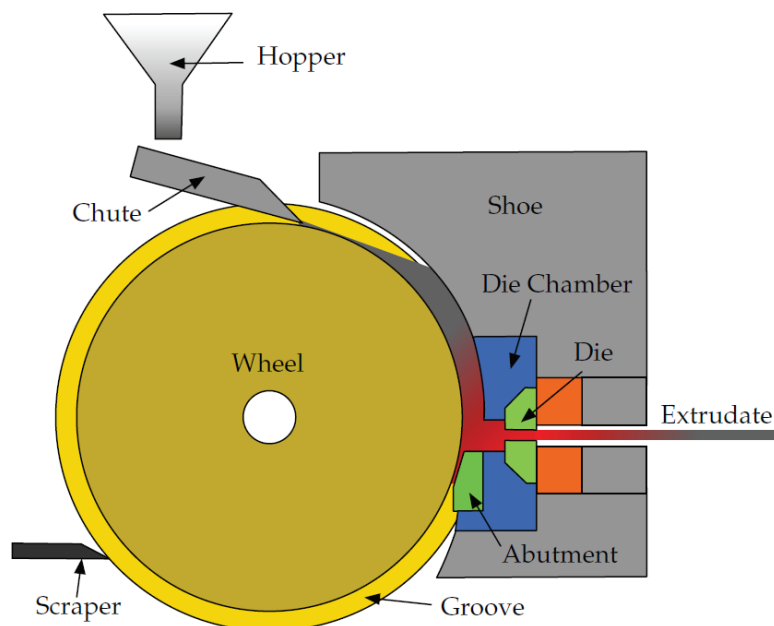
FIGURE 2.20: Schematic of equipment used in the Conform process [136].

2.6 The Ti-Fe system and alloys

2.6.1 Iron as an alloying element

The Ti-Fe phase diagram in Figure 2.21 shows that Fe is a β eutectoid type alloying element with limited solubility in both α and β phases. It is the most effective Ti β stabilising element by mass, as per Equation 2.2, therefore it would be expected that Fe is extensively used in Ti alloys to stabilise the β phase, especially when considering its low cost relative to other β stabilisers such as Mo and V. Although Fe is present in many alloys, it is usually in small amounts. This is due to processing issues encountered with Fe in conventional Ti alloy production which can adversely affect the quality of the alloys. If there was a way to avoid these issues, greater use of Fe would be appealing and could lead to the development of lower cost Ti alloys.
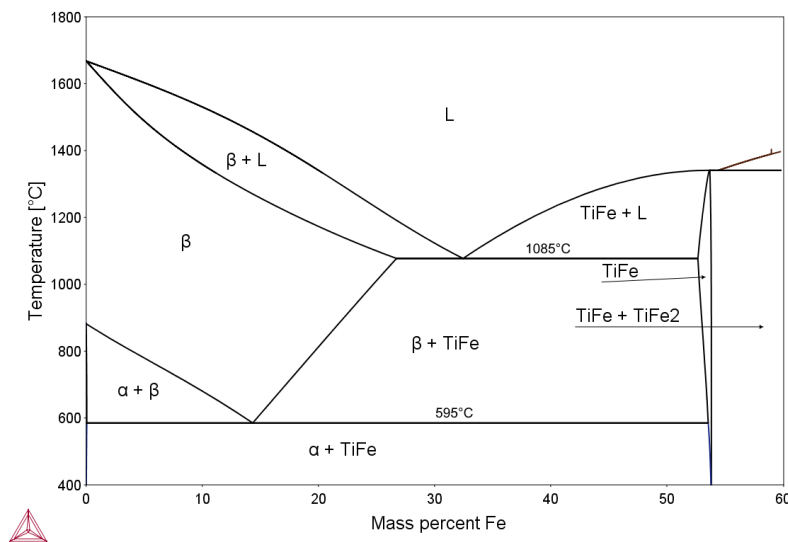
FIGURE 2.21: Calculated Ti-Fe binary phase diagram, showing the eutectoid behaviour at lower iron concentrations (calculated using Thermo-Calc Software TTTI3 ThermoTech Ti-based Alloys Database) [138].

Fe, along with other β eutectoid alloying elements, sufficiently extends the temperature range of solidification after VAR. This causes enrichment of Fe in the last liquid to solidify, leading to segregation. This segregation results in a phenomena known as β flecks, β stabilised regions up to a few millimetres in length with a relatively high concentration of Fe. β flecks are detrimental to mechanical properties, as they act as nucleation sites for cracking, leading to reduced fatigue performance [139]. The stability of the intermetallic phase TiFe also prevents high Fe contents in Ti alloys. Intermetallic phases are particularly

brittle, therefore their presence will reduce the ductility of an alloy, which is undesirable in most applications. Although formation of TiFe is thermodynamically favourable, it is a kinetically slow process and therefore can be avoided with a sufficiently high cooling rate from the β region [3].

Fe in conventional Ti alloys

As shown in Table 2.1, Fe is deliberately added in small amounts to the CP Ti grades (up to 0.5 wt.% in grade 4), where it is used to generate small amounts of β phase which pin α grain boundaries to prevent excessive grain growth during recrystallisation [3]. It is also present is various other alloys in small amounts ($\sim$2 wt.%), the most common of which is Ti-10V-2Fe-3Al, a high strength β alloy developed by Titanium Metals Corporation (TIMET) for airframe components with excellent forgeability [140], [141].

Alloying containing >2 wt.% Fe are unusual, due to the processing difficulties discussed earlier. One example, however, is TIMETAL-LCB (low-cost beta, Ti-6.8Mo-4.5Fe-1.5Al), developed by TIMET to create a β alloy by using the least amount of alloying additions, and contains 4.5 wt.% Fe. It was designed to be a low cost, high strength alloy for automotive coil spring applications [18]. Apparently, no major segregation issues are experienced during the solidification of this alloy, although it is not clear how this is achieved [142].

2.6.2   Production of Ti-Fe alloys via solid-state alloying

Alloying in the solid state by using blended elemental powder metallurgy eliminates the issue of Fe segregation and provides an opportunity to make high Fe content Ti alloys which were previously not possible. The blended elemental approach is very simple: metal powders are mixed in a specific ratio to give the desired alloy composition. The mixture is then used in a PM process (several of which are described in Section 2.5), to produce a billet or component. The heat required in these processes allows for the diffusion of the different elements, leading to a chemically homogeneous alloy. In this case, alloying is achieved through solid-state diffusion of the elements, meaning that fast diffusion rates are important to prevent long processing times. Fe has a high diffusion

rate in Ti, making it a suitable alloying element to consider as it aids the sintering and formation of homogeneous microstructures when using blended elemental PM [143].

There are several publications on using blended elemental PM to create binary Ti-Fe alloys, or to replace other β stabilisers, such as Mo and V, with Fe [144]. The main motivation for this research area is the development of low-cost Ti alloys with comparable mechanical properties to conventional ones, by using Fe.

Extensive research has been done on the production of binary Ti-Fe from blended elemental powders by researchers led by Leandro Bolzoni, with alloys up to 7 wt.% Fe being made and SEM and XRD analysis finding no trace of TiFe found in the sintered material. This was achieved using the press and sinter method, which led to significant porosity, and densities up to 96% theoretical achieved. This level of porosity and the large grain sizes formed due to high processing temperature, led to relatively poor mechanical properties [145], [146]. Further studies using press and sinter found similar results, indicating that this PM technique does not provide sufficient consolidation of the powders when using sintering temperatures up to 1300°C for 1 hour [147]–[151]. Higher relative densities by press and sinter have since been achieved, however this requires multiple long sintering stages and/or further thermomechanical processing [21], [152]–[154]. Despite the limitations of press and sinter, these publications show that homogeneous $\alpha+\beta$ microstructures can be generated for Ti-5Fe and Ti-7Fe alloys, demonstrating that these alloys can be created via solid-state alloying, without segregation and intermetallic formation.

2.6.3   The diffusion of iron in titanium

Fe, like the other β eutectoid stabilising elements, has a fast diffusion rate in Ti, meaning that homogeneous alloys can be produced without excessive processing times, making it an appealing alloying element for solid-state alloying with Ti.

The diffusion rate of Fe is $\sim10^5$ times greater in α phase than α Ti self diffusion from 900–1100 K, and ~10 times greater in β phase than β Ti self diffusion (as shown in Figure 2.4). Self diffusion in metals occurs via the vacancy diffusion mechanism, so given that Fe diffuses faster than Ti self diffusion, there must be an interstitial mechanism involved [155]. Figure 2.22 displays how the diffusion rate of Fe in β Ti and Ti-xFe alloys varies with temperature. Faster diffusion rates are measured at higher temperatures and in the

Ti-xFe alloys where there is a lower concentration gradient, as discussed earlier in Section 2.1.6.

Given the faster diffusion rate of Fe in Ti than Ti self diffusion, the Kirkendall effect would be expected to occur in this system. Some studies on the diffusion bonding of Ti alloys with steel discuss the potential for Kirkendall pore formation, although it does not seem to be significantly present under the processing conditions used. Instead, poor mechanical strength of the join is attributed to the formation of brittle intermetallic phases at the interface [157], [158]. Micrographs of Ti and 304 stainless steel diffusion couples, presented in Figure 2.23, show how the diffusion layer increases with temperature and the effect of Fe, Cr and Ni (other β eutectoid stabilisers in the steel) on the Ti microstructure. This shows that diffusion of these elements is sufficient to retain a layer of β on the Ti side of the interface. This gradually becomes an $\alpha+\beta$ and then fully α microstructure with increasing distance from the interface and decreasing contents of these β stabilising elements.
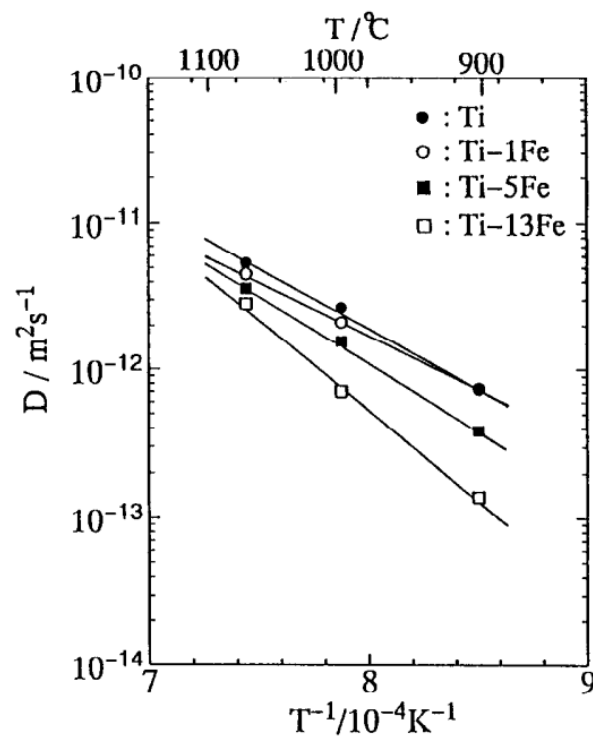
FIGURE 2.22: Temperature dependence of Fe diffusion rates in β Ti and Ti-xFe alloys [156].
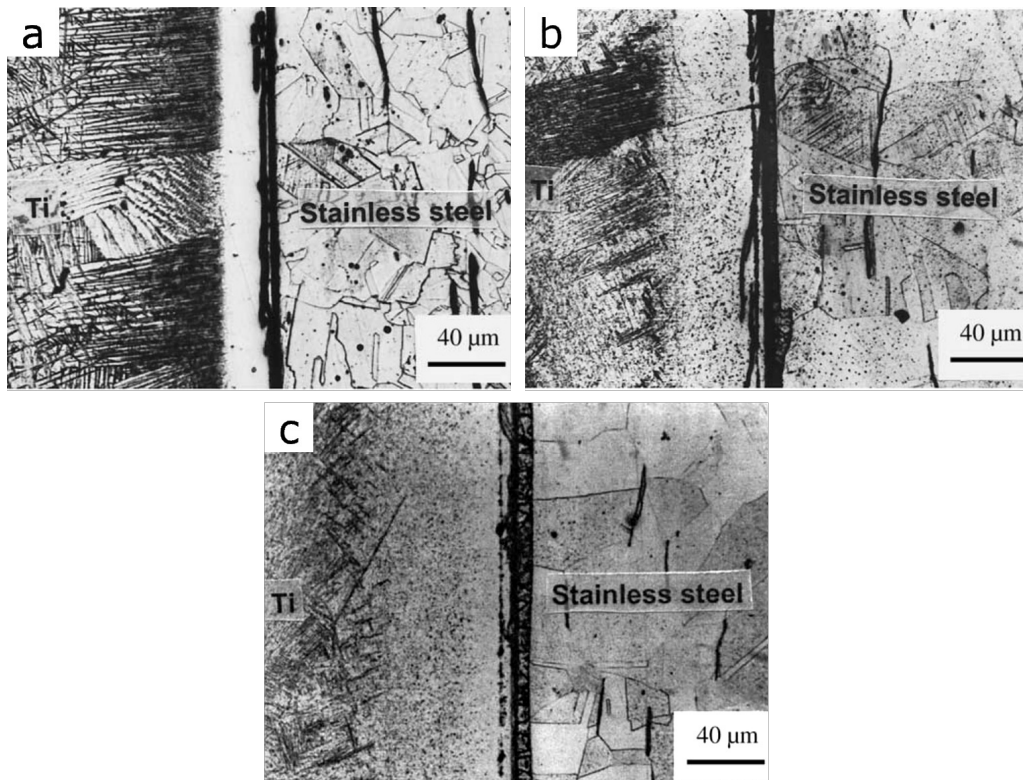
FIGURE 2.23: Optical micrographs of Ti/stainless steel diffusion couples bonded for 2 hours at a) 850°C, b) 900°C and c) 950°C [157].

2.7   Summary

This literature review has covered a range of topics related to the research aims. Relevant aspects of Ti materials science have been studied to ensure a good understanding of the fundamentals. An overview of the conventional Ti production route is followed by detailed focus on the alternative extraction technologies which have been proposed in an attempt to reduce the cost of Ti alloys. The FFC-Cambridge process arguably has the most potential, and subsequently most research interest, of all the alternative extraction technologies, but much work is required to successfully scale it to industrial levels. Using the process with synthetic rutile feedstock has potential for production of a relatively cheap source of Ti alloy powder, and so could have a significant role to play in the future of the Ti industry.

Several powder metallurgy techniques are considered as a means to create Ti components with the benefit of reduced material wastage from machining. This includes FAST and interesting recent developments of the technology for Ti processing and recycling of machining swarf. Combination of synthetic rutile derived Ti alloy powders from the FFC-Cambridge process with PM techniques such as FAST offers an exciting alternative Ti production route, which could be more cost-effective.

The Ti-Fe system is then examined for new Ti alloy development using these alternative processing technologies, due to the low cost of Fe and the ability to use solid-state alloying to prevent segregation issues experienced in conventional melt based Ti alloy metallurgy. Fe is also found to be a good candidate for solid-state Ti alloy development due to its high diffusion rate.

Overall, this review shows that there is scope for development of Ti-Fe alloys using these solid-state extraction and processing technologies, the FFC-Cambridge process and FAST, respectively. Synthetic rutile derived Ti alloy development via the FFC-Cambridge process is still a very new area of research, and so this work aims to build upon the promising previous results. FAST has not been extensively used for solid-state alloying, especially in the Ti-Fe system, so it is of interest to see if it can be used to improve upon previous press and sinter based work.

Chapter 3

Experimental methods and materials

3.1 Electrolytic reduction of metal oxides via the FFC-Cambridge process

3.1.1 Oxide preparation

Synthetic rutile powder was first fired to reduce the C content through oxidation, preventing high C levels in the resulting alloys. Mixing of metal oxides was performed using a Turbular mixer for 1 hour prior to being placed into the reduction vessel.

3.1.2 R&D scale reductions
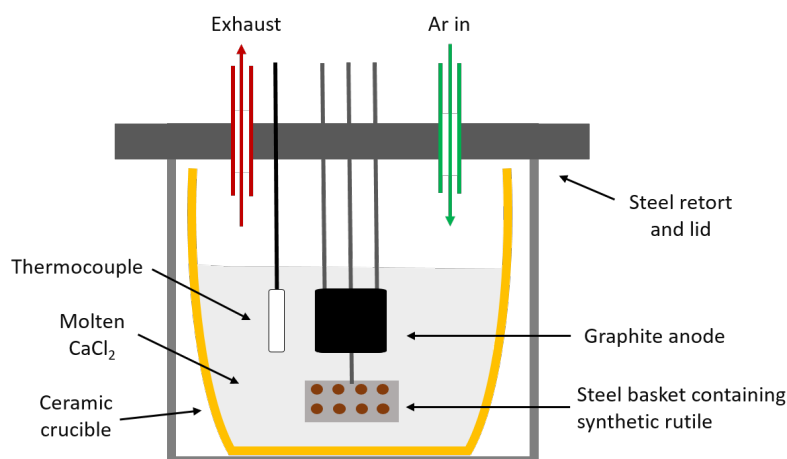
FIGURE 3.1: Diagram of R&D scale electrolytic cell used at Metalysis.

The cell, shown schematically in Figure 3.1, consists of a stainless steel retort and lid into which the anode, cathode and thermocouple rods were placed. The anode rods were connected to a graphite block and the cathode rod was connected to a stainless steel basket.

The basket was lined with a stainless steel mesh and the oxide powders were placed inside. A layer of $CaCl_2$ was used to cover the powder to ensure it remained in the basket once submerged in the molten salt. 1.6 kg of dried $CaCl_2$ in a ceramic crucible was placed into the retort along with some CaO. The lid was then placed onto the retort, with the basket, anode and thermocouple inside. An exhaust pipe was attached to remove and analyse the gases produced and a water loop connected to cool the lid of the vessel. An Ar line was connected and the system sealed to allow the reduction to proceed under an inert atmosphere.

The temperature was ramped up to 950°C, melting the salt and allowing the electrodes to be submerged into the electrolyte. An electric current was then applied to initiate the electrolysis. The system was held at these conditions for the desired time and then the electrodes withdrawn from the salt. The system is then allowed to cool to room temperature before disassembly of the cell.

The material removed from the reduction cell requires further processing and cleaning to give the final powder product. Firstly, the basket containing the product was soaked in water to allow the salt to dissolve away. The product was then finely ground by hand using a mortar and pestle and thoroughly washed to remove any residual salt and graphite particles from degradation of the anode. An acid wash in dilute aqua regia solution was used to further clean the resulting powders and reduce the surface oxide thickness. The powders were then dried under an inert Ar atmosphere at 80°C. A magnet sweep was used to collect any of the steel mesh which may have remained in the powders, and then they were sieved to a standard size range of 75–212 μm. Particles below 75 μm generally have higher C contents and so were discarded. The final powders were then ready for analysis techniques and further processing.

3.1.3   Development scale reductions

The development scale is a considerable size up from the R&D scale, from $\sim$20 g of oxide to $\sim$5 kg (for TiO_2). Although the underlying process is the same, there are changes in the temperature, voltage and reduction times due to the larger amount of oxide to be reduced. Exact details of the reduction parameters are sensitive to Metalysis, and therefore not included here. The material removed from the cell is post-processed in a similar way to

R&D, but on a larger scale and with initial crushing done mechanically rather than by hand. More sintering occurs on this scale, and so more processing is required to break up the material to <212 μm powder. Therefore, the material was sieved to 75–500 μm for analysis and further processing.

3.2 Consolidation of metal powders via field assisted sintering technology

Processing of metal powders by field assisted sintering technology (FAST) was performed using an FCT Systeme GmbH type HP D 25 furnace (Figure 3.2). Alloy powders were placed within cylindrical graphite moulds with internal diameters of either 20 mm or 60 mm, depending on the desired size of the final consolidated material. Graphite foil is used to line the inner surface of the mould, as well as above and below the powder, to act as a protective barrier between the powder and the graphite tooling. This allows for easy sample removal after processing, preventing damage to the tooling and allowing it to be reused many times. Two rams slot into the mould, either side of the powder, then the tooling is pressed using a tabletop hydraulic press to 20 MPa. This ensures good contact between the powder particles prior to processing, which results in more effective heating once the electrical current is applied. After pressing, two support pieces are slotted onto either end of the tooling, with Figure 3.3 and Figure 3.4 showing the prepared tooling stacks, ready for insertion into the vacuum vessel, between two copper electrodes. When using the larger 60 mm tooling, 5 mm thick carbon fibre reinforced carbon (CFRC) plates are placed between the tooling and electrodes. This is done to improve power efficiency, reduce the temperature of the electrodes and make the temperature distribution across the tooling more homogeneous [159].

A program recipe is created with the desired processing parameters. All programs in this work consisted of the following segments:

1. Vacuum pump pulls a vacuum in the vessel

2. Pressing to 20 MPa

3. Uncontrolled heating to 450°C

FIGURE 3.2: Photograph of the FCT Systeme GmbH type HP D25 furnace
used for all FAST processing.

4. Controlled heating to maximum temperature combined with pressing to maximum
   pressure

5. Dwell at maximum temperature and pressure for a set time

6. Power off, uncontrolled cooling to room temperature

The equipment uses real-time temperature data from an optical pyrometer, along with a
proportional–integral–derivative (PID) controller, to control the amount of power applied
at any given time, depending on the current temperature and programmed temperature.
The pyrometer has a lower temperature limit of 450°C, so heating is only controlled by
a programmed fixed 'power limit' up to this temperature. For the controlled heating
from 450°C to maximum temperature, a heating rate of 100°C/min was used for all
experiments. A maximum pressure of 35 MPa was also used for all experiments, based on
previous research using the same machine to process a range of Ti powders [129]. A DC
pulse pattern of 15 ms on, 5 ms off was also employed based on previous work with this
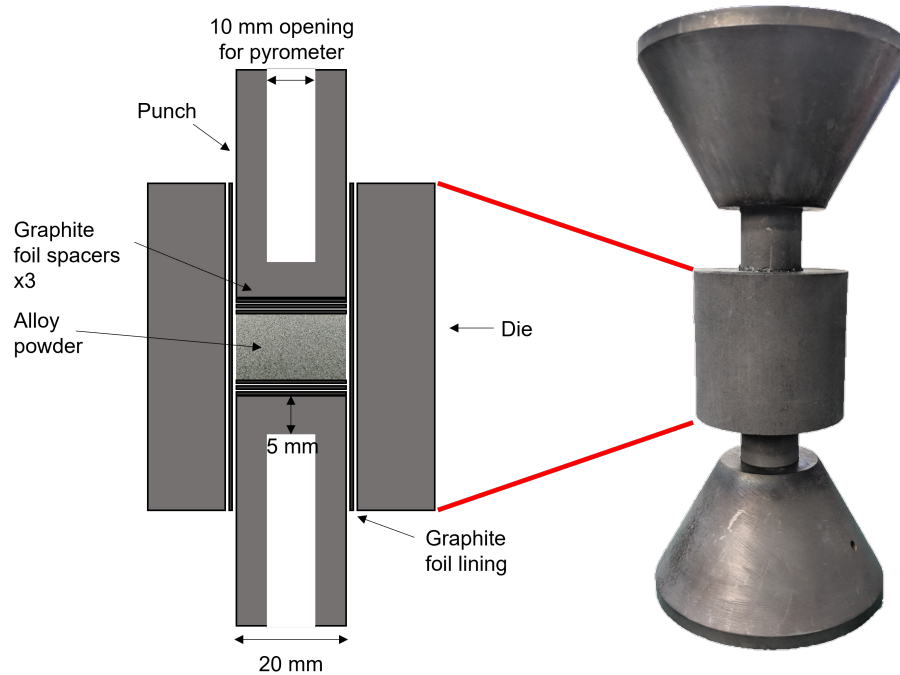
FIGURE 3.3: Cross-sectional diagram of 20 mm internal diameter graphite tooling and photograph of assembled tooling.

FIGURE 3.4: Left: photograph of assembled tooling (60 mm internal diameter) with supports, right: photograph of assembled tooling placed into the FAST vacuum vessel and covered with a graphite felt jacket.

equipment. Maximum temperature and dwell time were the only variables altered.

After processing, the vessel is repressurised using air from the atmosphere and the tooling is removed. The tooling is disassembled and the consolidated sample removed. Any residual graphite foil is removed and the samples are ready for sectioning or machining.

3.3   Metallographic sample preparation

Consolidated samples were sectioned using a Struers Secotom-50 with a SiC cut-off wheel. Both powder and sectioned surfaces of consolidated samples were hot mounted using a Buehler SimpliMet 3000 mounting press. Conductive bakelite was used so that they could be analysed using scanning electron microscopy. Some powder samples were cold mounted in epoxy resin for optical microscopy. A Struers Tegramin-25 was used sample grinding and polishing. The surfaces were ground for 1 min using P800, P1200 and P2500 SiC grit papers, followed by polishing with a colloidal silica suspension for 10 min.

3.4   Characterisation and analysis techniques

3.4.1   Particle size distribution

Particle size distribution of the powders was measured using a Malvern Mastersizer 3000 with wet dispersion in distilled water. A mean average of 10 measurements was used.

3.4.2   Chemical analyses

O and N analysis of powders was performed at Metalysis by inert gas fusion using an ELTRA ON-900. C analysis was done using an ELTRA CS-800. Trace element analysis was performed by inductively coupled plasma mass spectrometry (ICP-MS) using a Thermo X series 2. Further elemental analysis of major elements was done by X-ray fluorescence (XRF) on consolidated material, using a PANalytical Zetium.

3.4.3   Phase analysis

X-ray diffraction (XRD) patterns were obtained using a Bruker D2 Phaser using a Cu-Kα radiation source (1.5406 Å wavelength). A step size of 0.02° was used with a time of 0.5 s per step and the sample was rotated at 15 rpm during the scan. The resulting XRD patterns generated were analysed by comparison with crystallographic data from crystallographic information files (CIFs) obtained from the Crystallography Open Database [160]. Figure 3.5 shows the XRD patterns for all phases of relevance in this research.
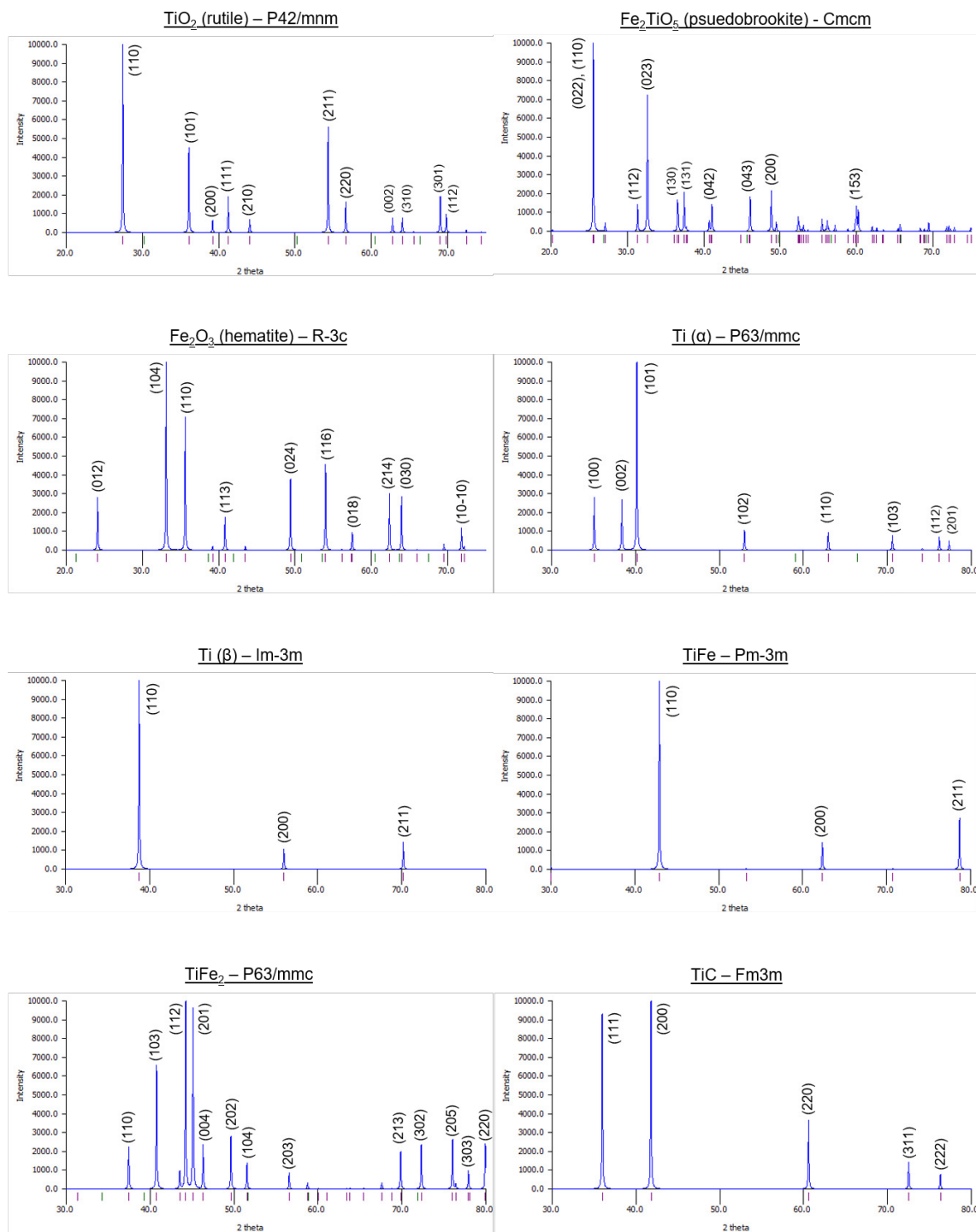
FIGURE 3.5: XRD patterns of the potential phases present in the oxides and Ti alloys studied. Peaks are labelled with their corresponding crystallographic planes. The patterns were calculated from CIFs using the program *Mercury*, a crystal structure visualisation tool developed by the Cambridge Crystallographic Data Centre [160]–[169].

3.4.4 Microscopy and spectroscopy

Both optical microscopy and scanning electron microscopy (SEM) were used to study the microstructures of the materials and fracture surfaces after tensile testing. A Nikon Eclipse LV150 light microscope was used for optical microscopy, with cross-polarised light filters inserted to reveal the crystal structure of Ti alloys. In addition, an Olympus BX51 optical microscope was used with a moving stage and Clemex Vision software, allowing for the automatic capture of high resolution mosaic images from multiple high magnification images stitched together. This was used for porosity analysis in the FAST consolidated alloys, by capturing a 10 mm^2 area and applying a colour threshold leave only the porosity visible. The percentage area was measured using ImageJ software to give a good estimate of the level of porosity in the sample [170].

SEM was performed using an FEI Inspect F50 with an acceleration voltage of 20 keV. Backscattered electron detector mode was used to analyse variations in chemistry, with brighter features corresponding to regions with higher Z contrast. This is very useful when observing dual phase Ti microstructures, as the α and β phases will have differing brightness in the images. Secondary electron detector mode was used for imaging of features present in the fracture surfaces of tensile specimens after failure. Energy-dispersive X-ray spectroscopy (X-EDS) was done using the same machine, but with an Oxford Instruments attachment and AZtec software. Electron probe micro analysis (EPMA) was performed using a JEOL JXA-8530F+, which uses a combination of wavelength dispersive spectroscopy and X-EDS detectors to achieve high resolution elemental analysis.

3.5 Mechanical property testing

3.5.1 Microhardness testing

Vickers hardness measurements were carried out using a ZwickRoell Durascan-80, with different forces used depending on the size of the features being tested. The HV (hardness-Vickers) value used is the number of kilograms of force applied by the diamond tipped indenter. This force was held for 15 s as per ASTM E92 [171].

3.5.2   Tensile testing

Tensile testing was performed using a ZwickRoell universal material testing machine, model Z050, equipped with a 50 kN load cell. The width and thickness of each specimen's gauge length were measured at three locations and the mean averages used for calculating the cross-sectional area. Two short lengths of wire were attached to the specimens to allow for tracking by the camera extensometer. Wedge grips were used to hold the ends of the specimens and a constant crosshead speed of 0.6 mm/min was applied until failure. The camera extensometer, combined with testXpert II testing software, recorded the force and displacement, which are then converted into stress and % elongation values.

The elastic modulus (E) was estimated for each specimen in the elastic region where the stress/strain relationship is linear. For specimens tested in Chapter 5, 0.2–0.5% elongation was chosen (or to maximum elongation if 0.5% was not reached), due to some unusual behaviour below 0.2% when loading was initially applied. For specimens tested in Chapter 6, 0–0.3% elongation was chosen, as this behaviour did not occur and because some specimens began to plastically deform above 0.2%.

The yield strengths (YS) were approximated by finding the 0.2% offset. A straight line with gradient E (from previously estimated values) from point 0.2, 0 was constructed, and the intercept with the stress/elongation curve gave the YS.

3.6 Materials

3.6.1 Oxide powders

Synthetic rutile

Supplier: Iluka Resources

Particle size: 150–212 μm (supplier)

Chemistry:

TABLE 3.1: Elemental composition of synthetic rutile powder, measured by XRF. Data provided by Iluka Resources.

Element	Ti	Fe	Mn	Al	Si	C	Mg	Nb	V	S	Zr	Cr	Ca	O
Content /wt.%	56.11	2.90	0.69	0.59	0.42	0.36	0.22	0.21	0.15	0.14	0.09	0.04	0.02	Bal

Backscattered electron micrographs of the synthetic rutile powder are presented in Figure 5.5.

Iron (III) oxide

Supplier: Sigma-Aldrich

Particle size: <5 μm (supplier)

99% purity

Backscattered electron micrographs of the Fe_2O_3 powder are presented in Figure 5.5.

3.6.2 Metal powders

Ti alloy powders

TABLE 3.2: Summary of information on the Ti alloy powders used. Chemistry data for CP Ti (Alfa Aesar) from certificate of analysis provided by supplier. Chemistry of other alloy powders tested by Intertek. All values in wt.% unless specified. Particle size values as provided by supplier.

Alloy	Supplier	Production method	Ti	Fe	O	C	N	H	Particle size
CP Ti	Phelly Materials	HDH	99.74	<0.05	0.143	0.005	0.003	0.015	45–150 μm
	Alfa Aesar		>99.8	0.0021	0.25	0.011	0.0076	0.012	<45 μm
Ti-6Al-4V	TIMET	PREP	88.38	0.26	0.181	0.023	0.003	32 ppm	45–105 μm
Ti Beta-C (Ti-3Al-8V-6Cr-4Mo-4Zr)	TLS Technik Spezialpulver	GA	75.03	<0.05	0.092	0.004	0.018	22 ppm	<250 μm
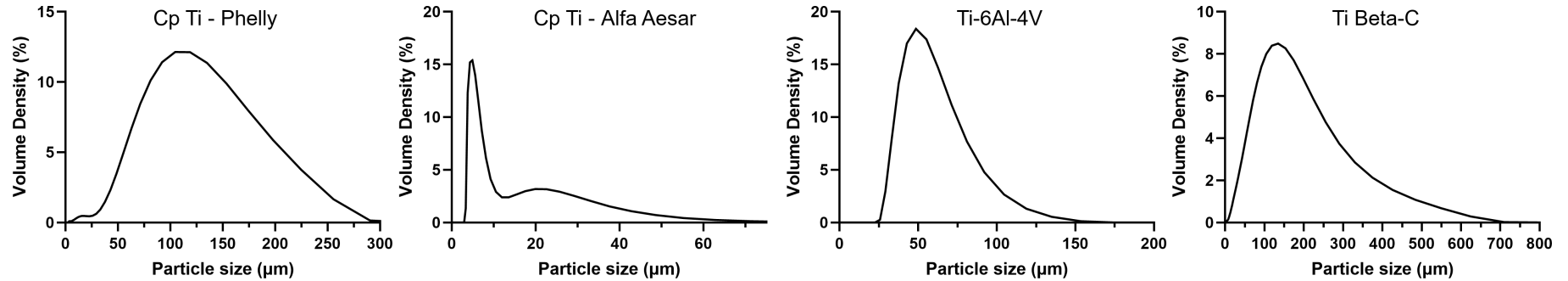
FIGURE 3.6: Measured particle size distribution of each Ti alloy powder.
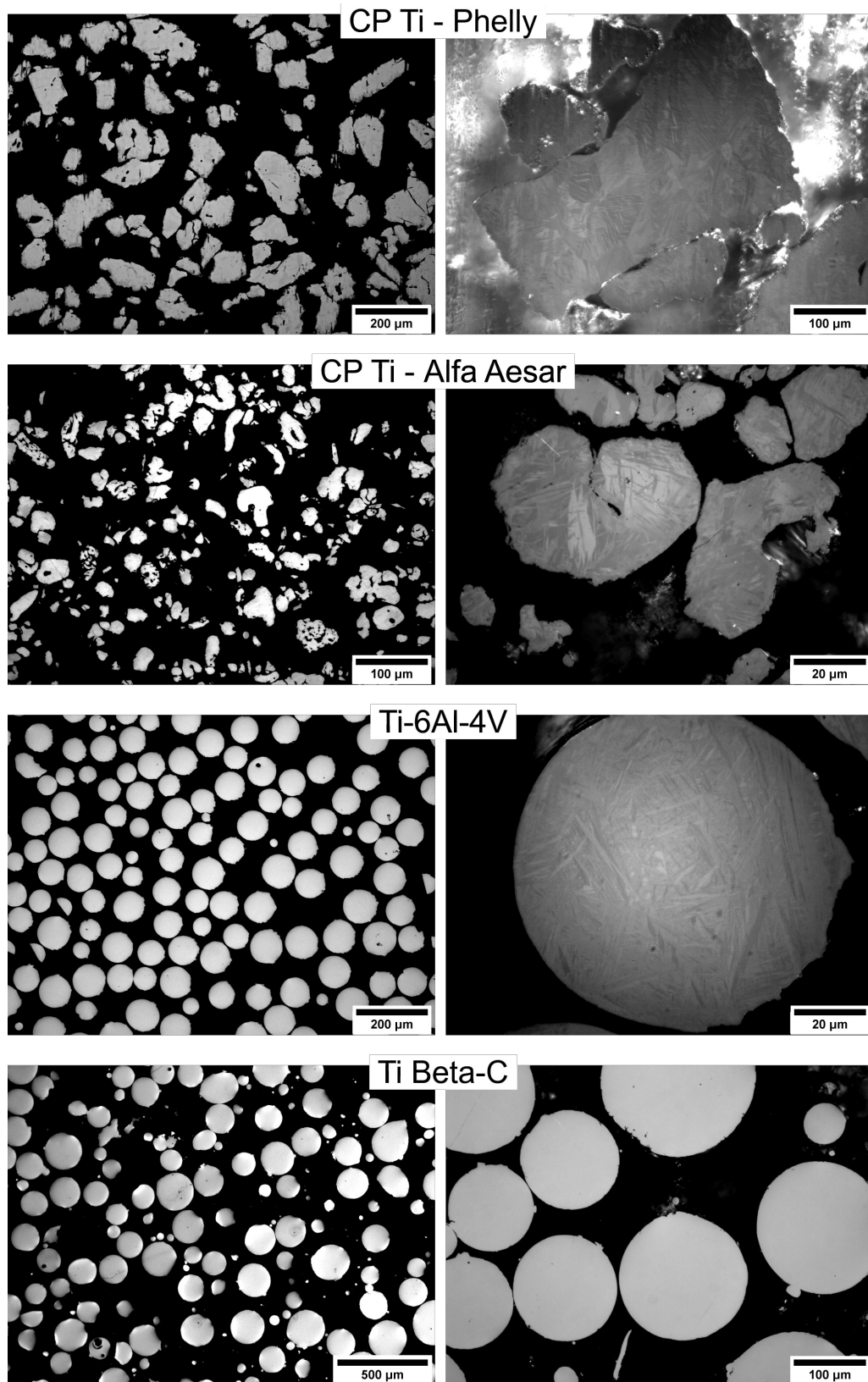
FIGURE 3.7: Optical micrographs showing cross-sections of Ti alloy powder particles at two magnifications, to show morphology and microstructure.

Fe powder

Supplier: Goodfellow UK

Particle size: <60 μm (supplier), measured (Figure 3.9).

Chemistry: >99 wt.% Fe, <1400 ppm Si, <200 ppm C (according to datasheet provided by supplier).
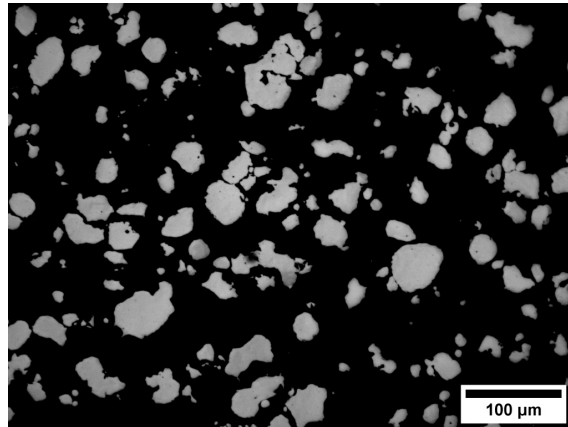
FIGURE 3.8: Optical micrograph showing cross-sections of Fe powder particles.
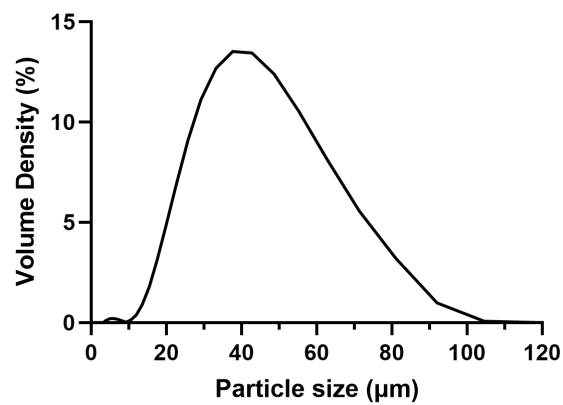
FIGURE 3.9: Measured particle size distribution of Fe powder.

Chapter 4

Investigating the diffusion behaviour of the Ti-Fe system during FAST processing

Experimental data from this chapter contributed to an article published in the journal Calphad (Elsevier), entitled 'Mobilities of Ti and Fe in disordered TiFe-BCC assessed from new experimental data' [172]. This publication was achieved in collaboration with researchers at KTH Royal Institute of Technology in Stockholm, Sweden. I (Simon John Graham) am the second author and performed all Ti-Fe diffusion couple experimental work (except for EPMA analysis, performed by Dr. Dikai Guan), as well as contributing to writing, editing, and providing data and figures, some of which are included in this chapter.

4.1   Introduction

As reviewed in Section 2.3.4, the synthetic rutile derived Ti alloy powder produced via FFC-Cambridge process was heterogeneous, with individual particles significantly differing in both chemical compositions and microstructures. Processing of these powders using field assisted sintering technology (FAST) not only achieves the desired consolidation, but also acts as a homogenisation heat treatment for the alloy. This is possible without particularly long processing times, due to the relatively fast solid-state diffusion exhibited by Fe in Ti. Before exploring the production of higher Fe content SR derived Ti alloys and binary Ti-Fe alloys from blended elemental powders, it is important to first investigate the diffusion

behaviour of the Ti-Fe system during FAST processing in more detail. This would help in determining the necessary conditions which would ensure that sufficient diffusion occurs to achieve homogenisation and prevent presence of intermetallic phases within the alloys. Analysing the microstructures formed across the diffusion zone also allows for a better understanding of the relationship between Fe content in Ti solid solution and resulting microstructures for alloy development purposes.

Investigating diffusion between two metals is typically done using diffusion couples, where flat surfaces of the two metals are held in contact at a set temperature for a set amount of time. The amount of diffusion which has occurred is then determined through chemical analysis across the interface or by the use of tracers such as radioisotopes. For example, the use of the radioisotope ^{59}Fe has been used to analyse this system previously [156], [173]. FAST can be used as a relatively simple method to produced diffusion couples, as it is capable of high heating rates up to the desired temperature for diffusion analysis, while applying a constant force for sustained contact between the two metals.

4.2 Experimental procedure

The diffusion couple setup was composed of a solid piece of CP Ti, with a layer of Fe powder above. This solid-powder setup was chosen to give a cleaner interface than would be achievable through vertical layering of two powders. The resulting straight line interface is also easier for chemical and microstructural analysis, along with measurements of diffusion distances perpendicular to the interface.

10 g of CP Ti powder (Phelly - details in Section 3.6.2) was consolidated within a 20 mm diameter graphite mould via FAST, using a maximum temperature of 1000°C with a 10 min dwell time. The surfaces of the resulting consolidated pellet were ground using silicon carbide grit paper up to P1200 to remove the graphite layer and generate a flat surface for the diffusion couple. After the surface was cleaned with isopropanol, the CP Ti pellet was then reinserted into the graphite mould, and 10 g of Fe powder (Section 3.6.2) was poured on top. The same FAST parameters were once again used, however with varying dwell temperatures and times. The diffusion couples were then sectioned, ground and polished prior to analysis.

Diffusion couples were processed at three different dwell temperatures: 800°C, 900°C and 1000°C. These were chosen due to the differing Ti and Fe phases which would exist at these temperatures. Pure Fe has a phase transformation from BCC α ferrite to FCC γ austenite at 912°C, whereas pure Ti has a phase transformation from HCP α to BCC β phase at 882°C. Therefore, processing at these three temperatures not only compares the diffusion with respect to temperature, but also the phases (Table 4.1). Temperatures higher than 1000°C were not considered due to the eutectic transformation at 1085°C which was expected (from the Ti-Fe phase diagram in Figure 2.21) to cause melting at the interface . Dwell times of 0, 15, 30, 45 and 60 min were used to study the increase in diffusion distance over time and to investigate how the diffusion rate changes over time.

TABLE 4.1: Phases of Ti and Fe at different processing temperatures

Temperature / °C	Ti phase	Fe phase
800	α	α
900	β	α
1000	β	γ

Electron probe microanalysis (EPMA) was performed across the interfaces. A scan line with step size of 1 μm and 250 μm length was measured, with 250 μm into the Ti and 50 μm into the Fe. SEM micrographs were also taken using both this equipment and the Inspect F50.

A further diffusion couple was processed at 1000°C with a 120 min dwell time, for microhardness measurements as described in Section 3.5.1. A straight diagonal line of indents were performed at an angle of $\sim$30° to the interface and over a length of $\sim$1.2 mm. A force of 100 g (HV 0.1) was used for these indents.

4.3   Results and discussion

4.3.1   Diffusion analysis by scanning electron microscopy

0 min dwell

At 800°C (Figure 4.1), the Fe particles have begun to sinter together, however they are not fully consolidated. There is no visible bonding with the Ti, therefore no evidence of diffusion is seen and no new phases are present in addition to α Fe and α Ti.

Figure 4.2 shows that at 900°C, the Fe is has almost fully consolidated but has not bonded well with the Ti. There are some distinct regions where bonding has occurred however, with some diffusion clearly visible at these sites, indicated by roughly semicircular regions of retained β phase (Figure 4.2 b). This phase appears brighter under backscattered electron imaging due to the higher Z contrast from the Fe stabilised β. At the bonded interface there seems to be another phase present, expected to be intermetallic TiFe and/or TiFe$_2$. This suggests that sufficient consolidation and bonding between the Fe powder and the Ti surface is required for significant diffusion to take place.

Figure 4.3 shows that once 1000°C is reached, most of the Fe surface has bonded to the Ti, with only a few regions of porosity (identifiable as black features) present. At these sites (an example of which is highlighted with a red circle in Figure 4.3) where there is no bonding, it is clear to see that less diffusion of the Fe has occurred into the Ti, with less β phase present. Where there is bonding, a layer of β phase $\sim$10 μm in thickness has been retained. Fe has essentially no solubility in the α phase, so it can be estimated that the presence of β phase indicates the extent of diffusion. Figure 4.3 b reveals some channels of β which penetrate deeper into the α Ti, suggesting enhanced diffusion pathways along grain boundaries. Diffusion is known to occur at much faster rates along grain boundaries as they act like sinks for the diffusing species [174].
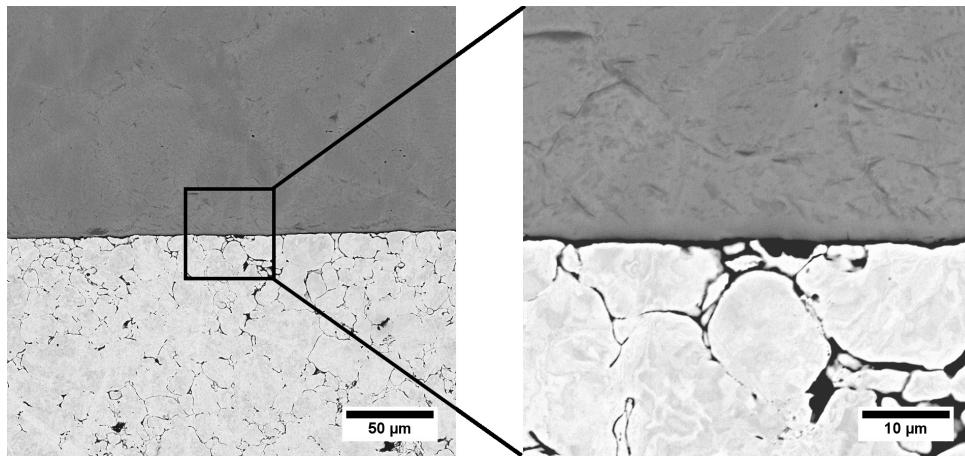
FIGURE 4.1: Backscattered electron micrographs showing interface of Ti-Fe diffusion couple processed at 800°C with no dwell. (Top is Ti side in darker grey, bottom is Fe side)
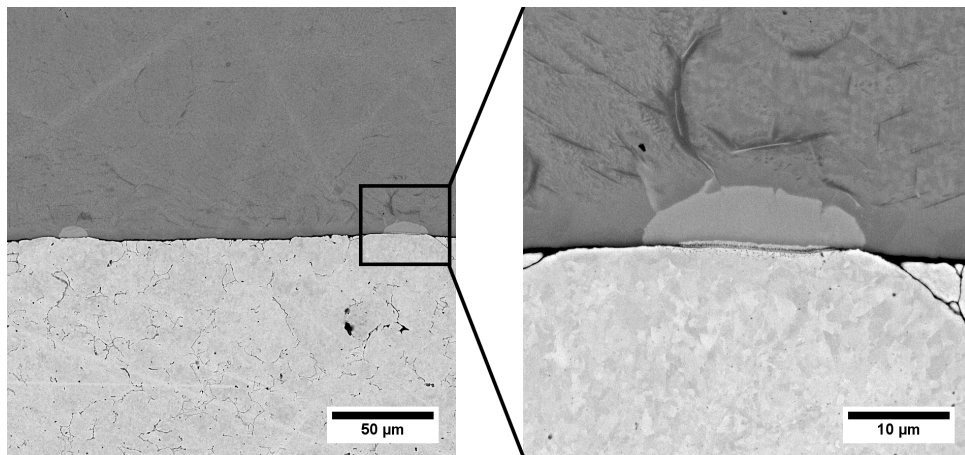
FIGURE 4.2: Backscattered electron micrographs showing interface of Ti-Fe diffusion couple processed at 900°C with no dwell.
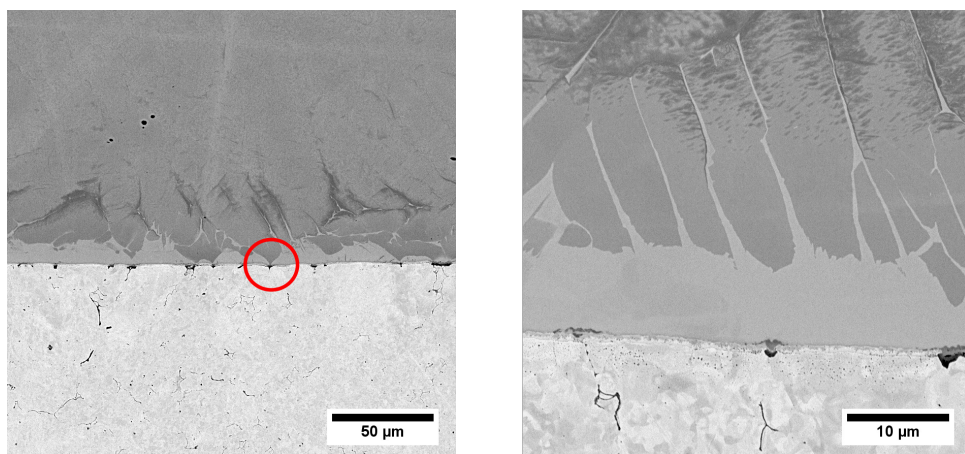
FIGURE 4.3: Backscattered electron micrographs showing interface of Ti-Fe diffusion couple processed at 1000°C with no dwell.

60 min dwell

Figure 4.4 illustrates the substantial increase in the Fe diffusion rate into Ti with temperature, with increasing thicknesses of the Fe rich β phase layers.

At 800°C (Figure 4.4 a), a thin layer of β phase has formed with a maximum thickness of $\sim$8 μm, less even than the diffusion couple processed at 1000°C with 0 min dwell. Like the 0 min dwell samples, the layer is irregular, which looks again to be due to poor bonding between the two metals in some areas, limiting diffusion. Some thin channels of β are once again visible, which again indicate enhanced grain boundary diffusion.

The 900°C sample gives the cleanest interface, with the Fe fully bonded to the Ti and no defects present. Despite the initial irregular diffusion seen in Figure 4.2, after 60 min the diffusion is consistent along the interface. Figure 4.4 b clearly shows the different microstructural layers formed, with decreasing Fe content moving further into the Ti side from the interface. Here, the β layer is $\sim$40 μm, beyond which α phase begins to appear. A second layer containing both α and β phases exists for a further $\sim$60 μm, beyond which much larger α regions are present, with some channels of β penetrating deeper into the Ti.

At 1000°C, Figure 4.4 c essentially shows the same again, but these microstructural layers are more spread out due to increased Fe diffusion. In this case, the β layer is $\sim$100 μm thick before α phase is visible. Interestingly, the Fe region in this diffusion couple contains far more porosity compared to the lower temperatures. This was initially surprising as full consolidation is achieved at the lower temperatures, and therefore this would also be expected at 1000°C. It is likely that this porosity is a result of the Kirkendall effect. As discussed in Section 2.6.2, this effect occurs in systems like this when one species has a higher diffusion rate into the other than the opposite. In this case, the diffusion rate of Fe into Ti is far greater than Ti into Fe and Fe self diffusion, causing vacancy accumulation in the Fe side. Over this time period, extensive Fe diffusion has occurred, leading to significant porosity generation.

These micrographs are very similar to those in Figure 2.23, where Ti has been bonded with a stainless steel. Similar intermetallic and microstructural layers are visible, and β layer thicknesses are comparable. Direct comparison cannot be done though, due to

the presence of significant amounts of other elements in the steel (Cr and Ni), as well as different processing conditions.
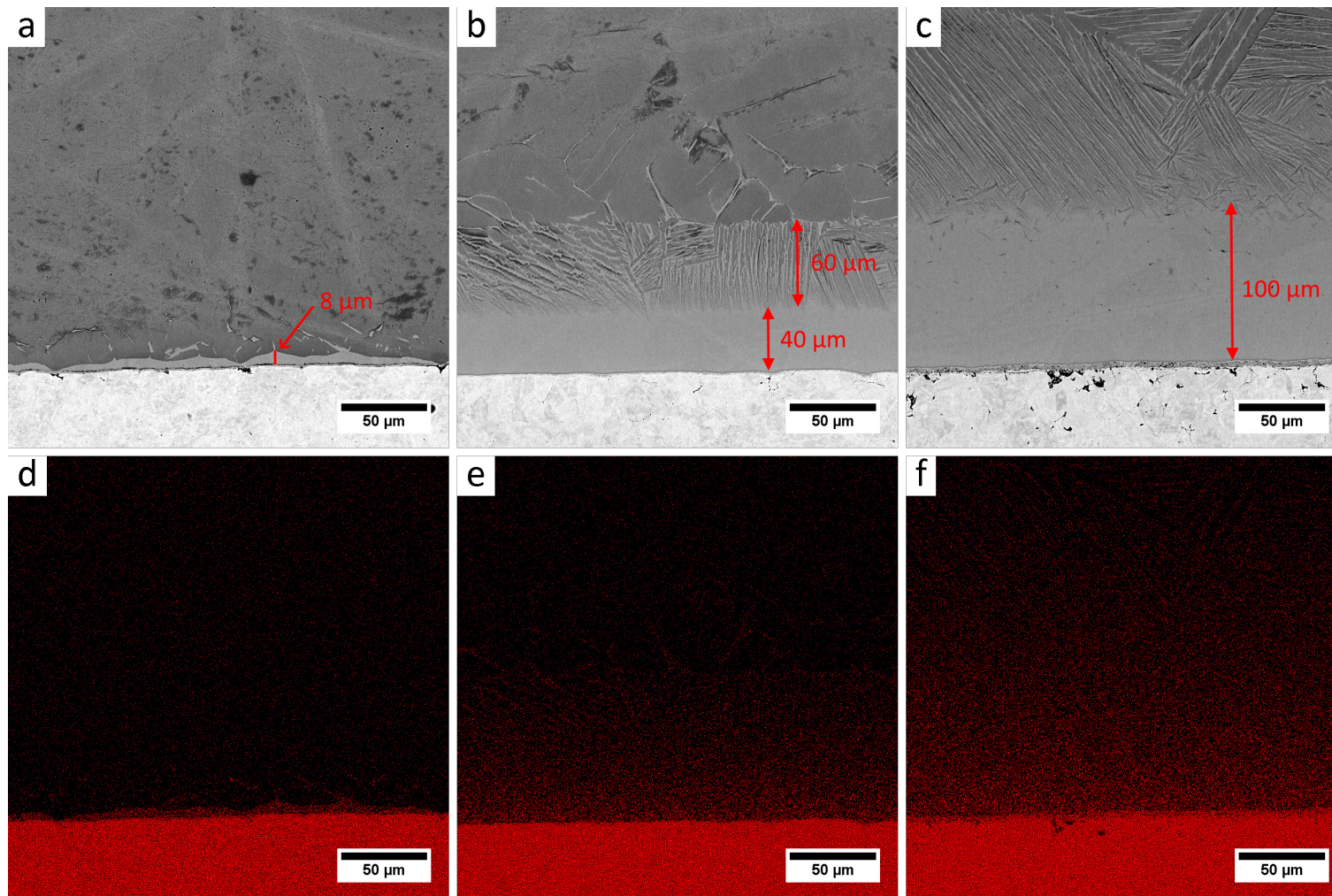
FIGURE 4.4: Backscattered electron micrographs of Ti-Fe diffusion couples processed for 60 min with corresponding X-EDS Fe element maps (all same magnification). a & d) 800°C, b & e) 900°C, c & f) 1000°C.

Analysis of the interfacial intermetallic layer

Backscattered electron microscopy reveals a distinct layer at the interfaces of all the diffusion couples where bonding occurred. The layer increases in thickness at higher temperatures and dwell times, therefore the 60 min, 1000°C diffusion couple gives the best opportunity for analysis. Figure 4.5 shows the 60 min, 1000°C diffusion couple interface at higher magnification, with these processing conditions producing a layer ∼3 μm thick. A 15 μm X-EDS line scan was performed across the interface to measure the change in chemistry and composition of this layer. The line scan data shows that the composition of this layer is approximately equal wt.% Fe and Ti, which corresponds to 46 at.% Fe and 54 at.% Ti. X-EDS mapping of the two elements across the interface also confirms this. These values suggest that the layer is primarily composed of the intermetallic phase TiFe, although it could be a multi-phase region, with other phases including TiFe$_2$ and β Ti possibly present also. The data also highlights the differing maximum solubility of each element in the other, with ∼5 wt.% maximum Ti in the Fe compared to ∼20 wt.% Fe in β Ti solid solution.

It is important to understand what occurs at the interface as the intermetallic layer is integral for the diffusion process. Figure 4.2 b reveals that this layer forms immediately once the two metals join, and facilitates Fe diffusion across the interface into the Ti. It is unknown what effect the thickness of this layer has on the diffusion kinetics, as two new interfaces have effectively been created: Fe/intermetallic layer and intermetallic layer/Ti. Formation of this layer is also well understood to prevent the effective joining of steels and Ti alloys, due to the brittle nature of these intermetallic phases. This has led to research on using interlayers such as copper in an attempt to prevent the formation of TiC and Ti-Fe intermetallics [175].
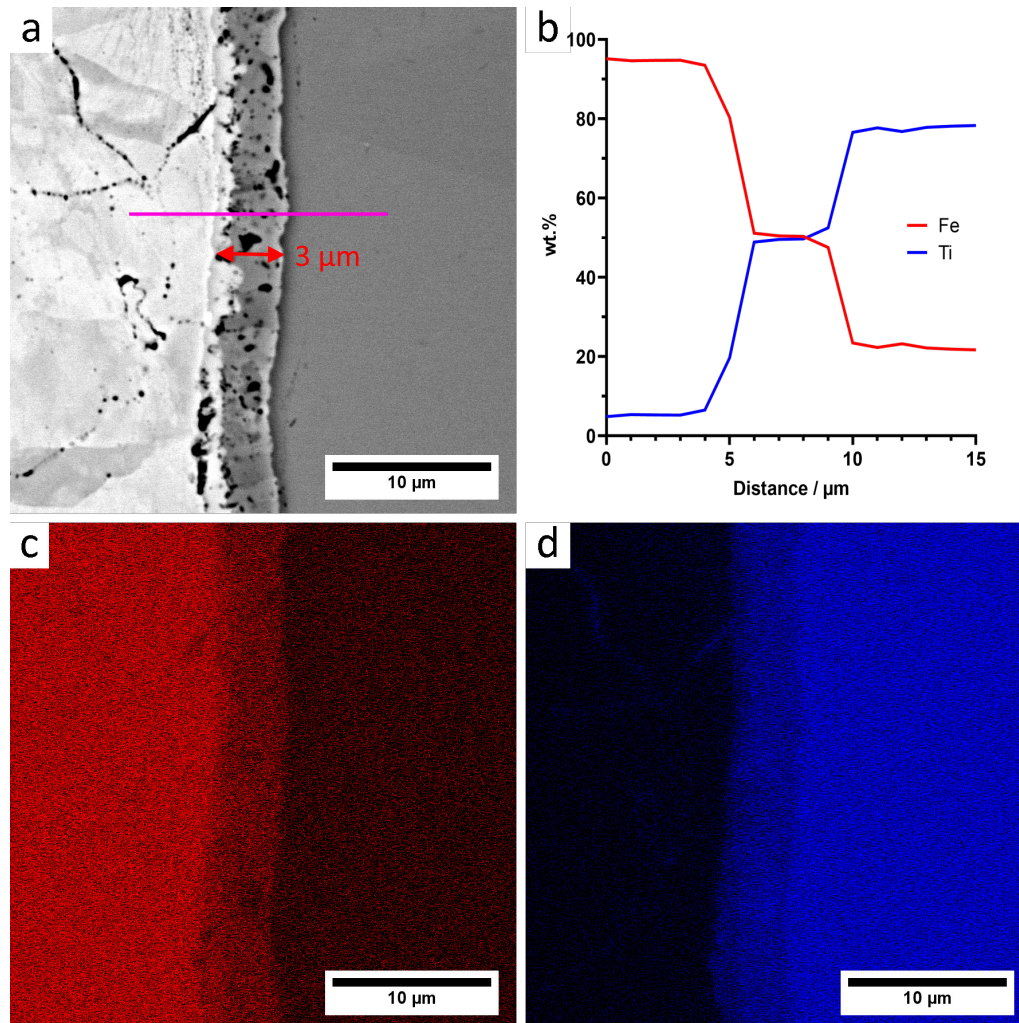
FIGURE 4.5: a) Backscattered electron micrographs of interface of 60 min, 1000°C diffusion couple, with 15 μm line scan location overlaid, b) corresponding wt.% of Ti and Fe from X-EDS line scan data, c and d) X-EDS element maps of the same region with detected Fe in red and Ti in blue.

4.3.2 Diffusion analysis using electron microprobe

EPMA data was obtained for the diffusion couples processed at all temperatures and dwell times from 15 min, in order to measure the changing chemistry over a larger distance and how the temperature and dwell time affects it. The irregular bonding and diffusion in the 800°C samples mean that line scans are not necessarily a good representation of the diffusion. Also, because there is very little diffusion occurring, even after 60 min (Figure 4.4), the data is not included here. The line scans for the 900°C and 1000°C samples measure over the regular microstructural layers seen in Figure 4.4, and so give useful data.

Figure 4.6 illustrates how the diffusion distances of Fe into Ti increase with both temperature and dwell time. The diffusion profiles all look similar but spread out different amounts depending on the extent of diffusion. Temperature is clearly the more significant variable, with the diffusion profile for 1000°C after 15 min similar to 900°C after 60 min. A mole fraction Fe of around 1 is measured in the bulk Fe, which then decreases slightly closer to the interface, due to some diffusion of Ti into the Fe. Some significant dips are seen in a few of the datasets, confirmed due to the line scan measuring over the Kirkendall porosity when consulting the corresponding backscattered electron micrographs. Crossing the interface, there is a sharp drop in the Fe content, followed by a gradual decrease, indicating the Fe in solid solution within the Ti β phase. After the β layer, the data then becomes less smooth due to the emergence of the $\alpha + \beta$ region, where the Fe content is variable depending on which of the two phases the EPMA happens to measure along the line scan. Peaks in the Fe content mean a measurement was taken on some β phase, whereas troughs signify α phase. After this, the Fe content falls to 0, indicating where the diffusion front did not reach and the Ti is fully α phase. It is difficult to pinpoint at exactly what distance this occurs though, likely due to the enhanced grain boundary diffusion of Fe meaning that it will continue to be detected in trace amounts far deeper into the Ti.

More detailed analysis is achieved when looking more closely at the data from the 900 and 1000°C, 60 min samples (Figure 4.6). A short shelf is seen at the interfaces of the 1000°C sample, caused by the intermetallic layer studied in Figure 4.5. Although this layer is present in all the samples, it is only thick enough to be detected using a step size of 1 μm in those processed at 1000°C. The composition agrees well with the previous X-EDS measurement in Figure 4.5, with a mole fraction Fe of 0.46 once again measured. The
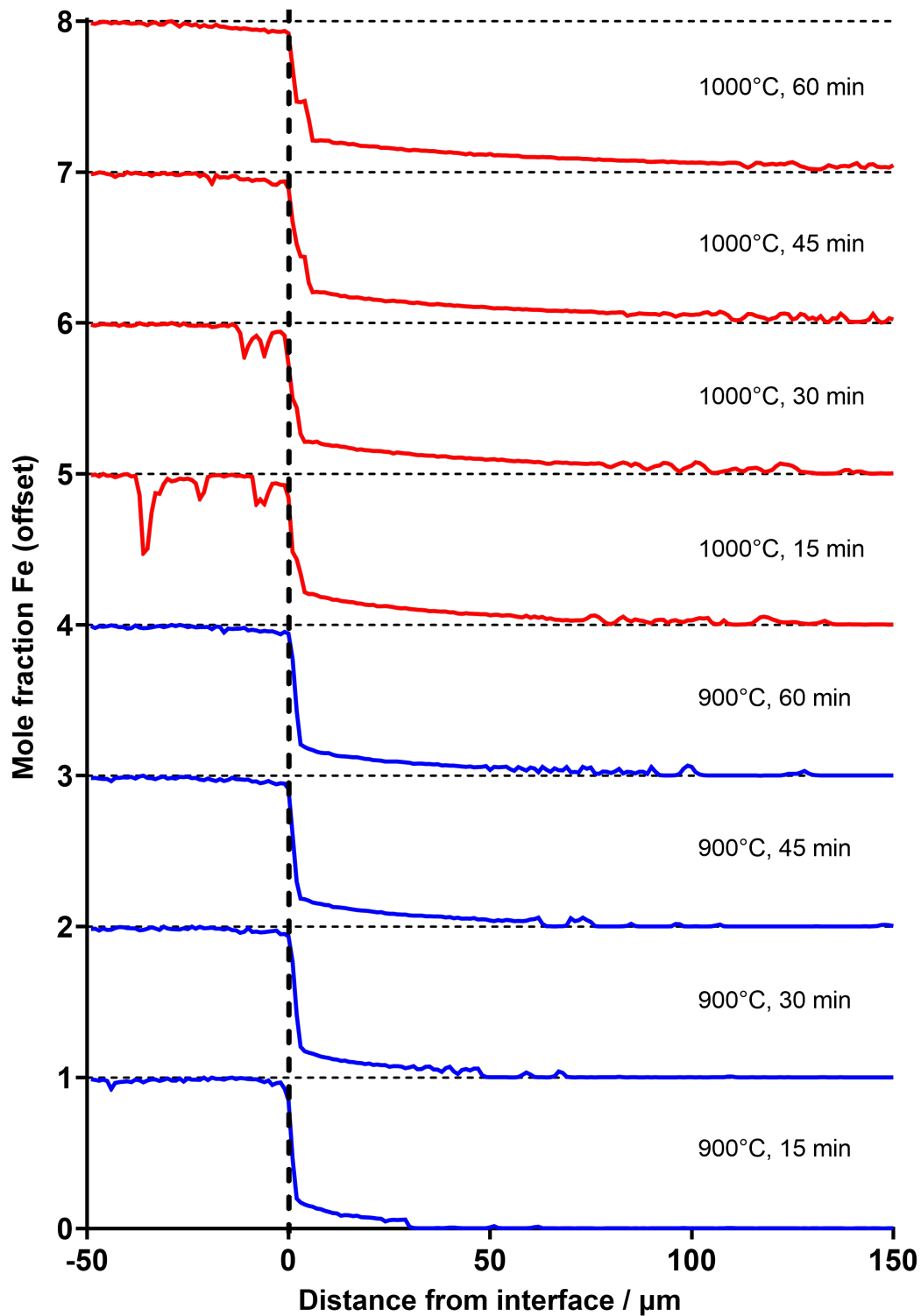
FIGURE 4.6: Data from EPMA line scans across the 900°C and 1000°C diffusion couple interfaces, measuring Fe mole fraction 50 μm from the interface into the Fe and 150 μm into the Ti.
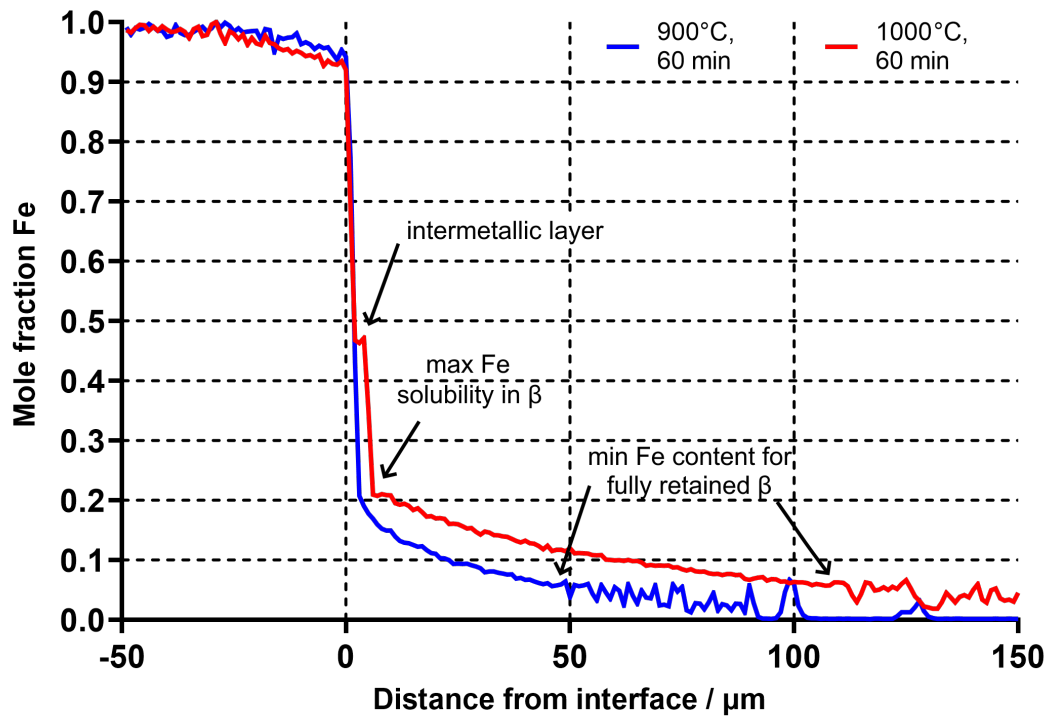
FIGURE 4.7: Comparison of EPMA data for 900°C and 1000°C at 60 min dwell.
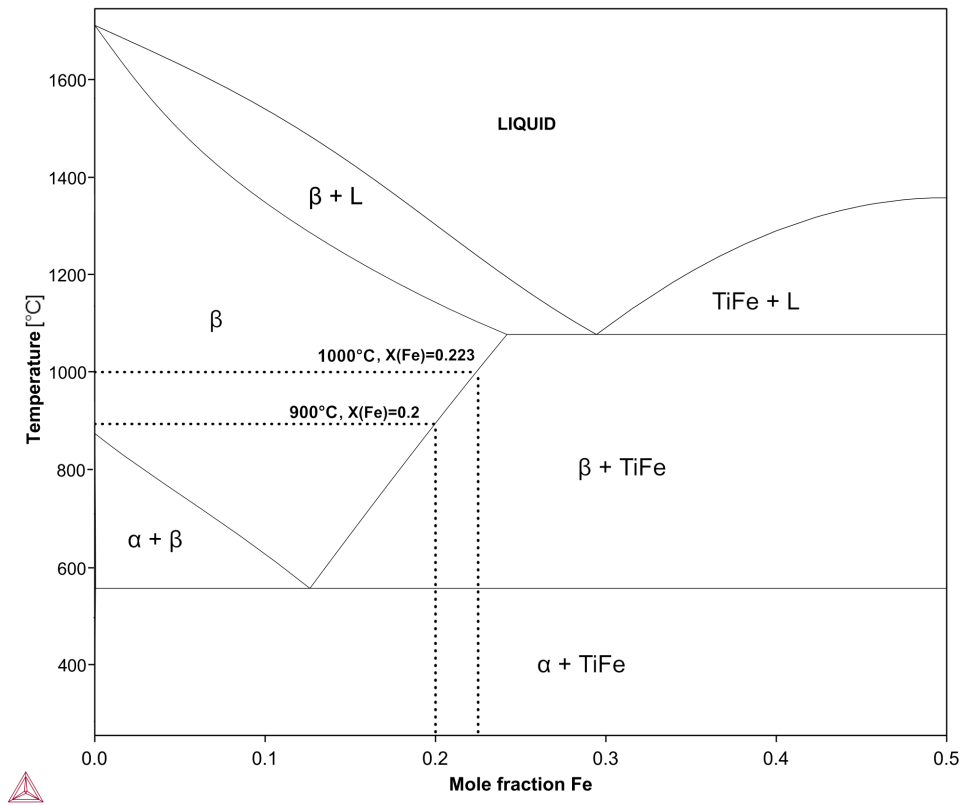
FIGURE 4.8: Ti-Fe phase diagram with annotations to show Fe solubility limit in *β*-Ti at both 900°C and 1000°C. Modified from [172].

highest Fe content in the β phase is $\sim$0.2 mole fraction, also in agreement with the X-EDS data. This value represents the maximum solubility of Fe in the β phase of Ti, and would be expected based on the calculated phase diagram (Figure 4.8). The solubility increases at higher temperatures, so the maximum Fe concentration in the 1000°C β Ti should be higher, although they are too similar to discern in this data. The minimum amount of Fe to fully retain the β phase is estimated at $\sim$0.06 mole fraction, at which α precipitates begin to emerge. Using this range of 0.06–0.2 mole fraction Fe, the thickness of the β phase is estimated for each diffusion couple. Figure 4.9 shows how the the thickness changes with processing temperature and dwell time, with the data demonstrating that the rate of diffusion reduces over time. This is to be expected as there is a less dramatic concentration gradient and so the driving force for further diffusion decreases. This is also consistent with the diffusion data in Figure 2.22, where diffusion rates are slower in Ti containing more Fe in solid solution.
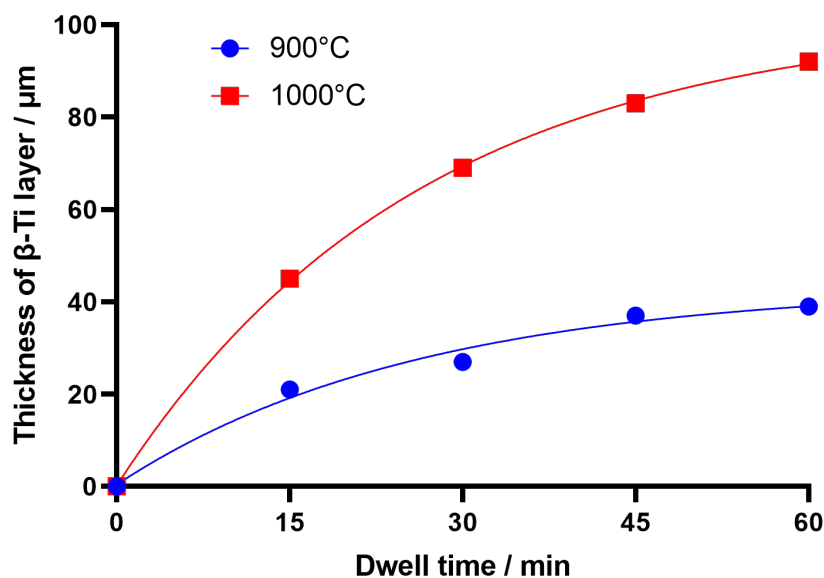
FIGURE 4.9: Graph of β-Ti layer thickness against FAST dwell time at both 900°C and 1000°C. Thicknesses estimated from EPMA data, when 0.06< Fe mole fraction >0.2. Non-linear regression curve fitted to the data, using 0, 0 points despite some diffusion seen at the 0 min dwell stage.

4.3.3 Microhardness across diffusion couple interface

An additional Ti-Fe diffusion couple was produced using a 120 min dwell time at 1000°C. This was done to further spread out the Ti microstructural layers so that microhardness measurements could be taken to understand how the microstructure and amount of Fe content in solid solution affects the hardness of Ti. Figure 4.10 shows these results, with a clear trend of increasing hardness approaching the interface. The first four indents all have similar hardness values of ∼240 and are therefore measured in the CP Ti where no Fe has diffused. The next four have a significantly higher hardness >300. This corresponds to the $\alpha+\beta$ microstructural layer, with the highest value measured at indent 8, where the remaining α is relatively fine. The next group of indents start in the β only region, with the highest hardness measured at indent 11, where there the Ti is fully saturated with ∼20 wt.% Fe and the most solid solution strengthening occurs. Indent 12 falls directly on the intermetallic layer, although it also overlaps into the Ti and Fe sides and so this value is not representative of the intermetallic layer only. The final, larger indents are in the Fe, which is much softer at ∼100. Indent 13 has a higher hardness than the others, likely due to some solid solution strengthening from ∼5 wt.% Ti which dissolved into the Fe.
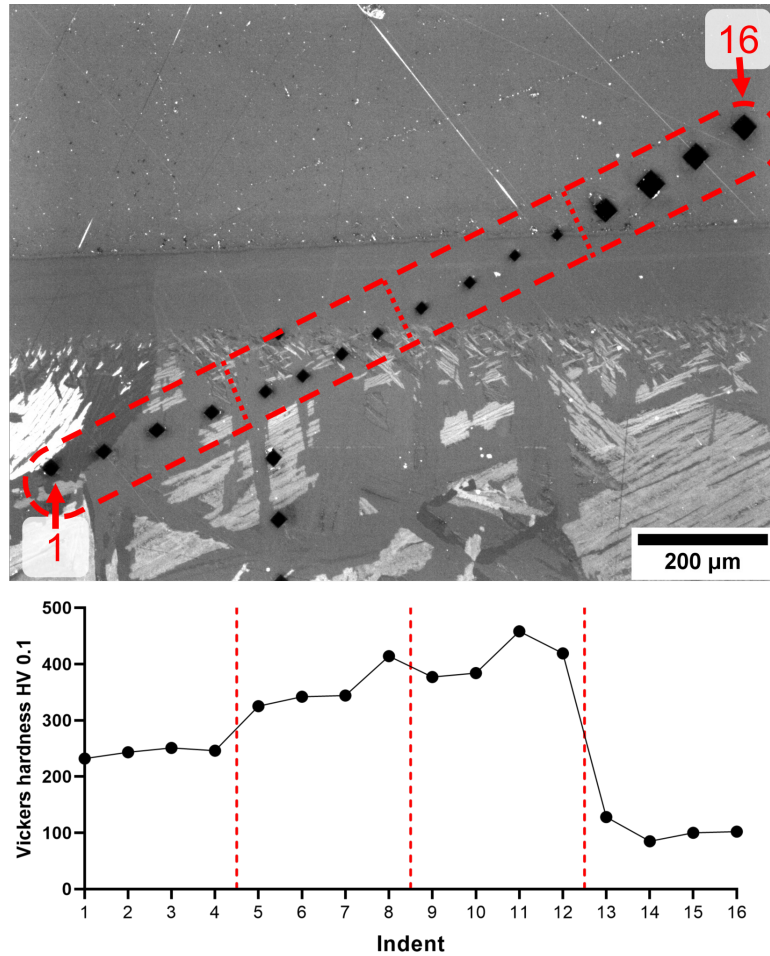
FIGURE 4.10: Optical micrograph using cross-polarised light of Vickers microhardness indents across a Ti-Fe diffusion couple interface, processed at 1000°C for 120 min, with corresponding hardness values below.

4.4 Conclusions

The results have highlighted the significant effect of processing temperature on the extent of Fe diffusion into Ti, over a relatively narrow 200°C window. As expected, there is no linear relationship between diffusion rate and temperature, rather an exponential one, as highlighted in Figure 4.4. At 800°C, diffusion is sluggish, with only a thin layer of retained β present in the analysed sample. The extent of diffusion was greater at 900°C and then at 1000°C, with clear layers of β and $\alpha+\beta$ microstructures seen depending on the Fe content. X-EDS and EPMA analysis gave Fe concentration profiles across the interface and into the Ti, allowing for quantitative analysis of the effect of processing parameters and compositions of each region:

- Bulk α-Fe

- α-Fe with up to ~5 wt.% Ti in solid solution

- Intermetallic layer with ~50:50 wt.% Ti and Fe - suggesting it is mainly comprised of the TiFe phase

- β-Ti region with a range of ~20–6 wt.% Fe in solid solution, decreasing with distance from the interface

- Dual phase $\alpha+\beta$ region with increasing amounts of α further from the interface

- Bulk α-Ti

These findings are similar to those in publications on bonding steels with Ti using FAST, as discussed in Section 2.6.3, however they are not directly comparable due to the presence of other alloying elements such as Cr, Ni and C which complicate the system and produce other intermetallic phases at the interface [157], [176].

The effect of the phases present at the three different temperatures (listed in Table 4.1) remains unknown from this analysis alone. The diffusion rate of Fe is known to be higher in α Ti slightly below the β-transus compared to in β Ti slightly above (as shown in Figure 2.4), although going to higher temperatures in the β phase quickly overcomes this.

Given the results, it seems most sensible to use a temperature of 1000°C when processing heterogeneous Ti-Fe alloy powders using FAST. The necessary dwell time is dependent

on the shape and size of the powder particles, along with then extent of chemical heterogeneity. Although data from this chapter is a useful guide, it only measures diffusion in a single direction, whereas diffusion between the angular particles produced by the FFC-Cambridge process make the system more complicated. Therefore, some optimisation of the FAST processing parameters will still be required.

The EPMA data combined with SEM also gives an indication of what microstructures will be generated depending on the Fe content of a Ti alloy processed under the same conditions. It would therefore be expected that Ti-Fe alloys with Fe contents from 6–20 wt.% will be fully β alloys, and that Fe contents <6 wt.% would be $\alpha+\beta$ alloys. This is useful for future alloy development with the binary Ti-Fe system.

Measurement of the hardness across the microstructural layers gave a good understanding of the effect of Fe content and resulting microstructures, with a trend of increasing hardness values due to solid solution strengthening. There is a correlation between the hardness and strength of materials, and so this information gives a useful understanding of the potential mechanical properties of binary Ti-Fe alloys.

It would be of interest to repeat this investigation using hot pressing instead of FAST to determine if the application of an electric current through the diffusion couple during processing has any effect on the diffusion rate and/or intermetallic layer formation. Modification of the DC pulse rate may also have an effect. Some studies provide evidence that the growth rate of intermetallic phases in the Ti-Ni system can be greatly increased when electric current is applied [177], [178]. They postulate that DC enhances atomic diffusion by causing an increase in the concentration of defects, or by electromigration. Given Ni has a similar atomic radius and diffusion coefficients to Fe, it could be possible that Fe diffusion would be affected in a similar way [179].

Overall, analysis of a range of Ti-Fe diffusion couples produced using FAST has generated an important understanding of the diffusion behaviour of this system. This aids the selection of parameters to be used when processing powders with FAST for solid-state alloying of Ti-Fe based alloys. The importance of this research is made evident by a following publication in collaboration with researchers at KTH Royal Institute of Technology in which the experimental EPMA data is used to optimise existing interaction mobility

parameters of Ti and Fe in β-Ti in a thermodynamic database [172].

Chapter 5

Co-reduction of synthetic rutile and iron (III) oxide via the FFC-Cambridge process to produce pseudo-binary Ti-Fe alloys
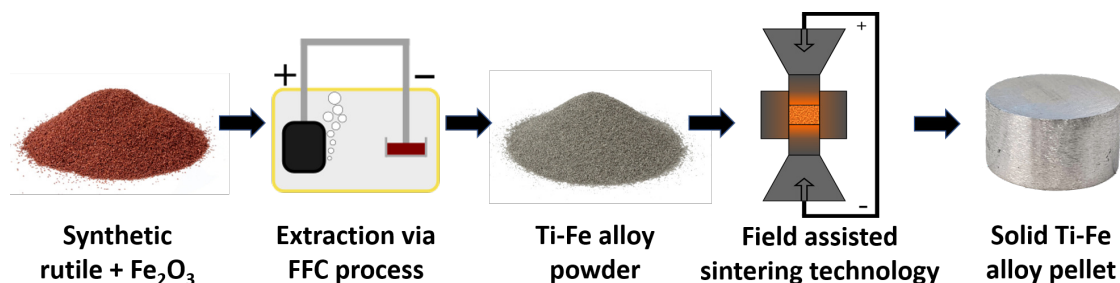
FIGURE 5.1: Proposed alternative Ti extraction and processing route investigated in this Chapter, utilising synthetic rutile and Fe_2O_3.

Section 5.2 of this chapter consists of an article published in the Journal of Materials Science (Springer), entitled 'Direct electrochemical production of pseudo-binary Ti–Fe alloys from mixtures of synthetic rutile and iron(III) oxide' [180]. The article is open access and licensed under a Creative Commons Attribution 4.0 International License, allowing for its reproduction. I (Simon John Graham) am the primary author and contributed all experimental work and writing. Co-authors Dr. Lyndsey Benson and Prof. Martin Jackson were industrial and academic supervisors, respectively. Note that as this is a self-contained publication, unmodified from the published version, there is inevitably some content overlap with Chapters 2 and 3 of this thesis.

5.1 Introduction

Ti alloy powders produced via the FFC-Cambridge process can be consolidated using FAST, leading to an appealing alternative Ti production route from ore to bulk material. Direct use of synthetic rutile (SR), an abundant and cost-effective Ti feedstock, further improves any potential cost-reduction. The reduction of SR via the FFC-Cambridge process to produce Ti with small amounts of remnant elements has been reported and well understood [17], [85]. Therefore, the work presented in this chapter aims to build upon this, by considering the co-reduction of SR with Fe_2O_3 to directly produce a range of $\alpha+\beta$ and β Ti alloys, with Fe_2O_3 chosen due to its low cost and Fe being a potent β stabiliser. The results from Chapter 4 also confirm that Fe diffusion in Ti is suitably quick at 1000°C, which is in the typical temperature range for FAST processing of Ti alloys, and so any heterogeneity in the reduced powders can be eliminated.

The material is analysed to monitor changes in chemistry, phases and microstructures resulting from each stage of processing; from the SR + Fe_2O_3 mixtures, to reduced Ti-xFe alloy powders, to FAST consolidated Ti-xFe alloys. Some mechanical property assessment of the bulk alloys post-FAST is also performed to compare with conventional Ti alloys and to determine their potential as materials in various applications.

Metalysis own the patents for commercialisation of the FFC-Cambridge process and supported the experiments done at their Materials Discovery Centre (Rotherham, UK). Reductions of the SR + Fe_2O_3 mixtures were first done using their R&D scale reduction cells, as discussed in Section 3.1.2, with the results presented as a published journal article (Section 5.2). Section 5.3 covers further work reducing the same oxide mixtures but on the larger development scale (Section 3.1.3), allowing for the production of tensile specimens for additional mechanical property testing.

5.2 Direct electrochemical production of pseudo-binary Ti–Fe alloys from mixtures of synthetic rutile and iron(III) oxide

Simon J. Graham[1], Lyndsey L. Benson[2], and Martin Jackson[1]

[1]Department of Materials Science and Engineering, The University of Sheffield, Sir Robert Hadfield Building, Mappin Street, Sheffield S1 3JD, UK

[2]Metalysis Materials Discovery Centre, Units 4A & 4B, Brindley Way, Catcliffe, Rotherham S60 5FS, UK

5.2.1 Abstract

Combining the FFC-Cambridge process with field-assisted sintering technology (FAST) allows for the realisation of an alternative, entirely solid-state, production route for a wide range of metals and alloys. For titanium, this could provide a route to produce alloys at a lower cost compared to the conventional Kroll-based route. Use of synthetic rutile instead of high purity TiO_2 offers further potential cost savings, with previous studies reporting on the reduction of this feedstock via the FFC-Cambridge process. In this study, mixtures of synthetic rutile and iron oxide (Fe_2O_3) powders were co-reduced using the FFC-Cambridge process, directly producing titanium alloy powders. The powders were subsequently consolidated using FAST to generate homogeneous, pseudo-binary Ti–Fe alloys containing up to 9 wt.% Fe. The oxide mixture, reduced powders and bulk alloys were fully characterised to determine the microstructure and chemistry evolution during processing. Increasing Fe content led to greater β phase stabilisation but no TiFe intermetallic phase was observed in any of the consolidated alloys. Microhardness testing was performed for preliminary assessment of mechanical properties, with values between 330–400 Hv. Maximum hardness was measured in the alloy containing 5.15 wt.% Fe, thought due to the strengthening effect of fine α phase precipitation within the β grains. At higher Fe contents, there was sufficient β stabilisation to prevent a phase transformation on cooling, leading to a reduction in hardness despite a general increase from solid solution strengthening.

5.2. Direct electrochemical production of pseudo-binary Ti–Fe alloys from mixtures of synthetic rutile and iron(III) oxide

95
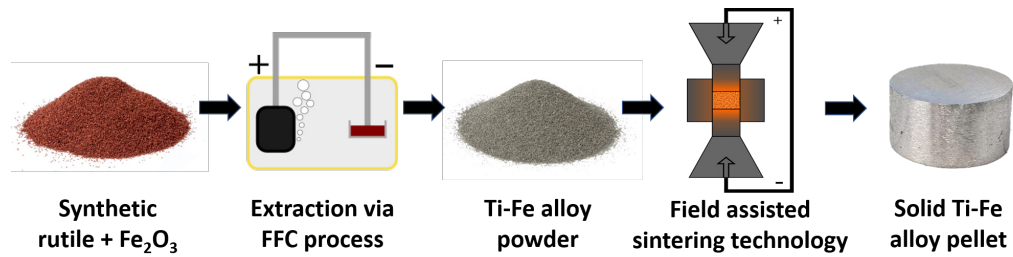
FIGURE 5.2: Proposed alternative Ti extraction and processing route used in this study.

5.2.2 Introduction

Titanium and its alloys have impressive properties, including high strength to weight ratio, corrosion resistance and biocompatibility, making them desirable for use in a wide variety of applications. The costs associated with current production prevent widespread use however, despite relative abundance of the ores. Therefore, there are many circumstances, for example in the automotive industry, where it would be preferable to use a Ti alloy, but an inferior material is used due to lower cost. Significantly reducing costs requires the realisation of an alternative production route, which is becoming increasingly plausible with novel extraction and processing techniques. Combining the FFC-Cambridge process with field-assisted sintering technology (FAST) offers an alternative, entirely solid-state processing route (Figure 5.2).

Ti extraction via the FFC-Cambridge process

The FFC-Cambridge process was first reported in 2000 by researchers Fray, Farthing and Chen as an electrolytic method for extracting Ti metal from its oxide [5]. The process has since been shown to be capable of reducing many different metal oxides, including those of tantalum, chromium and cerium [56], [61], [62]. Mixed-metal oxides can also be reduced simultaneously, allowing for the direct production of alloys, as well as more novel materials like high-entropy alloys and those derived from lunar regolith simulant material [64], [66], [77], [78], [80]. The process uses an electrochemical cell, consisting of a metal oxide cathode and a graphite anode, submerged in a molten salt electrolyte, usually $CaCl_2$. Applying sufficient voltage causes ionisation of the oxygen at the cathode, which is then transported through the electrolyte to react with the graphite carbon anode. This overall oxygen transfer results in deoxidised metal(s) and generation of CO and CO_2 gas

(Equations 5.1-5.3).

$$M_xO_y + 2ye^- \longrightarrow xM + yO^{2-} \tag{5.1}$$

$$C + 2O^{2-} \longrightarrow CO_2 + 4e^- \tag{5.2}$$

$$C + O^{2-} \longrightarrow CO + 2e^- \tag{5.3}$$
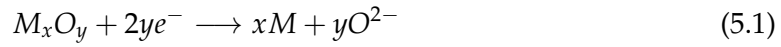
This is a simplified description of the process however, and various studies have been published on understanding the process in more detail. Partial reductions have been used to study the reduction pathway of metal oxides, revealing that they reduce via intermediate suboxides and Ca compounds [57], [72], [181]–[183]. Ca^{2+} ions are incorporated from the electrolyte and facilitate the transfer of O^{2-} ions to the anode. Additions of CaO were found to accelerate the rate of electro-deoxidation of TiO_2 by providing an initial source of O^{2-} ions. This sustains the ionic current, preventing Cl_2 formation and increasing current efficiency [74]. There has been some debate on the nature of O^{2-} ion transport through the electrolyte, with a recent study suggesting that when low amounts of CaO are present, transport occurs by diffusion and not migration [75].

Meanwhile, UK technology company Metalysis has been improving and scaling up the FFC-Cambridge process to create alloy powders on a commercial scale, designing facilities with the capability to produce tens to hundreds of tonnes of alloys per annum. Improvements to the process include the ability to directly reduce oxides in powder form, without the need for compaction into preform pellets [8]. The FFC-Cambridge process has gained particular interest for producing Ti and its alloys, due to the potential advantages it has over conventional Kroll-based extraction. These include being a single-step process, using oxide directly rather than $TiCl_4$ and having lower projected costs. Current titanium alloy powder production methods involve further processing of billets, such as atomisation or hydride- dehydride, which further increases their price.

Therefore, the ability to directly produce alloy powders makes the FFC-Cambridge process appealing for a range of downstream powder metallurgy manufacturing routes. To assess projected costs, a life cycle analysis study estimated that Ti production via the FFC-Cambridge process could reduce 'gross energy requirements' and 'global warming

5.2. *Direct electrochemical production of pseudo-binary Ti–Fe alloys from mixtures of synthetic rutile and iron(III) oxide*

97

potential' by 10–15% compared to conventional Kroll production; with further reductions of 30–35% achievable using lower TiO_2 purity feedstock [184]. Developments to the process have been investigated to make it even more attractive for Ti extraction, including use of more sustainable feedstocks, improving current efficiencies, use of inert anodes which prevent CO_2 generation and production of near-net shape components from shaped oxide precursors [69], [71], [74], [185]. A recent study on the use of shaped oxide via the 'Near-net-shape Electrochemical Metallisation (NEM) process' attempted to quantify the environmental impacts of components produced using this method, compared to electron beam melting of Kroll derived, gas atomised powders. It found that the NEM process dramatically reduced the overall environmental impact by about 68% in comparison [70]. Overall, the continued research and improvement of Ti extraction via the FFC-Cambridge process, along with supporting evidence of the potential advantages, demonstrates the potential for further exploitation of this technology in the future.

Until recently, most research has used pigment grade rutile (TiO_2) to produce Ti via the FFC-Cambridge process; but significant cost reduction can be achieved using lower purity precursor materials instead [70], [82]. One example is synthetic rutile (SR), which contains around 90–95% TiO_2, and is usually further processed into $TiCl_4$ for use in conventional Kroll extraction [186]. It is produced from ilmenite ore ($FeTiO_3$) via an Fe removal process, such as the Becher process [43]. Some impurity elements such as Fe, Al and Mn remain, with their relative amounts depending on the ilmenite source and processing conditions. Previous studies have directly reduced this material using the FFC-Cambridge process, producing a Ti alloy powder naturally containing these impurities as alloying elements [17]. The reduction pathway was also fully characterised and was found to be consistent with that of pure TiO_2 but with variations due to reductions of the other remnant elements. Overall, further investigation of SR as a feedstock in this production route is attractive for cost reduction while benefitting from already present alloying elements.

Field-assisted sintering technology (FAST)

FAST (also referred to as spark plasma sintering) is a consolidation technique suitable for many different powdered materials, including Ti powders [129]. It combines uniaxial pressure and joule heating, from pulsed direct current, to achieve high heating rates

and rapid sintering. Consolidation occurs in the solid-state, preventing any melt-related defects which can arise during conventional processing. Segregation defects have limited the use of some alloying elements in Ti, including Fe, and so FAST can be used for new alloy development using these elements. Although FAST is currently only able to produce billets up to 300 mm in diameter, it can be combined with a subsequent forging step to create near-net shape components, developed as the FAST-*forge* process [130]. Ti alloy powder derived from SR reduction in the FFC-Cambridge process has previously been consolidated using FAST, generating a homogeneous $\alpha+\beta$ microstructure with compressive mechanical properties comparable to Ti–6Al–4V processed under the same conditions [85].

Fe additions in Ti alloys

Fe is the most effective Ti β phase stabiliser by mass, thus less Fe is required to achieve the same level of β stabilisation as other elements. Fe is also considerably cheaper than Ti and commonly used β stabilisers such as V and Mo, although it is not used in many commercial Ti alloys. Restricted use of Fe is generally due to processing issues associated with the melting process which can affect the quality of the resulting alloys. Segregation of Fe during vacuum arc remelting can lead to localised regions of high β stability known as β flecks, which cause worse than expected mechanical performance [19]. Solid-state alloying using blended elemental powder metallurgy has been shown to avoid these issues. Ti alloys up to 7 wt.% Fe have been produced by press and sintering of blended elemental and alloy powders to produce homogeneous microstructures with no trace of intermetallic phases [20], [146], [187].

Most metastable β alloys, such as Ti–3Al–8V–6Cr– 4Mo–4Zr (Beta C) and Ti–15V–3Cr–3Al–3Sn, contain lots of costly alloying elements. An addition of only 3.5 wt.% Fe is required to retain 100% β phase after quenching to room temperature, therefore Fe could be used to replace other β stabilising elements at a lower cost [24].

The Ti–Fe binary phase diagram (Figure 5.3) shows that Fe is a β-eutectoid stabiliser and therefore has limited solubility in both Ti phases as it forms an intermetallic TiFe phase [138]. This phase is brittle and so formation must be avoided to prevent poor mechanical performance. Despite formation of TiFe being thermodynamically favourable, it is a

5.2. Direct electrochemical production of pseudo-binary Ti–Fe alloys from mixtures of synthetic rutile and iron(III) oxide

99
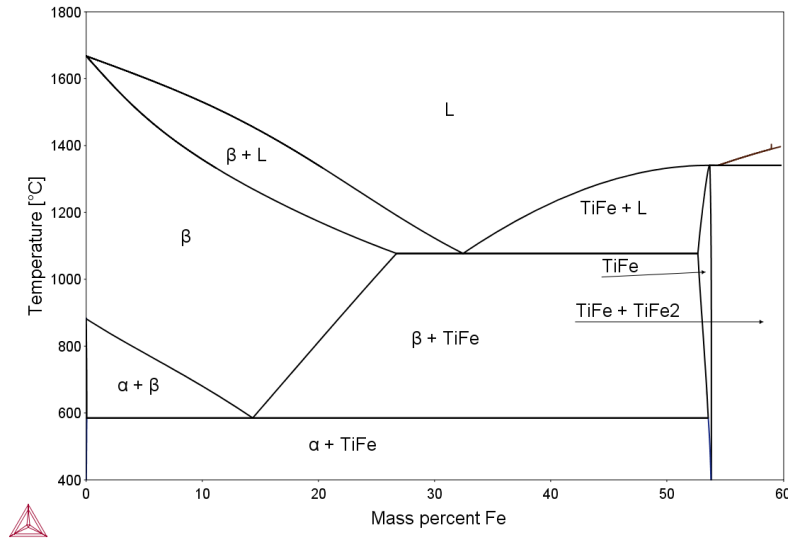
FIGURE 5.3: Ti–Fe phase diagram calculated using Thermocalc TTTI3 database [138].

kinetically slow process and therefore can be avoided using a sufficient cooling rate from the β region [188].

In this study, the proposed two-step FFC-Cambridge process coupled with the FAST processing route presents an opportunity to create high Fe content Ti alloys, which after further large-scale development, may be able to replace pre-existing alloys and reduce the cost of Ti alloy components. Exploiting a cheaper feedstock in SR further contributes to cost reduction and reduces reliance on alloying additions. SR contains remnant Fe from precursor ilmenite which becomes an alloying element once reduced. Enhancing this Fe content is possible by co-reducing SR with Fe_2O_3 additions, as Fe_2O_3 can be reduced using the FFC-Cambridge process [58], [189], [190]. Therefore, this study investigates the co-reduction of SR and Fe_2O_3, followed by FAST consolidation, to produce a range of pseudo-binary Ti–Fe alloys. Material characterisation is performed at each stage and some final alloy properties are analysed.

5.2.3 Materials and methods

Synthetic rutile + Fe_2O_3 oxide preparation

Heat-treated synthetic rutile (provided by Iluka Resources, 150–212 μm) and Fe_2O_3 (Sigma-Aldrich, <5 μm, >99%) powders were mixed using a Turbular mixer for 1 h. Five different

Chapter 5. Co-reduction of synthetic rutile and iron (III) oxide via the FFC-Cambridge
100
process to produce pseudo-binary Ti-Fe alloys
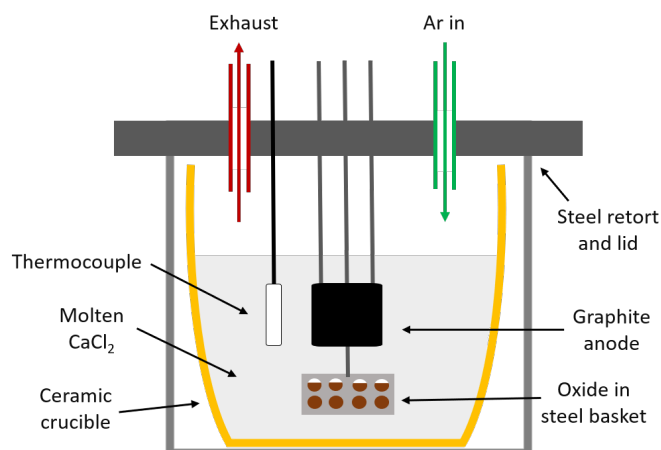
FIGURE 5.4: Schematic of FFC reduction cell used.

oxide compositions were made in addition to undoped SR, containing 1, 2.5, 5, 7.5 and 10 wt.% Fe_2O_3.

Reduction of mixed oxides via the FFC-Cambridge process and post-processing

Reductions were carried out using 20 g of each oxide composition, using R&D scale cells at Metalysis. Figure 5.4 shows a schematic of the reduction cells used. The same electrolysis parameters were used as in previous work where SR was successfully reduced to a titanium alloy containing 4000 ppm O, except that a longer reduction time of 18 h was used after initial experiments showed a further reduction O levels [17].

1.6 kg of dried $CaCl_2$ with CaO (0.4 wt.%) was placed into a ceramic crucible within a steel retort. The oxide was placed into a steel basket lined with a stainless steel mesh. The cell was then sealed and heated to 950°C to melt the salt. Argon was continuously flushed through to create an inert atmosphere and remove gaseous by-products. The basket and graphite anode were then submerged into the molten salt electrolyte and the electrolysis began. A constant current of 5 A is applied following an initial ramp which prevents high voltages and decomposition of the electrolyte. The corresponding voltage therefore fluctuates to maintain the constant current. Exhaust gases were monitored using mass spectrometry to follow reduction progress and confirm that no Cl_2 formation occurs. Reductions were performed for 18 h and the basket raised out of the salt. Once cool, the basket was removed from the cell and the material inside post-processed. This involved soaking in water followed by light grinding into a powder. The powder was then soaked

5.2. *Direct electrochemical production of pseudo-binary Ti–Fe alloys from mixtures of synthetic rutile and iron(III) oxide*

101

in a solution of dilute aqua regia, washed with water and dried in a vacuum furnace at 80°C. The resulting powders were then sieved to a size range of 75–212 μm and ready for analysis and consolidation.

Consolidation of Ti alloy powders

The alloy powders were consolidated using FAST with an FCT Systeme GmbH type HP D25 spark plasma sintering furnace. Powders were placed within a graphite mould set, lined with graphite foil for ease of removal. Optimised parameters included a 100°C / min ramp rate to a maximum temperature of 1100°C, followed by a dwell of 1 h at a pressure of 35 MPa. 5 g of powder was used in a 20 mm diameter mould to create a disc of around 3 mm height. The discs were then cut perpendicular to the compression direction to expose a surface for metallographic preparation and analysis.

Characterisation techniques

The feedstock, alloy powders and consolidated material were all analysed using various techniques. An FEI Inspect F50 scanning electron microscope (SEM), with an acceleration voltage of 20 keV, was used to view powder morphology and characterise the microstructure. An Oxford Instruments energy-dispersive X-ray spectrometer (X-EDS) was used alongside SEM to determine chemical compositions in specific regions. Interstitial element contents of O, N and C were measured by an ELTRA ON-900 and an ELTRA CS-800. Bulk alloy chemistry was measured by X-ray fluorescence (XRF) using a PANalytical Zetium, with a mean average of 3 results taken. Phase analysis was done using X-ray diffraction (XRD) using a Bruker D2 Phaser with Cu-Kα radiation. Porosity was measured using a high-resolution mosaic of a 10 mm^2 area, taken with an Olympus BX51 optical microscope. A colour threshold was then applied to leave only the porosity visible and the percentage area was measured using ImageJ software [170].

Microhardness testing

Vickers hardness measurements were carried out using a Struers Durascan-80, with a force of 5 kg (HV5), held for 15 s. A 5 $\times$ 5 grid of 25 measurements was tested, covering an area

Chapter 5. Co-reduction of synthetic rutile and iron (III) oxide via the FFC-Cambridge
102
process to produce pseudo-binary Ti-Fe alloys

of 10 mm^2 in the centre of each sample. The mean average hardness was calculated, along with 95% confidence intervals on the means.

5.2.4 Results and discussion

Characterisation of synthetic rutile and Fe$_2$O$_3$ powders prior to electrolytic reduction

Elemental analysis of the SR was used to determine the alloying elements expected to be present in the reduced powders. X-ray fluorescence (XRF) data revealed that it contained approximately 4 wt.% β stabilising elements, mainly Fe, and <1 wt.% Al. Therefore, it would be expected that the resulting alloy will also contain these elements and so will have significant β stabilisation compared to pure Ti.

Figure 5.5 shows that the SR particles vary in both size and morphology. The particles exhibit significant porosity, due to the conversion from the precursor ilmenite ore. XRD analysis determined that the heat-treated SR consisted of two major phases, with all peaks being assigned to TiO$_2$ (rutile) or Fe$_2$TiO$_5$ (pseudobrookite) (Figure 5.6). Although the Fe$_2$TiO$_5$ phase is only present in small amounts, it is visible in backscattered SEM as brighter Z contrast regions due to its higher density. Mixing the SR with Fe$_2$O$_3$ caused the much finer Fe$_2$O$_3$ particles to adhere to the surfaces of the SR, though this was not uniform due to the angular morphology of the particles. Some particles were coated with greater amounts of Fe$_2$O$_3$ than others, which was expected to lead to significant chemical heterogeneity in the material postreduction.

Characterisation of Ti–xFe alloy powders

Figure 5.7 shows that the resulting powders exhibited a variation of sizes and morphologies, which is typical for milled powders such as those derived from the hydride–dehydride process. Some internal porosity was still present, although it had noticeably reduced during the reduction from the initial SR powder. No features were visible within the pores, suggesting that they did not contain any material, however any gases present would have been released once exposed from metallographic preparation. Microstructural variation was seen between particles, suggesting significant chemical heterogeneity as predicted due to non-uniform coating of Fe$_2$O$_3$.

5.2. Direct electrochemical production of pseudo-binary Ti–Fe alloys from mixtures of synthetic rutile and iron(III) oxide

103
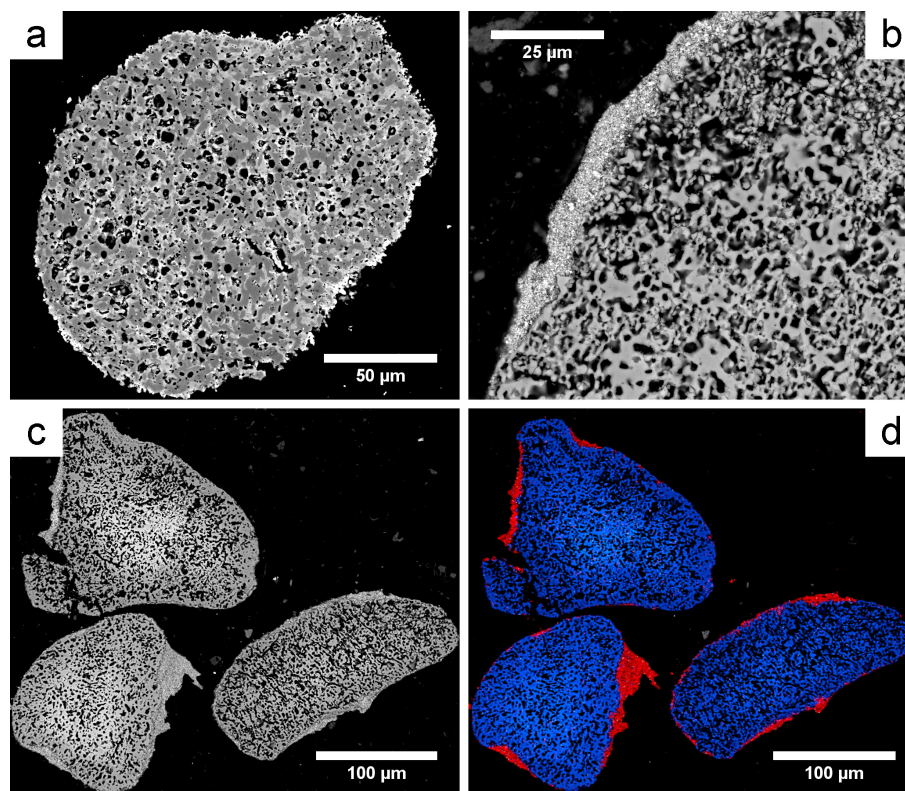
FIGURE 5.5: Backscattered electron micrographs of: **a:** SR particle, **b:** SR particle with surface Fe_2O_3, **c:** SR + Fe_2O_3 particles, **d:** X-EDS element map of **c** showing Ti (blue) and Fe (red).
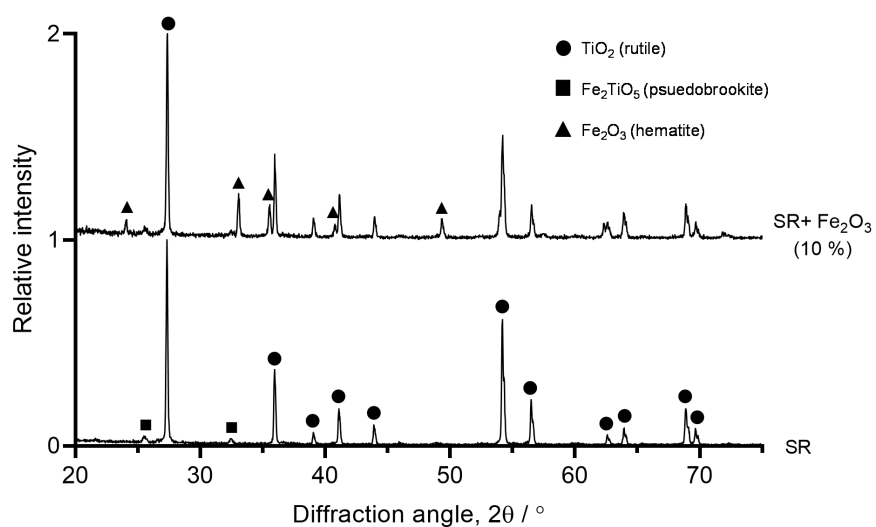
FIGURE 5.6: XRD patterns SR and SR + Fe_2O_3 (10 wt.%) mixture.

Chapter 5. Co-reduction of synthetic rutile and iron (III) oxide via the FFC-Cambridge
104
process to produce pseudo-binary Ti-Fe alloys
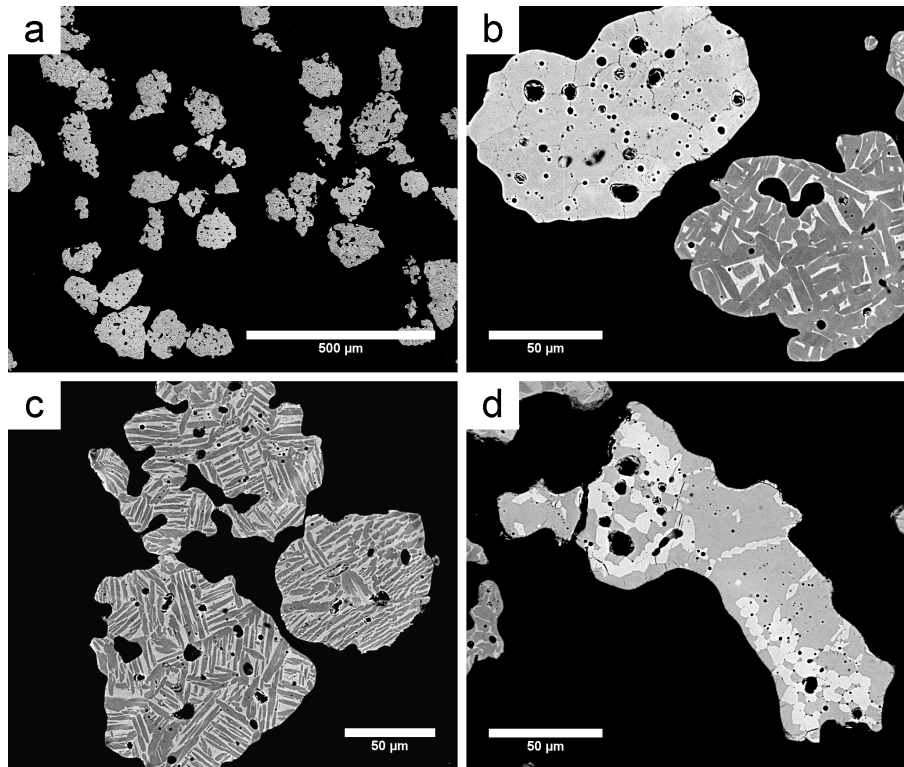
FIGURE 5.7: Backscattered electron micrographs of reduced Ti–xFe alloy powders, derived from a range of SR + Fe_2O_3 mixtures. a: range of powder particles (powder sample from 4.64 wt.% Fe alloy – see Table 1), b: α-rich and β-rich particles (6.21 wt.% Fe), c: particles with $\alpha+\beta$ microstructures (3.41 wt.% Fe), d: β stabilised particle containing brighter TiFe phase (9.03 wt.% Fe).

Figure 5.7 a–c shows examples of the types of particles observed in all samples, including α-rich, $\alpha + \beta$ and β-rich microstructures. A few particles in the powders derived from 7.5 and 10 wt.% Fe_2O_3 oxide compositions contained a third phase, determined by X-EDS to be intermetallic TiFe (Figure 5.7 d). These particles therefore must have originally had more Fe_2O_3 locally and so contained enough Fe to retain the TiFe phase on completion of the reduction. No $TiFe_2$ or metallic Fe was observed in the final powders, although these will have formed during early stages of the reduction, before further Fe diffusion into the Ti matrix [17].

The interstitial O and C contents of the powders were measured at this stage (Table 5.1), whereas Fe content was measured post-consolidation (discussed later). O contents had a range of around 2000 ppm (1668–3745 ppm), which is significant for Ti alloys. O is a potent a stabilising element and small variations considerably affect mechanical properties. For example, alloy grades 1 to 4 differ in max O content by just 0.22 wt.%, but yield strengths can vary from about 170–480 MPa [191]. The increase in strength causes decreased ductility

5.2. Direct electrochemical production of pseudo-binary Ti–Fe alloys from mixtures of
synthetic rutile and iron(III) oxide

105

and so Ti alloys typically do not exceed 0.4 wt.% O.

TABLE 5.1: O, C and Fe contents of the reduced Ti–xFe alloys with corresponding oxide compositions. O and C measured directly from powder, Fe measured by XRF from bulk material post-consolidation

Oxide Fe_2O_3 content / wt.%	O / ppm	C / ppm	Fe / wt.%
0	3460	1519	1.84
1	3351	927	2.22
1	2238	1467	3.65
2.5	2224	1424	3.41
2.5	2742	1189	5.15
5	1668	1256	6.21
5	3682	1619	8.02
7.5	1934	774	4.64
7.5	1891	832	7.19
10	3745	896	9.03

There are many potential reasons for this variation, including slight deviations in process parameters between reductions, the use of multiple reduction cells and inherent inconsistencies in manual post-processing of the powders. There seems to be no correlation between residual O content and oxide composition used, suggesting it has no significant effect, but this may be concealed by the other influencing variables.

C contents also varied; with C pickup occurring during the reduction process due to degradation of the graphite anode. Loose C covers the surface of the reducing material and some diffuses into Ti solid solution. For this small-scale reduction, the relative surface area of the powder exposed to this material is high, causing higher than desirable C levels. Such levels can be reduced when scaling up the process, due to a lower relative surface area. Thorough washing of the material after removal from the cell removes most of the C pickup, although this is limited, especially when done manually. Some C may be present

Chapter 5. Co-reduction of synthetic rutile and iron (III) oxide via the FFC-Cambridge
106
process to produce pseudo-binary Ti-Fe alloys

on the surface of the particles, but this was not observable using SEM as the samples were mounted in conductive bakelite. C is also an α stabiliser but only has a maximum solubility of 0.48 wt.% in the a phase at 920°C [192]. It therefore forms a ceramic phase (TiC) on cooling, even at low concentrations. This carbide phase is brittle and therefore undesirable in the alloys. No evidence of carbide was seen in the powder micrographs, suggesting C levels were sufficiently low to prevent formation.

Consolidation of Ti–xFe alloy powders by field-assisted sintering

The chemical heterogeneity, angularity and porosity of these powders make them unsuitable for powder metallurgy techniques such as additive manufacturing, where a defined level of sphericity and powder size is required. In contrast, FAST is far more flexible with respect to input powder feedstock, as demonstrated by a successful study on directly consolidating irregular machining swarf particulate [132]. Therefore, it can process these powders without issues to create alloy billets for subsequent forging and/or finish machining. Optimisation of the FAST process was necessary for these powders to ensure chemical homogeneity and uniform microstructures. Although FAST can sinter powder within minutes, longer dwell times are required in this case to facilitate the necessary solid-state diffusion. Fe rapidly diffuses in Ti and is known to enhance sintering, therefore the parameters could be relatively moderate [143].

Initial consolidation of the powder was achieved based on previous FAST processing of SR derived alloy powders, using a dwell temperature of 1000°C for 30 min. Figure 5.8 shows that these conditions were insufficient for complete diffusion, as localised regions of α and β remained. These were likely due to larger particles which were particularly rich or deficient in Fe, such as those in Figure 5.7b. After an investigation on the effects of both temperature and dwell time, it was found that a dwell at 1100°C for 60 min was able to produce homogeneous microstructures. Higher temperatures and longer dwell times are expected to have the same effect but would be unnecessary, costly, and could cause undesirable grain growth. Figure 5.9 shows a profile of the FAST process, using these optimised conditions. Sintering is achieved within around 10 min, while the system ramps to maximum temperature. Diffusion then continues during the dwell, followed by uncontrolled cooling to room temperature and thermal contraction to final volume.

5.2. *Direct electrochemical production of pseudo-binary Ti–Fe alloys from mixtures of synthetic rutile and iron(III) oxide*

107
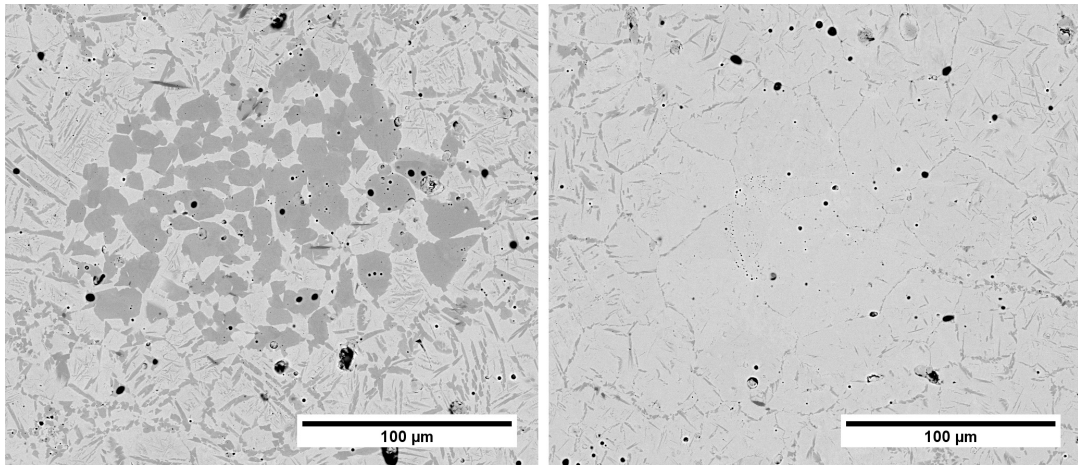
FIGURE 5.8: Backscattered electron micrographs of initial FAST consolidation of 4.64 wt.% Fe alloy at 1000°C with a 30 min dwell, showing local regions of high α (left) and high β (right) stabilisation.
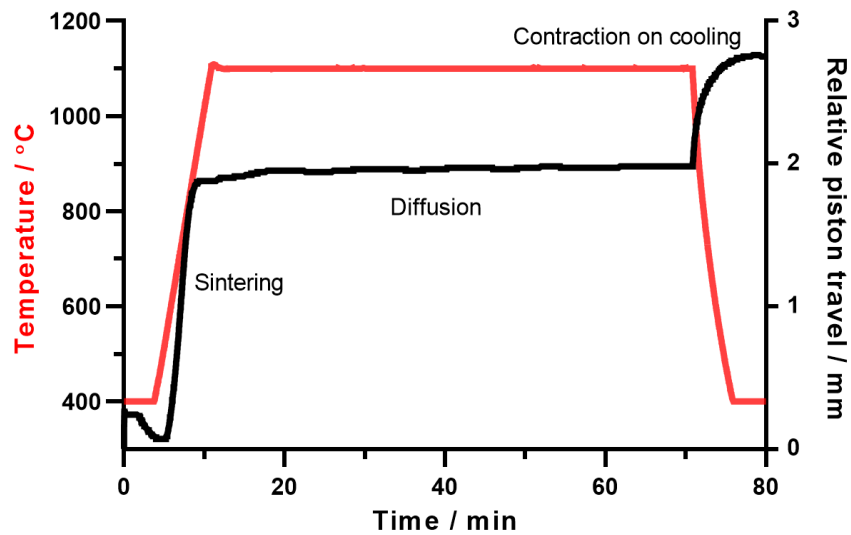
FIGURE 5.9: Temperature profile of FAST processing at 1100°C with a 60 min dwell and powder consolidation behaviour, indicated by the relative movement of the graphite punches.

Chapter 5. Co-reduction of synthetic rutile and iron (III) oxide via the FFC-Cambridge
108
process to produce pseudo-binary Ti-Fe alloys

Analysis of consolidated Ti–xFe alloys

Elemental compositions of the bulk alloys were determined using XRF, showing that alloys with a range of Fe contents from 1.84 to 9.03 wt.% were produced (Table 5.1). The final Fe contents do not correspond well with the initial oxide compositions, indicating that significant amounts of Fe were lost during the reduction process. Figure 5.10 shows the comparison of oxide composition against final Fe content. Previous work on reducing SR using the FFC-Cambridge process has shown that the Fe content in the alloy is approximately 0.5 times the theoretical maximum [86]. Therefore, this was expected to some degree, although it was unknown exactly how the Fe_2O_3 would react during the reduction compared to Fe_2TiO_5.
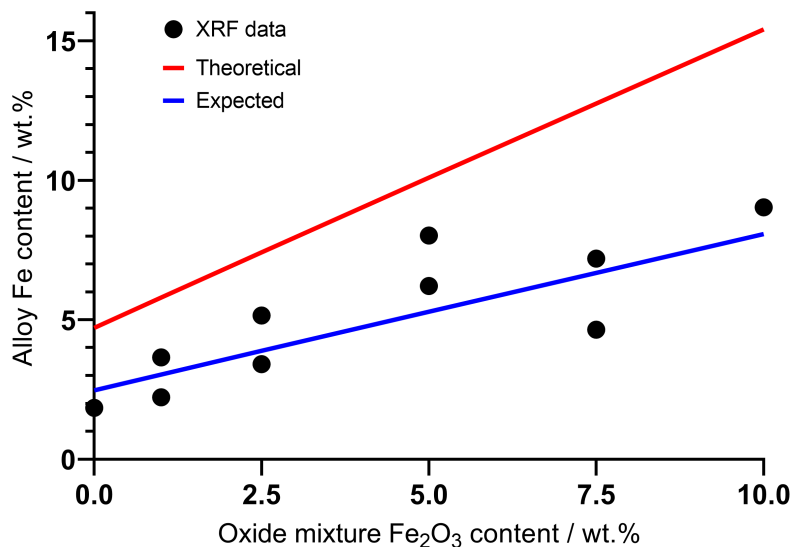
FIGURE 5.10: Fe contents of reduced alloys compared with initial oxide mixtures, calculated theoretical and expected (52% theoretical) Fe contents also shown.

The loss of Fe must occur physically and/or chemically. Given the Fe_2O_3 is only loosely coating the surface of the SR particles, it is likely that some separation occurs on submersion of the oxide into the molten salt. It is also possible that there is a side reaction of the salt with the Fe_2O_3 and the Fe_2TiO_5, which causes leaching of the Fe and thus reduces the expected content in the resulting alloy. This requires further understanding to accurately predict alloy chemistry from oxide composition; however, this was beyond the scope of this study. The inconsistencies in the process are unideal, yet this oxide mixture has not been investigated previously and so it is anticipated more consistent results can

5.2. Direct electrochemical production of pseudo-binary Ti–Fe alloys from mixtures of synthetic rutile and iron(III) oxide

109

be achieved in the future, via improved mixing and better adhesion of the surface layer. Heat treatment of the oxide mixture may also improve mixing and Fe retention through diffusion and formation of the Fe_2TiO_5 phase at the surfaces of the SR particles.

Alloying elements aside from Fe were also detected by XRF, as was expected from the impurities in the SR feedstock, with Al, Si, Mn and Nb contents between 0.2–0.5 wt.% and consistent between each alloy. Cr contents were significantly higher than would be expected from the SR alone, varying from 0.61–2 wt.%. It is therefore presumed that Cr pickup occurs due to contamination from the stainless steel mesh in which the oxide sits during electrolysis. Further investigation and use of a different mesh material would be required to confirm this. The presence of these elements will affect the microstructure due to their differing effects on α and β stabilisation. Therefore, despite some α stabilisation from the Al, this should cause an overall slight increase in β stability compared to that from the Fe alone.

Although no $CaCl_2$ residue was observed on analysis of the powders, both Ca and Cl were detected at around 0.2 wt.% in all the alloys. While some Ca may have been retained from the SR, this suggests that some electrolyte contamination was present despite washing of the powders. More thorough grinding and washing of the powders during post processing could prevent this. It is unknown exactly what effect FAST processing would have on any $CaCl_2$ contamination, however formation of Cl_2 gas, which could become trapped as porosity within the material, is probable and requires further investigation.

Figure 5.11 shows how the microstructure of the alloys varies with increasing Fe content. At lower Fe contents, $\alpha + \beta$ microstructures are observed, comprising of coarse α laths with fine secondary α between them. Equiaxed prior β grains are clearly identifiable as the grain boundaries are decorated with α. With increasing Fe content, the α laths reduce in size until only the β phase remains. A small amount of α phase was seen in the 8.02 wt.% Fe sample, although this sample does have a relatively high O content which explains this. No intermetallic TiFe phase was seen post-FAST, despite being present in some of the powders. This confirms that there was sufficient diffusion to allow the Fe from this phase to fully dissolve into the Ti matrix. Although some porosity remains, likely due to internal porosity in the original powder particles (Fig. 5.7) or Cl_2 formation, all samples were found to have a density >99%.

Chapter 5. Co-reduction of synthetic rutile and iron (III) oxide via the FFC-Cambridge process to produce pseudo-binary Ti-Fe alloys

110
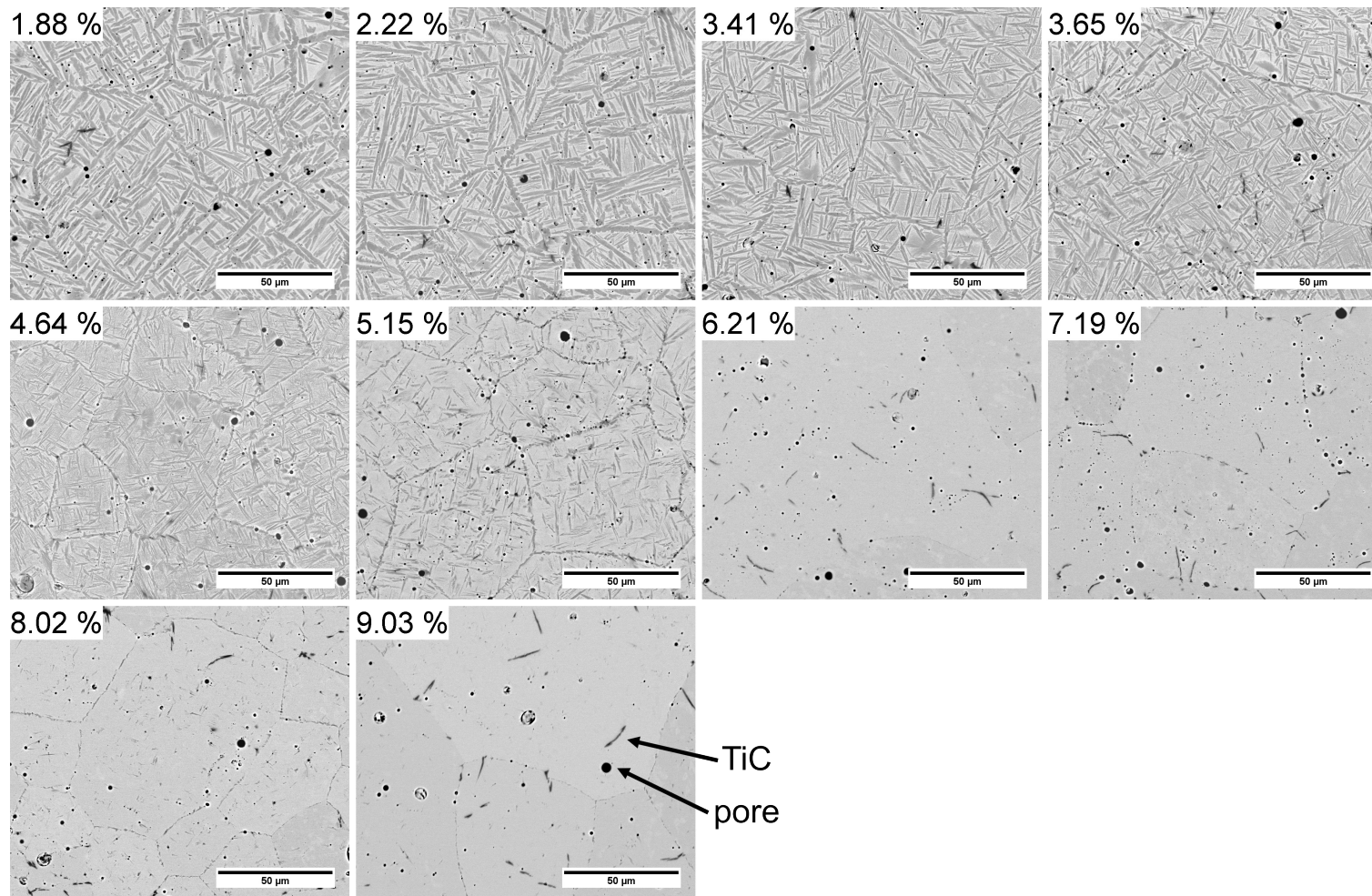
FIGURE 5.11: Backscattered electron micrographs of Ti–xFe consolidated alloys, in order of increasing Fe content, wt.% (labelled).

5.2. Direct electrochemical production of pseudo-binary Ti–Fe alloys from mixtures of synthetic rutile and iron(III) oxide

111

Small amounts of TiC are seen after consolidation, visible as thin black needles in the SEM micrographs. These needles were not seen in the powders which suggests that the FAST process has caused them to precipitate out from solid solution, or that residual C was coating the powder particles rather than being present internally. C pickup is known to occur during FAST, resulting from use of a graphite mould setup which is in contact with the powder. A previous study has shown this to be around 100–200 ppm; however, it may be more significant here due to the lower mass of powder used and larger relative surface area exposed to the graphite foil [129]. Further research is required to better understand C contamination and the formation of the TiC phase through this production route.

XRD patterns for the alloys complement well the microstructures in Figure 5.11, as there is a clear increase in the ratio of β:α intensities with increasing Fe content (Figure 5.12). From 6.21 wt.% Fe, α peaks are no longer detected, confirming single phase β alloys. This shows that, under these processing conditions, the formation of fully β alloys becomes favourable between 5.15 and 6.21 wt.% Fe, but other factors also affect the microstructure, such as the presence of other alloying elements and interstitial contents. Although some α was possibly present in the micrograph from the 8.02 wt.% sample, no corresponding peaks were measured from XRD, suggesting that α content was minimal. Despite TiC needles being observed in the SEM micrographs, the corresponding XRD peaks were not visible, indicating that this phase must only be present in a very small amount. This agrees with the C analysis of the powders which all showed < 2000 ppm which prevents significant carbide formation. Therefore, it is not expected that this phase will have noticeable impacts on the mechanical properties of the alloys.

The samples made on this scale were not large enough to perform a thorough assessment of their mechanical properties; however, microhardness testing was performed to determine any effects of increasing Fe content and varying microstructures. Figure 5.13 shows that there is not a simple relationship between the Fe content and hardness. The hardness values seem to increase up to a maximum of around 400 Hv for the 5.15 wt.% alloy, before dropping down to around 340 Hv. This is likely due to the strengthening effect of finer α laths that have precipitated on cooling during the FAST process, which are not present at Fe contents >5.15 wt.%. Fine-scale α formation is known to increase alloy strength by creating more α/β interfaces which block dislocation movement [33], [193]. The general

Chapter 5. Co-reduction of synthetic rutile and iron (III) oxide via the FFC-Cambridge
112
process to produce pseudo-binary Ti-Fe alloys
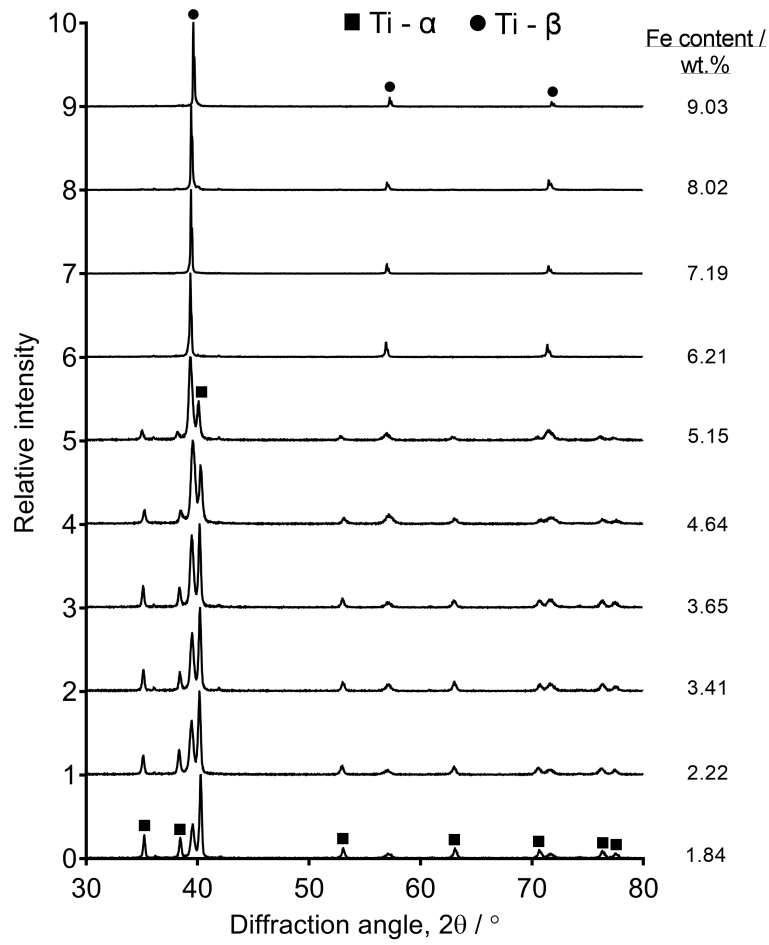
FIGURE 5.12: XRD patterns of consolidated Ti–xFe alloys, with increasing Fe content.
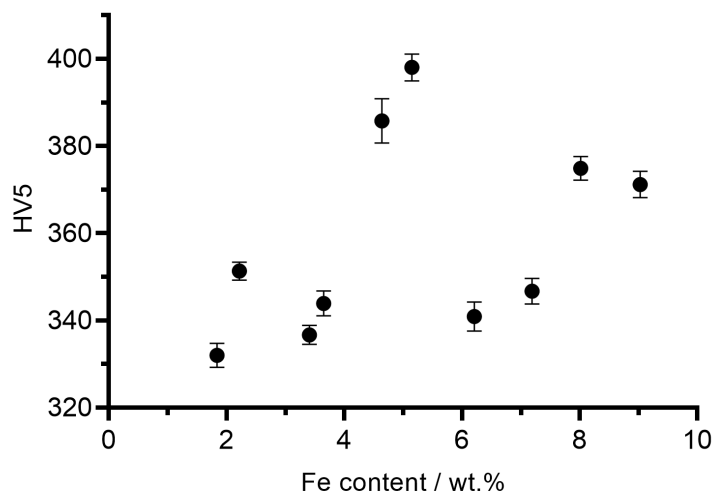
FIGURE 5.13: Vickers hardness of the consolidated Ti–xFe alloys.

5.2. Direct electrochemical production of pseudo-binary Ti–Fe alloys from mixtures of
113
synthetic rutile and iron(III) oxide

trend of increasing hardness can be attributed to solid solution strengthening, as more Fe is being forced into the Ti matrix. Again, there are other factors to consider besides Fe content which can affect the hardness. O content has a dramatic effect on the strength of Ti alloys and therefore it is difficult to compare these alloys when they have varying O contents. Despite this, no correlation was found between the O content of the alloys and their hardness, with an R^2 value of 0.03.

Chapter 5. Co-reduction of synthetic rutile and iron (III) oxide via the FFC-Cambridge
114
process to produce pseudo-binary Ti-Fe alloys

5.2.5 Conclusions

Overall, this study has once again demonstrated the flexibility of the FFC-Cambridge process for co-reducing mixed metal oxides to directly produce alloys. Co-reduction of synthetic rutile (SR) and Fe_2O_3 produced a range of pseudo-binary Ti–Fe alloys, presenting the possibility of using unconventional and cheaper feedstocks in the process to create lower cost Ti alloys. After optimisation, FAST enabled the consolidation of the alloy powders and the diffusion required to create homogeneous material. A range of microstructures was observed, from $\alpha + \beta$ to fully β, with α phase no longer detected at a concentration between 5.15 and 6.21 wt.% Fe. Fe contents up to 9.03 wt.% were achieved without any intermetallic formation, with further work required to discover the limit of Fe solubility in Ti under these conditions.

The inconsistencies in the experiments, along with the many variables involved, made alloy comparisons and reproducibility of results difficult. Predicting final alloy composition is challenging, due to poor understanding of the mechanism of Fe loss during reduction and pickup of Cr. Contents of the remnant elements from the SR, mainly Al, Si, Mn and Nb, were consistent across the alloys, however.

Interstitial contents also varied between the alloys, due to slight variations in both the reductions and post-processing of the material on this small scale. Nevertheless, this oxide mixture has not been investigated previously, and so it is anticipated that future improvements could solve these issues. For example, more effective mixing of the oxides should improve Fe retention and, consequently, the predictability of alloy composition. This could be done by mixing using a binder, or perhaps by heat-treating the mixture to chemically bind the oxides together as Fe_2TiO_5. Improved mixing should also make the resulting alloy powders more chemically homogeneous, allowing for complete diffusion to be achieved using a shorter FAST dwell duration.

Interstitial content variation could also be reduced by altering aspects of the extraction process. Optimisation of the FFC-Cambridge process for this oxide mixture could further reduce O contents and lower the range between powders. Automated post-processing of the powders would assist in the removal of surface C, decreasing variation in C contents and preventing any carbide formation. The use of inert anodes in the FFC-Cambridge

5.2. Direct electrochemical production of pseudo-binary Ti–Fe alloys from mixtures of synthetic rutile and iron(III) oxide

115

process would remove C from the system entirely, producing O_2 gas instead and improving current efficiency [67], [185]. Future developments will be monitored, but currently only a few materials have shown promise as inert anodes in the FFC-Cambridge process, and more research is required to assess their longevity over many reduction cycles.

The quantities of the alloy powders generated meant that mechanical testing was limited to microhardness only. These data suggested that there are two main strengthening effects which increase the hardness values: solid solution strengthening from increasing Fe content and the precipitation of fine secondary α on cooling. Further assessment of the mechanical properties of these alloys is an important next step in understanding their potential as materials. This involves generating greater quantities of powder to produce larger FAST billets from which various specimens can be machined. Conventional Ti alloy powders consolidated using the same FAST conditions can then be tested for comparisons. Binary Ti–Fe alloys can also be produced using FAST from blended elemental powders, giving far greater control over Fe content. Investigating this would allow for comparisons with these SR + Fe_2O_3 derived alloys to understand any effects of production via the FFC-Cambridge process and the presence of other remnant elements from the SR.

Chapter 5. Co-reduction of synthetic rutile and iron (III) oxide via the FFC-Cambridge
116
process to produce pseudo-binary Ti-Fe alloys

5.3 Larger development scale reductions

SR and Fe_2O_3 mixtures were also reduced using the development scale cells at Metalysis, where kilograms of oxide can be processed. This scale is an important intermediate step between R&D and full commercial application of the FFC-Cambridge process. Greater quantities of the alloy powders allow for the production of larger FAST billets from which specimens can be machined for more substantial mechanical property assessment.

Oxide compositions up to 5 wt.% Fe_2O_3 were chosen for reduction at the development scale. Given that the cooling rate is not controllable with the FAST equipment used, a larger mass of material has a lower cooling rate, which in this case benefits the thermo-dynamically favourable formation of TiFe as per Figure 2.21. Therefore, the lower Fe_2O_3 compositions were chosen to prevent the production of Ti-xFe alloys with too high Fe contents which could be prone to intermetallic formation.

5.3.1 Experimental procedure

SR and Fe_2O_3 powders were mixed as described in Section 5.2.3, to produce compositions containing 1, 2.5 and 5 wt.% Fe_2O_3 (Figure 5.14). 1.25 kg of each composition, along with 1.25 kg of undoped SR, were reduced using the development scale as described in Section 3.1.3. Due to limited availability of material and cell time, all four compositions were reduced simultaneously in a single run by using a tray split into quadrants. It was unsure how the slight variations in composition would affect the process compared to reducing each separately, however this could be compared to results from the R&D scale. It was hoped that by reducing simultaneously, the O and C contents in the alloys would be more consistent than seen at the R&D scale.

The resulting alloy powders were analysed using the same techniques as discussed in Section 5.2.4. FAST consolidation was completed using the same processing parameters as for R&D scale: 100°C/min ramp up to 1100°C, with a dwell time of 1 h and a pressure of 35 MPa. These parameters were chosen based on the findings of Chapter 4 and after FAST optimisation (discussed in Section 5.2.4), which was done simultaneously for both R&D and development scale to ensure consistent processing achieved homogeneous

FIGURE 5.14: Top: photograph of SR + Fe_2O_3 oxide mixtures after mixing, with increasing red colouration due to higher Fe_2O_3 content. Bottom: photograph of oxide mixtures placed in quadrants of steel basket before being placed into reduction cell.

microstructures. 150 g of each powder was consolidated using a 60 mm internal diameter mould, producing discs with thicknesses of ∼11 mm.

Two commercial alloy powders were also consolidated using the same FAST parameters, a Ti-6Al-4V powder and a Beta-C (Ti-3Al-8V-6Cr-4Mo-4Zr) powder (details in Section 3.6.2). This was done for comparative purposes as these are two commonly used Ti alloys which are well understood and researched. Ti-6Al-4V is an $\alpha+\beta$ alloy, with comparable microstructures to those seen in the lower Fe content alloys in Figure 5.11. Beta-C, meanwhile, is a metastable β alloy, which is more comparable with the higher Fe content alloys which fully retain the β phase on cooling.

Tensile specimens were then designed and extracted from each disc using wire electrical discharge machining (EDM) and finish machining. Due to the limited amount of material and the size of the discs, specimens could not be made to the ideal ASTM E8/E8M standard for tension testing of metallic materials [194]. The design used was based on

Chapter 5.   Co-reduction of synthetic rutile and iron (III) oxide via the FFC-Cambridge
118
process to produce pseudo-binary Ti-Fe alloys
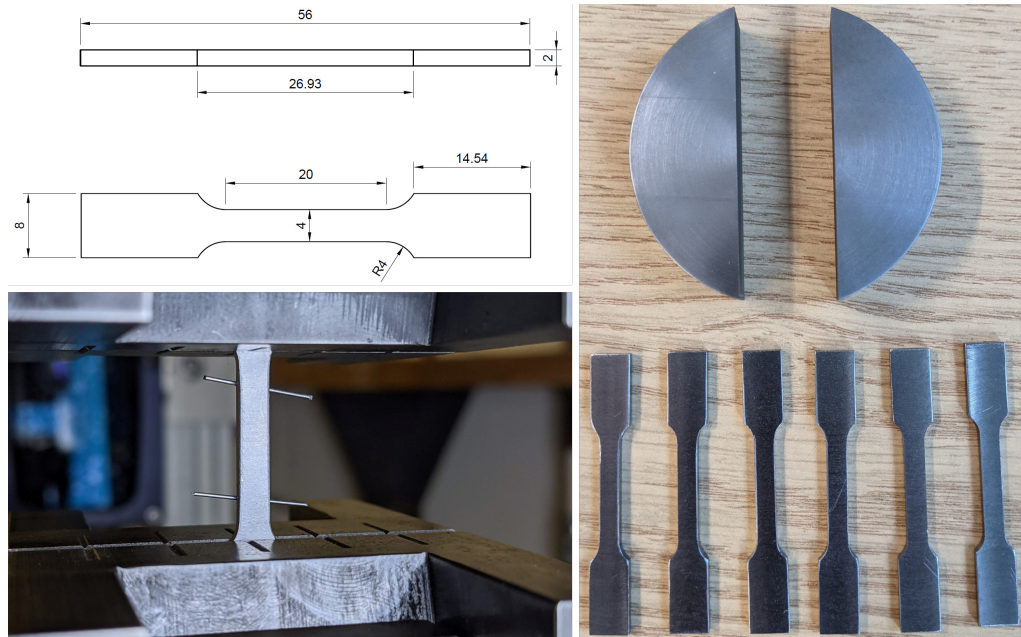
FIGURE 5.15: Top left: drawing of tensile specimen design, dimensions in mm, right: photograph of tensile specimens machined from 60 mm FAST disc, bottom left: photograph of a tensile specimen held between the grips of the testing machine.

this standard however, but could not be simply scaled down as this would have meant that the grip sections would be too small to be held properly in the grips of the testing rig. The dimensions of the specimen design are shown in Figure 5.15, with tensile testing performed as described in Section 3.5.2.

5.3.2   Analysis of reduced alloy powders

Samples of the reduced powders were taken for microstructural analysis and O, N and C contents were measured as described in Section 3.4.2. Similarly to the alloy powders produced at the R&D scale, particles exhibited a range of sizes, morphologies and microstructures. Figure 5.16 (like Figure 5.7) shows examples of the types of particles seen in all of the powders from each starting oxide mixture, from fully α phase to fully β stabilised. The brighter TiFe phase was not detected when analysing the powders under backscattered electron imaging. This is unsurprising, as particles containing TiFe were only observed in the powders derived from the 7.5 and 10 wt.% Fe_2O_3 oxide compositions, which were not reduced at this scale.

There were some significant differences in the O, C and Fe contents compared to those produced at the R&D scale (Table 5.1). Less variation was seen in the interstitial values,
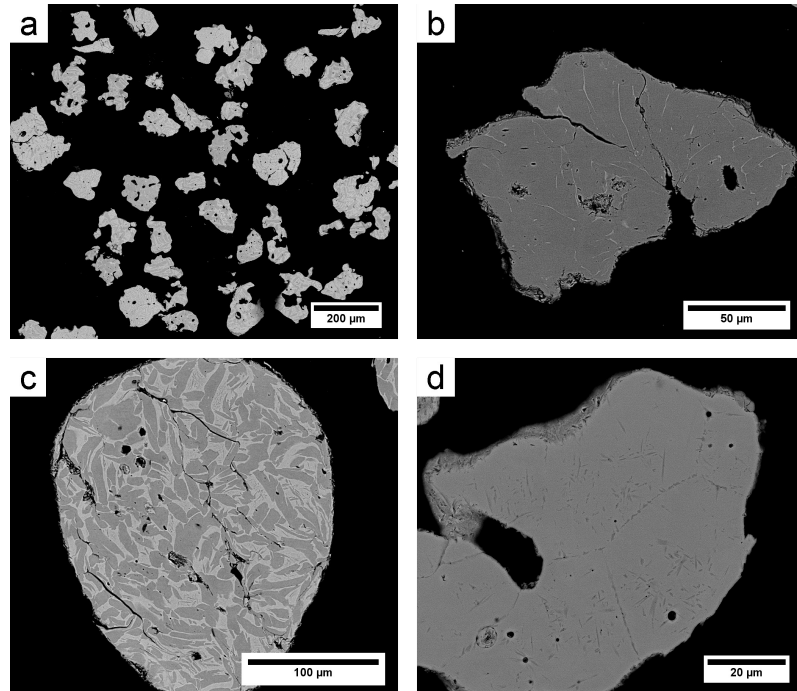
FIGURE 5.16: Backscattered electron micrographs of reduced development scale Ti-xFe alloy powders. a: 1% Fe_2O_3 derived, b: 2.5% derived, c: 5% derived, d: 2.5% derived

TABLE 5.2: O, C and Fe contents of the development scale reduced Ti–xFe alloys with corresponding oxide compositions. O and C measured directly from powder, Fe measured by XRF from bulk material post-consolidation

Oxide Fe_2O_3 content / wt.%	O / ppm	C / ppm	Fe / wt.%
0	4825	227	3.65
1	4413	230	4.49
2.5	3740	269	5.56
5	4917	262	6.39

meaning that the effects of Fe contents in the alloys can be directly compared more easily.

O contents were generally higher, with a mean O content of 4476 ppm compared to 2694 ppm. The range was narrower though, which is expected due to the oxide mixtures being reduced simultaneously, preventing any variation in the conditions experienced within the cell. The higher O content suggests that the reduction parameters used at this scale are not sufficiently optimised for this material, with potential to improve the O contents through adjustments in the future. As discussed in Section 2.1.2 and 5.2.4, these higher than desirable O contents have two major effects on the alloys: increased α stabilisation and decreased ductility (along with some strengthening). Therefore, it is expected that

Chapter 5. Co-reduction of synthetic rutile and iron (III) oxide via the FFC-Cambridge
120
process to produce pseudo-binary Ti-Fe alloys

these alloys will have a greater amount of α phase compared to similar Fe content alloys and poor ductility when tested under tensile loading.

The C contents were significantly lower than measured in the R&D powders, with a mean of 247 ppm compared to 1190 ppm. As explained in Section 5.2.4, C contamination occurs during the reduction process due to degradation of the graphite anode, causing C particles to be deposited onto the surface of the reducing material. Therefore, the amount of C pickup is related to the surface area to volume ratio, with a reduced relative surface area available at this larger scale. It is subsequently expected that less TiC phase would be visible in both the bulk alloys compared to the amount seen in the R&D alloys. Reduced C at larger reduction scales is promising for future scaling up of the FFC-Cambridge process for Ti production.

5.3.3 Analysis of FAST consolidated material

The remaining material after extraction of tensile specimens, shown in Figure 5.15, was sectioned for elemental analysis via XRF, microstructural analysis via SEM, phase analysis via XRD, and Vickers microhardness testing.

The range of Fe contents was lower than expected compared with results from the R&D scale. The undoped SR without Fe_2O_3 addition produced an alloy with a much higher Fe content than the R&D scale and previous studies, containing 3.65 wt.% Fe compared to 1.84 wt.% measured in Section 5.2.4 and a value of 2.47 wt.% quoted in reference [86]. This is likely to have been an effect of the simultaneous reduction causing contamination of the Fe through the salt or between the different compositions in each quadrant of the basket.

Cr contents were significantly lower than the alloys produced at the R&D scale, with an average 0.37 wt.% compared to 1.21 wt.%. It is presumed that the reduced Cr pickup is also related to the decrease in the surface area to volume ratio of the material during reduction, in a similar way to C contamination. Relatively less of the material is in contact with the stainless steel mesh, meaning that less diffusion or physical pickup of Cr can occur.

Ca and Cl were detected in similar amounts seen in the alloys produced at the R&D scale, with averages of 0.14 and 0.17 wt.% respectively compared to 0.20 and 0.19 wt.%. Unlike

for C and Cr, Ca and Cl contamination is less of a surface effect and it is assumed that this is why values remain similar at this scale. This is because the $CaCl_2$ electrolyte is molten and so flows between the oxide particles, especially earlier in the reduction process when the powder particles are discrete. Although $CaCl_2$ is removed by thorough washing of the product, evidently some remains, either still in salt form or the individual elements dissolved in Ti solid solution. Cl is a common impurity in Kroll based Ti metal also, due to the $TiCl_4$ intermediate used, although at much lower concentrations than present in these alloys [195].

Mn, Nb and Si are the other elements present in significant quantities, with averages of 0.36, 0.42 and 0.40 wt.% measured respectively. These elements are retained from impurities within the original SR, as presented in Section 3.6.1. As shown in Figure 2.2 and Equation 2.2, they are β stabilisers and therefore, in combination with the Fe and Cr, will contribute to this stabilisation effect.

Microstructures were similar to those from the R&D scale, with the α laths decreasing in size with increasing Fe content (Figure 5.17). There is still α phase visible in the 6.39 wt.% sample, in contrast to the R&D scale samples where no α remained from 6.21 wt.%. Increased α retention is likely mostly due to the higher O content in these alloys, which is stabilising the α phase despite increasing β stability from the Fe. The lower Cr contents will also cause reduced β stabilisation. Porosity was again consistently <1%, but there was far less TiC visible due to decreased C contents. XRD analysis again confirmed an increasing ratio of $\beta{:}\alpha$ intensities with increasing Fe content, however without complete loss of the α peaks (Figure 5.19).

Optical microscopy was used for analysis of the Ti-6Al-4V and Beta-C samples, due to them being mostly single phase and so microstructural features do not show up well in SEM micrographs. Figure 5.18 shows the microstructures of the two commercial alloys processed under the same FAST conditions as the SR + Fe_2O_3 derived powders. The Ti-6Al-4V microstructure consists of large prior β grains with transformed α. The Beta-C microstructure consists of β grains of various sizes, with many having diameters well over 500 μm. These large grains are due to the FAST processing conditions, with a long dwell time of 1 h and high temperature of 1100°C encouraging grain growth.

Chapter 5. Co-reduction of synthetic rutile and iron (III) oxide via the FFC-Cambridge
122
process to produce pseudo-binary Ti-Fe alloys
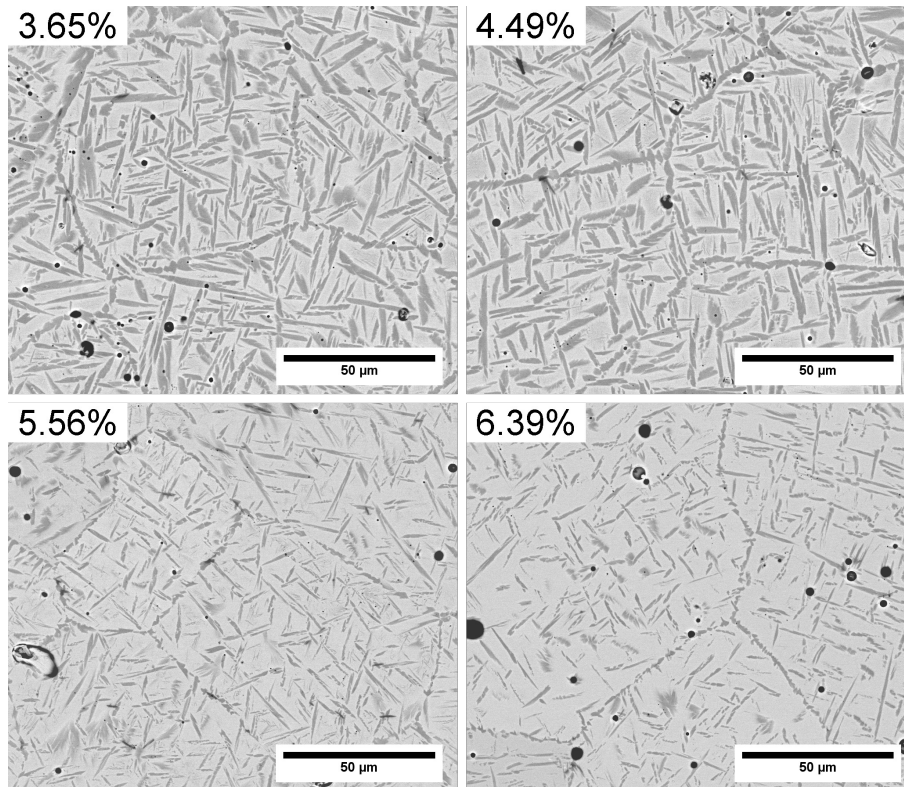
FIGURE 5.17: Backscattered electron micrographs of development scale
Ti-xFe consolidated alloys, in order of increasing Fe content, wt.%

XRD patterns in Figure 5.19 also show the differences between Ti-6Al-4V and Beta-C, with the former being mostly α and latter completely β. The ratio of peaks in the Beta-C XRD pattern is quite different to the β only patterns seen in Figure 5.12. This is likely due to the large particle size of the powder used and long FAST processing time which produced large grains. XRD peaks correspond to particular crystallographic planes, therefore a relatively small number of large grains in a sample can distort the typical ratio of peaks.

5.3.4   Hardness testing

Microhardness testing was performed as described in Section 3.5.1, with the results displayed in Figure 5.20. The hardness of 330 for Ti-6Al-4V was as expected based on a range of 300–400 quoted in the literature, however Beta-C was softer than expected at 270 compared to 300–450 [23]. Beta-C contains more alloying additions than Ti-6Al-4V, and therefore should exhibit greater hardness and strength due to solid solution strengthening. One explanation for the low hardness is that the large β grains caused a reduction in hardness and strength due to reduced grain boundary strengthening, as per the Hall-Petch relationship discussed in Section 2.1.5. The as-FAST microstructure is also not ideal for
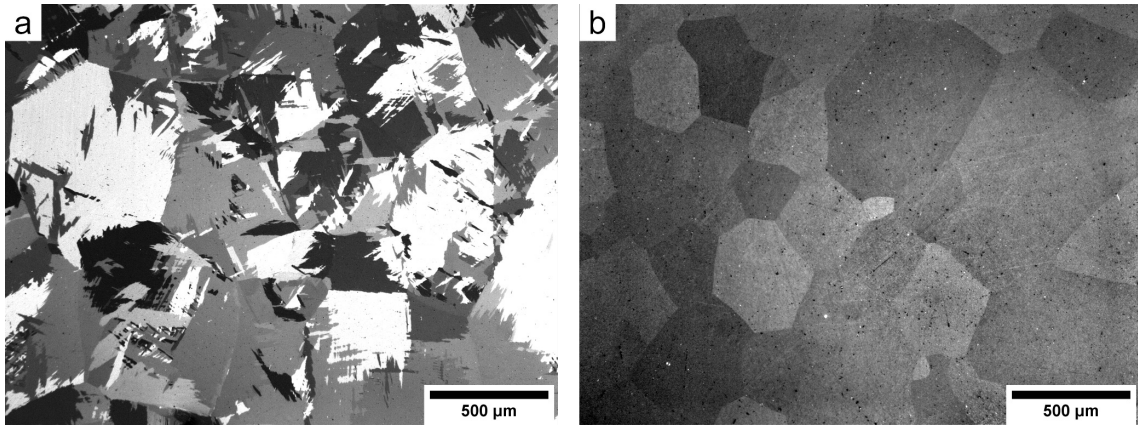
FIGURE 5.18: Optical micrographs of consolidated Ti-6Al-4V and Beta-C using cross-polarised light.
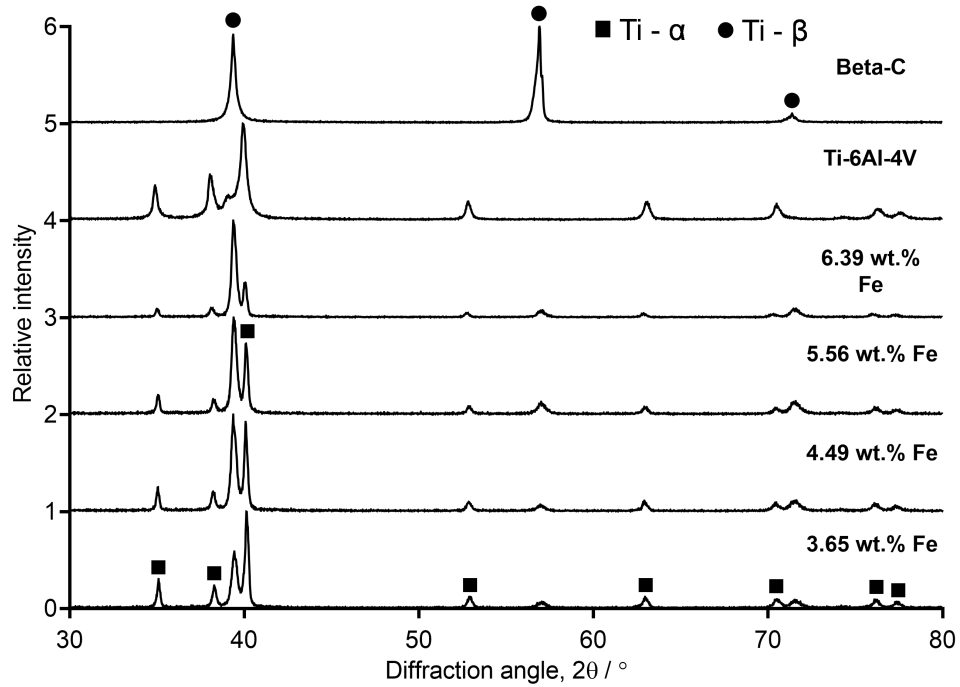
FIGURE 5.19: XRD patterns of consolidated Ti-6Al-4V, Beta-C and development scale Ti-xFe alloys.

Chapter 5. Co-reduction of synthetic rutile and iron (III) oxide via the FFC-Cambridge
124
process to produce pseudo-binary Ti-Fe alloys

Beta-C, which, like most β alloys, requires ageing to precipitate fine α phase to achieve higher strength [196].

The Ti-xFe alloy hardness values were higher with increasing Fe content, due to solid solution strengthening and finer α precipitation. This was in agreement with the previous measurements done on the Ti-Fe diffusion couples, displayed in Figure 4.10. In contrast to the R&D scale results in Figure 5.13, the hardness did not drop at higher Fe contents, because none of the alloys were fully β stabilised and so retained the strengthening effect of the fine secondary α. The higher O contents will have also contributed to increased hardness, although the effect is difficult to distinguish given the other variables which have an effect.
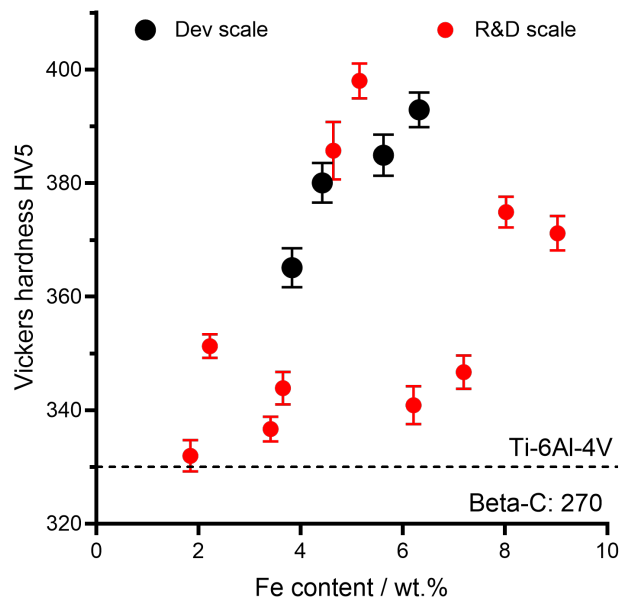
FIGURE 5.20: Measured Vickers hardness values from development scale Ti-xFe alloys, with R&D scale, Ti-6Al-4V and Beta-C measurements for comparison.

5.3.5   Tensile testing

The data collected from tensile testing of each Ti-xFe alloy, along with Ti-6Al-4V and Beta-C alloys, is displayed in Figure 5.21, with key values extracted and listed in Table 5.3.

The tensile behaviour of both Ti-6Al-4V and Beta-C alloys is as expected when compared to general reported values [23]. There are no specific figures for each alloy as the mechanical properties depend on the processing history, so instead a range is provided. For Ti-6Al-4V,

all measured values except for elongation (El) fit within the quoted ranges (E = 110–140 GPa, YS = 800–1100 MPa, UTS = 900–1200 MPa and El = 13–16%).

Beta-C, like many metastable β alloys, is expected to exhibit slightly higher strength, but lower ductility than Ti-6Al-4V. In this case the opposite outcome is seen. Compared to expected values from the literature (E = 86–115 GPa, YS = 800–1200 MPa, UTS = 900–1300 MPa and El = 6–16%), all values except for elongation are towards the low end. This is similar to the previous hardness results and consistent with reduced strength caused by larger grain sizes. The thermal treatment experienced during the FAST processing is unnecessary in conventional Ti metallurgy, and avoided to limit grain growth. In this case, it was justified for comparative purposes with the Ti-xFe alloys, where a long dwell time was required to facilitate diffusion.

TABLE 5.3: Mechanical property values of commercial Ti alloys and development scale Ti-xFe alloys, extracted from tensile testing data. Values are mean averages of 6 specimens. E - Young's modulus, YS - 0.2% offset yield strength, UTS - ultimate tensile strength, El - elongation at break. E and offset YS estimated. '-' indicates either no yielding or no intersect with 0.2% offset line.

Alloy	Powder O content / ppm	E / GPa	YS /MPa	UTS / MPa	El / %
Ti-6Al-4V	1810	118	931	994	7.1
Beta-C	920	80	846	854	14.6
3.65 wt.% Fe	4825	103	-	1040	1.0
4.49 wt.% Fe	4413	103	-	971	0.9
5.56 wt.% Fe	3740	96	-	934	0.9
6.39 wt.% Fe	4917	106	-	462	0.4

The experimental Ti-xFe alloys were far more brittle than the conventional alloys, with all but one specimen fracturing in the elastic region before any yielding. It is expected that the main cause of the brittleness is the high O content, although other factors including the Fe content, presence of other elements, and porosity may have contributed to varying degrees. Although it is difficult to assess the effect of Fe content, the lowest elongation was observed in the highest Fe content alloy, potentially suggesting that it has a detrimental effect on ductility.

Chapter 5. Co-reduction of synthetic rutile and iron (III) oxide via the FFC-Cambridge
126
process to produce pseudo-binary Ti-Fe alloys

Fractography

Analysing the fracture surfaces of the tensile specimens reveals features which correspond to the tensile behaviours in Figure 5.21 and determine the failure mechanism. Both Ti-6Al-4V and Beta-C fractured via a ductile tear, an example of which is shown in Figure 5.22 a. Further analysis shows that they failed by a mechanism known as microvoid coalescence, as evidenced by the equiaxed dimples present on the fracture surfaces (Figure 5.17 b & d). This is a common failure mechanism in metallic alloys, where microvoids nucleate at grain boundaries, interfaces between the matrix and inclusions or second-phase particles, or porosity. With increasing tension, the microvoids coalesce, leading to fracture [197]. This corresponds with the tensile testing data, as these alloys exhibited significant plastic deformation before fracture.

The Ti-xFe alloys were brittle and so clean breaks were formed, as seen in Figure 5.22 b. No dimple regions were observed in during fracture analysis of the Ti-xFe alloys, indicating a different failure mechanism. The relatively flat and smooth surfaces in the two higher Fe content alloys indicate a trans-granular cleavage mechanism, with cleavage steps across planes visible in Figure 5.22 j & l. Although density was >99%, the presence of some porosity may have contributed somewhat to poor performance. Porosity is known to have a much greater effect on the fatigue properties of materials compared with tensile though, and so this effect is likely negligible in comparison to the affect of O content [198].

FIGURE 5.22: Photograph of fractured tensile specimens: a) Example of a Beta-C specimen, b) example of a 5.56 wt.% Fe specimen.
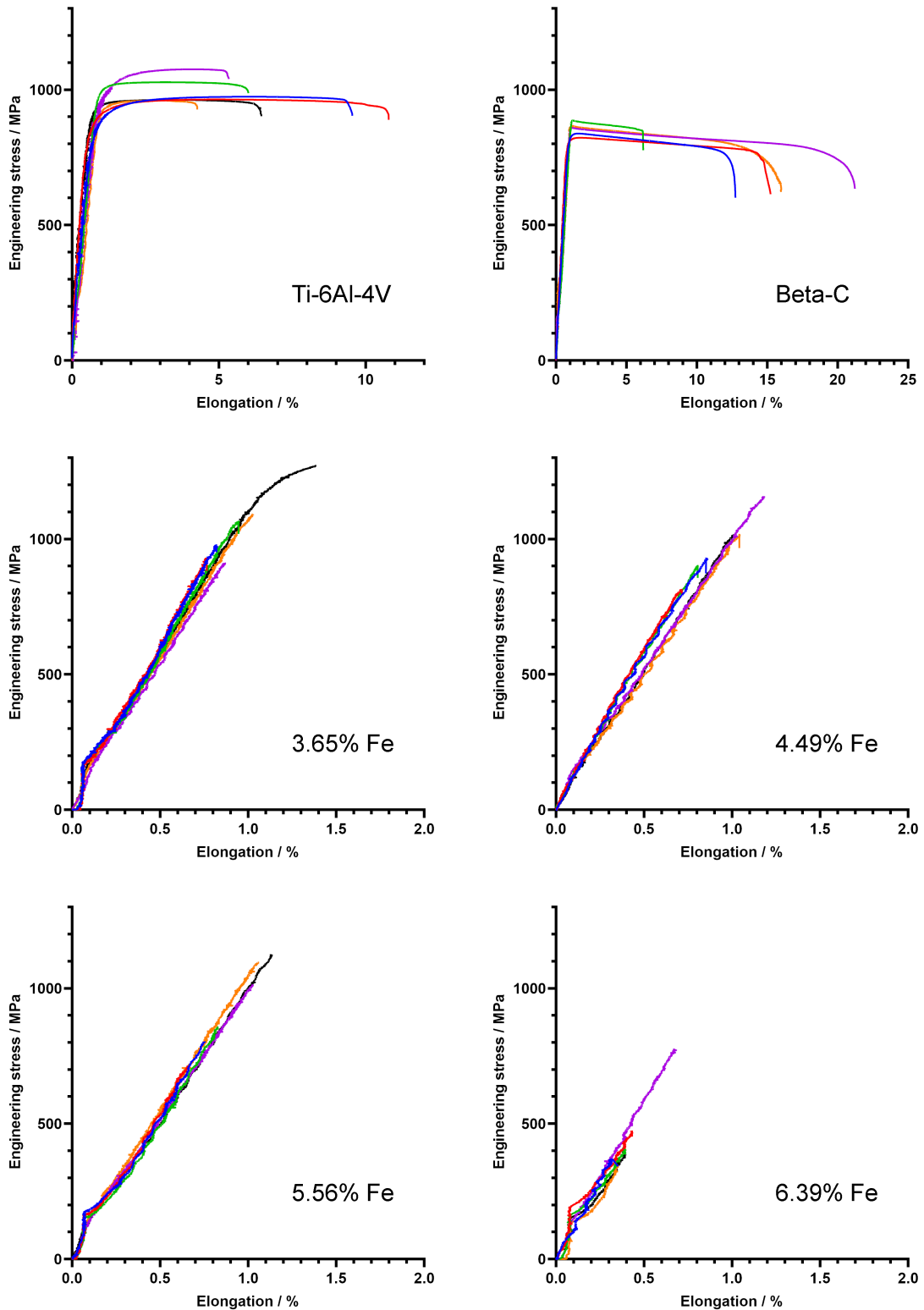
FIGURE 5.21: Stress/elongation graphs of the conventional alloys and experimental Ti-xFe alloys, illustrating the material behaviour under tension.

Chapter 5. Co-reduction of synthetic rutile and iron (III) oxide via the FFC-Cambridge process to produce pseudo-binary Ti-Fe alloys

128
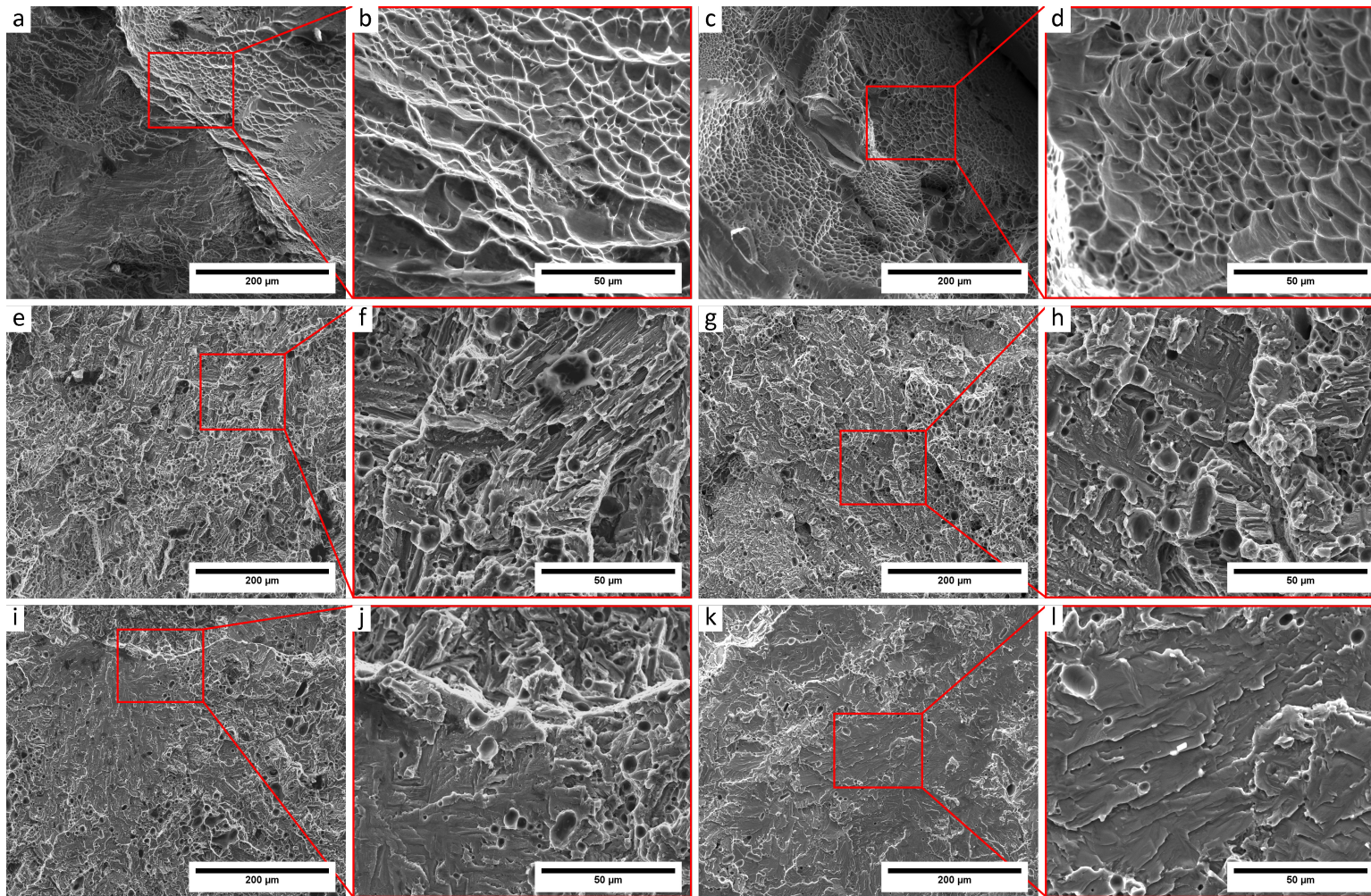
FIGURE 5.23: Secondary electron micrographs at two magnifications of the fracture surfaces from one specimen of each alloy: a & b) Ti-6Al-4V, c & d) Beta-C, e & f) 3.65 wt.% Fe, g & h) 4.49 wt.% Fe, i & j) 5.56 wt.% Fe, k & l) 6.39 wt.% Fe.

5.3.6 Conclusions

Overall, this work has built upon previous studies into Ti alloy production via the FFC-Cambridge process, by creating various Ti-Fe alloys from $SR+Fe_2O_3$ mixtures. Combining the FFC-Cambridge process with FAST has proven to be an effective solid-state production and processing route for titanium alloys. There are still many challenges which need to be addressed before these technologies can be combined on a commercial scale, however this research acts as an important step towards this end goal.

Although Ti alloys with a range of Fe contents were created, the final Fe content was unpredictable and not wholly dependant on the starting oxide composition. The mechanism for Fe loss, whether physical or chemical, needs further research, so that it can be prevented or factored in when creating reducing future oxide compositions. Commercially available alloys have very strict tolerances for alloying elements, and so consistency needs to be achieved to ensure that alloys have reliable properties.

O contents proved to be generally too high and inconsistent, therefore optimising the reduction of these and other mixed metal oxides must be a priority. Most Ti alloy powders contain <0.2 wt.% O and so to compete with conventionally produced powders, values below this must be achieved consistently. Altering parameters of the reduction process, such as temperature, time, and voltage, may be successful in achieving this. This oxide mixture has never been reduced previously, and so an optimisation study would be necessary across all reduction scales. C contents were shown to improve when scaling up the process due to reduced surface area to volume ratio, therefore it is expected that this is less of a concern going forward.

Mechanical performance of the alloys was disappointing, mainly due to high O contents from the development scale reductions. This limited any comparison of the alloys and the effect of Fe content on mechanical properties, as all alloys failed prematurely.

Chapter 6

Production of binary Ti-Fe alloys from blended elemental powders using FAST

6.1 Introduction

Chapters 4 and 5 showed that FAST can facilitate the diffusion required to create homogeneous microstructures from heterogeneous Ti-Fe alloy powders, without excessive processing times. The results suggest that Ti-Fe alloys could also be produced using FAST from blended elemental powders. As covered in Section 2.6.1, several publications explore the use of powder metallurgy and solid-state alloying to create Ti-Fe alloys. FAST can achieve reduced porosity and lower processing times compared to traditional press and sinter approaches, making it a suitable technique for this work.

Producing Ti-Fe alloys in this way would solve some of the issues encountered in Chapter 5, allowing for assessment of their properties with Fe content being the only variable. The alloys produced via the FFC-Cambridge process had too many variables which affected the mechanical properties: O and C contents were inconsistent, along with Fe contents which were unpredictable. The presence of other elements retained from the synthetic rutile will have also affected the properties in unknown ways, despite being fairly consistent in content. The compositions of Ti-Fe alloys made via a blended elemental route have defined binary compositions based solely on the chemistry and ratio of the powders used. Therefore, Fe content is isolated as the only variable between the alloys, allowing for a

better understanding of its effect on microstructure and mechanical properties. These alloys can also be compared with those produced by the FFC-Cambridge process to assess the effects of higher O and C contents, as well as the remnant elements from the SR.

Using the results from Chapters 4 and 5 provides some useful understanding of the FAST processing conditions required for sufficient diffusion and to achieve homogeneous microstructures, however there are additional variables which must be considered:

- Powder particle sizes

  The particle size affects the amount of diffusion required for homogeneity. FAST consolidation of the blended powders will occur within minutes and the Fe particles will become Fe regions surrounded by Ti. Diffusion occurs at the interfaces, and therefore larger Fe regions will have a lower interface area to volume ratio, leading to relatively slower diffusion. This means that more time will be required for the same amount of Fe to fully dissolve into the Ti matrix. Also, if the Ti particles are too large then the diffusion zones (similar to as seen in Section 4.3) may not overlap sufficiently. In this case, although the Fe may fully dissolve into the Ti matrix, the Fe concentration will not be homogeneous on the macroscale.

- Mixing effectiveness

  Blending of the elemental powders must be sufficient to ensure that the Fe particles are evenly dispersed amongst the Ti particles, once again to ensure Fe content is homogeneous on the macroscale. Ideally this would be done with a dedicated piece of equipment, such as the Turbular mixer used earlier for consistent and thorough mixing of the oxide powders. Mixing of metal powders, especially those with small particle sizes, must be done carefully, however, to avoid heat formation and prevent the possibility of ignition.

- Temperature

  Processing at a higher temperature increases the rate of diffusion, however the Ti-Fe system has eutectic transition at $\sim$1085°C, where melting will begin to occur (see Figure 2.21). Some other studies have heated well beyond this temperature, however, and suggest that the diffusion is fast enough to prevent considerable melting. With processes such as press and sinter and HIP, the sample is contained, so some localised

melting is not an issue. With hot pressing and FAST however, the sample is not fully contained and so any melting must be avoided to prevent leakage from the graphite mould.

This eutectic transition was not an issue in Chapter 5 where a temperature of 1100°C was used for FAST processing, as with these powders the Fe was already dissolved in Ti solid solution. Therefore, it is possible to first process the Ti+Fe blends below 1085°C until the Fe has fully dissolved, followed by processing at a higher temperature to further enhance the diffusion rate.

- Dwell time

Although results from Chapter 4 clearly show that processing temperature is far more significant to diffusion than time, an increase in the hold time will allow more diffusion to take place. Excessive processing times should be avoided though to prevent unnecessary grain growth which is detrimental to mechanical properties.

- Powder blend composition

The composition of the powder blend will have an effect on the diffusion rates later in the processing. One of the factors of diffusion rates is the extent of the concentration gradient present. Similar to what is shown earlier in Figures 2.22 and 4.9, as the Ti becomes more saturated with Fe, the driving force for further diffusion is reduced. In alloy compositions with higher Fe content, this saturation will happen earlier in the processing, and so achieving homogeneity across the material may be more challenging.

The aim of this work is therefore to create a range of binary Ti-Fe alloys from blended elemental Ti and Fe powders using FAST, with compositions covering a similar range to those produced previously via the FFC-Cambridge process: 0, 2.5, 5, 7.5 and 10 wt.% Fe. The resulting microstructure of each alloy is studied, followed by tensile testing for comparison with the results presented in Section 5.3.5.

6.2 Experimental procedure

CP Ti (Phelly and Alfa Aesar) and Fe powders (powder details in Section 3.6.2) were weighed and mixed together in a weighing boat. Unfortunately, the Turbular mixer used

previously was no longer accessible and so no specific mixing equipment was available. Mixing was initially done by stirring the powders with a spatula, however a more effective mixing technique was employed later: pouring the powders between two weighing boats five times, combined with hand mixing with a spatula for 2 min between each pour.

The blended powders were then processed using FAST (as detailed in Section 3.2), firstly using 20 mm diameter moulds to create samples for microstructural analysis and FAST optimisation, then using 60 mm diameter for extraction of tensile specimens. Tensile specimens were once again extracted using wire EDM and finish machining, to the same dimensions used for the FFC-Cambridge derived alloys (Figure 5.15). Specimens were also tested in the same way as described in Section 3.5.2 and microhardness was performed as described in Section 3.5.1, with once again a 5x5 grid of 25 measurements tested, covering an area of 10 mm^2 in the centre of each sample.

6.3 Results and discussion

6.3.1 Initial experiments with Phelly CP Ti powder

Initial experiments were done with an already available CP Ti powder from supplier Phelly (details in Section 3.6.2), which had an advertised particle size of 45–150 μm compared to the <60 μm Fe. These tests were done at 1000°C, below the eutectic temperature of 1085°C to prevent any melting, with the goal of determining the dwell time required at this temperature to achieve homogeneity. Figure 6.1 provides examples of some of these initial tests using blends of 5 wt.% and 10 wt.% Fe, with homogeneity never achieved despite long processing times of up to 120 min. Distinct regions of $\alpha+\beta$ are visible, alongside regions which are fully β stabilised. Comparing with results from Chapters 4 and 5, it would be expected that these processing conditions would be sufficient for the necessary diffusion to take place, and that at 5 wt.% Fe should give a $\alpha+\beta$ microstructure. Given this is not the case, it was likely that the mixing was insufficient, leading to enriched Fe regions and thus β stability.

From these tests, it was decided to use a CP Ti powder with a smaller particle size as this would both reduce the amount of diffusion required and improve mixing, given it would have a similar particle size to the Fe powder.
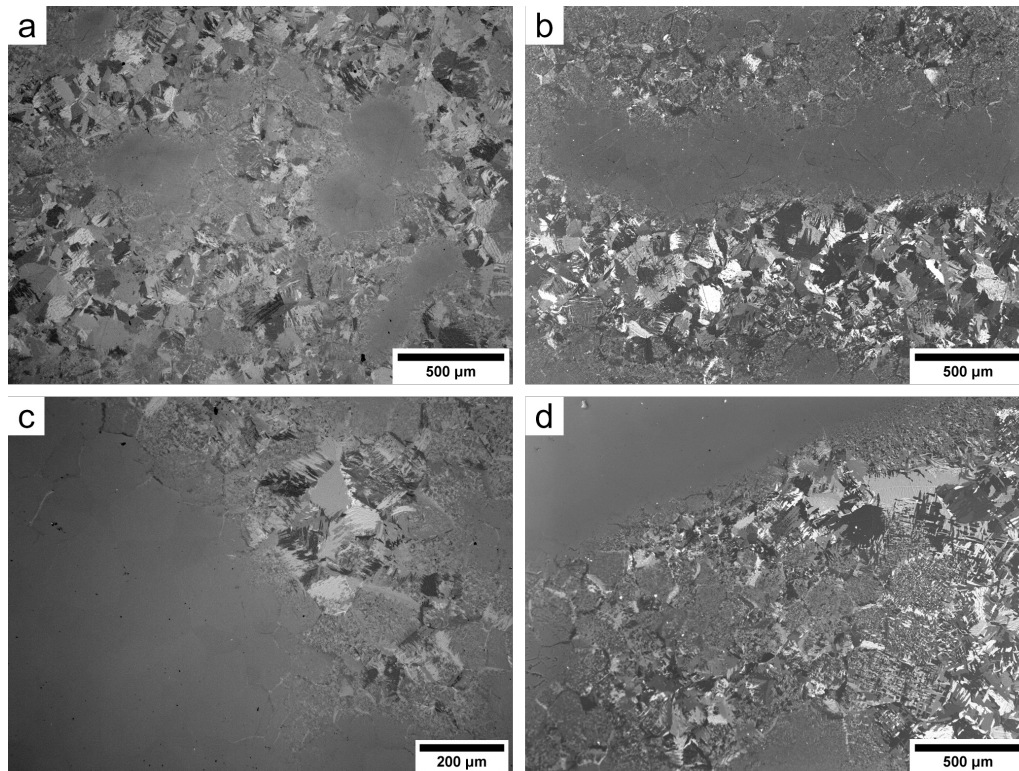
FIGURE 6.1: Optical micrographs using cross-polarised light of FAST pro-
cessed Ti+Fe blends at 1000°C. a) 5 wt.% Fe, 30 min dwell, b) 5 wt.% Fe, 90
min dwell, c) 10 wt.% Fe, 60 min dwell, d) 10 wt.% Fe, 120 min dwell.

6.3.2   FAST optimisation with AA CP Ti powder

The CP Ti Phelly powder was replaced with a powder supplied by Alfa Aesar, with smaller particle sizes of <45 μm (details in Section 3.6.2). An alternative powder blending technique was also used, as explained earlier, which improved the mixing and generating a good dispersion of Fe particles, as highlighted in Figure 6.2. All following blended experiments were therefore done using these powders and this mixing technique.

A full study on the processing of this powder mixture was then done for both 5% and 10% wt.% Fe compositions to understand the process of the Fe particles dissolving into Ti, and to determine the required FAST dwell time to achieve homogenisation. Figure 6.3 shows the progression of Fe particle dissolution over time. At 0 min, the Fe particles are clearly seen amongst the α Ti. A considerable amount of diffusion has occurred during the heating up to 1000°C though, visible as a layer of β Ti around each Fe particle. This is more pronounced in the 10 wt.% Fe sample, due to more overlapping of these diffusion regions. After a 15 min dwell, almost all of the Fe has dissolved, with only small amounts of presumably the larger particles present. This agrees with the data from Chapter 4,
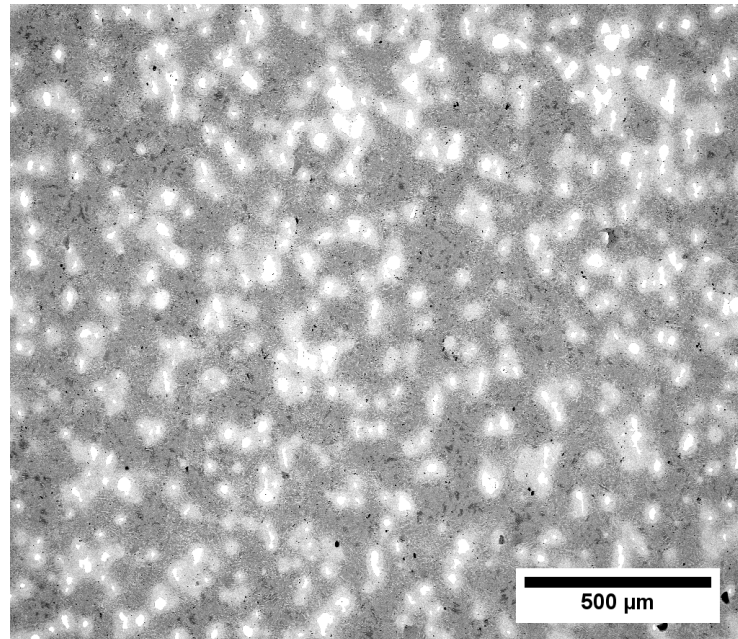
FIGURE 6.2: Backscattered electron micrograph of 10% wt.% Fe sample processed at 1000°C with a 0 min dwell, highlighting the effectiveness of the powder mixing process. Fe particles appear brighter than Ti due to higher Z contrast.

where EPMA data showed that a 15 min dwell at 1000°C resulted in total Fe diffusion of > 100 μm from the interface (Figure 4.6). Given a maximum Fe particle size of up to 100 μm (according to data in Figure 3.9), this seems to correspond well, although this system is more complicated as diffusion can occur outwards from the particle in more than one direction. Further time is required however to homogenise the bulk material once the Fe is in solid solution. The microstructures of both compositions seem to have homogenised after a 60 min dwell time, with the 5 wt.% Fe composition generating a $\alpha+\beta$ microstructure and 10 wt.% Fe being essentially all β but for some α precipitation at the grain boundaries. Backscattered electron micrographs in Figure 6.4 also confirm this, with similar microstructures to those seen in Figure 5.11, but without any TiC phase.

5% Fe   10% Fe
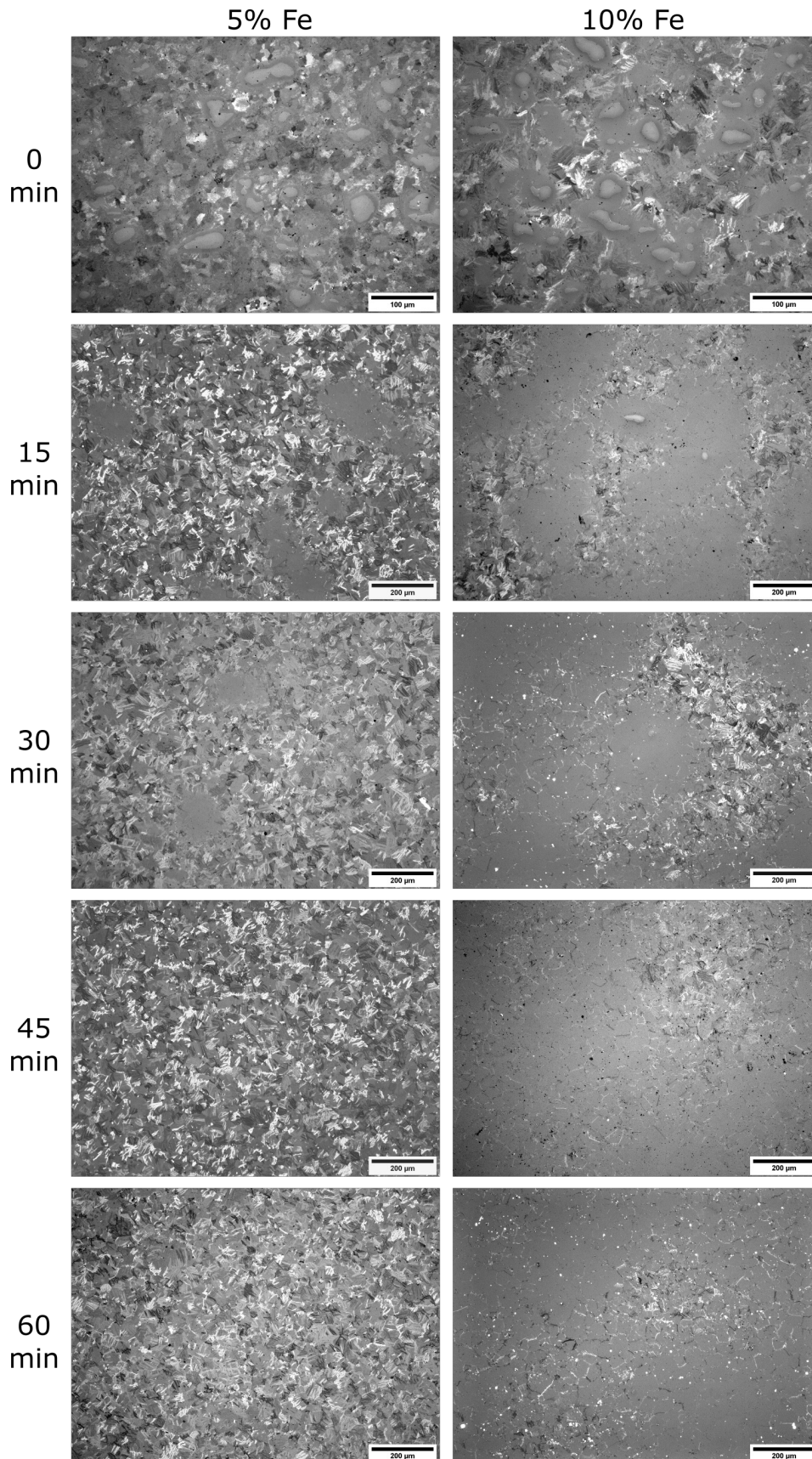
FIGURE 6.3: Optical micrographs using cross-polarised light of Ti + 5 and 10 wt.% Fe blends processed using FAST at 1000°C for a range of dwell times.
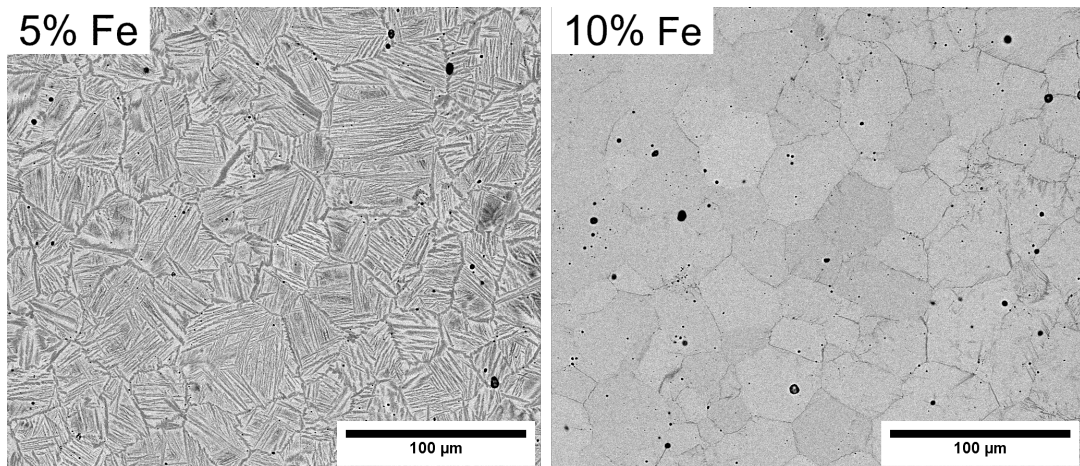
FIGURE 6.4: Backscattered electron micrographs of Ti + 5 and 10 wt.% Fe
blends processed using FAST at 1000°C with a 60 min dwell.

6.3.3   Determining the solubility limit of Fe in Ti

To determine the solubility limit of Fe in Ti under these processing conditions, powder blends with 12.5 wt.% Fe and 15 wt.% Fe were also subjected to 1000°C, 60 min dwell. The 12.5 wt.% Fe sample was almost entirely β phase, similarly to the 10% sample, but for a few additional bright features visible in the backscattered electron micrographs, as shown in Figure 6.5 b. These features were more common in the 15 wt.% Fe sample, with examples shown in Figure 6.5 c. Initially, this was thought to be intermetallic TiFe phase formation during cooling, as this would be expected at higher Fe contents according to the Ti-Fe phase diagram. X-EDS analysis (results in Table 6.1) of one of these regions revealed that it was actually an Fe particle at its core, with 5 wt.% Ti having diffused in, similar to what was seen in Figure 4.5. Figure 6.5 d also shows the particle has formed layers between the core (Site 1) and surrounding β Ti. The layer analysed at Site 2 was measured to be 68.4 at.% Fe, roughly corresponding to the intermetallic phase TiFe$_2$, and at Site 3 there was 48.2 at.% Fe, roughly corresponding to the intermetallic phase TiFe. These layers and their relative thicknesses are quite different to what was seen in the Ti-Fe diffusion couples studied in Chapter 4, where a relatively thin intermetallic layer, composed mainly of TiFe, was present between the bulk Fe and Ti. It is assumed that these Fe rich regions are larger Fe particles which could not fully dissolve into the Ti once it became fully saturated.

Given these findings, it was clear that the Fe content should be limited at 10 wt.%. These remaining Fe particles and intermetallic phases at their interfaces would likely act as weak points during tensile testing. Although the results here and from diffusion couples show that Ti can hold up to $\sim$ 20 wt.% Fe when processed with these parameters, this would require perfect homogenisation on an atomic scale, which is difficult, if not impossible, to achieve. Another reason to limit the Fe content is that the larger scale 60 mm diameter FAST billets experience a slower cooling rate during processing, further increasing the possibility of thermodynamically favourable TiFe formation.

6.3.4   Larger scale FAST consolidation

For direct comparison with the FFC-Cambridge process alloys, Ti-6Al-4V and Beta-C covered in Section 5.3, it would be ideal to process at the same conditions of 1100°C with a 60 min dwell. Although this temperature is above the eutectic at 1085°C, it has been
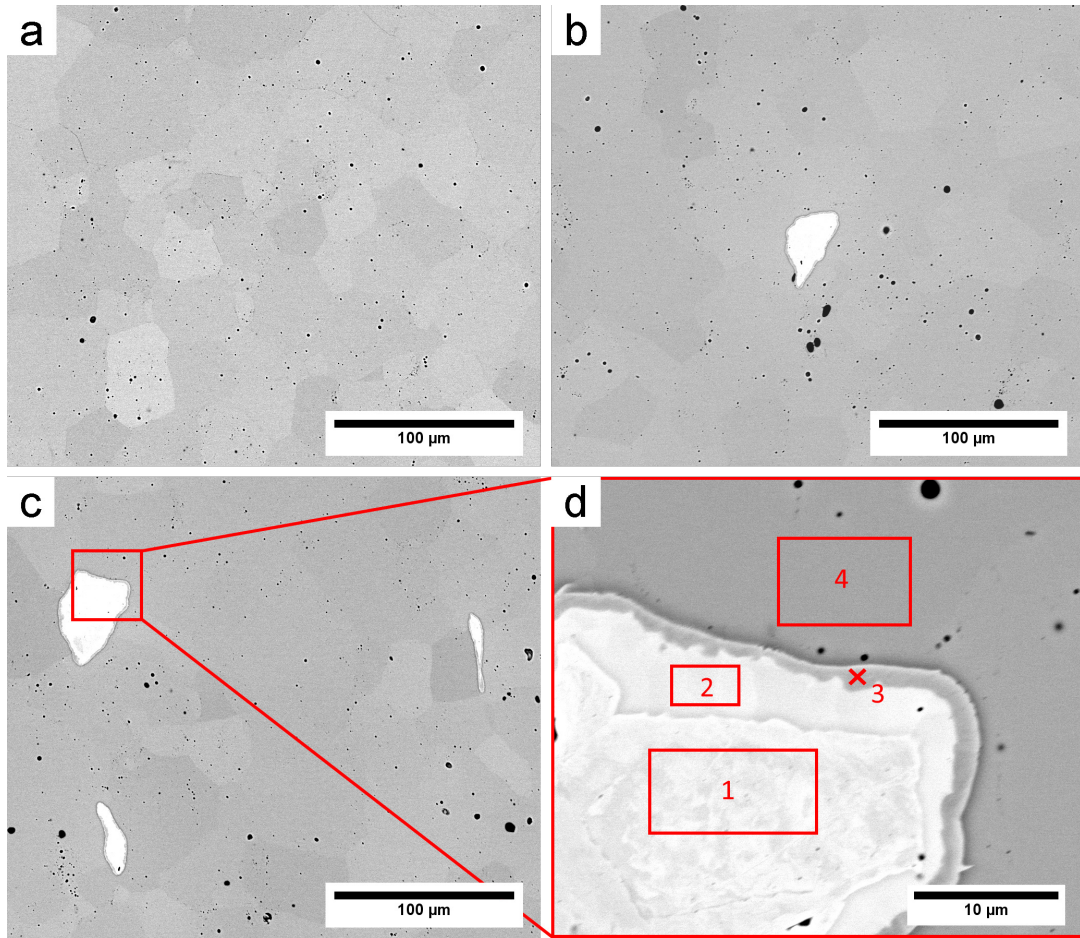
FIGURE 6.5: Backscattered electron micrographs of a+b) 12.5 wt.% Fe sample, c) 15 wt.% Fe sample, d) Higher magnification of brighter phase in c, labelled with locations of X-EDS analysis (results of which are in Table 6.1). Both samples processed using FAST at 1000°C, 60 min dwell.

TABLE 6.1: X-EDS data of regions highlighted in Figure 6.5, along with corresponding phases.

Site	Fe wt.%	Fe at.%	Ti wt.%	Ti at.%	Expected phase
1	95.0	94.2	5.0	5.8	α Fe
2	71.6	68.4	28.4	31.6	$TiFe_2$
3	52.1	48.2	47.9	51.8	TiFe
4	23.1	20.5	76.9	79.5	β Ti

shown in Figure 6.3 that almost all the Fe has dissolved into the Ti after a 15 min dwell at 1000°C. Therefore, the blended powders were processed in this way, followed by a 45 min dwell at 1100°C to replicate conditions as close as possible whilst ensuring that no significant melting occurs. At this scale, powder blends of 2.5, 5, 7.5 and 10 wt.% Fe were processed, along with CP Ti powder only for comparative purposes. Tensile specimens extracted from the resulting Ti-xFe alloys, and remaining material sectioned for analysis.

Figure 6.6 shows that all the alloys exhibited homogeneous microstructures, with the leftmost column highlighting this across a larger surface area. Optical microscopy revealed a basket weave structure of α laths in the CP Ti sample. This microstructure was not present in the smaller scale, 0 min dwell samples in Figure 6.3, though this is likely due to the Fe particles and diffusion regions preventing significant α grain growth during processing. This microstructure is similar to those presented in another publication using FAST, where it was found that there are variations in CP Ti microstructure depending on sample size and resulting cooling rate [199].

As expected, with increasing Fe content, the β phase fraction increases, from none in the CP Ti to being fully retained in the Ti-10Fe alloy. The Ti-2.5Fe, Ti-5Fe and Ti-7.5Fe alloy microstructures are similar, with acicular α laths within the prior β grains and more globular α decorating the prior β grain boundaries. The α laths are thinner and separated by more β at higher Fe contents. In the Ti-10Fe alloy, only a small amount of α phase is still visible at the grain boundaries, with no intragranular laths present. The XRD patterns in Figure 6.7 correspond well with the micrographs, with the peak ratio of β:α increasing with Fe content, until only β peaks are detected in Ti-10Fe.

The CP Ti powder used contains 0.25 wt.% O, which will have some α stabilising effect, although less so than seen in the development scale FFC-Cambridge process derived alloys which contained $\sim$0.4 wt.% (Section 5.3). Fe is the only other element affecting the β phase stability, in contrast to those alloys where other β stabilisers, including Cr, Mn, Nb and Si, were present in significant amounts. The Ti-7.5Fe microstructure contains more α than seen in both the 5.56 and 6.39 wt.% Fe containing alloys in Figure 5.17, suggesting that the β stabilising effect of the remnant elements in synthetic rutile overcompensates for the increased α stabilisation provided by the greater O content. The XRD patterns also agree with this, as there is a lower β:α peak ratio for Ti-7.5Fe compared to both the 5.56

and 6.39 wt.% Fe alloys in Figure 5.19.

Porosity in the alloys is minimal, with the FAST processing conditions achieving >99.5% density in all the alloys, with no variation due to Fe content. This is a slight improvement on the >99% density measured in the alloys produced in Chapter 5 via the FFC-Cambridge process, likely due to significantly less porosity within the initial powder particles.

Microhardness measurements once again show a general increase in hardness with Fe content. The results agree with the other hardness testing in Chapters 4 and 5, where the presence of fine secondary α provides extra strengthening and, consequently, a peak in the hardness value. In Ti-10Fe, there is no significant α phase formed, which coincides with a slight drop in hardness. The increase with hardness with Fe content is more pronounced in this set of alloys compared to those investigated in Chapter 5. This is probably due to the presence of other alloying elements in the synthetic rutile derived alloys, which provides greater solid solution strengthening than the Fe alone.
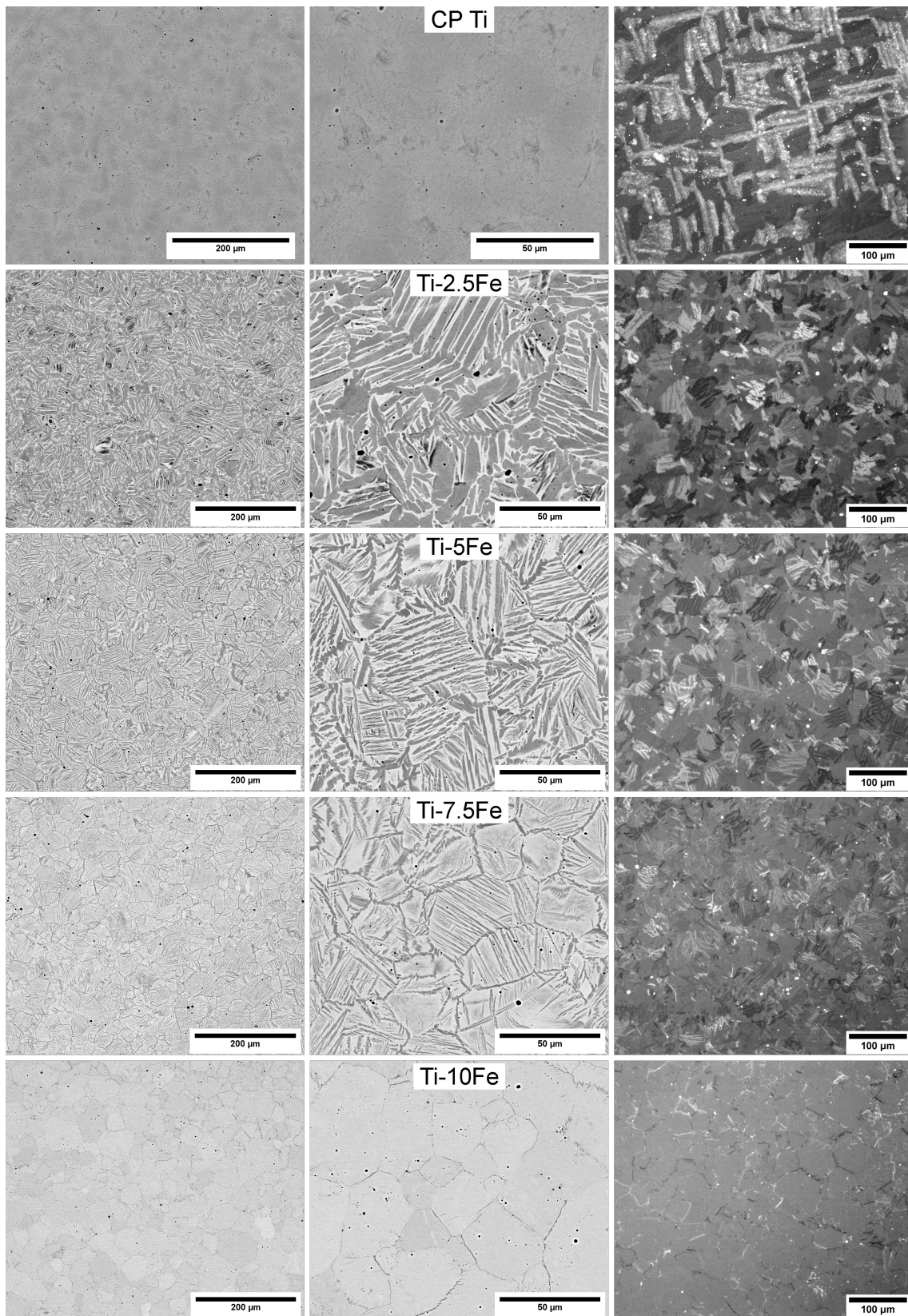
FIGURE 6.6: Micrographs of blended Ti-xFe alloys. Left and centre columns: backscattered electron micrographs at two magnifications, right column: optical micrographs using cross-polarised light.
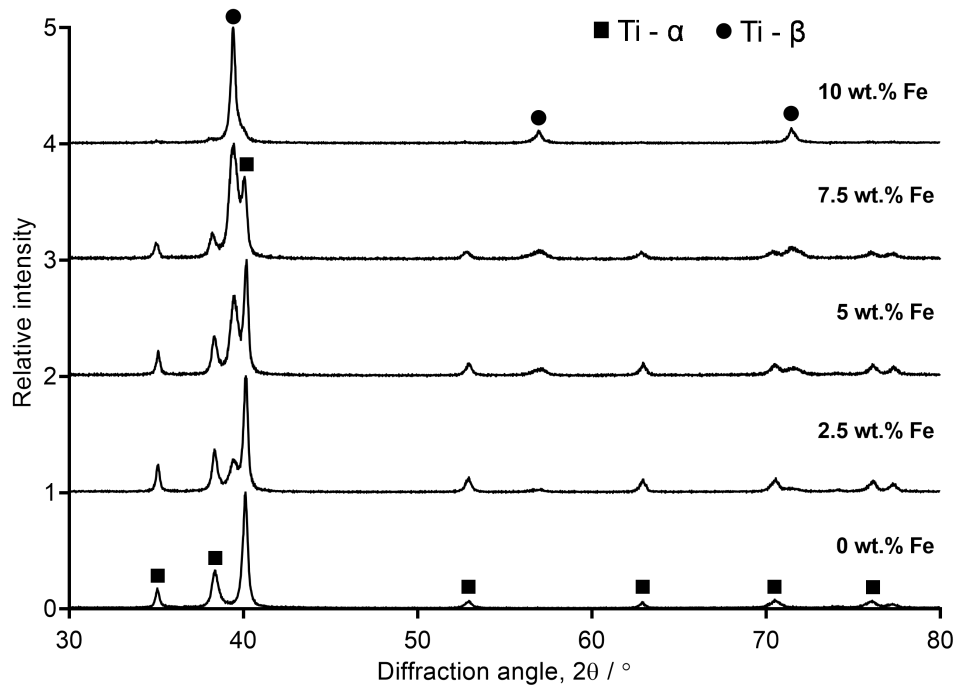
FIGURE 6.7: XRD patterns of blended Ti-xFe alloys.
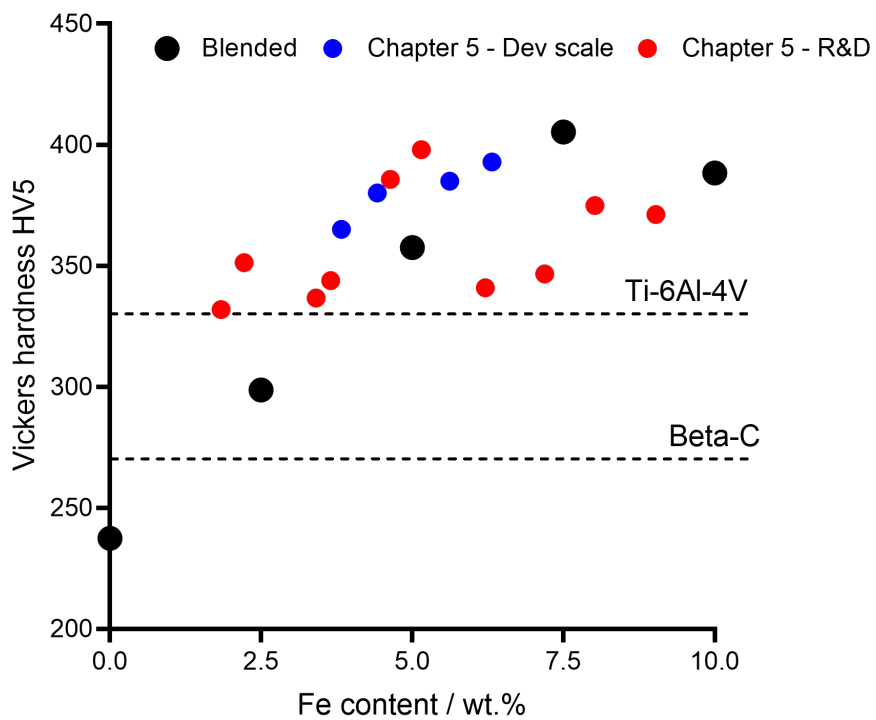
FIGURE 6.8: Measured Vickers hardness values from blended Ti-xFe alloys, with hardness values from alloys studied in Chapter 5 for comparison.

6.3.5 Tensile testing

Figure 6.9 illustrates the stress/strain data for the alloys and the effect of the Fe content on the tensile properties listed in Table 6.2. The elongation to failure for the CP Ti specimens seemed low at 4.2% when compared to literature values for conventionally processed CP Ti (Table 6.3). The AA CP Ti powder used for this work contained 0.25 wt.% O, which is on the boundary between grades 2 and 3. It would, therefore, be expected that this material would fail at an elongation somewhere between 15% and 24%. Other publications have presented the tensile UTS and El values for CP Ti powders consolidated using FAST. There seems to be a range of values, which seem to be most influenced by the O content, with higher O contents causing higher strength and lower ductility, as would be expected. The processing time of 1 hour was considerably longer than in these other studies, which likely caused increased grain growth. Theoretically, this should improve the ductility at the expense of reduced strength as larger grains mean fewer grain boundaries and so more dislocation movement is possible along slip planes (opposite to the Hall-Petch relationship covered in Section 2.1.5). Overall, this suggest that perhaps the O content in the powder used for this research was higher than indicated in the supplier's chemistry datasheet (Table 3.2). O pickup during FAST processing is minimal due to being performed under a vacuum, so it is unlikely that the processing has caused the reduced ductility.

As the blended Ti-xFe alloys were produced using the same CP Ti powder, it can be assumed that this is the main cause of the brittle nature of the alloys. Despite this, the effect of increasing Fe content can still be assessed compared to the CP Ti results. Increasing the Fe content up to Ti-2.5Fe and Ti-5Fe causes increased strength and decreased ductility. Similar to the explanation of the earlier microhardness results, the increase in strength can be attributed to a combination of solid solution strengthening and refinement of the α precipitates. This strengthening comes at a cost of reduced ductility, as dislocation movement is impeded. Specimens from the Ti-7.5Fe and Ti-10Fe alloys were too brittle to reach the yield strength, resulting in no plastic deformation before failure.

Comparison of Ti-Fe alloys from literature

Other publications on the production of Ti-Fe alloys from blended elemental powders provide an insight into the potential mechanical properties of these alloys and are useful

TABLE 6.2: Mechanical property values of CP Ti and blended Ti-xFe alloys, extracted from tensile testing data. Values are mean averages of 6 specimens. E - Young's modulus, YS - 0.2% offset yield strength, UTS - ultimate tensile strength, El - elongation at break. E and offset YS estimated. '-' indicates either no yielding or no intersect with 0.2% offset line.

Alloy / wt.%	E / GPa	YS /MPa	UTS / MPa	El / %
CP Ti	106	529	666	4.2
Ti-2.5Fe	115	750	936	4.6
Ti-5Fe	113	1063	1143	1.8
Ti-7.5Fe	112	-	1081	1.0
Ti-10Fe	103	-	520	0.5

TABLE 6.3: Reported ultimate tensile strength (UTS) and elongation to failure (El) values of CP Ti from literature.

Publication	O content / wt.%	Powder used	FAST processing parameters	UTS /MPa	El / %
Lütjering & Williams [3]	0.18	-	Convention-ally processed	>240	24
	0.4			>550	15
Zadra et al. [126]	0.13	< 45 μm GA	1100°C, 60 MPa, 5 min	430	45
	0.31			700	13
Shahedi Asl et al. [200]	0.57	< 75 μm HDH	1050°C, 50 MPa, 5 min	440	3
Shon et al. [201]	0.65	< 45 μm	850°C, 30 MPa, 10 min	780	2
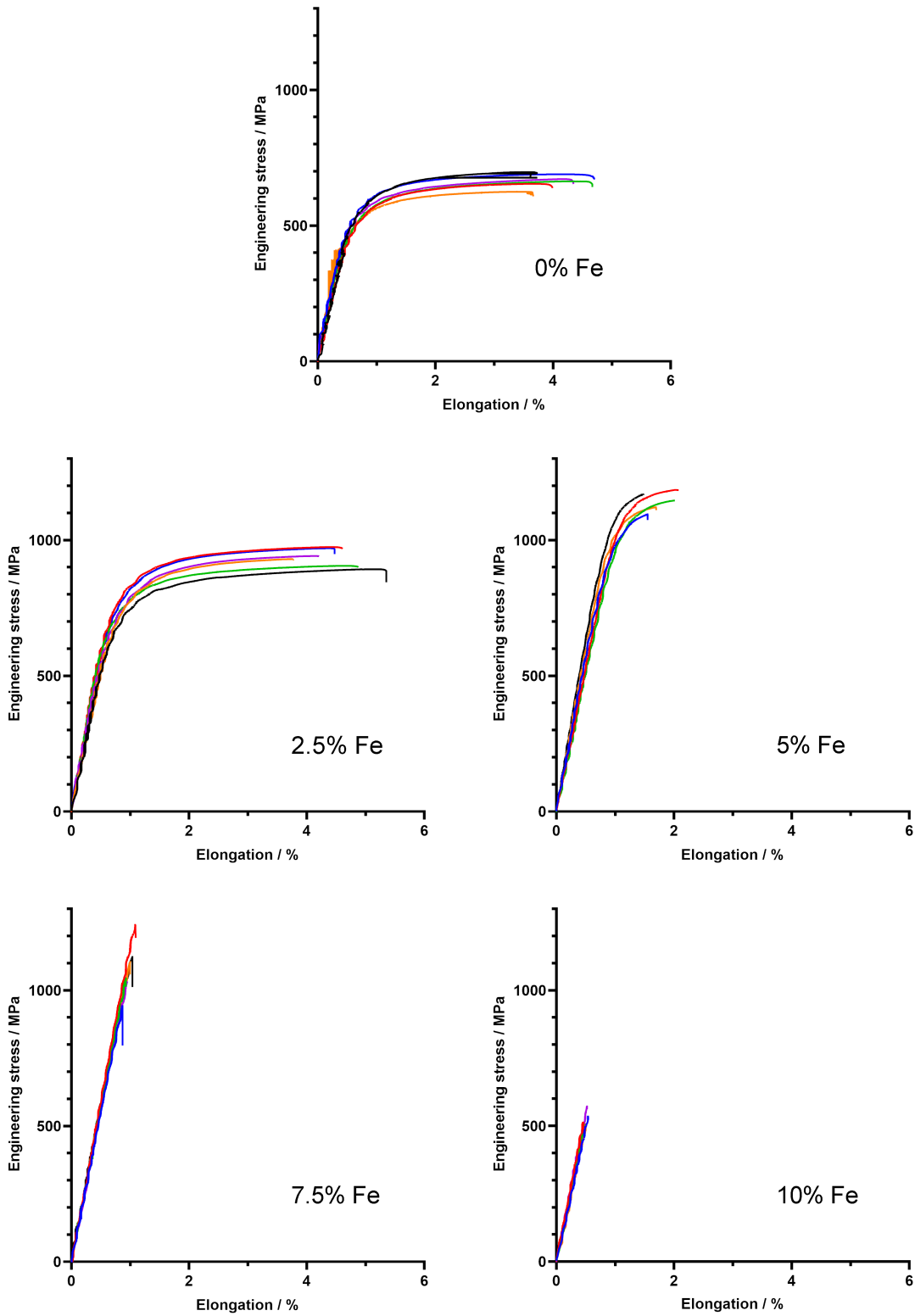
FIGURE 6.9: Stress/elongation graphs of the Ti-xFe alloys from blended elemental powders, illustrating the material behaviour under tension.

for comparison. Figure 6.10 presents tensile data from four publications. Figures 6.10 a+b show that elongation values of as-sintered Ti-Fe alloys were <5%, with one author suggesting that the brittleness was caused by high O contents and the presence of acicular α lamellae [151]. The Ti-5Fe FAST processed result in Figure 6.9 has higher strength but lower ductility than those in Figure 6.10 b. Given the chemistry is very similar, this suggests that the difference is mainly based on the microstructures formed from different processing. Figures 6.11 a+c compares the microstructure for both as-sintered alloys, revealing the finer α lamellae present in the FAST produced alloy. This finer microstructure gives higher strength as there are more barriers to dislocation movement, but at the cost of reduced elongation. It is likely that the finer α laths are a result of the relatively fast cooling rate experienced after the electrical current is removed during FAST processing, compared to that in a vacuum furnace. In FAST, the graphite tooling is in direct contact with the water cooled electrodes, providing effective cooling, whereas heat transfer occurs far slower in a vacuum environment without this assisted cooling.

Further research into the literature shows that the mechanical properties of as-sintered Ti-Fe alloys can be significantly improved with additional thermomechanical processing. Figures 6.10 c+d show that extrusion of the alloys greatly increases their ductility, with elongations >25% in Ti-Fe alloys which have also been heat treated [202]. Figure 6.10 c also shows that forging increases the strength by refining the microstructure, whilst retaining the same level of ductility [21]. Figure 6.11 b shows the microstructure of a Ti-5Fe alloy after extrusion, containing much smaller α precipitates which have more equiaxed morphology.
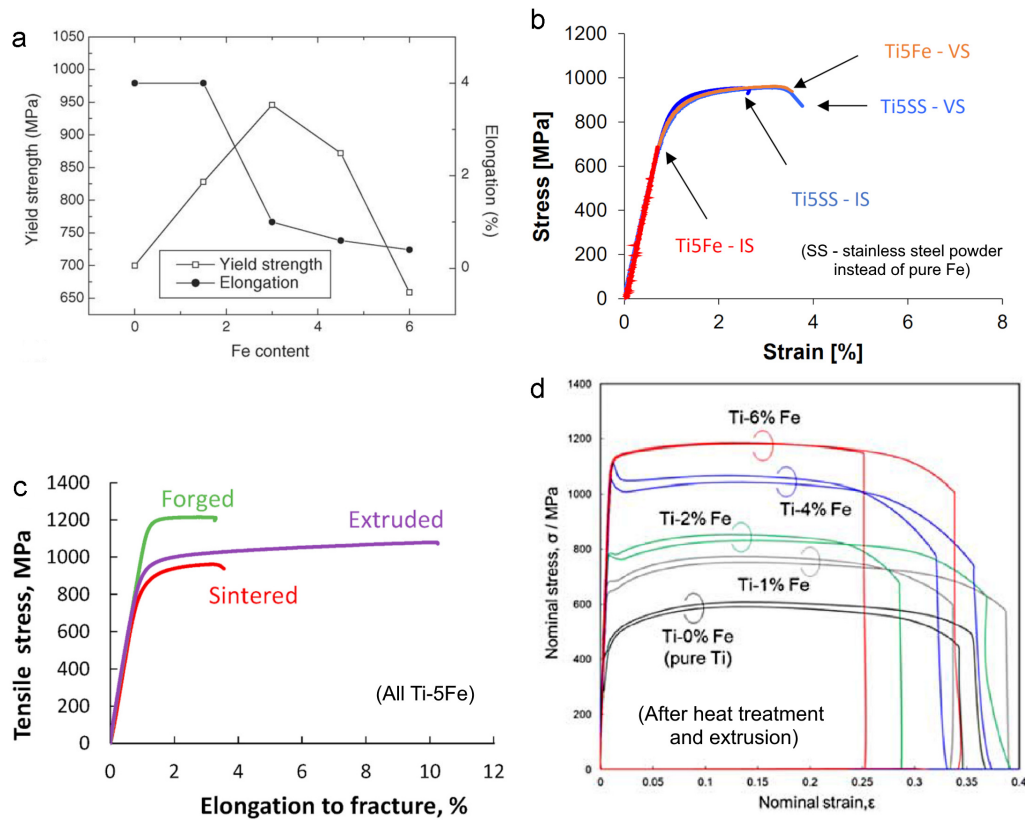
FIGURE 6.10: Tensile results from literature of comparable Ti-Fe alloys produced via sintering of blended elemental powders. Relevant details are as follows: a) Ti HDH powder with 0.34 wt.% O, cold press and sintered at 1250°C for 30 min [203]; b) Ti HDH powder with 0.23 wt.% O, increasing to 0.3–0.4% after sintering, vacuum sintered (VS) (at 1000°C for 2 hours, followed by 1250°C for 2 hours) or induction sintered (IS) (at 1000°C for 8 min, followed by 1150°C for 2 hours) [151]; c) Same as b using VS, sintered material then open die forged or hot extruded [21]; d) Ti HDH powder, O content measured as ∼ 0.25% after sintering, sintered using FAST at 1000°C for 1 hour, heat treated at 1000°C for 3 hours, then hot extruded [202].
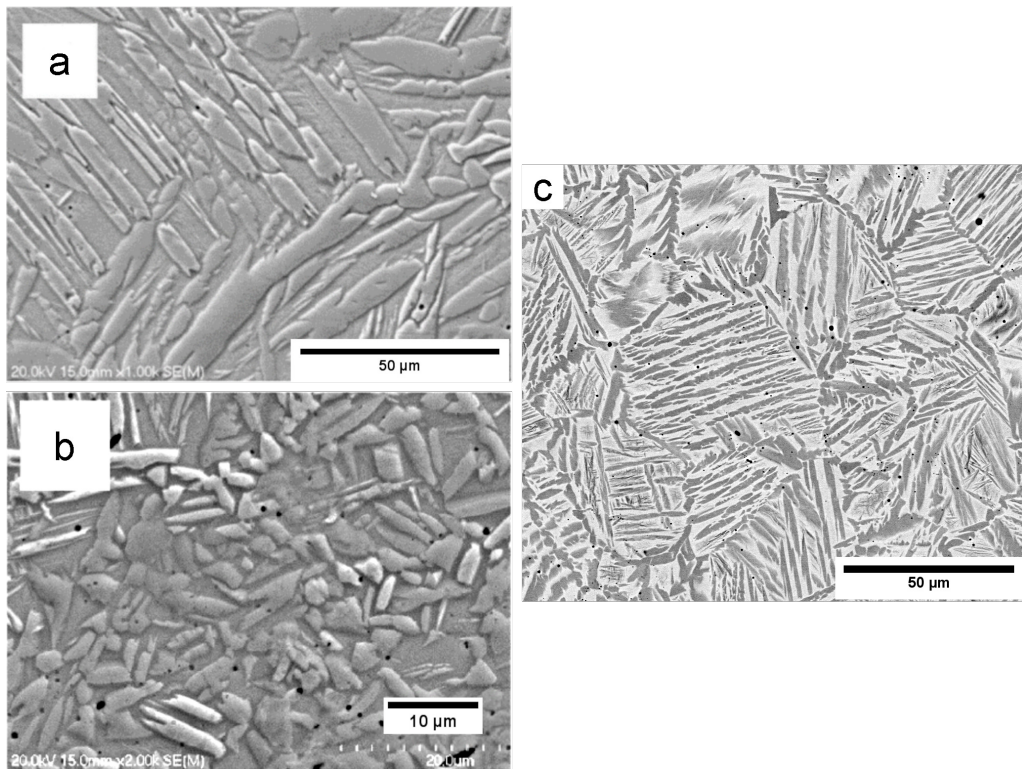
FIGURE 6.11: Comparison of Ti-5Fe microstructures. a) Secondary electron micrograph of as-sintered material from [151], b) secondary electron micrograph of extruded material from [21] (transverse to the extrusion load), c) Backscattered electron micrograph of FAST processed from Figure 6.6
.

Fractography

Analysis of the fracture surfaces once again reveals features which correspond with the failure behaviour of each alloy under tensile loading, and thus the effect of increasing Fe content. Figure 6.12 presents an example specimen fracture surface from each alloy composition.

The CP Ti fracture surfaces exhibit an interesting combination of rough and smooth regions, suggesting some sort of hybrid failure mechanism (Figure 6.12 a & b). The dimples produced from the microvoid coalescence mechanism are visible, corresponding with the higher ductility compared to the other alloys. Amongst the dimple regions, many long and thin smooth features are also seen. These areas also seem to be orientated both parallel and perpendicular to each other, which corresponds to α laths in the basket weave structure observed in Figure 6.6. This suggests that the smooth regions occur due to brittle fractures at grain boundaries between two α laths.

The Ti-xFe alloys have consistent fracture surfaces and features in comparison. When comparing Figure 6.12 b & d, the Ti-2.5Fe alloy exhibits similar dimples as seen in the CP Ti, excluding the aforementioned smooth regions. The amount of dimples is far lower in both the Ti-5Fe and Ti-7.5Fe alloys, confirming that the failure mechanism is less ductile. Cleavage steps are visible in the fracture surfaces, particularly in Figure 6.12 h, which are indicative of brittle failure [197]. Figure 6.12 i & j highlights the extremely brittle nature of the Ti-10Fe alloy, with the smooth surfaces without any dimples being a good example of an intergranular cleavage mechanism.
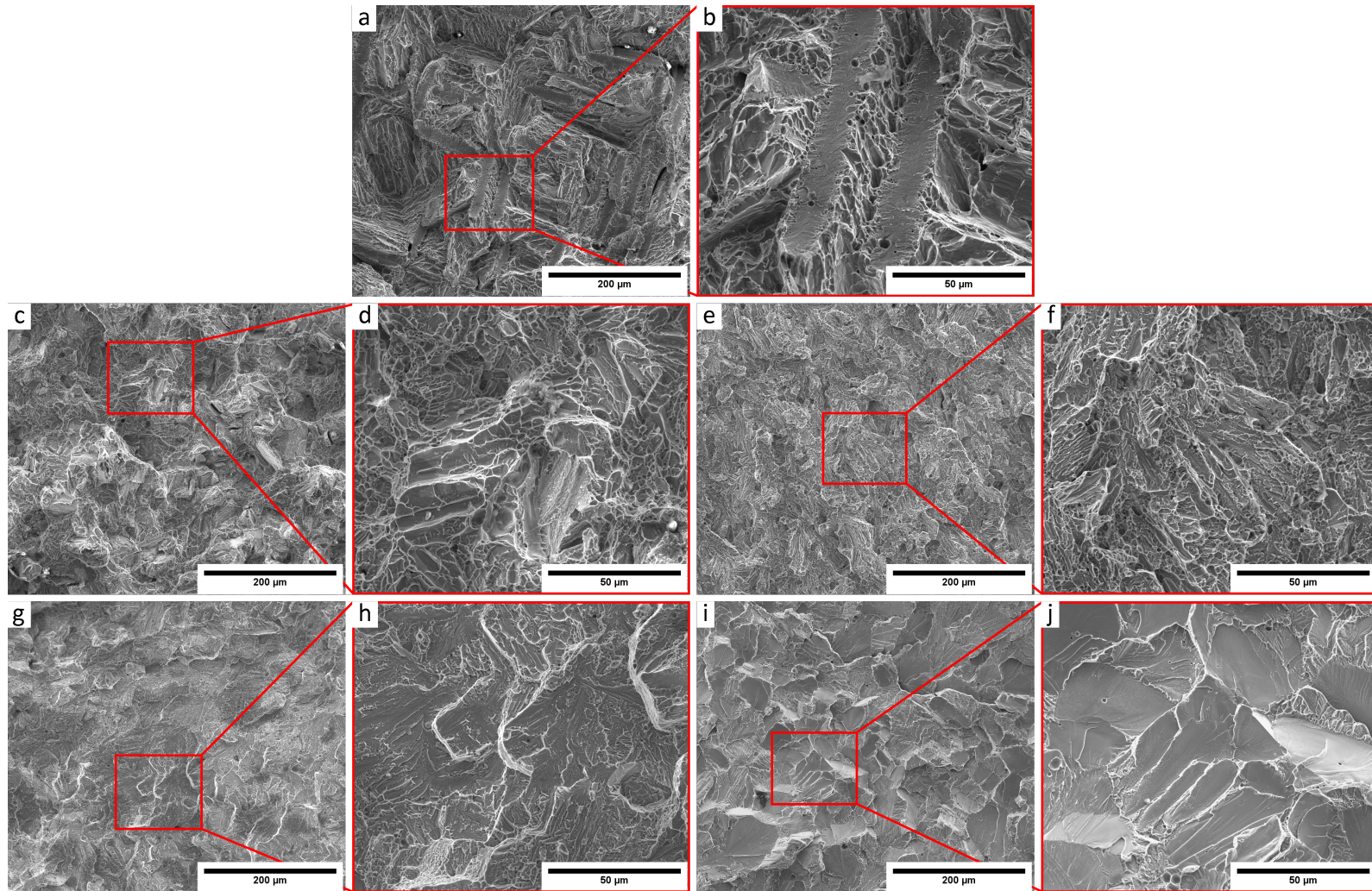
FIGURE 6.12: Secondary electron micrographs at two magnifications of the fracture surfaces from one specimen of each blended Ti-xFe alloy: a & b) CP Ti, c & d) Ti-2.5Fe, e & f) Ti-5Fe, g & h) Ti-7.5Fe, i & j) Ti-10Fe.

6.4 Conclusions

The results of this chapter show that FAST is an effective technique for the production of binary Ti-Fe alloys up to 10 wt.% Fe via solid-state alloying of blended elemental powders. Powder particle size and mixing effectiveness proved to be important in ensuring chemical homogeneity during FAST processing. The best results were achieved when the Ti and Fe powders were of a similar particle size and thoroughly mixed. FAST optimisation also revealed that for these powders dwell time of 1 hour at 1000°C was sufficient for complete diffusion of the Fe for homogeneity, with most of the Fe dissolving into Ti solid solution after just 15 min. Alloys containing >10 wt.% Fe were found to contain remnant Fe particles which had not fully dissolved, signifying that 10 wt.% Fe should be the limit for producing Ti-Fe alloys by this route to avoid jeopardising their mechanical performance.

Following these findings, Ti-xFe alloys up to 10 wt.% Fe were produced on a larger scale. The alloys all contained minimal residual porosity and were microstructurally homogeneous, with all the Fe dissolving into Ti solid solution when using the optimised FAST parameters. By varying the Fe content, a range of microstructures were generated, with an increasing amount of β phase retained at higher Fe additions. The Ti-2.5Fe, Ti-5Fe and Ti-7.5Fe alloys were all dual phase $\alpha+\beta$ alloys, whereas the Ti-10Fe was a metastable β alloy, with only small amounts of grain boundary α present. The presence of fine α in the Ti-7.5Fe alloy resulted in the highest hardness values measured, in a similar result to the alloys in Chapter 5.

Tensile performance of the alloys was poor, with low ductility suspected to be attributed to the CP Ti powder used and/or unideal microstructures generated in the as-FAST condition. The Fe additions led to significant solid solution strengthening, however also exacerbated the low ductility of the Ti, causing particularly brittle failure. Analysis of the fracture surfaces complemented the elongation values seen, with evidence of reduced microvoid coalescence and increased intergranular cleavage found in the higher Fe content alloys. The poor ductility of these alloys makes them poor candidates for many material applications, at least in the as-FAST condition.

In order to verify that the CP Ti powder used was a cause of the low ductility in the alloys, it would be of interest to repeat this research using an powder of the same particle size

from an alternative supplier. This would allow for comparison of both the microstructure and mechanical properties, with any variations being solely due to the change in CP Ti powder. Performing independent analysis of the powder chemistries, especially O content, would also be of benefit to confirm the validity of the values provided by the supplier. Unfortunately, the capability for this kind of testing was not available during this study.

Comparison with other Ti-Fe alloys from blended elemental powders in the literature provided some comparison of microstructures and mechanical properties. It was found that there are a multitude of factors which affect the alloy microstructure, and that it is not a simple case of alloy chemistry and density. Different processing techniques give differing microstructures, thus affecting the tensile performance. Future further thermomechanical processing steps should be considered for these alloys, as the literature clearly shows considerable improvement in ductility as a result of microstructural refinement.

Chapter 7

Conclusions and further work

7.1 Conclusions

In summary, the research in this thesis presents important developments in the production and processing of Ti alloy powders using both the FFC-Cambridge process and field assisted sintering technology. The use of Fe as a major alloying element was a major focus, due to its low cost as both a metal and oxide, effectiveness as a β stabiliser, and rapid rate of solid-state diffusion in Ti. These three properties combined make it an ideal choice for alloying with Ti via these solid-state processes.

Most of the main objectives listed in Section 1.2 were met, with the following sections summarising the findings of each of the research chapters.

The diffusion behaviour of the Ti-Fe system during FAST processing

Analysis of Ti-Fe diffusion couples produced in Chapter 4 highlighted the significant effect of FAST processing temperature on the diffusion rate of Fe into Ti. Although total diffusion distances were difficult to accurately determine, the thickness of the retained β layer was useful for comparison of processing temperatures. This confirmed that the relationship between diffusion rate and temperature was indeed an exponential one, as described in Equation 2.3. The results of this chapter were beneficial in the later processing of heterogeneous Ti-xFe alloy and blended elemental powders, where the diffusion distances required were partly dependent on the alloy powder particle sizes. An understanding of the effect of Fe content on the microstructure and hardness was achieved which was also useful for Ti-Fe alloy development. A range of Ti alloy microstructures, from fully

α to fully saturated β, was observed between 0–20 wt.% Fe, showing that Fe additions could be used to generate a wide variety of Ti-Fe alloys. The formation of an intermetallic layer at the interface was also observed, with its thickness increasing at higher processing temperatures. The chemistry data for these diffusion couples was used in a publication to further knowledge of the diffusion behaviour of this system, confirming the importance and novelty of the work.

Direct electrochemical production of pseudo-binary Ti-Fe alloys from synthetic rutile and iron oxide

Chapter 5 establishes that an entirely solid-state production route to create Ti-Fe alloys is feasible by consolidating alloy powders from the FFC-Cambridge process using FAST. A range of alloys with various α:β ratios, microstructures and mechanical properties were produced through electrolytic reduction of mixtures of synthetic rutile and Fe_2O_3. Although Fe contents were lower than theoretical, due to loss of Fe to the electrolyte, it was clear that higher Fe contents exhibited greater β phase stabilisation. Not only does this work demonstrate the effective combination of the FFC-Cambridge process and FAST, but it also exploits a more readily available Ti precursor in SR. The ability to directly use this material without first converting to pure TiO_2 or $TiCl_4$ makes this production route even more promising. Once again, the publication of this work as a journal article confirms its acceptance as high quality, novel research. Reductions on Metalysis' development scale demonstrates the ability to scale-up the technology, although doing so brings new challenges. The inconsistencies in the alloy compositions and generally high O contents mean that further optimisation of the oxide preparation and reduction parameters is required. The high O contents caused all the alloys to have poor ductility under tensile loading, which was unsurprising due to the well known detrimental effect of excessive O on Ti alloys. This is the first time that this oxide mixture has been reduced using the FFC-Cambridge process and so it is expected that improvements could be achieved in the future, especially considering that other Ti alloy powders with low O contents (down to 0.15 wt.%) have been produced previously [8].

Production of binary Ti-Fe alloys from blended elemental powders using FAST

In Chapter 6, FAST was proven to be an effective technique for creating Ti-Fe alloys via the blended elemental powder approach, with the applied heat and pressure facilitating sintering and Fe diffusion. After some optimisation of the powder blending technique and FAST processing time, fully dense and homogeneous alloy compositions up Ti-10Fe were produced. This is an improvement on the many publications using press and sinter, with higher density achieved using lower processing temperatures, shorter dwell times, and powders with coarser particle sizes. It was discovered that alloys containing >10 wt.% Fe still contained undissolved Fe particles, suggesting that this was the limit under these processing conditions. These alloys also exhibited low ductility, possibly due to the O content of the CP Ti powder used, although more investigation is required to determine this. The alloys exhibited similar microstructures and mechanical properties to those produced earlier by the FFC-Cambridge process, although the differences in O content and presence of other alloying elements make understanding any variations challenging. Currently, the blended elemental approach is not economical for Ti alloy production on a large scale, regardless of the alloy properties. As discussed in Section 2.5.1, powdered metals, especially Ti, are expensive as they require an extra atomisation or hydride dehydride step on top of the conventional processing route. Unless there is a source of low cost CP Ti powders with a sufficiently small particle size, this alloy production is not feasible. The FFC-Cambridge process and other alternative extraction processes could provide cheaper CP Ti powders in the future though, along with the potential use of surplus powders from additive manufacturing or reprocessed machining swarf.

Overall, the research in this thesis presents important developments in the production and processing of Ti alloy powders using the FFC-Cambridge process and FAST. By combining these solid-state, powder-based extraction and processing technologies, an alternative production route for Ti alloys which are difficult to produce conventionally, is realised. There is also potential for this route to be more cost effective, which would reduce the cost of Ti components and make them available for use in a wider range of applications. This ultimately depends on successful scale-up of the technologies, which, although considered to a degree in this work, needs far more research focus from both academia

and industry to become a reality. Prior to the financial difficulties experienced during the course of this project, Metalysis was developing and increasing production capacity of the FFC-Cambridge process, although it is unknown where things stand today. FAST is certainly becoming of wider interest as an advanced materials processing technique, for both research purposes and industrial scale production. Larger machines are being manufactured, as highlighted by the commissioning of an FCT Systeme GmbH type HP D250 furnace, capable of producing billets up to 250 mm in diameter, at The University of Sheffield in 2021.

7.2 Further work

There is much additional work which could be done to build upon the results presented in this thesis. This includes investigating ways in which the experiments covered could be repeated to improve the properties of the alloys produced, along with work which expands upon the findings.

Further investigations on Ti-Fe diffusion couples

As discussed in Section 4.4, it would be of interest to repeat the thermal processing of Ti-Fe diffusion couples using an alternative method to FAST which does not rely on Joule heating to achieve heating. Repeating the production of Ti-Fe diffusion couples using a hot press system with external inductive or resistance heating, along with subsequent analysis by EPMA, would allow for a direct comparison where the only variable is the application of direct current during processing. The results would determine whether the flow of current through the diffusion couple affects diffusion rates, similar to the enhanced diffusivity observed in the Ti-Ni and Ti-W systems by other researchers, thought to occur due to electromigration [177], [178], [204].

The diffusion couples in Chapter 4 were produced in a way that the direction of diffusion was parallel with the flow of electrical current and force. If indeed the electric current has an effect, it is probable that diffusion rates would differ depending on the orientation of the interface between the metals. The diffusion couples could be instead produced with the metals side by side to explore this. Investigating any effect of modifications to the FAST DC pulse pattern would also be of interest.

Optimisation of FFC-Cambridge process for the electrolytic reduction of SR + Fe_2O_3 mixtures

O contents of the alloys produced via the FFC-Cambridge process were higher than typically tolerable in Ti alloys, especially at the development scale. This resulted in poor ductility of the alloys during tensile testing, making them unsuitable for future use in any real world applications. Despite this, it is expected that reduced O contents could be achieve through optimisation of the reduction parameters. The parameters used in Chapter 5 were based on previous work on the reduction of TiO_2 and SR, however the introduction of Fe_2O_3 may have affected the process. The next step would be to repeat the experiments with modified cell voltages and reduction times to find the combination which achieves the lowest O levels.

Retention of Fe was also inconsistent, which is not acceptable if production of these alloys were to be done on a commercial scale. As suggested in Section 5.2.5, mixing of the SR and Fe_2O_3 could be improved through use of a binder or heat treatment to chemically bind them as new phases, like Fe_2TiO_5. Using SR with a finer particle size might also help create a homogeneous mixture, rather than having Fe_2O_3 unevenly coat the SR particle surfaces, as seen in Figure 5.5.

A better understanding into the mechanism of Fe loss, whether mechanical or through reactions with the $CaCl_2$ electrolyte, would also be useful. This could be done through chemistry and phase analysis of the residual salt to determine if Fe is present as Fe_2O_3 or some other species.

Direct electrolytic reduction of high Fe content SR

The Becher process, covered in Section 2.2.1, removes Fe from ilmenite ore to produce SR. Therefore, it is counter-intuitive to later add Fe_2O_3 to enhance the Fe content. Instead, partial Fe removal from ilmenite could achieve similar results, whilst also likely solving the Fe retention issue as it will be contained within the SR particles. Direct reduction of higher Fe content SR powders would also make the overall production route more efficient.

Initial studies on the reduction of several high Fe content SR powders using the FFC-Cambridge process were done prior to the work presented in this thesis. The reduced powders were very similar to those presented in Figure 5.7 although homogeneous alloys were not obtained as FAST optimisation had not yet been done. Due to limited amounts of material and compositions, it was decided that the Fe content would instead be enhanced through controlled additions of Fe_2O_3, leading to the work in Chapter 5. It would be of interest to revisit this work in the future, especially to confirm whether Fe contents of the resulting alloys would be more consistent than those derived from SR + Fe_2O_3 mixtures.

Repeating blended elemental work using an alternative, lower O content CP Ti powder

An alternative CP Ti powder could be used to repeat some of the work in Chapter 6, in order to determine the cause of low ductility in the FAST consolidated material and Ti-Fe alloys. It would ideal to firstly have the O content of the, CP Ti (Alfa Aesar) powder and consolidated material measured as this could explain the brittleness of the alloys. Another powder with a significantly lower O content, preferably grade 1 (max 0.18% O), could then be used. The amount of α phase observed in the Ti-Fe alloys during microstructural analysis should be lower, as there will be less stabilising effect from O. Repetition of the tensile testing should also give greater elongation in the CP Ti, which should translate into the Ti-Fe alloys, although to what extent would be interesting.

Investigating use of the FFC-Cambridge process and blended elemental approach for other Ti alloys

The focus of this thesis has been on the Ti-Fe system, aside from small amounts of other remnant alloying elements from SR being present in the alloys in Chapter 5. The reasons for choosing this system have been explained earlier, although there are other β eutectoid stabilisers which could also be considered, including Mn, Cr, Co, Ni, Cu and Si. According to Metalysis, metal oxides of all these elements can be reduced using the FFC-Cambridge process, though, in the literature, only NiO has been co-reduced of with TiO_2 [77]. These elements are all more expensive additions than Fe, and are weaker β stabilisers, so there is less motivation to use them.

The other β eutectoid stabilisers are also fast diffusers in Ti, and could also be considered for solid-state alloying with Ti via FAST [155]. For example, this has been explored with the Ti-Cr and Ti-Ni systems [205], [206]. Given the higher cost of metal powders, this is unlikely to be economical when scaled-up, especially compared to Fe, unless otherwise surplus powders are readily available.

Non-binary systems could also be considered. Most alloys contain more than one alloying element, and so there are endless possibilities for alloy development using these technologies. This extends beyond conventional alloy compositions too, due to the benefits of solid-state processing in avoiding melt related defects. For example, Ti-Mo-Zr-Cr alloys have been produced by blended elemental powder metallurgy, for biomedical applications [207].

Investigating the effect of further thermomechanical processing on as-sintered Ti-Fe alloys

Assuming that the O content of the Ti-Fe alloys can be reduced in the future, further processing of them would be the obvious next step in assessing their suitability and applications alongside conventional alloys. Other researchers have found that subsequent thermomechanical processing on the as-sintered material can greatly improve mechanical properties, as discussed in Section 6.3.5, and so replicating this work would be of interest.

FAST-DB and FAST-*forge* (covered in Section 2.5.5) are exciting processing methods which could also be applied to these Ti-Fe alloys. This would allow for the production of near-net shape components, with the potential for using multiple alloys in different part of the component for site-specific properties. Additionally, larger alloy billets and preforms can be made by using larger FAST machines, enabling the production of various components.

Reference list and permissions

[1] M. Jackson, "Automotive Applications for Titanium," in *Encyclopedia of Automotive Engineering*, Chichester, UK: John Wiley & Sons, Ltd, Oct. 2014, pp. 1–15, ISBN: 978-1-118-35417-9 978-0-470-97402-5. DOI: `10.1002/9781118354179.auto156`.

[2] E. Kraft, *Summary of Emerging Titanium Cost Reduction Technologies*, Jan. 2004.

[3] G. Lütjering and J. C. Williams, *Titanium* (Engineering Materials and Processes), Second. Berlin: Springer-Verlag Berlin Heidelberg, 2007, ISBN: 978-3-642-09054-7.

[4] A. Pramanik, "Problems and solutions in machining of titanium alloys," *The International Journal of Advanced Manufacturing Technology*, vol. 70, no. 5-8, pp. 919–928, Feb. 2014, ISSN: 0268-3768, 1433-3015. DOI: `10.1007/s00170-013-5326-x`.

[5] G. Z. Chen, D. J. Fray, and T. W. Farthing, "Direct electrochemical reduction of titanium dioxide to titanium in molten calcium chloride," *Nature*, vol. 407, no. 6802, pp. 361–364, Sep. 2000, ISSN: 0028-0836, 1476-4687. DOI: `10.1038/35030069`.

[6] S. Oosthuizen, "In search of low cost titanium: The Fray Farthing Chen (FFC) Cambridge process," *Journal of the Southern African Institute of Mining and Metallurgy*, vol. 111, pp. 199–202, 2011, ISSN: 2225-6253.

[7] M. Bertolini, L. Shaw, L. England, K. Rao, J. Deane, and J. Collins, "The FFC Cambridge Process for Production of Low Cost Titanium and Titanium Powders," *Key Engineering Materials*, vol. 436, pp. 75–83, May 2010, ISSN: 1662-9795. DOI: `10.4028/www.scientific.net/KEM.436.75`.

[8] I. Mellor, L. Grainger, K. Rao, *et al.*, "Titanium powder production via the Metalysis process," in *Titanium Powder Metallurgy*, M. Qian and F. H. (Froes, Eds., Boston: Butterworth-Heinemann, 2015, pp. 51–67, ISBN: 978-0-12-800054-0. DOI: `10.1016/B978-0-12-800054-0.00004-6`.

[9] "Metalysis leads charge for change in titanium production," *Metal Powder Report*, vol. 64, no. 9, pp. 6–11, 2009, ISSN: 0026-0657. DOI: `10.1016/S0026-0657(09)70213-9`.

[10] T. Childerhouse and M. Jackson, "Near Net Shape Manufacture of Titanium Alloy Components from Powder and Wire: A Review of State-of-the-Art Process Routes," *Metals*, vol. 9, no. 6, p. 689, Jun. 2019, ISSN: 2075-4701. DOI: `10.3390/met9060689`.

[11]   I. Mellor and G. Doughty, "Novel and Emerging Routes for Titanium Powder Production - An Overview," *Key Engineering Materials*, vol. 704, pp. 271–281, Aug. 2016, ISSN: 1662-9795. DOI: 10.4028/www.scientific.net/KEM.704.271.

[12]   N. S. Weston, B. Thomas, and M. Jackson, "Processing metal powders via field assisted sintering technology (FAST): A critical review," *Materials Science and Technology*, vol. 35, no. 11, pp. 1306–1328, Jul. 2019, ISSN: 0267-0836, 1743-2847. DOI: 10.1080/02670836.2019.1620538.

[13]   P. Cavaliere, B. Sadeghi, and A. Shabani, "Spark Plasma Sintering: Process Fundamentals," in *Spark Plasma Sintering of Materials*, P. Cavaliere, Ed., Cham: Springer International Publishing, 2019, pp. 3–20, ISBN: 978-3-030-05326-0 978-3-030-05327-7. DOI: 10.1007/978-3-030-05327-7_1.

[14]   M. Tokita, "Progress of Spark Plasma Sintering (SPS) Method, Systems, Ceramics Applications and Industrialization," *Ceramics*, vol. 4, no. 2, pp. 160–198, Apr. 2021, ISSN: 2571-6131. DOI: 10.3390/ceramics4020014.

[15]   O. Guillon, J. Gonzalez-Julian, B. Dargatz, *et al.*, "Field-Assisted Sintering Technology/Spark Plasma Sintering: Mechanisms, Materials, and Technology Developments: FAST/SPS: Mechanisms, Materials, and Technology Developments," *Advanced Engineering Materials*, vol. 16, no. 7, pp. 830–849, Jul. 2014, ISSN: 14381656. DOI: 10.1002/adem.201300409.

[16]   T. S. Mackey, "Upgrading ilmenite into a high-grade synthetic rutile," *JOM*, vol. 46, no. 4, pp. 59–64, Apr. 1994, ISSN: 1047-4838, 1543-1851. DOI: 10.1007/BF03220676.

[17]   L. L. Benson, I. Mellor, and M. Jackson, "Direct reduction of synthetic rutile using the FFC process to produce low-cost novel titanium alloys," *Journal of Materials Science*, vol. 51, no. 9, pp. 4250–4261, May 2016, ISSN: 0022-2461, 1573-4803. DOI: 10.1007/s10853-015-9718-1.

[18]   Y. Kosaka, S. P. Fox, K. Faller, and S. H. Reichman, "Properties and Processing of TIMETAL LCB," *Journal of Materials Engineering and Performance*, vol. 14, no. 6, pp. 792–798, Dec. 2005, ISSN: 10599495, 00000000. DOI: 10.1361/105994905X75637.

[19]   A. Mitchell, A. Kawakami, and S. Cockcroft, "Beta Fleck and Segregation in Titanium Alloy Ingots," *High Temperature Materials and Processes*, vol. 25, no. 5-6, pp. 337–349, Jan. 2006, ISSN: 2191-0324, 0334-6455. DOI: 10.1515/HTMP.2006.25.5-6.337.

[20]   L. Bolzoni, "Low-cost Fe-bearing powder metallurgy Ti alloys," *Metal Powder Report*, vol. 74, no. 6, pp. 308–313, Nov. 2019, ISSN: 00260657. DOI: 10.1016/j.mprp.2019.01.007.

[21]   S. Raynova, F. Yang, and L. Bolzoni, "The effect of thermomechanical treatments on the properties of powder metallurgy Ti–5Fe alloy," *Materials Science and Engineering: A*, vol. 801, p. 140 389, Jan. 2021, ISSN: 09215093. DOI: 10.1016/j.msea.2020.140389.

[22] R. R. Boyer, "Titanium and Its Alloys: Metallurgy, Heat Treatment and Alloy Characteristics," in *Encyclopedia of Aerospace Engineering*, Chichester, UK: John Wiley & Sons, Ltd, Dec. 2010, ISBN: 978-0-470-75440-5 978-0-470-68665-2. DOI: 10.1002/9780470686652.eae198.

[23] M. Peters, J. Hemptenmacher, J. Kumpfert, and C. Leyens, "Structure and Properties of Titanium and Titanium Alloys," in *Titanium and Titanium Alloys*, Weinheim, FRG: Wiley-VCH Verlag GmbH & Co. KGaA, Jan. 2005, pp. 1–36, ISBN: 978-3-527-60211-7 978-3-527-30534-6. DOI: 10.1002/3527602119.ch1.

[24] R. Kolli and A. Devaraj, "A Review of Metastable Beta Titanium Alloys," *Metals*, vol. 8, no. 7, p. 506, Jun. 2018, ISSN: 2075-4701. DOI: 10.3390/met8070506.

[25] I. Weiss and S. Semiatin, "Thermomechanical processing of alpha titanium alloys—an overview," *Materials Science and Engineering: A*, vol. 263, no. 2, pp. 243–256, May 1999, ISSN: 09215093. DOI: 10.1016/S0921-5093(98)01155-1.

[26] J. Murray, *Phase Diagrams of Binary Titanium Alloys* (Monograph Series on Alloy Phase Diagrams). ASM International, 1987, ISBN: 978-0-87170-248-7. [Online]. Available: https://books.google.co.uk/books?id=pfJUAAAAMAAJ.

[27] F. H. Froes, Ed., *Titanium: Physical Metallurgy Processing and Applications*. Materials Park, Ohio: ASM International, 2015, ISBN: 978-1-62708-079-8.

[28] M. Donachie, *Titanium: A Technical Guide, 2nd Edition*. ASM International, 2000, ISBN: 978-1-61503-062-0. [Online]. Available: https://books.google.co.uk/books?id=HgzukknbNGAC.

[29] J. C. Williams, A. W. Sommer, and P. P. Tung, "The Influence of Oxygen Concentration on the Internal Stress and Dislocation Arrangements in alpha Titanium," *Metallurgical Transactions*, vol. 3, pp. 2979–2984, Nov. 1972.

[30] O. P. Solonina and N. M. Ulyakova, "Effect of carbon on the mechanical properties and structure of titanium alloys," *Metal Science and Heat Treatment*, vol. 16, no. 4, pp. 310–312, Apr. 1974, ISSN: 0026-0673, 1573-8973. DOI: 10.1007/BF00679223.

[31] E. Tal-Gutelmacher and D. Eliezer, "The hydrogen embrittlement of titanium-based alloys," *The Journal of The Minerals, Metals & Materials Society*, vol. 57, no. 9, pp. 46–49, Sep. 2005, ISSN: 1047-4838, 1543-1851. DOI: 10.1007/s11837-005-0115-0.

[32] *ASTM B381-21: Standard Specification for Titanium and Titanium Alloy Forgings*, 2013. DOI: 10.1520/B0381-21.

[33] O. Ivasishin, P. Markovsky, Y. Matviychuk, S. Semiatin, C. Ward, and S. Fox, "A comparative study of the mechanical properties of high-strength beta-titanium alloys," *Journal of Alloys and Compounds*, vol. 457, no. 1-2, pp. 296–309, Jun. 2008, ISSN: 09258388. DOI: 10.1016/j.jallcom.2007.03.070.

[34] W. D. Callister, *Materials Science and Engineering: An Introduction*, 7th ed. New York: John Wiley & Sons, 2007, ISBN: 978-0-471-73696-7.

[35] I. Weiss and S. Semiatin, "Thermomechanical processing of beta titanium alloys—an overview," *Materials Science and Engineering: A*, vol. 243, no. 1-2, pp. 46–65, Mar. 1998, ISSN: 09215093. DOI: `10.1016/S0921-5093(97)00783-1`.

[36] J. D. Cotton, R. R. Boyer, R. D. Briggs, *et al.*, "Phase Transformations in Ti-5Al-5Mo-5V-3Cr-0.5Fe," in *Proceedings of the 11th World Conference on Titanium*, Kyoto, Japan, Jun. 2007.

[37] Z. Balogh and G. Schmitz, "Diffusion in Metals and Alloys," in *Physical Metallurgy*, Fifth, Elsevier, 2014, pp. 388–559.

[38] A. A. Yaroshevsky, "Abundances of chemical elements in the Earth's crust," *Geochemistry International*, vol. 44, no. 1, pp. 48–55, Jan. 2006, ISSN: 0016-7029, 1556-1968. DOI: `10.1134/S001670290601006X`.

[39] G. M. Bedinger, "Titanium mineral concentrates," U.S. Geological Survey, Tech. Rep., 2017.

[40] E. R. Force, "Geology of Titanium-Mineral Deposits," in *Geology of Titanium-Mineral Deposits*, E. R. Force, Ed., vol. 259, Geological Society of America, Jan. 1991, p. 0, ISBN: 978-0-8137-2259-7. DOI: `10.1130/SPE259-p1`.

[41] J. Gambogi, "Titanium Mineral Concentrates," U.S. Geological Survey, Tech. Rep., Jan. 2021, p. 2.

[42] V. Hugo, "Iluka's Synthetic Rutile Production," Iluka Resources Limited, Tech. Rep., Feb. 2012. [Online]. Available: `https://www.iluka.com/docs/default-source/mineral-sands-briefing-papers/iluka%27s-synthetic-rutile-production-june-2012` (visited on 01/05/2018).

[43] R. G. Becher, R. G. Canning, B. A. Goodheart, and S. Uusna, "A new process for upgrading ilmenitic mineral sands," *Proc. Australas. Inst. Min. Metall.*, vol. 214, pp. 21–44, 1965.

[44] C. Noubactep, "Metallic iron for environmental remediation: Learning from the Becher process," *Journal of Hazardous Materials*, vol. 168, no. 2-3, pp. 1609–1612, Sep. 2009, ISSN: 03043894. DOI: `10.1016/j.jhazmat.2009.02.110`.

[45] "Mineral Sands Technical Information," Iluka Resources, Information Brochure, 2009, pp. 15–17. [Online]. Available: `http://www.iluka.com/docs/default-source/industry-company-information/iluka-mineral-sands-technical-information-brochure-2009.pdf` (visited on 09/27/2018).

[46] W. J. Bruckard, C. Calle, S. Fletcher, M. D. Horne, G. J. Sparrow, and A. J. Urban, "The application of anthraquinone redox catalysts for accelerating the aeration step in the becher process," *Hydrometallurgy*, vol. 73, no. 1-2, pp. 111–121, Apr. 2004, ISSN: 0304386X. DOI: `10.1016/j.hydromet.2003.09.003`.

[47] W. Kroll, "The Production of Ductile Titanium," *Transactions of The Electrochemical Society*, vol. 78, no. 1, p. 35, 1940, ISSN: 00964743. DOI: `10.1149/1.3071290`.

[48] K. Nakamura, T. Iida, N. Nakamura, and T. Araike, "Titanium Sponge Production Method by Kroll Process at OTC," *Materials Transactions*, vol. 58, no. 3, pp. 319–321, 2017, ISSN: 1345-9678, 1347-5320. DOI: `10.2320/matertrans.MK201634`.

[49] J. Gambogi and S. J. Gerdemann, "Titanium Metal: Extraction to Application," in *Review of Extraction, Processing, Properties & Applications of Reactive Metals*, B. Mishra, Ed., Hoboken, NJ, USA: John Wiley & Sons, Inc., Sep. 2013, pp. 175–210, ISBN: 978-1-118-78841-7 978-0-87339-423-9. DOI: `10.1002/9781118788417.ch5`.

[50] M. A. Hunter, "Metallic Titanium," *Journal of the American Chemical Society*, vol. 32, no. 3, pp. 330–336, 1910. DOI: `10.1021/ja01921a006`. eprint: `https://doi.org/10.1021/ja01921a006`.

[51] H. B. Bomberger and F. H. Froes, "The Melting of Titanium," *The Journal of The Minerals, Metals & Materials Society*, vol. 36, no. 12, pp. 39–47, Dec. 1984, ISSN: 0148-6608, 1543-1851. DOI: `10.1007/BF03339212`.

[52] J. Brenk, S. Hassan-Pour, P. Spiess, and B. Friedrich, "Examination of an alternative method for the pyrometallurgical production of copper-chromium alloys," *IOP Conference Series: Materials Science and Engineering*, vol. 143, p. 012 016, Jul. 2016, ISSN: 1757-8981, 1757-899X. DOI: `10.1088/1757-899X/143/1/012016`.

[53] M. Peters and C. Leyens, "Fabrication of titanium alloys," in *Titanium and Titanium Alloys*, John Wiley & Sons, Ltd, 2003, ch. 8, pp. 245–261, ISBN: 978-3-527-60211-7. DOI: `10.1002/3527602119.ch8`. eprint: `https://onlinelibrary.wiley.com/doi/pdf/10.1002/3527602119.ch8`.

[54] B. Denkena and S. Jacob, "Approach for Increasing the Resource Efficiency for the Production Process of Titanium Structural Components," *Procedia CIRP*, vol. 35, pp. 45–49, 2015, ISSN: 22128271. DOI: `10.1016/j.procir.2015.08.054`.

[55] G. Z. Chen and D. J. Fray, "Invention and fundamentals of the FFC Cambridge Process," in *Extractive Metallurgy of Titanium*, Elsevier, 2020, pp. 227–286, ISBN: 978-0-12-817200-1. DOI: `10.1016/B978-0-12-817200-1.00011-9`.

[56] G. Z. Chen, E. Gordo, and D. J. Fray, "Direct electrolytic preparation of chromium powder," *Metallurgical and Materials Transactions B*, vol. 35, no. 2, pp. 223–233, Apr. 2004, ISSN: 1073-5615, 1543-1916. DOI: `10.1007/s11663-004-0024-6`.

[57] K. Mohandas and D. Fray, "Electrochemical Deoxidation of Solid Zirconium Dioxide in Molten Calcium Chloride," *Metallurgical and Materials Transactions B*, vol. 40, no. 5, pp. 685–699, Oct. 2009, ISSN: 1073-5615, 1543-1916. DOI: `10.1007/s11663-009-9263-x`.

[58]   G. Li, D. Wang, and Z. Chen, "Direct Reduction of Solid Fe2O3 in Molten CaCl2 by Potentially Green Process," *J. Mater. Sci. Technol.*, vol. 25, no. 06, pp. 767–771, 2009.

[59]   T. Matsuzaki, S. Natsui, T. Kikuchi, and R. O. Suzuki, "Electrolytic reduction of V3S4 in molten CaCl2," *Materials Transactions*, vol. 58, no. 3, pp. 371–376, 2017, ISSN: 1345-9678, 1347-5320. DOI: 10.2320/matertrans.M2016305.

[60]   G. Li, D. Wang, X. Jin, and G. Chen, "Electrolysis of solid MoS2 in molten CaCl2 for Mo extraction without CO2 emission," *Electrochemistry Communications*, vol. 9, no. 8, pp. 1951–1957, Aug. 2007, ISSN: 13882481. DOI: 10.1016/j.elecom.2007.05.007.

[61]   B. Claux, J. Serp, and J. Fouletier, "Electrochemical reduction of cerium oxide into metal," *Electrochimica Acta*, vol. 56, no. 7, pp. 2771–2780, Feb. 2011, ISSN: 00134686. DOI: 10.1016/j.electacta.2010.12.040.

[62]   R. Barnett, K. T. Kilby, and D. J. Fray, "Reduction of Tantalum Pentoxide Using Graphite and Tin-Oxide-Based Anodes via the FFC-Cambridge Process," *Metallurgical and Materials Transactions B*, vol. 40, no. 2, pp. 150–157, Apr. 2009, ISSN: 1073-5615, 1543-1916. DOI: 10.1007/s11663-008-9219-6.

[63]   A. M. Martinez, K. S. Osen, H. Gudbrandsen, C. Sommerseth, Z. Wang, and O. Darell, "Direct Method for Producing Scandium Metal and Scandium-Aluminium Intermetallic Compounds from the Oxides," *Light Metals 2018*, pp. 1559–1564, 2018. DOI: 10.1007/978-3-319-72284-9_203.

[64]   J. Sure, D. S. M. Vishnu, and C. Schwandt, "Direct electrochemical synthesis of high-entropy alloys from metal oxides," *Applied Materials Today*, vol. 9, pp. 111–121, Dec. 2017, ISSN: 23529407. DOI: 10.1016/j.apmt.2017.05.009.

[65]   C. Schwandt, J. A. Hamilton, D. J. Fray, and I. A. Crawford, "The production of oxygen and metal from lunar regolith," *Planetary and Space Science*, vol. 74, no. 1, pp. 49–56, Dec. 2012, ISSN: 00320633. DOI: 10.1016/j.pss.2012.06.011.

[66]   B. A. Lomax, M. Conti, N. Khan, N. S. Bennett, A. Y. Ganin, and M. D. Symes, "Proving the viability of an electrochemical process for the simultaneous extraction of oxygen and production of metal alloys from lunar regolith," *Planetary and Space Science*, vol. 180, p. 104 748, Jan. 2020, ISSN: 00320633. DOI: 10.1016/j.pss.2019.104748.

[67]   K. T. Kilby, S. Jiao, and D. J. Fray, "Current efficiency studies for graphite and SnO2-based anodes for the electro-deoxidation of metal oxides," *Electrochimica Acta*, vol. 55, no. 23, pp. 7126–7133, Sep. 2010, ISSN: 00134686. DOI: 10.1016/j.electacta.2010.06.049.

[68]   K. Rao, J. Deane, L. Grainger, J. Clifford, M. Conti, and J. Collins, "Electrolytic production of powder," WIPO Patent WO/2013/050772, Apr. 2013.

[69]   D. Hu, W. Xiao, and G. Z. Chen, "Near-Net-Shape Production of Hollow Titanium Alloy Components via Electrochemical Reduction of Metal Oxide Precursors in Molten Salts,"

Metallurgical and Materials Transactions B, vol. 44, no. 2, pp. 272–282, Apr. 2013, ISSN: 1073-5615, 1543-1916. DOI: 10.1007/s11663-013-9800-5.

[70] A. Dolganov, M. T. Bishop, M. Tomatis, G. Z. Chen, and D. Hu, "Environmental assessment of the near-net-shape electrochemical metallisation process and the Kroll-electron beam melting process for titanium manufacture," *Green Chemistry*, vol. 22, no. 6, pp. 1952–1967, 2020, ISSN: 1463-9262, 1463-9270. DOI: 10.1039/C9GC04036F.

[71] D. Hu, A. Dolganov, M. Ma, B. Bhattacharya, M. T. Bishop, and G. Z. Chen, "Development of the Fray-Farthing-Chen Cambridge Process: Towards the Sustainable Production of Titanium and Its Alloys," *The Journal of The Minerals, Metals & Materials Society*, vol. 70, no. 2, pp. 129–137, Feb. 2018, ISSN: 1047-4838, 1543-1851. DOI: 10.1007/s11837-017-2664-4.

[72] C. Schwandt and D. Fray, "Determination of the kinetic pathway in the electrochemical reduction of titanium dioxide in molten calcium chloride," *Electrochimica Acta*, vol. 51, no. 1, pp. 66–76, Oct. 2005, ISSN: 00134686. DOI: 10.1016/j.electacta.2005.03.048.

[73] F. Walsh and R. Wills, "The continuing development of Magnéli phase titanium sub-oxides and Ebonex® electrodes," *Electrochimica Acta*, vol. 55, no. 22, pp. 6342–6351, Sep. 2010, ISSN: 00134686. DOI: 10.1016/j.electacta.2010.05.011.

[74] C. Schwandt, D. Alexander, and D. Fray, "The electro-deoxidation of porous titanium dioxide precursors in molten calcium chloride under cathodic potential control," *Electrochimica Acta*, vol. 54, no. 14, pp. 3819–3829, May 2009, ISSN: 00134686. DOI: 10.1016/j.electacta.2009.02.006.

[75] C. Schwandt, "On the nature of the current and the absence of an IR-drop in an FFC-Cambridge-type electro-deoxidation cell," *Electrochimica Acta*, vol. 280, pp. 114–120, Aug. 2018, ISSN: 00134686. DOI: 10.1016/j.electacta.2018.05.083.

[76] D. Alexander, C. Schwandt, and D. Fray, "The electro-deoxidation of dense titanium dioxide precursors in molten calcium chloride giving a new reaction pathway," *Electrochimica Acta*, vol. 56, no. 9, pp. 3286–3295, Mar. 2011, ISSN: 00134686. DOI: 10.1016/j.electacta.2011.01.027.

[77] B. K. Jackson, D. Inman, M. Jackson, D. Dye, and R. J. Dashwood, "NiTi Production via the FFC Cambridge Process: Refinement of Process Parameters," *Journal of The Electrochemical Society*, vol. 157, no. 3, E36–E43, 2010, ISSN: 00134651. DOI: 10.1149/1.3289996.

[78] R. Bhagat, M. Jackson, D. Inman, and R. Dashwood, "The Production of Ti–Mo Alloys from Mixed Oxide Precursors via the FFC Cambridge Process," *Journal of The Electrochemical Society*, vol. 155, no. 6, E63–E69, Jun. 2008, ISSN: 0013-4651, 1945-7111. DOI: 10.1149/1.2904454.

[79] G. Li, X. Jin, D. Wang, and G. Z. Chen, "Affordable electrolytic ferrotitanium alloys with marine engineering potentials," *Journal of Alloys and Compounds*, vol. 482, no. 1-2, pp. 320–327, Aug. 2009, ISSN: 09258388. DOI: 10.1016/j.jallcom.2009.04.007.

[80] R. Bhagat, M. Jackson, D. Inman, and R. Dashwood, "Production of Ti–W Alloys from Mixed Oxide Precursors via the FFC Cambridge Process," *Journal of The Electrochemical Society*, vol. 156, no. 1, E1, 2009, ISSN: 00134651. DOI: 10.1149/1.2999340.

[81] J. Sure, D. S. M. Vishnu, R. V. Kumar, and C. Schwandt, "Molten Salt Electrochemical Synthesis, Heat Treatment and Microhardness of Ti–5Ta–2Nb Alloy," *Materials Transactions*, vol. 60, no. 3, pp. 391–399, Mar. 2019, ISSN: 1345-9678, 1347-5320. DOI: 10.2320/matertrans.MA201808.

[82] M. Ma, D. Wang, W. Wang, X. Hu, X. Jin, and G. Z. Chen, "Extraction of titanium from different titania precursors by the FFC Cambridge process," *Journal of Alloys and Compounds*, vol. 420, no. 1-2, pp. 37–45, Aug. 2006, ISSN: 09258388. DOI: 10.1016/j.jallcom.2005.10.048.

[83] H. Sun, J. Wang, X. Dong, and Q. Xue, "A literature review of titanium slag metallurgical processes," *Metalurgia International*, p. 10, 2010.

[84] Z. Zhou, Y. Hua, C. Xu, *et al.*, "Preparation of Ferrotitanium from Ilmenite by Electrolysis-Assisted Calciothermic Reduction in CaCl2-NaCl Molten Salt," *The Journal of The Minerals, Metals & Materials Society*, vol. 68, no. 2, pp. 532–539, Feb. 2016, ISSN: 1047-4838, 1543-1851. DOI: 10.1007/s11837-015-1723-y.

[85] L. L. Benson, L. A. Benson Marshall, N. S. Weston, I. Mellor, and M. Jackson, "On a Testing Methodology for the Mechanical Property Assessment of a New Low-Cost Titanium Alloy Derived from Synthetic Rutile," *Metallurgical and Materials Transactions A*, vol. 48, no. 11, pp. 5228–5232, Nov. 2017, ISSN: 1073-5623, 1543-1940. DOI: 10.1007/s11661-017-4333-1.

[86] L. L. Benson, "Production and development of titanium alloys derived directly from synthetic rutile using electrochemical deoxidation," Ph.D. dissertation, The University of Sheffield, Aug. 2017.

[87] C. Doblin, A. Chryss, and A. Monch, "Titanium Powder from the TiRO™ Process," *Key Engineering Materials*, vol. 520, pp. 95–100, Aug. 2012, ISSN: 1662-9795. DOI: 10.4028/www.scientific.net/KEM.520.95.

[88] C. Doblin, D. Freeman, and M. Richards, "The TiRO™ Process for the Continuous Direct Production of Titanium Powder," *Key Engineering Materials*, vol. 551, pp. 37–43, May 2013, ISSN: 1662-9795. DOI: 10.4028/www.scientific.net/KEM.551.37.

[89] *Coogee Titanium*. [Online]. Available: http://www.coogeetitanium.com.au/ (visited on 10/14/2020).

[90] G. Crowley, "How to extract low-cost titanium," *Advanced Materials & Processes*, vol. 161, pp. 25–27, 2003.

[91] W. H. Peter, C. A. Blue, J. O. Kiggans, and J. D. K. Rivard, *Powder metallurgy and solid state processing of Armstrong titanium and titanium alloy powders*, Presentation, Orlando, FL, Oct. 2007.

[92] D. MacDonald, R. Fernández, F. Delloro, and B. Jodoin, "Cold Spraying of Armstrong Process Titanium Powder for Additive Manufacturing," *Journal of Thermal Spray Technology*, vol. 26, no. 4, pp. 598–609, Apr. 2017, ISSN: 1059-9630, 1544-1016. DOI: 10.1007/s11666-016-0489-2.

[93] V. Duz, V. S. Moxson, A. G. Klevtsov, and V. Sukhoplyuyev, *ADMA Process for Hydrogenated Titanium Powder Production*, Las Vegas, Nevada, USA, 2013.

[94] V. Duz, M. Matviychuk, A. Klevtsov, and V. Moxson, "Industrial application of titanium hydride powder," *Metal Powder Report*, vol. 72, no. 1, pp. 30–38, Jan. 2017, ISSN: 00260657. DOI: 10.1016/j.mprp.2016.02.051.

[95] Y. Zhang, Z. Z. Fang, P. Sun, S. Zheng, Y. Xia, and M. Free, "A Perspective on Thermochemical and Electrochemical Processes for Titanium Metal Production," *JOM*, vol. 69, no. 10, pp. 1861–1868, Oct. 2017, ISSN: 1047-4838, 1543-1851. DOI: 10.1007/s11837-017-2481-9.

[96] J. K. Ephraim and R. Patel, "Solid-Solid Phase Transformation During the Reduction of Titanium Dioxide (Anatase) to Produce High-Grade Titanium Powder," *Advanced Engineering Materials*, vol. 17, no. 9, pp. 1276–1281, Sep. 2015, ISSN: 14381656. DOI: 10.1002/adem.201400535.

[97] T. H. Okabe, T. Oda, and Y. Mitsuda, "Titanium powder production by preform reduction process (PRP)," *Journal of Alloys and Compounds*, vol. 364, no. 1-2, pp. 156–163, Feb. 2004, ISSN: 09258388. DOI: 10.1016/S0925-8388(03)00610-8.

[98] V. Moxson, O. N. Senkov, and F. H. Froes, "Innovations in titanium powder processing," *The Journal of The Minerals, Metals & Materials Society*, vol. 52, no. 5, pp. 24–26, May 2000, ISSN: 1543-1851. DOI: 10.1007/s11837-000-0027-y.

[99] Y. Zhang, Z. Z. Fang, P. Sun, *et al.*, "Thermodynamic Destabilization of Ti-O Solid Solution by H2 and Deoxygenation of Ti Using Mg," *Journal of the American Chemical Society*, p. 4, 2016.

[100] H. Lefler, Z. Z. Fang, Y. Zhang, P. Sun, and Y. Xia, "Mechanisms of Hydrogen-Assisted Magnesiothermic Reduction of TiO2," *Metallurgical and Materials Transactions B*, vol. 49, no. 6, pp. 2998–3006, Dec. 2018, ISSN: 1073-5615, 1543-1916. DOI: 10.1007/s11663-018-1399-0.

[101] R. O. Suzuki, K. Ono, and K. Teranuma, "Calciothermic reduction of titanium oxide and in-situ electrolysis in molten CaCl2," *Metallurgical and Materials Transactions B*, vol. 34, no. 3, pp. 287–295, Jun. 2003, ISSN: 1073-5615, 1543-1916. DOI: 10.1007/s11663-003-0074-1.

[102] R. O. Suzuki, "Calciothermic reduction of TiO2 and in situ electrolysis of CaO in the molten CaCl2," *Journal of Physics and Chemistry of Solids*, vol. 66, no. 2-4, pp. 461–465, Feb. 2005, ISSN: 00223697. DOI: 10.1016/j.jpcs.2004.06.041.

[103] S. Jiao and H. Zhu, "Novel metallurgical process for titanium production," *Journal of Materials Research*, vol. 21, no. 09, pp. 2172–2175, Sep. 2006, ISSN: 0884-2914, 2044-5326. DOI: 10.1557/jmr.2006.0268.

[104] R. G. Reddy, P. S. Shinde, and A. Liu, "Review-The Emerging Technologies for Producing Low-Cost Titanium," *Journal of The Electrochemical Society*, vol. 168, no. 4, p. 042 502, Apr. 2021, ISSN: 0013-4651, 1945-7111. DOI: 10.1149/1945-7111/abe50d.

[105] D. Jewell, S. Jiao, M. Kurtanjek, and D. J. Fray, "Titanium metal production via oxycarbide electorefining," in *28th Annual ITA Conference Titanium 2012*, Atlanta, GA: International Titanium Association, Oct. 2012, p. 42.

[106] J. C. Withers, F. Cardarelli, J. Laughlin, and R. O. Loutfy, "Recent improvements for electrowinning titanium metal from composite anodes," in *International Round Table on Titanium Production in Molten Salts*, Cologne, Germany, Mar. 2008, p. 5.

[107] M. Qian and F. H. (Froes, "Preface," in *Titanium Powder Metallurgy*, M. Qian and F. H. (Froes, Eds., Boston: Butterworth-Heinemann, 2015, p. xix, ISBN: 978-0-12-800054-0. DOI: 10.1016/B978-0-12-800054-0.00036-8.

[108] C. Yolton and F. H. Froes, "2 - Conventional titanium powder production," in *Titanium Powder Metallurgy*, M. Qian and F. H. (Froes, Eds., Boston: Butterworth-Heinemann, 2015, pp. 21–32, ISBN: 978-0-12-800054-0. DOI: 10.1016/B978-0-12-800054-0.00002-2.

[109] J. J. Dunkley, "Metal Powder Atomisation Methods for Modern Manufacturing," *Johnson Matthey Technology Review*, vol. 63, no. 3, pp. 226–232, Jul. 2019, ISSN: 2056-5135. DOI: 10.1595/205651319X15583434137356.

[110] "Comparison of plasma and electrode inert gas atomized powder," Carpenter Additive, White Paper, 2020. [Online]. Available: https://www.carpenteradditive.com/eiga-titanium-powder-whitepaper (visited on 11/23/2021).

[111] P. Moghimian, T. Poirié, M. Habibnejad-Korayem, *et al.*, "Metal powders in additive manufacturing: A review on reusability and recyclability of common titanium, nickel and aluminum alloys," *Additive Manufacturing*, vol. 43, p. 102 017, Jul. 2021, ISSN: 22148604. DOI: 10.1016/j.addma.2021.102017.

[112] D. P. Barbis, R. M. Gasior, G. P. Walker, J. A. Capone, and T. S. Schaeffer, "Titanium powders from the hydride–dehydride process," in *Titanium Powder Metallurgy*, Elsevier, 2015, pp. 101–116, ISBN: 978-0-12-800054-0. DOI: 10.1016/B978-0-12-800054-0.00007-1.

[113] Z. Z. Fang, J. D. Paramore, P. Sun, *et al.*, "Powder metallurgy of titanium – past, present, and future," *International Materials Reviews*, pp. 1–53, Aug. 2017, ISSN: 0950-6608, 1743-2804. DOI: 10.1080/09506608.2017.1366003.

[114] B. Dutta and F. (Froes, "The Additive Manufacturing (AM) of titanium alloys," *Metal Powder Report*, vol. 72, no. 2, pp. 96–106, Mar. 2017, ISSN: 00260657. DOI: 10.1016/j.mprp.2016.12.062.

[115] B. Dutta, "The additive manufacturing (AM) of titanium alloys," in *Titanium Powder Metallurgy*, Boston: Butterworth-Heinemann, 2015, pp. 447–468, ISBN: 978-0-12-800054-0.

[116] T. Hussain, "Cold Spraying of Titanium: A Review of Bonding Mechanisms, Microstructure and Properties," *Key Engineering Materials*, vol. 533, pp. 53–90, Dec. 2012, ISSN: 1662-9795. DOI: 10.4028/www.scientific.net/KEM.533.53.

[117] P. Vo, D. Goldbaum, W. Wong, *et al.*, "Cold-spray processing of titanium and titanium alloys," in *Titanium Powder Metallurgy*, Elsevier, 2015, pp. 405–423, ISBN: 978-0-12-800054-0. DOI: 10.1016/B978-0-12-800054-0.00022-8.

[118] I. M. Robertson and G. B. Schaffer, "Review of densification of titanium based powder systems in press and sinter processing," *Powder Metallurgy*, vol. 53, no. 2, pp. 146–162, Jun. 2010, ISSN: 0032-5899, 1743-2901. DOI: 10.1179/174329009X434293.

[119] "Introduction to Hot Isostatic Pressing Technology," European Powder Metallurgy Association, Tech. Rep., 2018. [Online]. Available: http://www.tandfonline.com/doi/full/10.1179/pom.1994.37.1.27 (visited on 01/22/2022).

[120] R. M. German, "Sintering With External Pressure," in *Sintering: From Empirical Observations to Scientific Principles*, Elsevier, 2014, pp. 305–354, ISBN: 978-0-12-401682-8. DOI: 10.1016/B978-0-12-401682-8.00010-0.

[121] H. U. Kessel, J. Hennicke, J. Schmidt, *et al.*, ""FAST" field assisted sintering technology- a new process for the production of metallic and ceramic sintering materials," FCT Systeme GmbH, Tech. Rep., p. 37. [Online]. Available: https://www.fct-systeme.de/en/content/19/~nm.67/Download.html.

[122] "Introduction to Metal Injection Moulding," European Powder Metallurgy Association, Tech. Rep., 2018. [Online]. Available: http://www.tandfonline.com/doi/full/10.1179/pom.1994.37.1.27 (visited on 01/22/2022).

[123] V. Samarov, D. Seliverstov, and F. H. (Sam) Froes, "Fabrication of near-net-shape cost-effective titanium components by use of prealloyed powders and hot isostatic pressing,"

in *Titanium Powder Metallurgy*, Elsevier, 2015, pp. 313–336, ISBN: 978-0-12-800054-0. DOI: 10.1016/B978-0-12-800054-0.00018-6.

[124] W. Matizamhuka, "Spark plasma sintering (SPS) - an advanced sintering technique for structural nanocomposite materials," *Journal of the Southern African Institute of Mining and Metallurgy*, vol. 116, no. 7, pp. 1171–1180, 2016, ISSN: 24119717. DOI: 10.17159/2411-9717/2016/v116n12a12.

[125] C. Manière, U. Kus, G. Chevallier, *et al.*, "How to overcome the main challenges of SPS technology: Reproducibility, multi-samples and elaboration of complex shapes," in *Spark Plasma Sintering*, Elsevier, 2019, pp. 77–108, ISBN: 978-0-12-817744-0. DOI: 10.1016/B978-0-12-817744-0.00003-9.

[126] M. Zadra, F. Casari, L. Girardini, and A. Molinari, "Microstructure and mechanical properties of cp-titanium produced by spark plasma sintering," *Powder Metallurgy*, vol. 51, no. 1, pp. 59–65, Mar. 2008, ISSN: 0032-5899, 1743-2901. DOI: 10.1179/174329008X277000.

[127] O. E. Falodun, B. A. Obadele, S. R. Oke, *et al.*, "Influence of spark plasma sintering on microstructure and wear behaviour of Ti-6Al-4V reinforced with nanosized TiN," *Transactions of Nonferrous Metals Society of China*, vol. 28, no. 1, pp. 47–54, Jan. 2018, ISSN: 10036326. DOI: 10.1016/S1003-6326(18)64637-0.

[128] J. Bustillos, C. Zhang, A. Loganathan, B. Boesl, and A. Agarwal, "Ultralow Temperature Densification of a Titanium Alloy by Spark Plasma Sintering," *Advanced Engineering Materials*, vol. 22, no. 6, p. 2 000 076, Jun. 2020, ISSN: 1438-1656, 1527-2648. DOI: 10.1002/adem.202000076.

[129] N. S. Weston, F. Derguti, A. Tudball, and M. Jackson, "Spark plasma sintering of commercial and development titanium alloy powders," *Journal of Materials Science*, vol. 50, no. 14, pp. 4860–4878, Jul. 2015, ISSN: 0022-2461, 1573-4803. DOI: 10.1007/s10853-015-9029-6.

[130] N. Weston and M. Jackson, "FAST-forge - A new cost-effective hybrid processing route for consolidating titanium powder into near net shape forged components," *Journal of Materials Processing Technology*, vol. 243, pp. 335–346, May 2017, ISSN: 09240136. DOI: 10.1016/j.jmatprotec.2016.12.013.

[131] E. Calvert, B. Wynne, N. Weston, A. Tudball, and M. Jackson, "Thermomechanical processing of a high strength metastable beta titanium alloy powder, consolidated using the low-cost FAST- forge process," *Journal of Materials Processing Technology*, vol. 254, pp. 158–170, Apr. 2018, ISSN: 09240136. DOI: 10.1016/j.jmatprotec.2017.11.035.

[132] N. S. Weston and M. Jackson, "FAST-forge of Titanium Alloy Swarf: A Solid-State Closed-Loop Recycling Approach for Aerospace Machining Waste," *Metals*, vol. 10, no. 2, p. 296, Feb. 2020, ISSN: 2075-4701. DOI: 10.3390/met10020296.

[133] J. J. Pope, E. L. Calvert, N. S. Weston, and M. Jackson, "FAST-DB: A novel solid-state approach for diffusion bonding dissimilar titanium alloy powders for next generation critical components," *Journal of Materials Processing Technology*, vol. 269, pp. 200–207, Jul. 2019, ISSN: 09240136. DOI: 10.1016/j.jmatprotec.2019.02.011.

[134] O. Levano Blanch, D. Lunt, G. J. Baxter, and M. Jackson, "Deformation Behaviour of a FAST Diffusion Bond Processed from Dissimilar Titanium Alloy Powders," *Metallurgical and Materials Transactions A*, vol. 52, no. 7, pp. 3064–3082, Jul. 2021, ISSN: 1073-5623, 1543-1940. DOI: 10.1007/s11661-021-06301-w.

[135] J. Pope and M. Jackson, "FAST-forge of Diffusion Bonded Dissimilar Titanium Alloys: A Novel Hybrid Processing Approach for Next Generation Near-Net Shape Components," *Metals*, vol. 9, no. 6, p. 654, Jun. 2019, ISSN: 2075-4701. DOI: 10.3390/met9060654.

[136] B. M. Thomas, F. Derguti, and M. Jackson, "Continuous extrusion of a commercially pure titanium powder via the Conform process," *Materials Science and Technology*, vol. 33, no. 7, pp. 899–903, May 2017, ISSN: 0267-0836, 1743-2847. DOI: 10.1080/02670836.2016.1245256.

[137] S. A. Smythe, B. M. Thomas, and M. Jackson, "Recycling of Titanium Alloy Powders and Swarf through Continuous Extrusion (ConformTM) into Affordable Wire for Additive Manufacturing," *Metals*, vol. 10, no. 6, p. 843, Jun. 2020, ISSN: 2075-4701. DOI: 10.3390/met10060843.

[138] J.-O. Andersson, T. Helander, L. Höglund, P. Shi, and B. Sundman, "Thermo-Calc & DICTRA, computational tools for materials science," *Calphad*, vol. 26, no. 2, pp. 273–312, Jun. 2002, ISSN: 03645916. DOI: 10.1016/S0364-5916(02)00037-8.

[139] W. Zeng and Y. Zhou, "Effect of beta flecks on mechanical properties of Ti–10V–2Fe–3Al alloy," *Materials Science and Engineering: A*, vol. 260, no. 1-2, pp. 203–211, Feb. 1999, ISSN: 09215093. DOI: 10.1016/S0921-5093(98)00954-X.

[140] R. R. Boyer and G. W. Kuhlman, "Processing properties relationships of Ti-10V-2Fe-3Al," *Metallurgical Transactions A*, vol. 18, no. 12, pp. 2095–2103, Dec. 1987, ISSN: 0360-2133, 1543-1940. DOI: 10.1007/BF02647081.

[141] M. Jackson, N. Jones, D. Dye, and R. Dashwood, "Effect of initial microstructure on plastic flow behaviour during isothermal forging of Ti–10V–2Fe–3Al," *Materials Science and Engineering: A*, vol. 501, no. 1-2, pp. 248–254, Feb. 2009, ISSN: 09215093. DOI: 10.1016/j.msea.2008.09.071.

[142] Y. Kosaka and S. P. Fox, "Properties and Production Experiences of TIMETAL®LCB for Automotive Spring Applications," in *SAE 2003 World Congress & Exhibition*, Mar. 2003, pp. 2003-01–1181. DOI: 10.4271/2003-01-1181.

[143] W. Wei, Y. Liu, K. Zhou, and B. Huang, "Effect of Fe addition on sintering behaviour of titanium powder," *Powder Metallurgy*, vol. 46, no. 3, pp. 246–250, Oct. 2003, ISSN: 0032-5899, 1743-2901. DOI: 10.1179/003258903225005295.

[144] R. Siqueira, H. Sandim, A. Hayama, and V. Henriques, "Microstructural evolution during sintering of the blended elemental Ti–5Al–2.5Fe alloy," *Journal of Alloys and Compounds*, vol. 476, no. 1-2, pp. 130–137, May 2009, ISSN: 09258388. DOI: 10.1016/j.jallcom.2008.09.004.

[145] P. Esteban, E. Ruiz-Navas, and E. Gordo, "Influence of Fe content and particle size the on the processing and mechanical properties of low-cost Ti–xFe alloys," *Materials Science and Engineering: A*, vol. 527, no. 21-22, pp. 5664–5669, Aug. 2010, ISSN: 09215093. DOI: 10.1016/j.msea.2010.05.026.

[146] P. G. Esteban, L. Bolzoni, E. M. Ruiz-Navas, and E. Gordo, "PM processing and characterisation of Ti–7Fe low cost titanium alloys," *Powder Metallurgy*, vol. 54, no. 3, pp. 242–252, Jul. 2011, ISSN: 0032-5899, 1743-2901. DOI: 10.1179/174329009X457063.

[147] L. Bolzoni, E. Herraiz, E. Ruiz-Navas, and E. Gordo, "Study of the properties of low-cost powder metallurgy titanium alloys by 430 stainless steel addition," *Materials & Design*, vol. 60, pp. 628–636, Aug. 2014, ISSN: 02613069. DOI: 10.1016/j.matdes.2014.04.019.

[148] L. Bolzoni, E. Ruiz-Navas, and E. Gordo, "Understanding the properties of low-cost iron-containing powder metallurgy titanium alloys," *Materials & Design*, vol. 110, pp. 317–323, Nov. 2016, ISSN: 02641275. DOI: 10.1016/j.matdes.2016.08.010.

[149] L. Bolzoni, E. Ruiz-Navas, and E. Gordo, "Quantifying the properties of low-cost powder metallurgy titanium alloys," *Materials Science and Engineering: A*, vol. 687, pp. 47–53, Feb. 2017, ISSN: 09215093. DOI: 10.1016/j.msea.2017.01.049.

[150] S. Raynova, M. Imam, F. Yang, and L. Bolzoni, "Hybrid microwave sintering of blended elemental Ti alloys," *Journal of Manufacturing Processes*, vol. 39, pp. 52–57, Mar. 2019, ISSN: 15266125. DOI: 10.1016/j.jmapro.2019.02.002.

[151] S. Raynova, F. Yang, and L. Bolzoni, "Mechanical behaviour of induction sintered blended elemental powder metallurgy Ti alloys," *Materials Science and Engineering: A*, vol. 799, p. 140 157, Jan. 2021, ISSN: 09215093. DOI: 10.1016/j.msea.2020.140157.

[152] C. Romero, S. Raynova, F. Yang, and L. Bolzoni, "Ultrafine microstructures in eutectoid element bearing low-cost Ti-Fe alloys enabled by slow bainite formation," *Journal of Alloys and Compounds*, vol. 769, pp. 226–232, Nov. 2018, ISSN: 09258388. DOI: 10.1016/j.jallcom.2018.07.347.

[153] L. Bolzoni, S. Raynova, and F. Yang, "Work hardening of microwave sintered blended elemental Ti alloys," *Journal of Alloys and Compounds*, vol. 838, p. 155 559, Oct. 2020, ISSN: 09258388. DOI: 10.1016/j.jallcom.2020.155559.

[154] C. Romero, F. Yang, S. Wei, and L. Bolzoni, "Thermomechanical Processing of Cost-Affordable Powder Metallurgy Ti-5Fe Alloys from the Blended Elemental Approach: Microstructure, Tensile Deformation Behavior, and Failure," *Metals*, vol. 10, no. 11, p. 1405, Oct. 2020, ISSN: 2075-4701. DOI: `10.3390/met10111405`.

[155] M. Koiwa, "Diffusion in Materials - History and Recent Developments," *Materials Transactions JIM*, vol. 39, no. 12, pp. 1169–1179, 1998.

[156] H. Nakajima, S. Ohshidat, K. Nonakat, Y. Yoshida, and F. E. Fujital, "Diffusion of Iron in beta Ti-Fe alloys," *Scripta Materialia*, vol. 34, no. 6, pp. 949–953, 1996.

[157] M. Ghosh, K. Bhanumurthy, G. Kale, J. Krishnan, and S. Chatterjee, "Diffusion bonding of titanium to 304 stainless steel," *Journal of Nuclear Materials*, vol. 322, no. 2-3, pp. 235–241, Nov. 2003, ISSN: 00223115. DOI: `10.1016/j.jnucmat.2003.07.004`.

[158] A. Miriyev, A. Stern, E. Tuval, S. Kalabukhov, Z. Hooper, and N. Frage, "Titanium to steel joining by spark plasma sintering (SPS) technology," *Journal of Materials Processing Technology*, vol. 213, no. 2, pp. 161–166, Feb. 2013, ISSN: 09240136. DOI: `10.1016/j.jmatprotec.2012.09.017`.

[159] A. M. Laptev, J. Hennicke, and R. Ihl, "Influence of CFRC Insulating Plates on Spark Plasma Sintering Process," *Metals*, vol. 11, no. 3, p. 393, Feb. 2021, ISSN: 2075-4701. DOI: `10.3390/met11030393`.

[160] S. Grazulis, D. Chateigner, R. T. Downs, *et al.*, "Crystallography Open Database - an open-access collection of crystal structures," *Journal of Applied Crystallography*, vol. 42, no. 4, pp. 726–729, 2009. [Online]. Available: `https://doi.org/10.1107/S0021889809016690`.

[161] W. H. Baur and A. A. Khan, "Rutile-type compounds. IV. SiO2, GeO2 and a comparison with other rutile-type structures," *Acta Crystallographica Section B*, vol. 27, no. 11, pp. 2133–2139, 1971. [Online]. Available: `https://doi.org/10.1107/S0567740871005466`.

[162] L. Pauling, "The crystal structure of pseudobrookite," *Zeitschrift für Kristallographie - Crystalline Materials*, vol. 73, no. 1-6, pp. 97–112, 1930. DOI: `10.1524/zkri.1930.73.1.97`.

[163] E. N. Maslen, V. A. Streltsov, N. R. Streltsova, and N. Ishizawa, "Synchrotron X-ray study of the electron density in [alpha]-Fe2O3," *Acta Crystallographica Section B*, vol. 50, no. 4, pp. 435–441, 1994. [Online]. Available: `https://doi.org/10.1107/S0108768194002284`.

[164] T. Novoselova, S. Malinov, W. Sha, and A. Zhecheva, "High-temperature synchrotron X-ray diffraction study of phases in a gamma TiAl alloy," *Materials Science and Engineering A, Structural Materials: Properties, Microstructure and Processing*, vol. 371, no. 1-2, pp. 103–112, Apr. 2004, ISSN: 0921-5093. [Online]. Available: `http://inis.iaea.org/search/search.aspx?orig_q=RN:38073492`.

[165] B. W. Levinger, "Lattice Parameter of Beta Titanium at Room Temperature," *JOM*, vol. 5, no. 2, pp. 195–195, Feb. 1953, ISSN: 1047-4838, 1543-1851. DOI: `10.1007/BF03397474`.

[166] R. Ray, B. C. Giessen, and N. J. Grant, "The constitution of metastable titanium-rich Ti-Fe alloys:An order-disorder transition," *Metallurgical and Materials Transactions B*, vol. 3, no. 3, pp. 627–629, Mar. 1972, ISSN: 1543-1916. DOI: 10.1007/BF02642743.

[167] P. J. Brown, J. Deportes, and B. Ouladdiaf, "Magnetic structure of the Laves phase compound TiFe2," *Journal of Physics: Condensed Matter*, vol. 4, no. 49, pp. 10 015–10 024, Dec. 1992, ISSN: 0953-8984, 1361-648X. DOI: 10.1088/0953-8984/4/49/028.

[168] K. Aigner, W. Lengauer, D. Rafaja, and P. Ettmayer, "Lattice parameters and thermal expansion of Ti(CxN1-x), Zr(CxN1-x), Hf(CxN1-x) and TiN1-x from 298 to 1473 K as investigated by high-temperature X-ray diffraction," *Journal of Alloys and Compounds*, vol. 215, no. 1, pp. 121–126, Nov. 1994, ISSN: 0925-8388. DOI: 10.1016/0925-8388(94) 90828-1.

[169] C. F. Macrae, I. Sovago, S. J. Cottrell, *et al.*, "Mercury 4.0: From visualization to analysis, design and prediction," *Journal of Applied Crystallography*, vol. 53, no. 1, pp. 226–235, 2020. [Online]. Available: https://doi.org/10.1107/S1600576719014092.

[170] C. A. Schneider, W. S. Rasband, and K. W. Eliceiri, "NIH Image to ImageJ: 25 years of image analysis," *Nature Methods*, vol. 9, no. 7, pp. 671–675, Jul. 2012, ISSN: 1548-7091, 1548-7105. DOI: 10.1038/nmeth.2089.

[171] *ASTM E92: Standard Test Methods for Vickers Hardness and Knoop Hardness of Metallic Materials*, 2017. DOI: 10.1520/E0008_E0008M-16A.

[172] A. Salmasi, S. J. Graham, I. Galbraith, *et al.*, "Mobilities of Ti and Fe in disordered TiFe-BCC assessed from new experimental data," *Calphad*, vol. 74, p. 102 300, Sep. 2021, ISSN: 0364-5916. DOI: 10.1016/j.calphad.2021.102300.

[173] H. Nakajima, K. Yusa, and Y. Kondo, "Diffusion of iron in a diluted alpha-Ti-Fe alloy," *Scripta Materialia,*, vol. 34, no. 2, p. 5, 1995.

[174] R. W. Balluffi and R. F. Mehl, "Grain boundary diffusion mechanisms in metals," *Metallurgical Transactions A*, vol. 13, no. 12, pp. 2069–2095, Dec. 1982, ISSN: 1543-1940. DOI: 10.1007/BF02648378.

[175] G. Pardal, S. Ganguly, S. Williams, and J. Vaja, "Dissimilar metal joining of stainless steel and titanium using copper as transition metal," *The International Journal of Advanced Manufacturing Technology*, vol. 86, no. 5-8, pp. 1139–1150, Sep. 2016, ISSN: 0268-3768, 1433-3015. DOI: 10.1007/s00170-015-8110-2.

[176] N. Naveen Kumar, G. D. Janaki Ram, S. S. Bhattacharya, H. C. Dey, and S. K. Albert, "Spark Plasma Welding of Austenitic Stainless Steel AISI 304L to Commercially Pure Titanium," *Transactions of the Indian Institute of Metals*, vol. 68, no. S2, pp. 289–297, Sep. 2015, ISSN: 0972-2815, 0975-1645. DOI: 10.1007/s12666-015-0589-6.

[177] J. Garay, U. Anselmi-Tamburini, and Z. Munir, "Enhanced growth of intermetallic phases in the Ni–Ti system by current effects," *Acta Materialia*, vol. 51, no. 15, pp. 4487–4495, Sep. 2003, ISSN: 13596454. DOI: 10.1016/S1359-6454(03)00284-2.

[178] R. Li, P. Niu, S. Deng, T. Yuan, and G. Liu, "Diffusivity of Ti-Ni Diffusion Couple Enhanced by Pulse Current During Spark Plasma Sintering," *Metallurgical and Materials Transactions B*, vol. 51, no. 1, pp. 6–10, Feb. 2020, ISSN: 1073-5615, 1543-1916. DOI: 10.1007/s11663-019-01725-7.

[179] H. Nakajima and M. Koiwa, "Diffusion in Titanium," *ISIJ International*, vol. 31, no. 8, pp. 757–766, 1991.

[180] S. J. Graham, L. L. Benson, and M. Jackson, "Direct electrochemical production of pseudo-binary Ti–Fe alloys from mixtures of synthetic rutile and iron(III) oxide," *Journal of Materials Science*, vol. 55, no. 33, pp. 15 988–16 001, Nov. 2020, ISSN: 1573-4803. DOI: 10.1007/s10853-020-05136-x.

[181] D. J. Fray and G. Z. Chen, "Reduction of titanium and other metal oxides using electrodeoxidation," *Materials Science and Technology*, vol. 20, no. 3, pp. 295–300, Mar. 2004, ISSN: 0267-0836, 1743-2847. DOI: 10.1179/026708304225012242.

[182] C. Schwandt and D. J. Fray, "The Electrochemical Reduction of Chromium Sesquioxide in Molten Calcium Chloride under Cathodic Potential Control," *Zeitschrift für Naturforschung A*, vol. 62, no. 10-11, Jan. 2007, ISSN: 1865-7109, 0932-0784. DOI: 10.1515/zna-2007-10-1115.

[183] D. Sri Maha Vishnu, N. Sanil, L. Shakila, *et al.*, "A study of the reaction pathways during electrochemical reduction of dense Nb2O5 pellets in molten CaCl2 medium," *Electrochimica Acta*, vol. 100, pp. 51–62, Jun. 2013, ISSN: 00134686. DOI: 10.1016/j.electacta.2013.03.135.

[184] T. Norgate, S. Jahanshahi, and W. Rankin, "Assessing the environmental impact of metal production processes," *Journal of Cleaner Production*, vol. 15, no. 8-9, pp. 838–848, Jan. 2007, ISSN: 09596526. DOI: 10.1016/j.jclepro.2006.06.018.

[185] S. Jiao and D. J. Fray, "Development of an Inert Anode for Electrowinning in Calcium Chloride–Calcium Oxide Melts," *Metallurgical and Materials Transactions B*, vol. 41, no. 1, pp. 74–79, Feb. 2010, ISSN: 1073-5615, 1543-1916. DOI: 10.1007/s11663-009-9281-8.

[186] W. Zhang, Z. Zhu, and C. Y. Cheng, "A literature review of titanium metallurgical processes," *Hydrometallurgy*, vol. 108, no. 3-4, pp. 177–188, Jul. 2011, ISSN: 0304386X. DOI: 10.1016/j.hydromet.2011.04.005.

[187] E. Reverte, S. A. Tsipas, and E. Gordo, "Oxidation and Corrosion Behavior of New Low-Cost Ti-7Fe-3Al and Ti-7Fe-5Cr Alloys from Titanium Hydride Powders," *Metals*, vol. 10, no. 2, p. 254, Feb. 2020, ISSN: 2075-4701. DOI: 10.3390/met10020254.

[188] R. I. Jaffee, "The Physical Metallurgy of Titanium Alloys," *Progress in Metal Physics*, vol. 7, pp. 65–163, 1958. DOI: 10.1016/0502-8205(58)90004-2.

[189] M. Panigrahi, E. Shibata, A. Iizuka, and T. Nakamura, "Production of Fe–Ti alloy from mixed ilmenite and titanium dioxide by direct electrochemical reduction in molten calcium chloride," *Electrochimica Acta*, vol. 93, pp. 143–151, Mar. 2013, ISSN: 00134686. DOI: 10.1016/j.electacta.2013.01.089.

[190] M. Panigrahi, A. Iizuka, E. Shibata, and T. Nakamura, "Electrolytic reduction of mixed (Fe, Ti) oxide using molten calcium chloride electrolyte," *Journal of Alloys and Compounds*, vol. 550, pp. 545–552, Feb. 2013, ISSN: 09258388. DOI: 10.1016/j.jallcom.2012.09.029.

[191] M. Donachie, "Understanding the Metallurgy of Titanium," in *Titanium: A Technical Guide, 2nd Edition*, ser. Ingenieria e Ingenieria Civil, ASM International, 2000, ISBN: 978-1-61503-062-0. [Online]. Available: https://books.google.co.uk/books?id=HgzukknbNGAC.

[192] I. Cadoff and J. P. Nielsen, "Titanium-carbon phase diagram," *Journal of Metals*, vol. 5, no. 2, p. 248, 1953.

[193] S. A. Mantri, D. Choudhuri, A. Behera, J. D. Cotton, N. Kumar, and R. Banerjee, "Influence of Fine-Scale Alpha Precipitation on the Mechanical Properties of the Beta Titanium Alloy Beta-21S," *Metallurgical and Materials Transactions A*, vol. 46, no. 7, pp. 2803–2808, Jul. 2015, ISSN: 1073-5623, 1543-1940. DOI: 10.1007/s11661-015-2944-y.

[194] *ASTM E8/E8M: Standard Test Methods for Tension Testing of Metallic Materials*, 2016. DOI: 10.1520/E0008_E0008M-16.

[195] L. Liang, L. Dachun, W. Heli, L. Kaihua, D. Juhai, and J. Wenlong, "Removal of chloride impurities from titanium sponge by vacuum distillation," *Vacuum*, vol. 152, pp. 166–172, Jun. 2018, ISSN: 0042207X. DOI: 10.1016/j.vacuum.2018.02.030.

[196] S. Rajan Soundararajan, J. Vishnu, G. Manivasagam, and N. Rao Muktinutalapati, "Heat Treatment of Metastable Beta Titanium Alloys," in *Welding - Modern Topics*, IntechOpen, Jan. 2021, ISBN: 978-1-83881-895-1 978-1-83881-896-8. DOI: 10.5772/intechopen.92301.

[197] V. A. Joshi, *Titanium Alloys: An Atlas of Structures and Fracture Features*. Boca Raton: CRC/Taylor & Francis, 2006, ISBN: 978-0-8493-5010-8.

[198] S. Tammas-Williams, P. J. Withers, I. Todd, and P. B. Prangnell, "The Influence of Porosity on Fatigue Crack Initiation in Additively Manufactured Titanium Components," *Scientific Reports*, vol. 7, no. 1, p. 7308, Dec. 2017, ISSN: 2045-2322. DOI: 10.1038/s41598-017-06504-5.

[199] R. Chaudhari and R. Bauri, "Microstructure and Mechanical Properties of Titanium Processed by Spark Plasma Sintering (SPS)," *Metallography, Microstructure, and Analysis*, vol. 3, no. 1, pp. 30–35, Feb. 2014, ISSN: 2192-9262, 2192-9270. DOI: 10.1007/s13632-013-0112-6.

[200] M. Shahedi Asl, A. Sabahi Namini, A. Motallebzadeh, and M. Azadbeh, "Effects of sintering temperature on microstructure and mechanical properties of spark plasma sintered titanium," *Materials Chemistry and Physics*, vol. 203, pp. 266–273, Jan. 2018, ISSN: 02540584. DOI: 10.1016/j.matchemphys.2017.09.069.

[201] J. H. Shon, I.-B. Song, K.-S. Cho, *et al.*, "Effect of particle size distribution on microstructure and mechanical properties of spark-plasma-sintered titanium from CP-Ti powders," *International Journal of Precision Engineering and Manufacturing*, vol. 15, no. 4, pp. 643–647, Apr. 2014, ISSN: 2234-7593, 2005-4602. DOI: 10.1007/s12541-014-0382-1.

[202] J. Umeda, T. Tanaka, T. Teramae, *et al.*, "Microstructures analysis and quantitative strengthening evaluation of powder metallurgy Ti–Fe binary extruded alloys with ($A+\beta$)-dual-phase," *Materials Science and Engineering: A*, vol. 803, p. 140 708, Jan. 2021, ISSN: 09215093. DOI: 10.1016/j.msea.2020.140708.

[203] Y. Liu, L. Chen, H. Tang, C. Liu, B. Liu, and B. Huang, "Design of powder metallurgy titanium alloys and composites," *Materials Science and Engineering: A*, vol. 418, no. 1-2, pp. 25–35, Feb. 2006, ISSN: 09215093. DOI: 10.1016/j.msea.2005.10.057.

[204] S. Deng, T. Yuan, R. Li, *et al.*, "Influence of electric current on interdiffusion kinetics of W-Ti system during spark plasma sintering," *International Journal of Refractory Metals and Hard Materials*, vol. 75, pp. 184–190, Sep. 2018, ISSN: 02634368. DOI: 10.1016/j.ijrmhm.2018.04.014.

[205] H. Sina, S. Iyengar, and S. Melin, "Sintering and reaction behaviour in Ni-Ti powder mixtures," in *Advances in Powder Metallurgy & Particulate Materials - 2012 : Proceedings of the 2012 International Conference on Powder Metallurgy & Particulate Materials : PowderMet 2012, June 10-13, Nashville*, I. Donaldson and N. T. Mares, Eds., vol. 05, Metal Powder Industries Federation, Princeton, New Jersey, 2012, pp. 05–45–05–57, ISBN: 978-0-9853397-2-2.

[206] Y. Murayama, A. Okubo, and H. Kimura, "Mechanical Properties of Ti-Cr System Alloys Prepared by Powder Metallurgy," in *Proceedings of the 11th World Conference on Titanium*, Kyoto, Japan, 2007.

[207] A. B. Elshalakany, S. Ali, A. Amigó Mata, *et al.*, "Microstructure and Mechanical Properties of Ti-Mo-Zr-Cr Biomedical Alloys by Powder Metallurgy," *Journal of Materials Engineering and Performance*, vol. 26, no. 3, pp. 1262–1271, Mar. 2017, ISSN: 1059-9495, 1544-1024. DOI: 10.1007/s11665-017-2531-z.

Permissions

Chapter 2

Figures 2.1, 2.3 and 2.4 from [3] are licensed for use by Springer Nature under license number 5238940776340.

Figure 2.2 from [23] is licensed for use by John Wiley and Sons under license number 5238950075471.

Figure 2.7 from [52] is permitted for use by IOP Publishing as the article is distributed under the terms of the Creative Commons CC BY 3.0 license.

Figure 2.9 from [70] is licensed for use by the Royal Society of Chemistry under license number 1183807-1.

Figure 2.10 from [17] is permitted for use by Springer Nature as the article is distributed under the terms of the Creative Commons CC BY 4.0 license.

Figure 2.11 from [85] is permitted for use by Springer Nature as the article is distributed under the terms of the Creative Commons CC BY 4.0 license.

Figure 2.12 from [97] is licensed for use by Elsevier under license number 5238951253771.

Figure 2.14 from [102] is licensed for use by Elsevier under license number 5238951499533.

Figure 2.15 from [104] is licensed for use by IOP Publishing under license number 1183809-1.

Figure 2.17 from [10] is permitted for use by MDPI as the article is distributed under the terms of the Creative Commons CC BY 4.0 license.

Figure 2.19 from [135] is permitted for use by MDPI as the article is distributed under the terms of the Creative Commons CC BY 4.0 license.

Figure 2.20 from [136] is permitted for use by Taylor & Francis as the article is distributed under the terms of the Creative Commons CC BY 4.0 license.

Figure 2.4 from [156] is licensed for use by Elsevier under license number 5238961195897.

Figure 2.23 from [157] is licensed for use by Elsevier under license number 5238961351154.

Chapter 4

Some text, data and images in this chapter are also used in [172]. "Elsevier author rights allows authors to re-use portions, excerpts, and their own figures or tables in other works without permission or payment (with full acknowledgement of the original article)".

Chapter 5

Section 5.2 is from [180] and is permitted for use by Springer Nature as the article is distributed under the terms of the Creative Commons CC BY 4.0 license.

Chapter 6

Figure 6.10 a from [203] is licensed for use by Elsevier under license number 5238970620621.

Figure 6.10 b from [151] is licensed for use by Elsevier under license number 5238970748134.

Figure 6.10 c from [21] is licensed for use by Elsevier under license number 5238970859778.

Figure 6.10 d from [202] is licensed for use by Elsevier under license number 5238970970290.